Imperial College London

Testing, simulation and optimisation of additively manufactured structural hollow sections

By

Ruizhi Zhang

Department of Civil and Environmental Engineering

Imperial College London

London SW7 2AZ

A thesis submitted for the degree of

Doctor of Philosophy

February 2022, London

Statement of Originality

I confirm that this thesis 'Testing, simulation and optimisation of additively manufactured structural hollow sections' is my own work and that any material from published or unpublished work from others is appropriately referenced. This thesis is submitted to Imperial College London for the degree of Doctor of Philosophy and has not been submitted for a degree of any other qualification at another university.

Ruizhi Zhang

February 2022, London

Copyright Declaration

Abstract

Additive manufacturing (AM) is gaining increasing prominence in the construction industry, offering the potential for enhanced design freedom and reduced material use. However, the performance of additively manufactured metallic structural elements and the possible benefits associated with the attainable optimised geometries have seldom been investigated. The primary aim of this study is therefore to conduct an experimental and numerical investigation of additively manufactured metallic components, considering material behaviour, welded components and optimised tubular profiles.

An experimental investigation was first conducted to examine the microstructural and mechanical properties of AM materials. Two grades of powder bed fusion (PBF) stainless steel (316L and CX) were considered, and the weldability and joining characteristics of PBF 316L stainless steel were also examined. The underlying microstructures were characterised and correlated with the measured mechanical properties from tensile coupon tests.

At the cross-sectional level, axial compression tests were carried out on PBF circular hollow sections; advanced measuring techniques, including 3D laser-scanning and digital image correlation, were employed in the tests. Finite element (FE) models were developed to replicate the test results and to generate supplementary cross-sectional resistance data. Comparisons between design predictions and the test and FE data were made to evaluate the applicability of the existing codified design rules to additively manufactured cross-sections.

In order to increase the axial compressive resistance and to reduce the imperfection sensitivity of very slender circular cross-sections (or cylindrical shells), optimised corrugated shells were sought through the use of the Particle Swarm Optimisation algorithm in conjunction with cross-section profile generation and numerical analyses. An experimental investigation into the cross-sectional behaviour of the resulting optimised shells, additively manufactured by PBF in 316L and CX stainless steels, was undertaken. The test results verified that the corrugated cylindrical shells achieved significantly higher capacities than their circular counterparts and with reduced imperfection sensitivity.

Acknowledgements

This research was carried out under the supervision of Professor Leroy Gardner in the Department of Civil and Environmental Engineering at Imperial College London. I would like to express my deepest gratitude and appreciation to him for his expert advice and continuous support and encouragement throughout this project, and for his dedication and enthusiasm towards the work that have inspired me and shaped my attitudes to research. I would like to extend my sincere thanks to Dr Craig Buchanan for his expertise and guidance in conducting experiments and writing academic papers.

I would like to acknowledge the financial support for my PhD programme provided by the China Scholarship Council. Special thanks should be extended to Dr Mohsen Amraei, Ville-Pekka Matilainen, Professor Heidi Piili at LUT University and Professor Antti Salminen at University of Turku for manufacturing the test specimens for the experimental programme.

I am also thankful to Dr Ben Britton for offering me the opportunity to conduct microstructural tests in the Engineering Alloys Lab and Harvey Flower Electron Microscopy Suite in the Department of Materials at Imperial College London. Further thanks should be given to Dafni Daskalaki Mountanou, Dr Mahmoud Ardakani, Dr Thibaut Dessolier for their help in the microstructural tests. A major part of the experimental work was undertaken in the Structures Laboratory at Imperial College London. I am grateful to all the technicians who contributed to this project – Gordon Herbert, Paul Crudge, Les Clark, Alfredo Olivo, Trevor Stickland and Bob Hewitt, for their practical knowledge and continuous patience and advice.

I wish to express my deep appreciation to my wonderful friends and colleagues in the Steel Structures Group at Imperial College London for making this journey more enjoyable, including Dr Fiona Walport, Xi Guo, Harry Slack, Ben Weber, Ying Zhang, Luke Lapira, Dr Pinelopi Kyvelou, Dr Jun Ye, Dr Jie Wang, Cheng Huang, Zichang Yang, Yufei Zhu, Dr Nicolaos Hadjipantelis, Dr Gabriel Santos, Dr Constantinos Kyprianou and Dr Behnam Behzadi Sofianou. I am also grateful to my friends during my time at Imperial – Dr Ruiqiang

Zhang, Wing Wan, Dr Bowen Xu, Shiying Zheng, Kai Zhang, Dr Shangzhi Li, and Wenhao Yu and Jalal R J Al-Lami for their kind help in the Department of Materials.

I also wish to express my special thanks to some of my best friends, particularly Dr Wenjie Cui and Dr Fangce Guo, for their caring and kindness to me from first sight, Dr Xiang Yun and Dr Xin Meng, for supporting me on and beyond research and teaching me to look at the things from different perspectives; Dr Xi Chen and Dr Chunyan Quan, for always being independent, strong and passionate about life, standing by my side and sharing both happiness and sorrow with me during the toughest time of my PhD study, and Dr Fangying Wang, Dr Zhongxing Wang and Yong Zhu, for their optimism, work ethic, erudite knowledge and warmheartedness. My time at Imperial has been made significantly more enjoyable and enriching by our friendship, and all memorable moments we shared will remain with me forever.

To my best friends Chen Hu, I owe big thanks for her support and love when I was new in the UK, and Dr Bijun Xie, for her expert advice and aid but more importantly for her friendship, which I am very much appreciated.

Last but not least, I would like to express my deepest thanks to my parents – Xinwu Zhang and Yufang Fan, to my grandparents and to my sister and brother, for their unconditional love, never ending support and encouragement and belief in my abilities throughout my life, particularly during my PhD study. This thesis is dedicated to them with all my love.

Contents

Notation

A	Cross-sectional area
A_{eff}	Effective cross-sectional area
A_{Arch}	Cross-sectional area measured based on Archimedes' method
A_{Laser}	Cross-sectional area measured using 3D laser-scanning
b_{s}	Stiffener width
c_1	Cognitive acceleration factor
c_2	Social acceleration factor
D	Outer diameter
d_{10}, d_{50}, d_{90}	Characteristic particle sizes
d_{s}	Stiffener spacing
E	Young's modulus or Energy input of laser welding
E_0	Initial tangent modulus
$E_{0.2}$	Tangent modulus at the 0.2% proof stress
E_{red}	A reduced value of the elastic modulus
E_{sec}	Secant modulus at the 0.2% proof stress
f_{ult}	Compressive stress at the ultimate load of corrugated or stiffened shell

$f_{ult,cyl}$	Compressive stress at the ultimate load of reference circular shell
$f_{y,k}$	Yield strength
g	Gravitational acceleration
G	Temperature gradient
$\boldsymbol{G}_{best}^{k}$	Global best position of all particles in the swarm up to the kth iteration
h_s	Stiffener height
k	Current iteration number
k_{max}	Maximum number of iterations
L	Length
L_{cal}	Length measured using callipers
l_p	Perimeter of the cross-section centreline
M	Number of half-sine circumferential waves
$m_{1.0}$	Ramberg-Osgood strain hardening exponent between $\sigma_{0.2}$ and $\sigma_{1.0}$ points
m_u	Ramberg-Osgood strain hardening exponent between $\sigma_{0.2}$ and σ_u points
n	Ramberg-Osgood strain hardening exponent
N	Number of control points or Axial load
N_p	Swarm size
N_s	Stiffener number
N_u	Ultimate load
$N_{u,csm}$	Resistance prediction calculated according to continuous strength method

$N_{u,EC3}$	Resistance prediction calculated according to Eurocode 3
$N_{u,FE}$	Numerical ultimate load
$N_{u,pred}$	Predicted ultimate resistance
$N_{u,test}$	Experimental ultimate load
N_y	Yield load
P	Welding power or Axial load or Probability
P_0	Buckling load of perfect shell
P_+	Buckling load of imperfect shell with positive imperfection amplitude
P_-	Buckling load of imperfect shell with negative imperfection amplitude
$\boldsymbol{P}_{best,j}^{k}$	Best position of particle j over its history up to the kth iteration
P_{cl}	Classical elastic buckling load
P_{cr}	Buckling load
P_u	Ultimate load
$P_{u,wavy}$	Ultimate load of the optimised wavy shell
Q	Fabrication quality parameter
r	Radius of the shell middle surface
R	Solidification growth rate
r_1, r_2	Two random values within the range [0, 1]
R_{cr}	Critical buckling resistance ratio
R_d	Design elastic-plastic buckling resistance ratio

R_{GMNIA}	Buckling resistance ratio obtained from a GMNIA
R_k	Characteristic reference resistance ratio
R_{LBA}	Elastic critical buckling resistance ratio determined based on an LBA
R_{MNA}	Perfect plastic reference resistance ratio determined based on an MNA
R_{pl}	Plastic reference resistance ratio
S	Welding speed
S_0	Original cross-sectional area of the parallel length
t	Wall thickness
t_{mod}	Modified thickness
u_x, u_y and u_z	Displacements in the x, y and z direction
u_{Rx}, u_{Ry} and u_{Rz}	Rotations about the x, y and z axis
$\boldsymbol{V}_j^k$	Velocity vector of control points
V_{Arch}	Volume measured based on Archimedes' method
V_{Laser}	Volume measured using 3D laser-scanning
V_{max}	Maximum velocity
w	Inertia weight factor
W	Weight
W_{air}	Weight of test specimen in air
w_{max}	Maximum inertia weight
w_{min}	Minimum inertia weight

$W_{u,wavy}$	Weight of the optimised wavy shell
W_{water}	Weight of test specimen in water
α	Elastic buckling reduction factor in buckling strength assessment
β	Plastic range factor in buckling interaction
γ	Imperfection sensitivity factor
γ_M	Partial safety factor for resistance of cross-sections
δ	End shortening or Lateral deflection
$\mathbf{\Delta}$	A set of randomly selected imperfection amplitudes
Δr	Maximum allowable radial deviation of the control points or amplitude of half-sine waves
Δt	Pseudo time increment
δ_u	Deformation at ultimate load
$\delta_{u,FE}$	Numerical deformation at ultimate load
$\delta_{u,test}$	Experimental deformation at ultimate load
$\Delta\omega_k$	Characteristic imperfection amplitudes in EN 1993-1-6
ε	Engineering strain or Eurocode 3 material parameter
$\varepsilon_{0.2}$	Total strain at 0.2% proof stress
$\varepsilon_{1.0}$	Total strain at 1.0% proof stress
ε_f	Fracture strain over the marked gauge length
ε_u	Strain at ultimate stress

$\varepsilon_{u,gl}$	Average global strain at the ultimate stress over the parallel length
η	Interaction exponent for buckling
θ	Angle from the longitudinal axis of the coupon to the build plate
θ_i	Circumferential position
$\bar{\lambda}_0$	Squash limit slenderness
$\bar{\lambda}_c$	Cross-section slenderness
$\bar{\lambda}_p$	Plastic limit slenderness
$\boldsymbol{\rho}$	Radial position vector of control points or Density or Reduction factor for plate buckling
$\boldsymbol{\rho}_j^k$	Position vector of control points
ρ_i	Radial position
ρ_{max}, ρ_{min}	Upper and lower radius limits for the control points
ρ_w	Density of water
σ	Engineering stress
$\sigma_{0.2}$	0.2% proof stress
$\sigma_{1.0}$	1.0% proof stress
σ_{cr}	Elastic critical buckling stress
σ_u	Ultimate stress
υ	Poisson's ratio
ϕ	Angle between the long face of the coupon cross-section and the build

	plate
χ	Buckling reduction factor
χ_h	Hardening limit
ψ	Angle between the recoating direction and the longitudinal axis of the coupon
ω_0	Local imperfection amplitude
$\omega_{95\%}$	Deterministic imperfection amplitude with a CDF value of 95%
ω_a	Assumed imperfection amplitude in optimisation
ω_{max}	Maximum imperfection amplitude
ω_p	A given imperfection amplitude

List of Figures

List of Tables

List of Publications

The peer-reviewed journal articles that have originated from the work presented in this thesis are listed below:

Zhang, R., Gardner, L., Buchanan, C., Matilainen, V. P., Piili, H., & Salminen, A. (2021). Testing and analysis of additively manufactured stainless steel CHS in compression. *Thin-Walled Structures*, 159, 107270.

Zhang, R., Buchanan, C., Matilainen, V. P., Daskalaki-Mountanou, D., Britton, T. B., Piili, H., Salminen, A. & Gardner, L. (2021). Mechanical properties and microstructure of additively manufactured stainless steel with laser welded joints. *Materials and Design*, 208, 109921.

Zhang, R., Meng, X. & Gardner, L (2022). Shape optimisation of stainless steel corrugated cylindrical shells for additive manufacturing. *Engineering Structures*, Submitted.

Zhang, R., Gardner, L., Amraei, M., Buchanan, C. & Piili, H. (2022). Testing and analysis of additively manufactured stainless steel corrugated shells in compression. *Journal of Engineering Mechanics*, Submitted.

Zhang, R., Gardner, L., Amraei, M., Dessolier T., Britton, T. B. & Piili, H. (2022). Microstructure, mechanical properties and cross-sectional behaviour of additively manufactured stainless steel cylindrical shells. *Thin-Walled Structures*, Submitted.

The following is a list of conference proceeding papers based on the work presented in this thesis:

Zhang, R., & Gardner, L. (2020). 3D printed stainless steel structural components: Microstructure and properties. In *Proceedings of the 22nd Young Researchers' Conference of the Institution of Structural Engineers*, 4 September 2020, London, UK.

Zhang, R., Gardner, L., Meng, X., Buchanan, C., Matilainen, V. P., Piili, H., & Salminen, A. (2021). Optimisation and compressive testing of additively manufactured stainless steel corrugated shells. In *Proceedings of Eurosteel 2021 – 9th European Conference on Steel and Composite Structures*, 1–3 September, Sheffield, UK.

Zhang, R., & Gardner, L. (2022). Additively manufactured stainless steel corrugated shells: shape optimisation and experimental validation. In *Proceedings of the 23rd Young Researchers' Conference of the Institution of Structural Engineers*, 15 March 2022, London, UK.

Zhang, R., Gardner, L. & Buchanan, C. (2022). Testing of additively manufactured stainless steel material and cross-sections. In *Tenth International Conference on Advances in Steel Structures (ICASS2020)*, 3–5 August, Chengdu, China.

Zhang, R., Amraei, M., Piili, H. & Gardner, L. (2022). Microstructure, material properties and cross-sectional behaviour of additively manufactured stainless steel cylindrical shells. In *The International Colloquium on Stability and Ductility of Steel Structures (SDSS2022)*, 14-16 September, Aveiro, Portugal.

Chapter 1

Introduction

1.1 General background

Steel structures play a prominent role in the construction sector, underpinned by the continuous developments in material science, manufacturing techniques and design practice. Stainless steel, as a high-performance construction material that combines the strength and stiffness connected with ferrous alloys with the inherent corrosion resistance as a result of the high chromium content, is becoming increasingly popular in structural applications (Gardner, 2019). A notable early example of the use of stainless steel in construction is the Chrysler Building in New York, as shown in Figure 1.1. More recent applications of stainless steel put more emphasis on its favourable durability and mechanical properties rather than simply its aesthetics, including buildings, towers, domes, roofs in stadia, flood barriers, footbridges and road bridges.

Circular hollow sections (CHS) are a common section profile for structural elements, often with superior structural performance over both open and other closed sections. Circular hollow sections have excellent flexural stiffness and bending resistance about all axes, high torsional resistance, reduced drag loading in wind or fluids, considerably smaller exposed external area (leading to the reduced maintenance cost) and the ability to be filled with concrete for increased axial capacity or to have air or water circulated for fire protection, heating and ventilation (Wardenier, 2001). Owing to these desirable structural characteristics, circular hollow sections are often applied in buildings and halls, bridges, offshore and marine structures and hydraulic structures. The last few decades have witnessed continuously increased applications of stainless steel circular hollow sections in many landmark structures, such as the arch of Celtic Gateway Bridge completed in 2006 in UK (Figure 1.2) and the Double Helix Bridge built almost entirely using duplex stainless steel in Singapore, comprising a walkway surrounded by opposing double helix structures (Figure 1.3).

Figure 1.1: The Chrysler Building, New York
(https://thetowerinfo.com/buildings-list/chrysler-building/)

Additive manufacturing (AM), commonly referred to as 3D printing, is a disruptive technology that allows free-form parts to be built layer-by-layer based on a three-dimensional (3D) computer model (Frazier, 2014; Buchanan & Gardner, 2019). The roots of AM can be tracked back to photo sculpture in the 1860s and topoglyphs in the 1890s (Gao et al., 2015). Recent decades have seen an exponential rise in the development of AM techniques, alongside rapid advances in materials and automation (Song et al., 2017). As a result, AM systems are now commercially available for a wide range of materials, including polymers, ceramics, composites and metals (Frazier, 2014) and are used across a range of industries, such as the aerospace, automotive, nuclear, chemical and biomedical industries (Buchanan & Gardner, 2019; Olakanmi, Cochrane & Dalgarno, 2015; Ngo et al., 2018).

Figure 1.2: Stainless steel arch in the Celtic Gateway Bridge, UK
(https://structurae.net/en/structures/the-celtic-gateway-bridge)

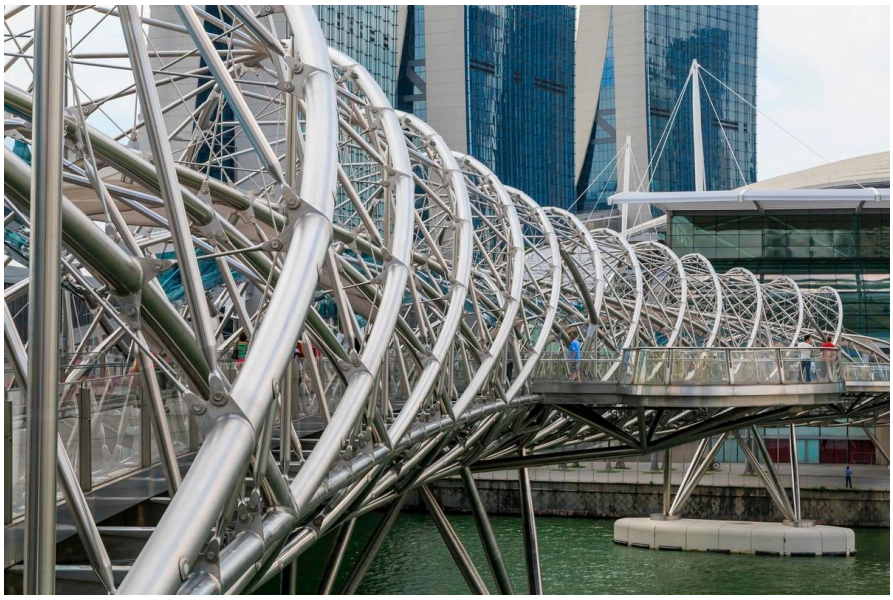

Figure 1.3: Stainless steel CHS truss in the Double Helix Bridge, Singapore
(https://www.ies.org.sg/)

AM offers a number of advantages over conventional processes used in the engineering sector, including the ability to generate complex geometries with high precision, design-customisation, reduced material use and reduced wastage (Buchanan & Gardner, 2019; Kanyilmaz et al., 2022;

Ye et al., 2021), and has been slowly explored in the construction industry. Early applications of AM in construction emerged in the late 1990s and were predominantly limited to cement-based materials (Wu, Wang & Wang, 2016); a notable example is the 1900 ft^2 concrete 3D printed home in New York, which took only 48 hours of print time using a large 3D printer and less than $6000 in materials (Figure 1.4). Although metal additive manufacturing is beginning to be viewed as a viable manufacturing technique and was employed to construct the world's first metal 3D printed pedestrian bridge that has been placed across a canal in Amsterdam in 2018 (Figure 1.5), it is still in its infancy in the construction industry.

Figure 1.4: Concrete 3D printed home, New York
(https://www.inputmag.com/tech)

Figure 1.5: The world's first metal 3D printed steel bridge
(https://www.3dnatives.com/)

To support the growth in use of additively manufactured metallic structural elements in construction, it is necessary to examine the structural performance of such elements, to assess the suitability of existing metallic design provisions and to explore the potential opportunities for the adoption of this novel manufacturing technique.

1.2 Research aims

The primary aim of this research is to study the structural performance of additively manufactured stainless steel structural hollow sections at the microstructural, material and cross-sectional level and to develop corrugated cylindrical shells with high local buckling resistances. More specifically, the objectives of this research project include:

- To examine the microstructure and mechanical properties of additively manufactured stainless steels;
- To assess the weldability of additively manufactured stainless steels for the manufacture of larger structural elements;
- To experimentally investigate the local buckling behaviour of additively manufactured stainless steel circular hollow sections in compression;
- To numerically simulate the structural performance of additively manufactured stainless steel circular hollow sections through finite element modelling and generate additional numerical data;
- To assess the accuracy of existing design provisions for additively manufactured stainless steel cross-sections;
- To optimise the cross-section profiles of corrugated cylindrical shells under axial compression;
- To experimentally investigate the local buckling behaviour of additively manufactured stainless steel corrugated cylindrical shells under axial compression;
- To evaluate the applicability of existing cross-section design provisions to additively manufactured stainless steel corrugated cylindrical shells.

1.3 Thesis outline

The microstructure, mechanical properties, optimisation and cross-sectional behaviour of stainless steel circular hollow sections additively manufactured by powder bed fusion (PBF) are addressed in this thesis. A total of seven chapters are presented in this thesis; the introductory chapter (i.e. Chapter 1) briefly describes the general background information of stainless steel circular hollow sections and additive manufacturing and the research aims of this thesis.

Chapter 2 presents a comprehensive review of the literature relevant to the research, including the essential technical knowledge associated with stainless steel powder bed fusion, circular hollow sections, previous experimental work and existing structural design methods and concepts for conventional manufacturing techniques.

Chapter 3 describes a series of experimental investigations into the microstructure and mechanical properties of additively manufactured stainless steels. Full details of the experiments conducted on additively manufactured austenitic and martensitic stainless steels, including those with laser welded joints, are provided. The measured mechanical properties are correlated with the observed microstructures and compared with those of conventionally manufactured stainless steels.

Chapter 4 presents the cross-sectional behaviour and design of additively manufactured circular hollow sections (CHS). An experimental study into additively manufactured stainless steel CHS and parallel numerical simulations are described. The suitability of existing design provisions for additively manufactured metallic cross-sections is then considered.

Chapter 5 introduces an optimisation methodology for free-form stainless steel corrugated cylindrical shells to be produced by additive manufacturing. Optimised cross-section profiles are explored with the objective of maximising local buckling resistance and minimising imperfection sensitivity using Particle Swarm Optimisation (PSO).

Chapter 6 describes an experimental programme performed on the corrugated cylindrical shells obtained through optimisation. The experiments and parallel numerical studies confirm the superiority of free-form corrugated cylindrical shells over circular and other non-circular

cylindrical shell designs and to highlight the advantages of the metallic additive manufacturing technique.

Chapter 7 summarises the key findings and conclusions from this research and the suggested future work.

Chapter 2

Literature review

2.1 Introduction

An introduction to the key concepts and a review of the literature relevant to this thesis are presented in this chapter. Five key topics are covered – metal additive manufacturing, stainless steel in construction, laser welding as a joining method, non-slender and slender circular hollow sections and structural optimisation for additive manufacturing.

2.2 Metal additive manufacturing

This section presents an overview of metal additive manufacturing (AM). The key manufacturing techniques, and the advantages and limitations of metal AM, are first introduced. The current use of AM in construction, as well as existing research on metal AM, are then described.

2.2.1 Overview of additive manufacturing

Additive manufacturing, also known as 3D printing, features the addition of material to build parts layer-by-layer directly from three-dimensional (3D) model data, as opposed to subtractive and formative manufacturing methodologies (ISO/ASTM, 2017). AM techniques commenced in the 1860s in the form of photo sculpture (Gao et al., 2015), and the 'photo-glyph recording' technique patented in the 1950s (Munz, 1956) bears a strong likeness to the modern stereolithography (STL) process, in which a 3D object is generated by first creating a cross-section pattern of the object to be printed. The following decades have seen the significant developments in commercially available manufacturing systems and a variety of feedstock

materials, including polymers, ceramics, composites and metals (Frazier, 2014). Modern AM technologies are classified into seven individual processes by EN ISO/ASTM 52900 (ISO/ASTM, 2017): binder jetting, directed energy deposition, material extrusion, material jetting, powder bed fusion, sheet lamination and vat photopolymerisation.

In recent years, AM techniques have become increasingly adopted in many industries, such as aerospace, automotive, nuclear, chemical and biomedical industries (Buchanan & Gardner, 2019; Olakanmi, Cochrane & Dalgarno, 2015; Ngo et al., 2018), due to their superior ability to produce complex functional components, reduced material waste, minimised assembly processes and reduced tooling costs (Buchanan & Gardner, 2019; Olakanmi, Cochrane & Dalgarno, 2015; Ngo et al., 2018). There are also, however, some limitations and technical challenges for widespread applications in certain industries, such as low printing efficiency, high production costs, considerable design efforts, choice of processing parameters, limited single part sizes for certain techniques and anisotropy and variability in mechanical properties (Buchanan & Gardner, 2019; Yan et al., 2019; Kyvelou et al., 2020); these need further exploration for different practical applications.

When it comes to the metals, three fundamental AM processes – sheet lamination, directed energy deposition (DED) and powder bed fusion (PBF) are categorised according to EN ISO/ASTM 52900 (ISO/ASTM, 2017), as schematically shown in Figure 2.1, with the DED and PBF techniques being considered as the most suitable for use in the construction sector (Olakanmi, Cochrane & Dalgarno, 2015; Ngo et al., 2018; Yan et al., 2019). Sheet lamination is a process where layers of sheet material are cut and bonded together to form the final object. DED is the process of depositing molten metallic powder or wire using focused thermal energy (from a laser, electron beam or plasma arc) to produce the final component; wire and arc additive manufacturing (WAAM) is an example of DED that is being particularly actively explored for construction applications (Kyvelou et al., 2020; Gardner et al., 2020). PBF involves melting metallic powder within a powder bed to form the final three-dimensional component layer-by-layer, and is referred to by equipment manufacturers using a range of terms, including selective laser melting, electron beam melting, direct metal laser sintering and selective laser sintering (Yan et al., 2019; Abdulhameed et al., 2019). The essential difference between PBF and DED is that the material is pre-placed upon the build plate in PBF instead of being fed directly into melt pools in DED (Gouge & Michaleris, 2018). PBF is used mainly for

producing small-scale elements with high precision, and is significantly slower than DED (~50 g/hour compared to ~10 kg/hr) (Yan et al., 2019).

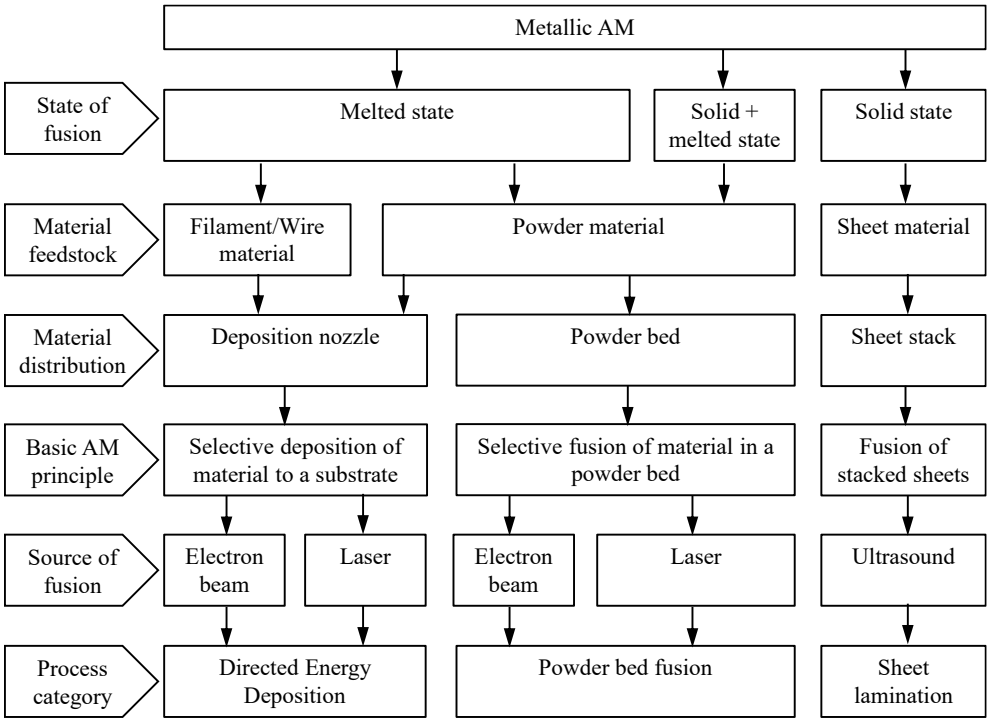

Figure 2.1: Overview of single-step metal AM processing principles (ISO/ASTM, 2017)

The typical laser-based PBF manufacturing process is schematically illustrated in Figure 2.2; the equipment features an ytterbium continuous wave fibre laser, a scanner and a build chamber filled with protective inert argon (EOS, 2010). The geometry of the target 3D part is described in an STL model, which can approximate any 3D model by a triangulated surface and is sliced into two-dimensional layers to be printed. The PBF process starts by spreading a thin layer of powdered material onto the build platform. Next, the powder is fused using a laser beam to form a single cross-section of the part. The build platform is then lowered by the layer thickness and a new layer of powder is deposited by the recoater. These steps are repeated until the entire object is built, after which the loose powder is removed. The un-melted powder can be recycled for future builds (Ruffo, Tuck & Hague, 2006), and the printed object is cut from the build plate.

The use of metal AM in construction is hindered by the high material and equipment cost despite the great material efficiency typically achieved, and long build times and limited single part dimensions, particularly for the aforementioned metallic PBF. Additional challenges for metal AM are the potential anisotropy and variability in mechanical properties along and across

the build direction, although the mechanical properties of additively manufactured metallic parts are in general comparable and even superior to their wrought and cast counterparts (Kok et al., 2018). Proper manufacture of overhanging features also necessitates the use of sacrificial support structures that have to be later removed at the expense of more labour and time (Calignano, 2014). The as-built parts additionally have an inherent rough surface texture from the manufacturing process, which may require post processing for some applications.

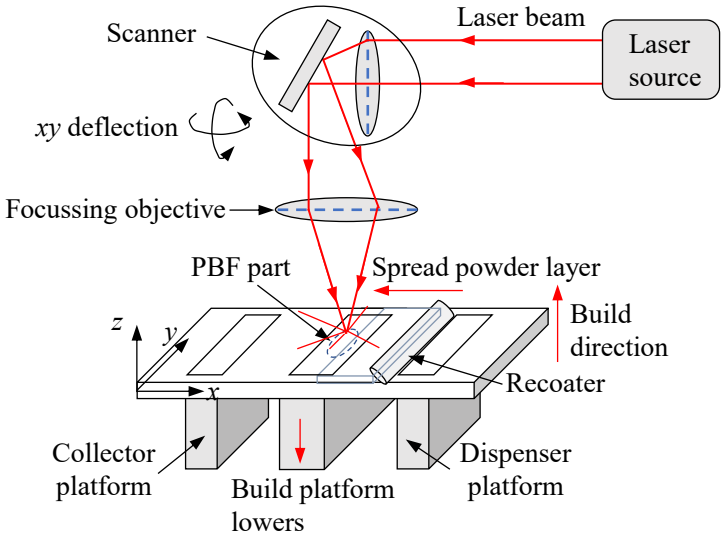

Figure 2.2: Schematic diagram of the laser-based powder bed fusion (PBF) process

2.2.2 Applications

The scope and impact of AM are continuing to expand as it gains acceptance and functionality, making it a viable production method across a wide range of industries. With the abilities to build complex internal structures and to simplify the assembly offered by AM, its applications in the aerospace industry have been well explored. An upgraded nacelle hinge bracket based on topology optimisation and additive manufacturing, as shown in Figure 2.3, achieved a mass reduction of 64% from the original part (Tomlin & Meyer, 2011). The automotive industry benefits from the use of AM to produce optimised lightweight structural components based on generative design algorithms. A brake calliper manufactured from Ti6Al4V by laser-based PBF, as shown in Figure 2.4, exhibited a high tensile strength up to 1250 N/mm^2 and good resistance to temperatures, with a 40% reduced mass compared with its aluminium counterpart.

Figure 2.3: Original HC101 steel (top) and topologically optimised Ti-6Al-4V (bottom) nacelle hinge brackets produced by AM for Airbus A320 airliner (Tomlin & Meyer, 2011)

Figure 2.4: Bugatti's titanium brake calliper printed using laser-based PBF (Wolfsburg, 2018)

Early applications of AM in construction commenced in the late 1990s and were predominantly limited to cement-based materials (Wu, Wang & Wang, 2016); an example of a concrete 3D printed house built in Germany is shown in Figure 2.5. AM of polymers was initially used for conceptual prototypes in construction instead of load-carrying components, since pure polymer parts built by AM exhibit low strength. The strength, stiffness and thermal conductivity can be enhanced through the addition of reinforcement materials to facilitate more widespread structural applications. Typical applications of AM of polymers in construction, are shown in Figure 2.6. The use of metal AM in the construction sector offers the ability to create highly complex customised structures, with the potential for enhanced structural efficiency, optimisation and integration of functional features, reduction of processing steps, improved sustainability and greater architectural freedom (Seifi, 2019). A prominent example of metal AM in construction is the 10.5 m span MX3D stainless steel footbridge (see Figure 2.7(a)), with

the bridge sections printed using four standard industrial robots in a production hall, assembled and then brought to the site (Gardner, 2019). Inspired by the MX3D footbridge, another WAAM steel bridge was constructed on-site above water from two sides with two welding robots (Feucht et al, 2021; Lange et al, 2021) (see Figure 2.7(b)). The manufacture of topologically optimised components and structures can be achieved through WAAM with scope for great innovation and design freedom, such as diagrid columns as supports for tree-houses (Laghi et al., 2020b) (see Figure 2.7(c)), cantilever trusses in carbon steel (Ye et al., 2021) (see Figure 2.7(d)), beam hooks that transfer the load from the beam to the column via bolts (Lange, Feucht & Erven, 2020), stiffeners in I-sections to prevent the flange from bending or buckling (Lange, Feucht & Erven, 2020), clamping elements for diagonal bracings, T-stub end plates, nodes for space frames (Lange, Feucht & Erven, 2020; Heimgartner, 2021) and skeletal floor structures (MX3D, 2021).

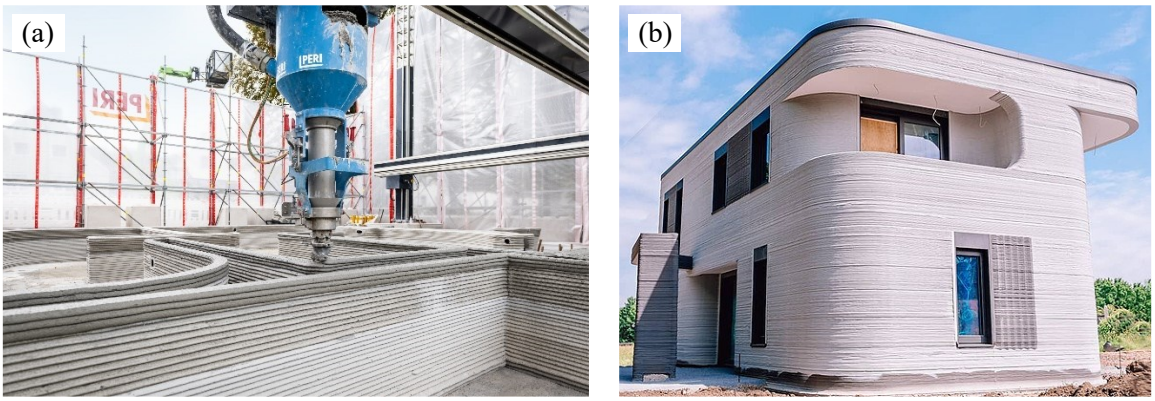

Figure 2.5: Germany's first concrete 3D printed residential building (a) during construction and (b) when completion (Ozdemir, 2021)

Figure 2.6: Examples of polymer 3D printed structures: (a) a curved pavilion model for off-grid living (Crolla et al., 2017) and (b) a micro home in Amsterdam

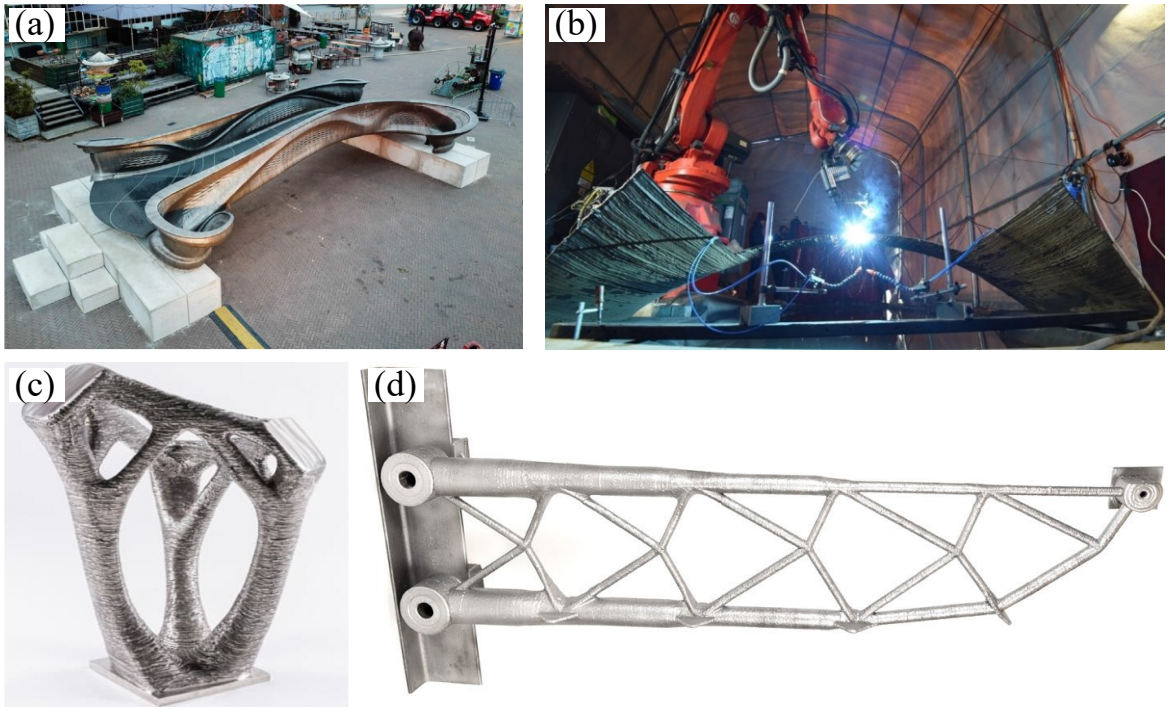

Figure 2.7: Examples of metallic parts produced by WAAM: (a) MX3D footbridge at Dutch Design Week 2018 (Gardner, 2019), (b) 3D-printed bridge on the Lichtwiese (TU Darmstadt, 2019), (c) duplex stainless steel connectors (Heimgartner, 2021) and (d) cantilever truss (Ye et al., 2021)

The first examples of PBF use in construction include topologically optimised laser-based PBF connection nodes manufactured in aluminium (Strauß & Knaack, 2016) (see Figure 2.8) and stainless steel (Galjaard et al., 2015) (see Figure 2.9), and the Messerschmitt-Bolkow-Blohm beams and optimised hinges produced by electron beam melting (EBM) in titanium (Smith et al., 2016). The current high cost of metallic PBF equipment and raw materials, along with the relatively slow printing speed of PBF, is a hindrance to wider adoption in the construction sector. In the case of the aforementioned stainless steel connection nodes, the optimised node produced by PBF cost roughly three times that of a conventionally produced node in 2014 (Buchanan & Gardner, 2019; Gardner, 2019; Galjaard et al., 2015). It is anticipated that with further developments in the manufacturing equipment and materials, along with greater adoption in practice, that production costs and build times will decrease substantially with time.

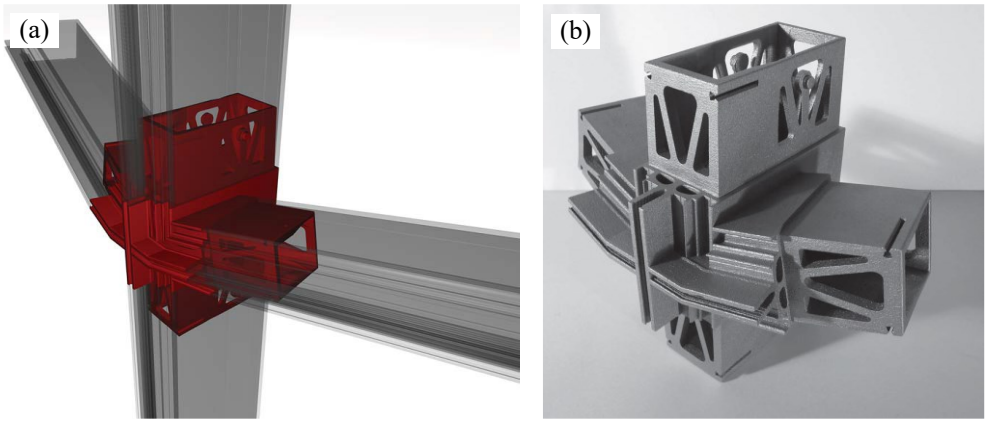

Figure 2.8: PBF aluminium nodes: (a) a rendering of a Nematox façade node (b) an aluminium prototype node (Strauß & Knaack, 2016)

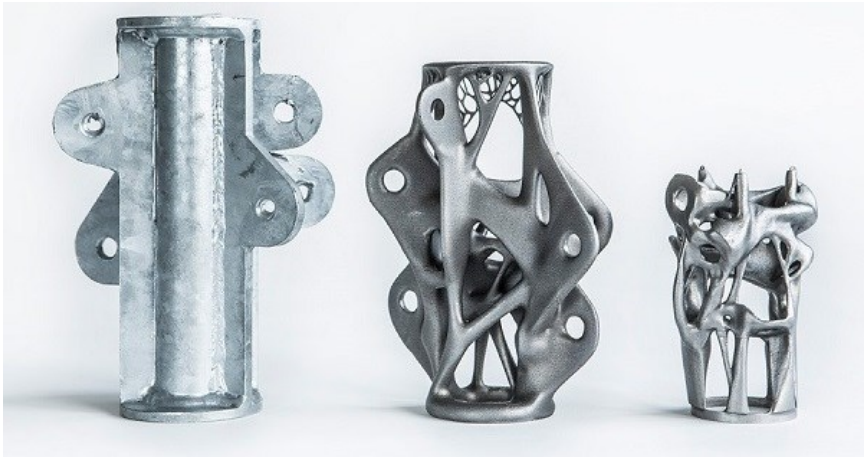

Figure 2.9: Traditional node produced by cutting and welding in galvanized steel (left) and two new nodes produced by AM in maraging steel, first optimised in 2014 (middle) and later re-optimised (right) (Galjaard et al., 2015)

2.2.3 Current research

Over the past two decades, extensive research into metal AM techniques has been carried out to explore printable high-performance materials, fabrication methods, advanced printing equipment and software. From the material point of view, not only the formulation and development of new feedstocks (such as functionally graded materials (Singh et al., 2017), non-homogeneous materials (Pham, 2021) and biodegradable metals for bone-tissue engineering (Koons, Diba & Mikos, 2020)), but also the influence of the printing parameters (such as the build direction, scanning strategy, laser power, scanning speed, layer thickness and hatch

spacing) and post processing (such as heat treatment) on the microstructure and mechanical properties of the finished parts using various AM fabrication methods, have been explored for different industrial applications. To date, mechanical and microstructural studies have been conducted into a range of additively manufactured metallic materials, including titanium alloys (Frazier, 2014; Rafi, Starr & Stucker, 2013; Mower & Long, 2016), aluminium alloys (Mower & Long, 2016; Rosenthal, Stern & Frage, 2014), nickel-based superalloys (Vilaro et al., 2012), copper alloys (Popovich et al., 2016), Inconel alloys (IN625 (Kreitcberg, Brailovski & Turenne, 2017), IN718 (Farber et al., 2018)), steel and stainless steels (H13 (Yan et al., 2019), P20 (Li et al., 2018), 15-5 PH (Rafi, Starr & Stucker, 2013), 17-4 PH (Mower & Long, 2016), 316L (Mower & Long, 2016), 304L (Zhang et al., 2021a)) and other metallic alloys (Niendorf et al., 2016; Yao et al., 2018). An orthotropic material model was proposed by Hadjipantelis et al. (2022) to model the distinctly anisotropic behaviour of WAAM stainless steel.

Experimental research into the structural performance of additively manufactured metallic elements and structures has explored square and circular hollow section (SHS and CHS) compression elements (Buchanan et al., 2017; Yan et al., 2019), lattice structures (Gümrük & Mines, 2013; Hussein, 2013; Ibrahim et al., 2020; Alghamdi et al., 2021), honeycomb structures with a negative Poisson's ratio (López Jiménez & Triantafyllidis, 2013; Zhang et al., 2019b; Panda et al., 2018) and stochastic structures with isotropic stiffness properties (Hossain et al., 2021) produced by laser-based PBF, three-point bending elements produced by EBM (Smith et al., 2016; Bellini et al., 2021), and SHS and CHS compression elements (Gardner et al., 2020; Kyvelou et al., 2021; Laghi et al., 2020a), rods in compression (Laghi et al., 2020b) and structural connections (Guo et al., Submitted) produced by WAAM. Structural testing and initial safety verification have been conducted on the MX3D footbridge (Gardner et al., 2020) and semi-hollow connections filled with concrete (Heimgartner, 2021). Preliminary comparisons were made to assess the existing structural design provisions for conventionally manufactured cross-sections, which were shown to be generally applicable to cross-sections built by metal AM (Buchanan et al., 2017).

A combination of structural optimisation and additive manufacturing methods has been considered as a means of producing lightweight and efficient parts for direct industrial applications; this approach has been employed in the design and manufacture of a cantilever truss of tubular sections (Ye et al., 2021), diagrid columns (Laghi et al., 2020b), beam and

column cross-sections (Tsavdaridis et al., 2017; Abdelwahab & Tsavdaridis, 2019; Grekavicius et al., 2016), structural connections (Seifi, 2019; Seifi et al., 2016; Abdelwahab & Tsavdaridis, 2019, 2021; Ren & Galjaard, 2015; Crolla et al., 2017; Galjaard et al., 2015) and lattice structures (Panesar et al., 2018; Lebaal et al., 2019). An example of the symbiosis of topology optimisation and additive manufacturing is shown in Figure 2.10; the optimised connection designs achieved a weight reduction of approximately 50% and an improvement in structural performance. AM related research in the construction sector also includes the utilisation of functionally graded materials in the AM process (Bobbio et al., 2017), optimisation of manufacturing paths (Chen et al., 2020), prototyping and testing (Lim et al., 2012), standardisation for 3D printed structural components and exploration for innovative applications, for example, AM techniques for strengthening and repairing.

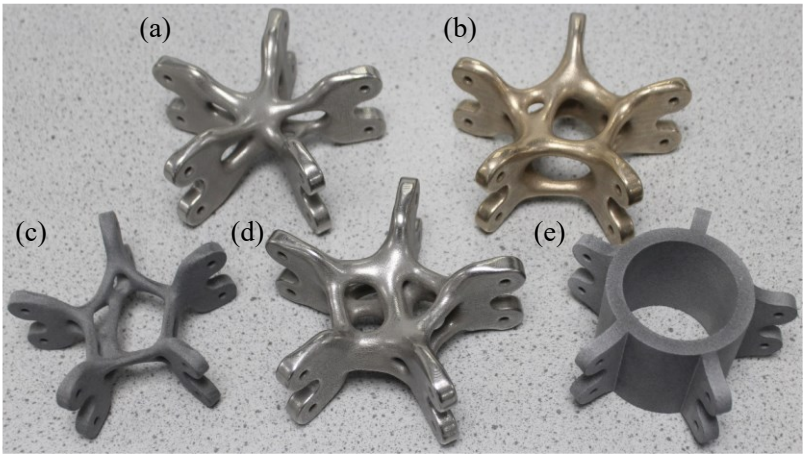

Figure 2.10: Topologically optimised and traditionally designed 3D printed connections (reproduced, (Abdelwahab & Tsavdaridis, 2019))

2.3 Stainless steel in construction

Although stainless steel combines the strength and stiffness associated with ferrous alloys with the corrosion resistance primarily from the high chromium content, it has historically been used only as a more specialist metallic material in the construction industry due to the high initial cost. Its use is increasing with the development of advanced design and construction methods and the general trend towards more sustainable construction. As a high value material, stainless steel particularly lends itself to the emerging opportunities in construction offered by additive manufacturing (Gardner, 2019). This section outlines the technical background, microstructural

and mechanical characteristics of AM stainless steels, and the existing material models for conventionally produced stainless steels.

2.3.1 Types of stainless steel

Stainless steel refers to iron alloys with excellent corrosion resistance, containing a minimum of 11% chromium. The predominant metallurgical phase that is present in the microstructure at room temperature, for example, austenite, ferrite and martensite, is generally used to categorise stainless steel alloys. Stainless steels with more than one phase, for example, approximately 50% ferrite and 50% austenite are designated as duplex stainless steels. Other designations include precipitation hardening grades that contain copper, aluminium, titanium, niobium and molybdenum, which form precipitates during ageing (Askeland & Wright, 2017). There are five types of stainless steel available with different metallurgical compositions and structure, corrosion resistance and mechanical properties, as summarised in Table 2.1.

Table 2.1: Characteristics and properties of stainless steels

Type of stainless steel	Main chemical elements	Hardenable	Ductility	Corrosion resistance	Weldability
Austenitic	12%-18% Cr, 8%-11% Ni	Cold working	Very high	High	Very high
Ferritic	11%-27% Cr, ≤0.25% C	Marginally by cold working	Medium	Medium	Low
Martensitic	12%-18% Cr, 0.15%-1.0% C	Quenching & Tempering	Low	Medium	Low
Duplex	18%-25% Cr, 3%-5% Ni, ≤3% Mo	Cold working	Medium	Very high	High
Precipitation hardening	~17% Cr, ~4% Ni	Age hardening	Medium	Medium	High

2.3.2 Microstructure-property correlation

Metallic additively manufactured components normally experience complex thermal histories during production, including directional heat flow and rapid solidification (Kok et al., 2018), which can lead to anisotropy in microstructure and hence mechanical properties (Yan et al., 2019; Kyvelou et al., 2020), not observed to such an extent in conventionally produced metallic materials. The underlying mechanisms associated with the different mechanical properties of

PBF stainless steels are discussed at the microstructural level in this subsection.

The correlation between the employed processing parameters (build direction (Mower & Long, 2016; Liverani et al., 2017; Guo et al., 2017; Delgado, Ciurana & Rodríguez, 2012; Deev, Kuznetcov & Petrov, 2016), laser power (Liverani et al., 2017; Deev, Kuznetcov & Petrov, 2016), scanning speed (Delgado, Ciurana & Rodríguez, 2012; Li et al., 2010; Sun et al., 2016), scanning strategy (Suryawanshi, Prashanth & Ramamurty, 2017), hatch spacing (Liverani et al., 2017), particle size (Spierings, Herres & Levy, 2011a) and layer thickness (Delgado, Ciurana & Rodríguez, 2012; Spierings, Herres & Levy, 2011a) and the exhibited mechanical properties, including hardness (Mower & Long, 2016; Delgado, Ciurana & Rodríguez, 2012; Liverani et al., 2017; Guo et al., 2017; Sun et al., 2016), tensile (Mower & Long, 2016; Delgado, Ciurana & Rodríguez, 2012; Liverani et al., 2017; Guo et al., 2017; Deev, Kuznetcov & Petrov, 2016; Li et al., 2010; Sun et al., 2016; Suryawanshi, Prashanth & Ramamurty, 2017), compressive (Buchanan et al., 2017), fracture (Mower & Long, 2016; Guo et al., 2017; Suryawanshi, Prashanth & Ramamurty, 2017; Zhang, Dembinski & Coddet, 2013) and fatigue behaviour (Mower & Long, 2016; Liverani et al., 2017; Suryawanshi, Prashanth & Ramamurty, 2017) has received particular attention. In many cases, yield and ultimate tensile strengths of PBF stainless steel parts were superior without reduced ductility despite the presence of pores, when compared with their conventionally produced counterparts, where reduced ductility is typically seen with higher strength (Liverani et al., 2017; Suryawanshi, Prashanth & Ramamurty, 2017; Alsalla, Smith & Hao, 2018; Wang et al., 2016; Leicht, Klement & Hryha, 2018). The higher strength has been associated with the formation of finer microstructures through rapid cooling, and the ductility has been related to the gliding of dislocations and twinning deformation mechanism (Suryawanshi, Prashanth & Ramamurty, 2017; Alsalla, Smith & Hao, 2018; Wang et al., 2016; Leicht, Klement & Hryha, 2018). It is well established that PBF parts show strong mechanical anisotropy, which is attributed to either the presence of lack-of-fusion defects (Mower & Long, 2016; Casati, Lemke & Vedani, 2016; Zhang et al., 2017; Mertens et al., 2014) or the crystallographic texture (Kyvelou et al., 2020) or the presence of elongated grains with an epitaxial growth parallel to the build direction (Leicht, Klement & Hryha, 2018; Mertens et al., 2014; Sistiaga et al., 2016).

2.3.3 Stainless steel material models

Significant effort has been dedicated to developing material models that can simulate the rounded stress-strain response of stainless steel using only a small number of standardised parameters. The most widely used Ramberg-Osgood model is based on the general expression, first proposed by Ramberg and Osgood (1943) and modified by Hill (1944), and employs three basic parameters – the Young's modulus E, the 0.2% proof stress $\sigma_{0.2}$ and the strain hardening exponent n, as given by Equation 2.1.

$$\varepsilon = \frac{\sigma}{E} + 0.002\left(\frac{\sigma}{\sigma_{0.2}}\right)^{n} \tag{2.1}$$

Mirambell and Real (2000) proposed a two-stage stress-strain model based on the conventional Ramberg-Osgood expression, but introduced a modified expression for stresses above the 0.2% proof stress, as given by Equation 2.2, where $E_{0.2}$ is the tangent modulus at the 0.2% proof stress, ε_u is the ultimate strain, $\varepsilon_{0.2}$ is the total strain at $\sigma_{0.2}$, σ_u is the ultimate stress, and m_u is the strain hardening exponent for the second stage.

$$\varepsilon = \frac{\sigma-\sigma_{0.2}}{E_{0.2}} + \left(\varepsilon_u - \varepsilon_{0.2} - \frac{\sigma_u-\sigma_{0.2}}{E_{0.2}}\right)\left(\frac{\sigma-\sigma_{0.2}}{\sigma_u-\sigma_{0.2}}\right)^{m_u} + \varepsilon_{0.2} \qquad \text{for } \sigma_{0.2} < \sigma \leq \sigma_u \tag{2.2}$$

Gardner and Nethercot (2004) proposed using the 1.0% proof stress $\sigma_{1.0}$ in place of the ultimate stress σ_u in Equation 2.2 to achieve a more accurate replication for the second stage and to include the compressive material behaviour, leading to an updated form of the second stage, as expressed by Equation 2.3, where $\varepsilon_{1.0}$ is the total strain at $\sigma_{1.0}$, and $m_{1.0}$ is the strain hardening exponent for the modelled curve passing through the 0.2% and 1.0% proof stresses.

$$\varepsilon = \frac{\sigma-\sigma_{0.2}}{E_{0.2}} + \left(\varepsilon_{1.0} - \varepsilon_{0.2} - \frac{\sigma_{1.0}-\sigma_{0.2}}{E_{0.2}}\right)\left(\frac{\sigma-\sigma_{0.2}}{\sigma_{1.0}-\sigma_{0.2}}\right)^{m_{1.0}} + \varepsilon_{0.2} \qquad \text{for } \sigma_{0.2} < \sigma \leq \sigma_u \tag{2.3}$$

Research on the material modelling of stainless steel and other metals, such as hot-rolled and cold-formed carbon steels and aluminium, has been well documented in the literature and only a select portion of the critical work relevant to this study are presented herein. A more detailed review of material models on metals can be found in Gardner and Yun (2018), Yun and Gardner

(2017) and Arrayago, Real and Gardner (2015).

2.4 Laser welding

2.4.1 Mechanical joining methods

The component size is limited by the internal build volume of the employed PBF AM equipment; the requirement for large-scale metallic components, particularly in the construction industry, necessitates joining smaller, individually built, PBF parts together (Casalino, Campanelli & Ludovico, 2013). Conventional welding techniques, such as gas tungsten arc welding (Feng et al., 2015), gas metal arc welding (Muhammad et al., 2016) and resistance spot welding (Kianersi, Mostafaei & Amadeh, 2014; Kocabekir et al., 2008), have been extensively utilised in the industry to mechanically join small conventionally produced metallic pieces together. Laser welding is an alternative mechanical joining process that results in narrower welds and heat-affected zones (HAZ), reduced thermal distortions to the surrounding base material and lower residual stresses than the aforementioned conventional welding techniques (Matilainen, Pekkarinen & Salminen, 2016; Tjong et al., 1995; Gardner, Bu & Theofanous, 2016; Bu & Gardner, 2019).

2.4.2 Microstructure and mechanical properties of laser welded parts

All welding processes can induce local changes in the microstructure, leading to different mechanical properties and corrosion resistance from the original base material (Molak et al., 2009). The base material examined in this study is 316L stainless steel; relevant research on the weld properties and underlying microstructure is briefly introduced in this subsection.

Conventionally formed 316L stainless steel with laser welded joints has been previously studied in terms of microstructure (Tjong et al., 1995; Ventrella, Berretta & Rossi, 2010; Furuya et al., 2009; Kell et al., 2005), microhardness (Tjong et al., 1995; Ventrella, Berretta & Rossi, 2010; Furuya et al., 2009), creep rupture (Tjong et al., 1995) and mechanical properties (Molak et al., 2009; Ventrella, Berretta & Rossi, 2010; Furuya et al., 2009), as well as dissimilar laser welding of conventional 316L stainless steel to other alloys, such as brass (Li et al., 2014) and titanium alloys (Tomashchuk, Grevey & Sallamand, 2015; Chen et al., 2014). Various microstructures

for laser welds in conventional 316L stainless steel have been observed, such as cellular and equiaxed dendritic structures (Tjong et al., 1995) and cellular dendritic structures (Ventrella, Berretta & Rossi, 2010; Kell et al., 2005), related to various cooling rates and G/R ratios (G is the temperature gradient, and R is the growth rate) of the laser welding (Tjong et al., 1995; Ventrella, Berretta & Rossi, 2010). Coarsening grains or the occurrence of dendrites in welds with high heat input, have been found to reduce the mechanical properties of the welded joints (Ventrella, Berretta & Rossi, 2010).

The microhardness (Casalino, Campanelli & Ludovico, 2013), weld geometry (Casalino, Campanelli & Ludovico, 2013; Matilainen, Pekkarinen & Salminen, 2016), microstructure (Casalino, Campanelli & Ludovico, 2013; Harraz et al., 2017) and mechanical properties (Casalino, Campanelli & Ludovico, 2013; Harraz et al., 2017) in laser welded similar and dissimilar parts of PBF 316L stainless steel have also been investigated, although only with the individual PBF parts built in the same orientation. In these studies (Casalino, Campanelli & Ludovico, 2013; Harraz et al., 2017), the laser welds were found to have a cellular and columnar dendritic microstructure with random grain orientations, no porosity and lower microhardness and tensile properties than the base material. Other studies have investigated the microstructure and mechanical properties of PBF titanium alloys with gas tungsten arc welding (He et al., 2017), PBF Ti-6Al-4V parts with laser welding (Yu et al., 2018), PBF AlSi10Mg parts with laser and tungsten inert gas welded joints (Zhang et al., 2019a), PBF titanium alloy with electron beam welds (Chen et al., 2018) and PBF 304 stainless steel with laser welding (Yang et al., 2019). However, there is little research in the literature on the correlation between the microstructure and mechanical properties of PBF 316L stainless steel parts with laser welded joints, with no prior consideration of joints between parts with different build orientations.

The mechanical properties within the weld region differ from those measured from the base metal, which requires the additional examination of local mechanical properties. A common technique for the measurement of the local stress-strain response across welds, is full-field non-contact digital image correlation (DIC) (Molak et al., 2009; Reynolds & Duvall, 1999; Boyce, Reu & Robino, 2006; Rossini et al., 2015; Leitão et al., 2012), which tracks random patterns applied to the specimen surface and is later processed to calculate the surface strain field.

2.5 Circular hollow sections

It is widely recognised among architects and structural engineers that circular hollow sections (CHS) have a stunning aesthetic appearance and good structural performance. This overview of circular hollow sections is separated into two parts – thick-walled CHS and very slender CHS (also referred to as thin-walled cylindrical shells) in this section.

2.5.1 Thick-walled CHS

The key aspects of thick-walled circular hollow sections, including previous stub column tests on CHS produced by cold forming and metal AM, current design methods and concepts for conventionally manufactured stainless steel CHS, are outlined in this subsection.

2.5.1.1 Previous experimental studies into thick-walled stainless steel CHS

A considerable number of laboratory tests have been conducted to investigate the cross-sectional behaviour of stainless steel CHS produced by conventional and metal additive manufacturing methods; the existing cross-section tests are collected and used later in this thesis for the assessment of design methods and concepts.

Stainless steel CHS stub column tests have been carried out on austenitic grades by Rasmussen and Hancock (1993), Talja (1997), Rasmussen (2000), Burgan, Baddoo and Gilsenan, (2000), Young and Hartono (2002), Kuwamura (2003), Gardner and Nethercot (2004), Uy, Tao and Han (2011), Zhao, Gardner and Young (2016b) and Buchanan, Real and Gardner (2018), on duplex grades by Bardi, Kyriakides and Yun (2006), Lam and Gardner (2008), Buchanan, Real and Gardner (2018) and Shu et al. (2019), and on ferritic grades by Stangenberg (2000) and Buchanan, Real and Gardner (2018). A full list of previous experimental studies on stainless steel CHS is provided in Table 2.2, together with the measured 0.2% proof strength $\sigma_{0.2}$.

There are, however, limited experimental data concerning the performance of structural elements, suitable for use in construction, manufactured by metal AM. Buchanan et al. (2017) conducted tests on square hollow section stub columns produced from stainless steel by PBF, while Yan et al. (2019) performed tests on square, rectangular and circular hollow section (SHS, RHS, and CHS, respectively) stub columns produced from H13 tool steel by PBF. Tests have

also been carried out on stainless steel SHS and CHS stub columns produced by WAAM (Buchanan, Wan & Gardner, 2020; Laghi et al., 2020a; Kyvelou et al., 2021). A summary of these existing experiments on metallic additively manufactured tubular sections and their corresponding material strengths are reported in Table 2.3.

Table 2.2: Existing stub column tests on cold-formed stainless steel CHS

Reference	Material type	Material grade (EN)	No. of tests	$\sigma_{0.2}$ (N/mm^2)
Rasmussen & Hancock (1993)	Austenitic	1.4307	3	405
Talja (1997)	Austenitic	1.4435 & 1.4541	3	-
Rasmussen (2000)	Austenitic	1.4307	2	-
Stangenberg (2000)	Ferritic	1.4003	7	-
Burgan, Baddoo & Gilsenan (2000)	Austenitic	1.4404 & 1.4541	3	294-352
Young & Hartono (2002)	Austenitic	1.4301	4	255-291
Kuwamura (2003)	Austenitic	1.4301 & 1.4318	10	235-440
Gardner & Nethercot (2004)	Austenitic	1.4301	4	337-469
Bardi, Kyriakides & Yun (2006)	Duplex	1.4410	20	561-622
Lam & Gardner (2008)	Duplex	1.4410	2	266-412
Uy, Tao & Han (2011)	Austenitic	1.4301	12	274-320
Zhao, Gardner & Young (2016)	Austenitic	1.4301	4	290-355
Buchanan, Real & Gardner (2018)	Austenitic	1.4432, 1.4307 & 1.4301	4	276-373
Buchanan, Real & Gardner (2018)	Duplex	1.4462	2	569-590
Buchanan, Real & Gardner (2018)	Ferritic	1.4512	4	333-361
Shu et al. (2019)	Duplex	1.4462	6	532-550

Table 2.3: Existing compression tests on additively manufactured tubular cross-sections

Reference	Material	Manufacturing method	Cross-section shape	No. of tests	$\sigma_{0.2}$ (N/mm^2)
Buchanan et al. (2017)	316L stainless steel	PBF	SHS	5	409
Yan et al. (2019)	H13 tool steel	PBF	SHS/RHS	17	707-1468
Yan et al. (2019)	H13 tool steel	PBF	CHS	10	707-1468
Buchanan, Wan & Gardner (2020)	308LSi stainless steel	WAAM	CHS	4	326
Buchanan, Wan & Gardner (2020)	308LSi stainless steel	WAAM	SHS	4	326
Laghi et al. (2020a)	308LSi stainless steel	WAAM	CHS	9	307
Kyvelou et al. (2021)	308LSi stainless steel	WAAM	SHS	14	261-271

2.5.1.2 Design methods for thick-walled stainless steel CHS

The current European design code for structural stainless steel, EN 1993-1-4 (CEN, 2015) adopts the concept of cross-section classification, as used for carbon steel, to account for the susceptibility of cross-sections to local buckling and to determine the corresponding resistance. Stainless steel CHS are classified into four discrete classes (i.e. Class 1, 2, 3 and 4) based on their local slenderness $D/t\varepsilon^2$, where D is the outer diameter, t is the wall thickness and $\varepsilon^2=235/\sigma_{0.2}\cdot(E/210000)$. The Class 3 slenderness limit of $D/t\varepsilon^2=90$ in EN 1993-1-4 is the slenderness limit up to which the cross-section can attain the yield load N_y given by the product of the 0.2% proof stress $\sigma_{0.2}$ and the gross cross-sectional area A in compression; above this limit, an effective area A_{eff} is utilised in place of the gross area A for slender cross-sections. The use of A_{eff}, with an upper local slenderness limit of $D/t\varepsilon^2=250$, is adopted in the latest draft of the revised EN 1993-1-4 (Chan, Gardner & Law, 2010).

The continuous strength method (CSM) is an alternative, deformation-based design approach that employs a base curve to determine the continuous relationship between the cross-section deformation capacity and the local slenderness, and a material model incorporating the benefits of strain hardening. Compared to traditional design methods, the CSM has been shown to predict the cross-section compression and bending resistances of CHS in a more accurate and consistent way. It has been developed for carbon steel (Gardner, 2008), stainless steel (Gardner, 2008; Afshan & Gardner, 2013b; Zhao, Afshan & Gardner, 2017) and aluminium (Gardner, 2008; Su, Young & Gardner, 2016) plated cross-sections, such as I sections, square hollow sections (SHS), rectangular hollow sections (RHS), as well as circular hollow sections under axial compression and bending in isolation, and also under combined compression and bending (Liew & Gardner, 2015). This method has been included in the AISC Design Guide for Structural Stainless Steel (AISC, 2013) and the latest edition of the European Design Manual for Structural Stainless Steel (SCI, 2017) and is due to be included in the upcoming revisions to EN 1993-1-4, AISC 370 and ASCE-8 for the design of stainless steel structures.

2.5.2 Thin-walled cylindrical shells

Thin-walled cylindrical shells are widely used in the aerospace, marine, chemical and construction industries due to their excellent flexural stiffness and resistance about all axes of bending, efficient distribution of mass and lightweight characteristics (Teng et al., 2005), with

typical industrial applications of cylindrical shells being shown in Figure 2.11. It is well recognised that local buckling is one of the main concerns for slender compression members. In this subsection, a summary of early shell buckling research, codified design methods and alternative shell designs against buckling is introduced.

(a) Wind turbine tower
https://www.windpowermonthly.com/

(b) Storage tank
https://www.sbsayrshire.com/

Figure 2.11: Typical industrial applications of cylindrical shells

2.5.2.1 Early shell buckling research and empirical design approach

In the late 1920s, the compressive load-carrying capacities of circular cylindrical shells were first shown to generally fall well below the theoretical elastic buckling loads of shells during tests. Extensive experimental studies into slender shells were then conducted to gain insight into the knock down of buckling loads, and initial geometric imperfections were recognised as the primary reason for the discrepancies between the theoretical buckling load predictions and the experimental results and the significant scatter of test data (Von Karman & Tsien, 1941; Donnell & Wan, 1950; Koiter, 1970). Due to a lack of a theoretical solution, empirical knock-down factors were proposed by NASA SP 8007 in 1968 (Weingarten, Morgan & Seide, 1965; NASA, 1968) based on lower bounds to available experimental data to provide design guidance for engineers, though this approach can lead to overly conservative buckling load predictions. The experiments available for the original NASA SP 8007 included approximately 200 compression tests and 145 bending tests on isotropic cylinders made from aluminium, steel and duralumin; the knock-down factors derived from these experiments as a function of radius-to-

thickness ratio are shown in Figure 2.12, along with the original NASA lower-bound curve. According to NASA NP 8007, the buckling load P_{cr} of a cylindrical shell can be estimated using Equations 2.4 and 2.5, where P_{cl} is the classical elastic buckling load, E is the Young's modulus, t is the shell thickness and υ is the Poisson's ratio.

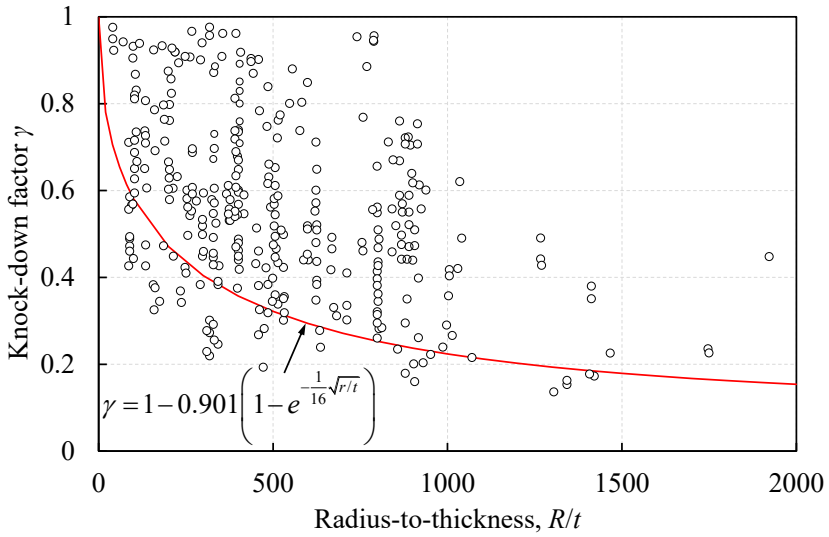

Figure 2.12: Experimental knock-down factors for cylindrical shells under axial compression compared with the lower bound curve from NASA guidelines (NASA, 1968)

$$P_{cr} = \gamma P_{cl} \tag{2.4}$$

$$P_{cl} = \frac{2\pi E t^2}{\sqrt{3(1-\nu^2)}} \tag{2.5}$$

An updated version of NASA SP-8007 (NASA, 2020) has been developed to include relevant experimental data associated with modern shell structures using advanced materials, manufacturing and structural configurations, and to incorporate structural analysis tools and new state-of-the-art practices for the design of thin-walled cylindrical shells under various loading scenarios.

2.5.2.2 Codified design methods

In EN 1993-1-6 (CEN, 2017), a three-stage capacity curve that relates the dimensionless characteristic resistances to the dimensionless slenderness, is employed for the buckling design of shells. The traditional method requires the calculation of the elastic critical buckling stresses

σ_{cr} and the appropriate reduction factors χ; the main formulae are presented in Figure 2.13, where R_{pl} and R_{cr} are respective plastic and elastic critical buckling resistances. An advanced numerical analysis – 'MNA/LBA Method' or 'Overall Method' adopts the concept of overall slenderness derived from global materially nonlinear analyses (MNA) and linear bifurcation analyses (LBA) analyses; the procedure is illustrated in Figure 2.14. A more advanced method utilises geometrically and materially nonlinear analyses with imperfections (GMNIA), MNA and LBA to compute the slenderness $\bar{\lambda}_c = \sqrt{R_{MNA}/R_{LBA}}$ and the buckling reduction factor χ=R_{GMNIA}/R_{MNA}.

According to EN 1993-1-6 (CEN, 2017), the geometric imperfections are assumed to be in the form of the lowest elastic buckling mode (i.e. eigenmode-affine) obtained from the LBA analyses, and a characteristic imperfection amplitude linked to the fabrication tolerance quality class, is employed to scale the imperfection mode. There are some alternative methods to delivering an accurate representation of real geometric imperfections that underpins the robustness of numerical simulations and avoids excessively conservative structural designs, such as a combination of different eigenmodes (Shayan, Rasmussen & Zhang, 2014) and the spectral representation approach (Stefanou, 2011; Zeinoddini & Schafer, 2012).

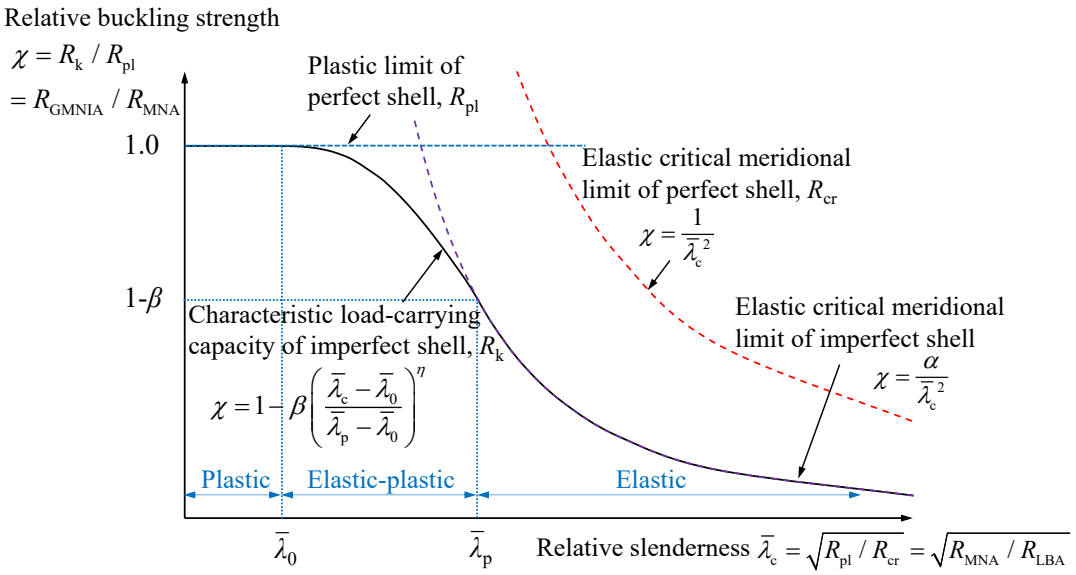

Figure 2.13: Illustration of the buckling capacity curve of EN 1993-1-6 for cylindrical shells

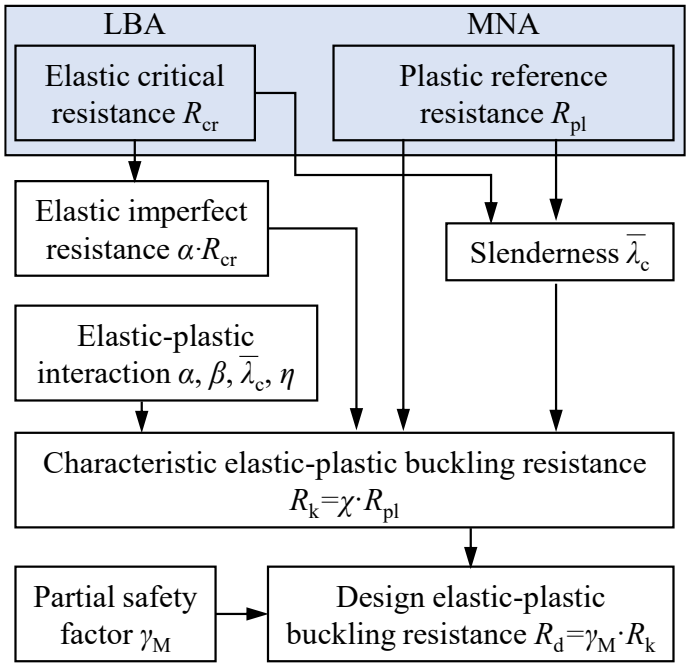

Figure 2.14: Flowchart of MNA/LBA method specified in EN 1993-1-6

2.5.2.3 Alternative shell forms against imperfections

The local buckling problem of slender circular cylindrical shells under axial compression greatly impairs their structural efficiency, and therefore, various approaches have been employed in order to mitigate this issue. Stiffened shells with various stiffener configurations (Hutchinson & Amazioo, 1967; Huybrechts, Hahn & Meink, 1999; Wang et al., 2017) have been proposed (Figure 2.15), aimed at enhancing the local buckling resistance of shells under axial compression and reducing the sensitivity to geometric imperfections (Huybrechts, Hahn & Meink, 1999; Wang et al., 2017). However, the sensitivity to geometric imperfections, although reduced to some extent, remains relatively high (Singer, Arbocz & Babcock, 1971; Hutchinson & Frauenthal, 1969), and the fabrication of stiffeners can be impractical and costly. Alternatively, intrinsically stiffened shells have been developed (Figure 2.15), such as pseudo-cylindrical concave polyhedral shells (Yoshimura Y., 1955; Knapp, 1976), 'Aster' shells with outward convex corrugations (Jullien & Araar, 1991; Araar, Derbali & Jullien, 1998; Combescure & Jullien, 2015), sinusoidally corrugated shells (Yadav & Gerasimidis, 2019, 2020) and wavy shells with general cross-section shapes (Ning & Pellegrino, 2015, 2017) (Figure 2.15); the latter three feature corrugated rather than circular cross-section profiles, which effectively reduce the local radius of curvature, thereby reducing the imperfection

sensitivity and enhancing the overall resistance to local buckling.

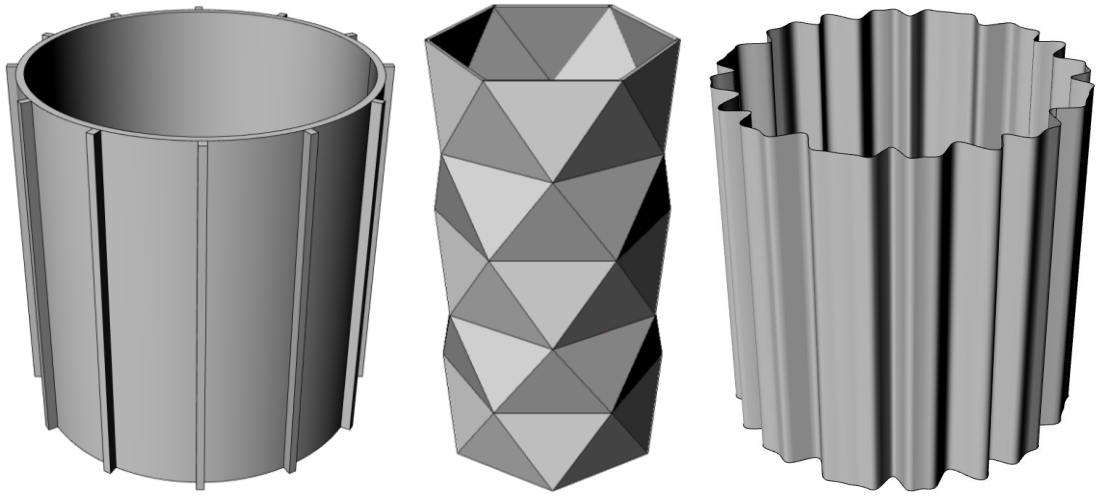

(a) (b) (c)

Figure 2.15: Shell designs for reduced imperfection sensitivity: (a) Stringer-stiffened, (b) pseudo-cylindrical concave polyhedral and (c) corrugated shells

2.6 Structural optimisation

Structural optimisation typically employs simplified algebraic equations that are solved by iterative numerical simulations, aiming to find the optimal structural design with the best performance under various constraints (Huang & Xie, 2010). The use of structural optimisation dates back about 120 years (Michell, 1904) and has now been widely adopted in many fields such as aerospace, automotive and building construction, due to the availability of high-speed computers and the rapid improvements in algorithms. In this section, the procedure and three key components of shape optimisation used in structural engineering – geometric modelling, structural analysis and optimisation algorithms, are first briefly described. The optimisation work and research gap on stiffened and corrugated cylindrical shells are then discussed.

2.6.1 Shape optimisation

Shape optimisation is a structural optimisation method, featuring the iterative modification of the predetermined boundaries of a structure. It has been successfully applied in the design of beams (Haug & Kwak, 1978; Imam, 1982; Umetani & Hirai, 1978), columns (Barnes, 1977; Farshad & Tadjbakhsh, 1973), members in torsion (Dems & Mroz, 1980; Choi & Haug, 1983)

and shells (Botkin, 1982; Botkin & Bennett, 1985; Week & Stelnke, 1983;, Åkerström, Jernström & Wierzbicki, 1981).

Shape optimisation attempts to integrate geometric modelling, structural analysis and optimisation algorithms; the general process of shape optimisation is shown in Figure 2.16. Shape optimisation starts with the selection of the geometric representation for the boundary shape, the definition of the design variables, the construction of the design model and the formulation of the optimisation problem. Upon the determination of the function values through the structural analysis, a new set of values of design variables can be generated through the optimisation algorithm. This procedure is repeated until the prescribed termination criteria are met.

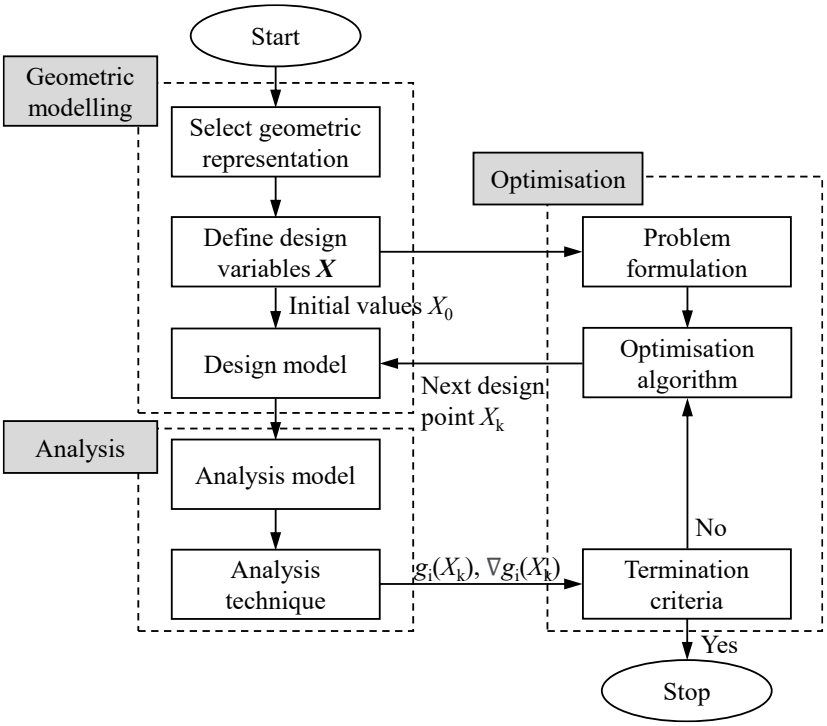

Figure 2.16: Flowchart of shape optimisation

In early studies on shape optimisation, the coordinates of the boundary nodes directly related to the finite element (FE) mesh, were employed as the design variables, but were shown to be unable to ensure a smooth boundary shape (Braibant & Fleury, 1984). Researchers started to use polynomials to guarantee the smoothness of the boundary in a separate design model from the analysis model, but the polynomial representation lacks local control of the curve and leads to an impractical oscillatory boundary shape when the polynomial order is high (Kristensen &

Madsen, 1976; Hsu, 1994). These issues were addressed using spline curves that became the most widely used geometric representation in shape optimisation (Braibant & Fleury, 1984; Luchi, Poggialini & Persiani, 1980).

Typical buckling analysis methods for stiffened shells are the FE method, the smeared stiffener method (SSM) and the hybrid model method. The FE method has been used as a main buckling analysis tool for stiffened shells, enabling the capture of the nonlinear post-buckling path but requiring a high computation time. SSM is based on a mathematical model to smear the skin and the stiffeners into an equivalent lamina, and the linear buckling load is calculated using the Rayleigh-Ritz method, providing computational speed but less prediction accuracy compared to a detailed FE method. Also, SSM was found to be not able to take imperfection sensitivity and post-buckling behaviour into account (Tian et al., 2018). The hybrid model method combines the efficiency of SSM with the accuracy of the FE method; equivalent stiffness coefficients are first calculated and then assigned to the stiffness properties in the FE model of the equivalent unstiffened shell.

In attempts to search for optimum or near-optimum solutions to shape optimisation problems involving a large number of design variables, evolutionary algorithms (EAs) that were inspired by biological evolution, have been introduced. EAs are a family of metaheuristic search methods, and the representatives of EAs are shown in Figure 2.17. Genetic algorithms were the first developed evolutionary-based techniques but were demonstrated to require high computation times. Some recent optimisation algorithms are capable of iteratively searching for global optimal design solutions at a reasonable computational cost, such as the evolution strategies (Hansen, Müller & Koumoutsakos, 2003; Hansen, 2006), differential evolution (Storn, 1997) and particle swarm optimisation (PSO) (Eberhart & Kennedy, 1995; Kennedy & Eberhart, 1995; Shi & Eberhart, 1998). The PSO algorithm is employed in the present thesis and will be described in Chapter 5.

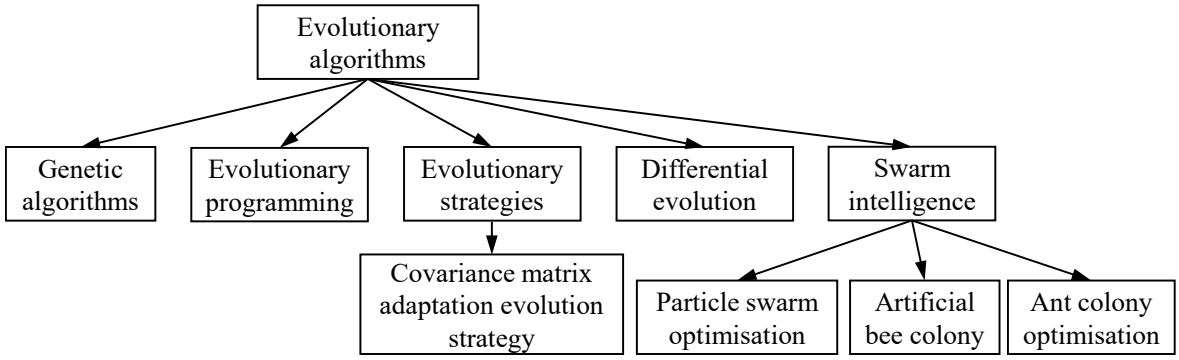

Figure 2.17: Representatives of evolutionary algorithms

2.6.2 Optimisation of cylindrical shells

The reduced load-carrying capacities of monocoque cylindrical shells resulting from imperfections necesscitate the development of optimisation approaches to reduce the imperfection sensitivity. Significant efforts have been devoted to the optimisation of stiffened shells with imperfection sensitivity taken into account. A surrogate-based optimisation framework based on multi-island genetic algorithms together with high fidelity non-linear FE analyses (Wang et al., 2014; Hao et al., 2013; Tian et al., 2018) or the hybrid model (Wang et al., 2017) or smeared stiffener methods (Tian et al., 2018) has been proposed for stiffened and hierarchical stiffened shells. Other EA related algorithms, for example, particle swarm optimisation (Hao et al., 2015; Meng et al., 2015), have been successfully applied to accelerate the optimisation process of the stiffened shells. Ning and Pellegrino (2015) optimised a free-form corrugated cylindrical shell through evolution strategy with covariance matrix adaption, following a general optimisation approach that incorporates geometrically nonlinear analyses into the optimisation procedure (Reitinger, Bletzinger & Ramm, 1994; Reitinger & Ramm, 1995).

Free-form corrugated cylindrical shells were demonstrated to have significantly improved load-carrying capacities and reduced imperfection sensitivities compared with their reference circular cylindrical shells through experiments (Ning & Pellegrino, 2017). However, studies into the shape optimisation of free-form corrugated cylindrical shells, remain rather scarce and limited mainly to geometrically nonlinear analysis with imperfections, but without incorporation of material nonlinearity (GNIA). One major barrier that hindered further research into the free-form wavy shells was the lack of practicality with conventional fabrication

techniques. With the recent advances in additive manufacturing, the fabrication of such free-form corrugated cylindrical shells using metallic materials has now become feasible at a constantly increasing efficiency and reducing costs (Gardner et al., 2020; Buchanan et al., 2017; Buchanan & Gardner, 2019).

2.7 Concluding remarks

An overview of the key topics relevant to this thesis has been presented in this chapter. With regards to metal additive manufacturing, its essential background information, current applications and existing metallic research have been highlighted. For stainless steels in construction, the correlation between the microstructure and mechanical characteristics of additively manufactured stainless steels and the material models, have been described, followed by a review of existing experimental studies into the weld properties. Existing cross-section tests on conventionally and additively manufactured stainless steel CHS have been outlined, along with the current stainless steel design methods and concepts. The imperfection sensitivity of thin-walled cylindrical shells has been highlighted, together with the design methods for slender tubular sections and alternative shell forms against buckling, with the available shape optimisation methods for cylindrical shells being finally introduced.

Chapter 3

Microstructure and mechanical properties of AM stainless steels

3.1 Introduction

Additively manufactured metallic parts experience a complex thermal history during their manufacturing process; this is known to influence both the microstructure and the resulting mechanical properties (Frazier, 2014; Kyvelou et al., 2020). An experimental investigation into the material characteristics of powder bed fusion (PBF) additively manufactured stainless steel is presented in this chapter. A series of microstructural and tensile coupon tests on PBF built 316L and CX stainless steels are first described. The joining of small PBF 316L stainless steel parts, to produce larger components, using laser welding with varying welding parameters, is then explored through microstructural characterisations and mechanical tests. This chapter aims to investigate the correlation between the underlying microstructure and the measured mechanical properties of PBF stainless steels and to provide new knowledge about the weldability of PBF stainless steel elements for use in the construction industry. The work in this chapter has been reported by Zhang et al. (2021a, 2021b).

3.2 Overview of experimental programme

The experimental investigation included tensile coupon tests, optical microscopy (OM) and scanning electron microscopy (SEM) observations and texture analysis on PBF 316L and CX stainless steels. Similar tests, along with Vickers microhardness tests, were conducted to examine the microstructural and material characteristics of PBF 316L stainless steel coupons

with laser welds in the centre. Two different stainless steel grades were examined – an austenitic grade 316L (also referred to as EN 1.4404 and X2CrNiMo17-12-2), which is widely used in the aerospace, marine, chemical and construction industries due to its high strength, corrosion resistance and good weldability characteristics (Trelewicz et al., 2016; Kianersi, Mostafaei & Amadeh, 2014), and a commercial martensitic precipitation hardening grade CX (with similar chemical composition to PH13-8 Mo), which has many potential applications in the aerospace, marine, defence, nuclear and injection molding industries due to its excellent strength and corrosion resistance, high hardness and high toughness (Asgari & Mohammadi, 2018; Sanjari et al., 2020). The OM analysis and microhardness tests were performed in the Engineering Alloys Lab, while the SEM and electron backscatter diffraction (EBSD) analyses were conducted in the Harvey Flower Electron Microscopy Suite, both in the Department of Materials at Imperial College London. The tensile coupon tests were conducted in the Structures Laboratory of the Department of Civil and Environmental Engineering at Imperial College London.

Table 3.1: Nominal chemical composition of the employed EOS 316L and CX stainless steel powders, as provided by the manufacturer (EOS, 2017, 2019)

Material	Cr (%)	Ni (%)	Mo (%)	Al (%)	C (%)	Mn (%)	Cu (%)	P (%)	S (%)	Si (%)	N (%)	Fe (%)
316L	17.00-19.00	13.00-15.00	2.25-3.00	-	≤0.03	≤2.00	≤0.50	≤0.025	≤0.01	≤0.75	≤0.1	balance
CX	11.00-13.00	8.40-10.00	1.10-1.70	1.20-2.00	≤0.05	≤0.40	-	-	-	≤0.40	-	balance

Table 3.2: Nominal material properties of parts built using the employed EOS stainless steel powders, as provided by the manufacturer (EOS, 2017, 2019)

Material	Source	θ (°)	E (N/mm^2)	$\sigma_{0.2}$ (N/mm^2)	σ_u (N/mm^2)	ε_f (%)
316L	As-built	0	185000	470-590	590-690	25-55
		90	180000	380-560	485-595	30-70
CX	As-built	Average	-	840	1080	14

All the specimens were printed in the Laboratory of Laser Processing of the School of Energy Systems at LUT University. The adopted feedstock materials were austenitic grade 316L and precipitation hardening martensitic grade CX stainless steel powders (EOS, 2017, 2019). The nominal chemical composition and as-built mechanical properties of the PBF materials provided in the manufacturer's datasheet (EOS, 2017, 2019) are reported in Tables 3.1 and 3.2,

respectively. In total, the test programme consisted of tensile tests on six 316L stainless steel coupons, six CX stainless steel coupons and 33 316L stainless steel coupons with laser welds, together with a series of microstructural tests on samples extracted from these coupons.

3.3 Specimen manufacture

3.3.1 PBF coupons

All the test coupons were manufactured using an EOS M290 system through laser-based powder bed fusion. The maximum part size that these PBF machines can build is approximately 400 mm × 400 mm × 400 mm, with a deposition rate of 13.3 cm^3/hour. The cost of the 316L stainless steel powder was approximately £60/kg from the original equipment manufacturer (Simpson, 2018), whereas the cost of conventionally formed 316L stainless steel plate material is £5/kg (Meps, 2020). The manufacturing process features a high-energy laser beam scanning across a layer of metallic powder, melting the powder at programmed locations according to an input STL model (Islam et al., 2012). A schematic view of the laser PBF manufacturing process is illustrated in Figure 3.1 and described below; the equipment features an ytterbium continuous wave fibre laser, a scanner and a build chamber filled with protective inert argon (EOS, 2010). The process involves drawing the part in CAD software, converting to an STL model and slicing into individual two-dimensional layers to be printed. For manufacture, a thin layer of powdered material is then deposited, melted and solidified into a cross-section, the platform is lowered by the layer thickness and the manufacturing process repeats until completion. The finished part is finally removed from the build plate. No post-building surface treatment was carried out on the printed elements in this study.

The employed 316L stainless steel powder had a particle size between 15 μm and 53 μm (EOS, 2017), while the particle size of CX stainless steel powder was between 20 μm and 65 μm (EOS, 2019). The processing parameters, as set by the EOS machine manufacturer (EOS, 2017, 2019), are summarised in Table 3.3. Using these standard parameters, a relative density of close to 100% should be achieved according to the manufacturer's datasheet (EOS, 2017, 2019). A bidirectional stripe hatching strategy with a stripe width (i.e. hatch length) of 12 mm and a hatch distance of 100 μm was adopted. The nominal dimensions of the coupons are shown in Figure 3.2. Figure 3.3 illustrates the build orientation of the printed coupons and the extracted positions

of metallurgic samples from the coupons. The reference coordinates for the PBF coupons consist of three perpendicular axes: the build direction (BD) and two transverse directions (TD1 and TD2). The build orientation angles of the tensile coupons are defined by three parameters, θ, ψ and ϕ, where θ is the angle from the longitudinal axis of the coupon to the build plate (i.e. $\theta = 0°$ is a horizontal coupon parallel to the build plate and $\theta = 90°$ is a vertical coupon), ψ is the angle between the recoating direction and the longitudinal axis of the coupon (with $\psi = 90°$ for all $\theta = 90°$ coupons) and ϕ is the angle between the long face of the coupon cross-section and the build plate. For the vertical coupons (θ=90°), ϕ=0° is a coupon with the short face of its cross-section parallel to the recoating direction and ϕ=90° with its long face parallel to the recoating direction. All the examined coupons were designed to be printed vertically (i.e. θ=90°), while as-received CX stainless steel coupons were unexpectedly printed horizontally (i.e. θ=0°).

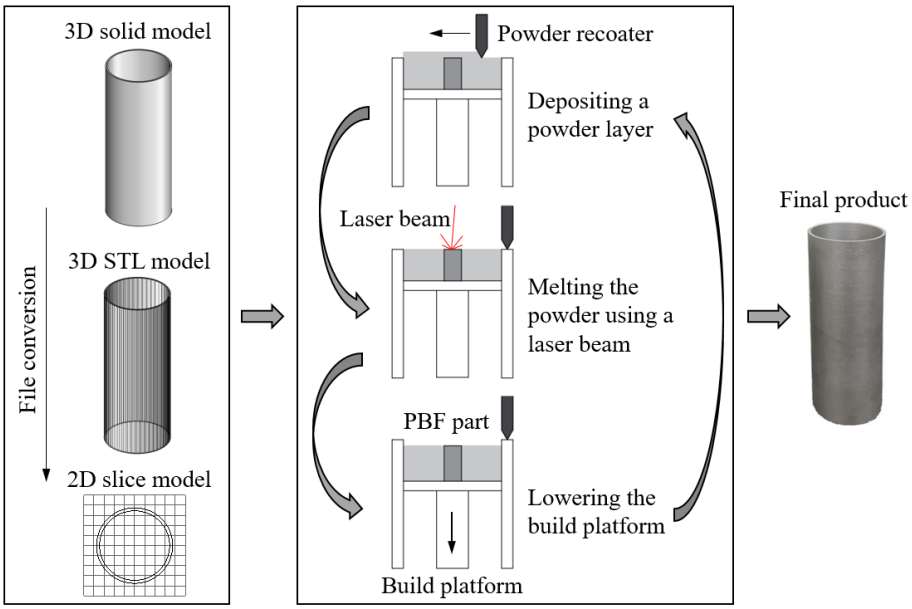

Figure 3.1: Schematic diagram of the laser powder bed fusion (PBF) process

Table 3.3: PBF processing parameters adopted in this study

Material	Laser type	Laser power (W)	Laser spot size (μm)	Scanning speed (mm/s)	Layer thickness (μm)	Hatch distance (μm)	Scanning rotation (°)	Preheated powder bed (°C)	Preheated powder	Protective gas
316L	Yb-fibre	220	100	900	40	100	45	80	No	Argon
CX	Yb-fibre	400	100	900	30	100	45	80	No	Argon

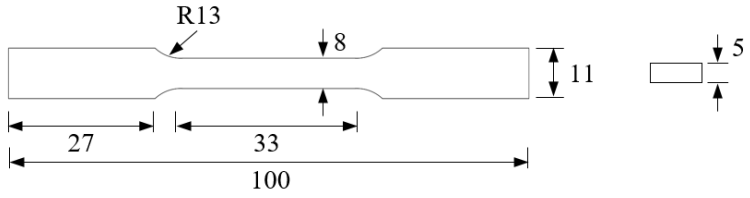

Figure 3.2: Dimensions of tensile coupons (dimensions in mm)

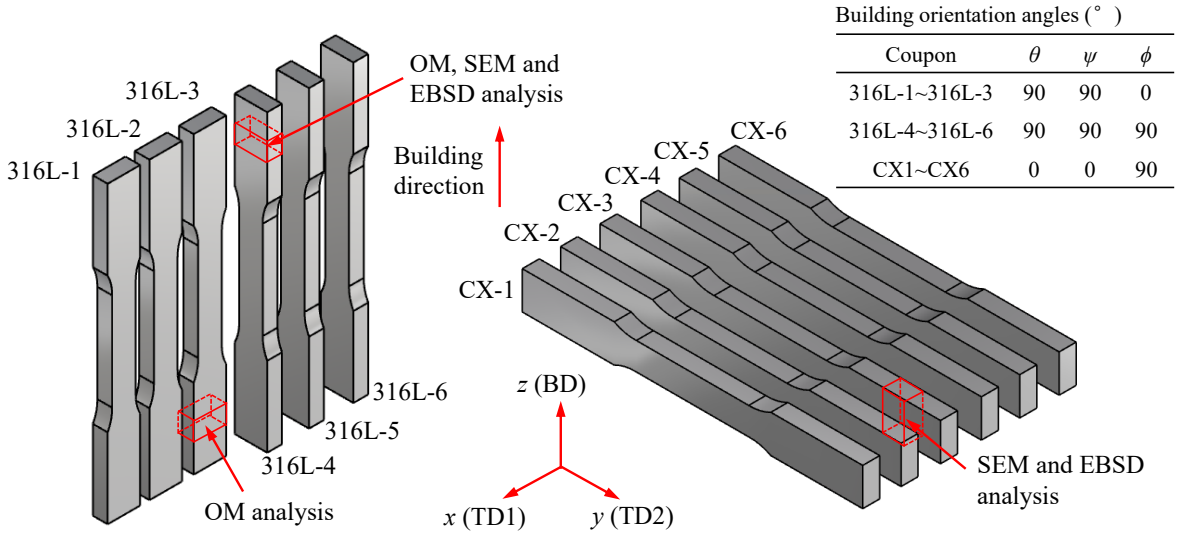

Building orientation angles (°)

Coupon	θ	ψ	ϕ
316L-1~316L-3	90	90	0
316L-4~316L-6	90	90	90
CX1~CX6	0	0	90

Figure 3.3: Schematic of test coupons, showing the building orientation angles and the extracted positions of the metallurgic samples

3.3.2 PBF coupons with laser welded joints

A total of 66 L-shaped plates were manufactured from 316L stainless steel powder using a modified EOS M280 research machine. All PBF plates were printed simultaneously with identical processing parameters on the same build platform. The parameters used were: a laser power of 200 W, a scanning speed of 1000 mm/s, a laser spot size of 100 µm, a layer thickness of 20 µm, a hatch distance of 100 µm and a scan angle of 45° between successive layers. The L-shaped plates were removed from the build plate and no additional surface treatment was applied.

The orientation of the printed L-shaped plates, and the later coupon half parts cut from these plates, with respect to the build direction, recoating direction and final loading direction, is shown in Figure 3.4, where θ is the angle from the longitudinal axis of the coupon to the build plane (the *xy* plane). The L-shaped plates, and coupon half parts, were built either horizontally

(θ=0°) and loaded parallel to the build plane, or vertically (θ=90°) and loaded normal to the build plane.

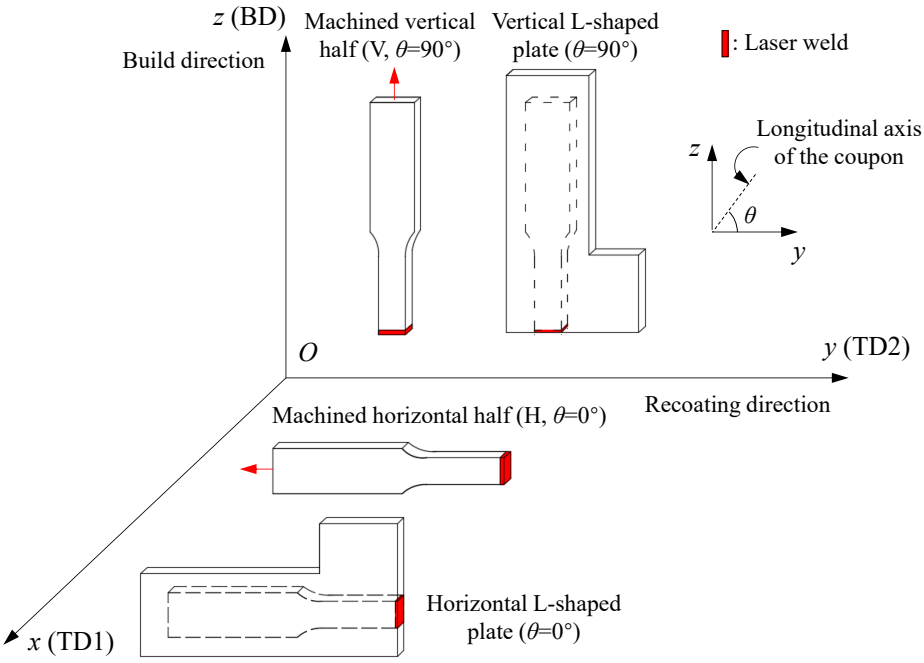

Figure 3.4: Orientation of L-shaped plates and machined coupon half parts relative to the build plane (the *xy* plane)

The L-shaped plates were joined by laser welding in the following combinations: (i) horizontal (H, θ=0° only), (ii) vertical (V, θ=90° only) and (iii) combined horizontal and vertical (X, with one half being built horizontally θ=0° and the other half being built vertically θ=90°). Starting plates were used to initiate the laser welds; the welds then proceeded from the starting plates onto the PBF specimens. After welding, the starting plates were removed by sawing, and the tensile coupons were machined from the remaining welded plates. This process is shown in Figure 3.5 for a combined X family coupon. The three coupon families produced (H, V and X) are shown in Figure 3.6. The laser welder had an optical fibre diameter of 300 µm. Two variations of welding power (P=3500 W or 4000 W) and welding speed (S=29.2 mm/s or 33.3 mm/s) were employed, as presented in Table 3.4. The heat input per unit length travelled by the laser beam E is calculated using Equation 3.1, where E is the energy input, P is the laser power and S is the welding speed. The nominal geometry of the final test specimens was in accordance with EN ISO 6892-1 (CEN, 2016), and is shown in Figure 3.7.

$$E = \frac{P}{S} \tag{3.1}$$

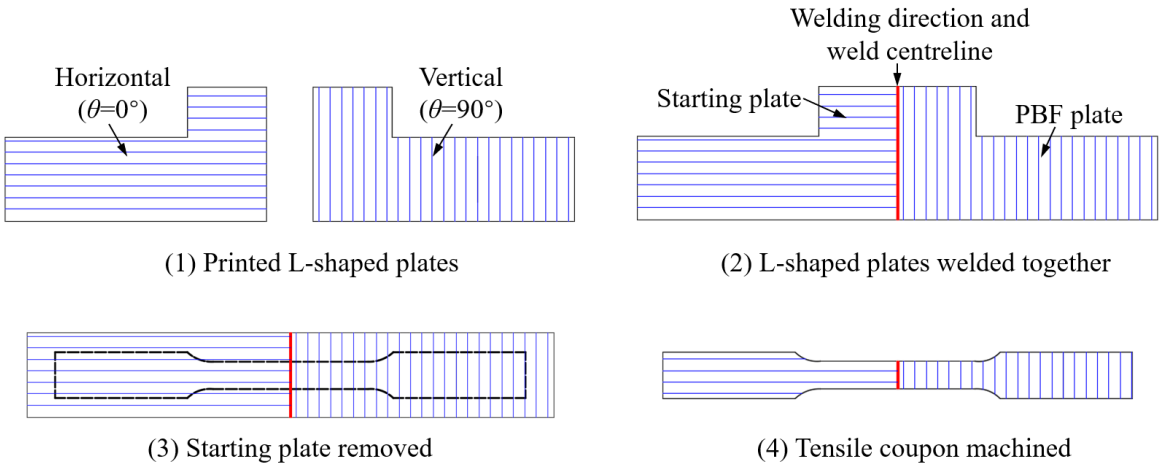

Figure 3.5: Laser welding and machining process for a combined X family tensile coupon

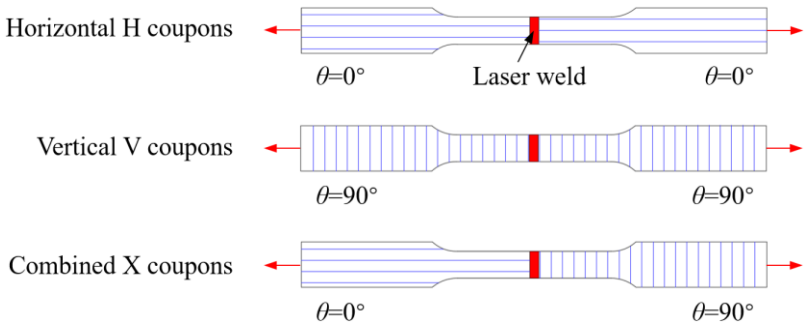

Figure 3.6: Welded tensile coupon families, showing the print layer direction of the half parts

Table 3.4: Adopted laser welding parameter sets for the welded tensile coupon families

Welding parameter set	Laser power (W)	Welding speed (mm/s)	Energy input (J/mm)	Optical diameter (µm)
1	3500	29.2	120	300
2*	3500	33.3	105	300
3	4000	29.2	137	300
4	4000	33.3	120	300

* Welding parameter set 2 was not used for the combined X family coupons.

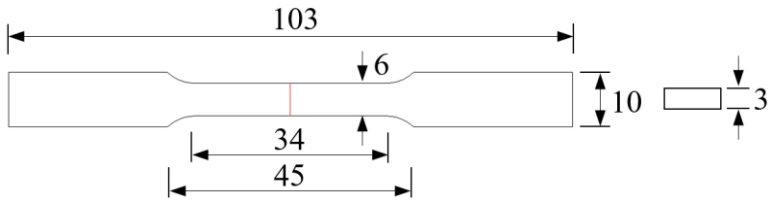

Figure 3.7: Dimensions of welded tensile coupons (dimensions in mm)

The test specimens were labelled beginning with the letter of the welded coupon family (H, V or X), followed by the welding parameter set from Table 3.4 (1, 2, 3 or 4) and finally the specimen repeat number (1, 2 or 3). For example, V1/3 denotes a vertical coupon (V) welded using welding parameter set 1, and the coupon is the third repeat (/3) in the V1 family. Three coupons were tested for each combination of coupon family and welding parameter set, with the exception that welding parameter set 2 was not used for the combined X family coupons, resulting in a total of 33 coupons. Material properties of inclined coupons have been reported in Buchanan et al. (2017), but laser-welded coupons featuring inclined coupon half parts have seldomly been examined; future research could be dedicated to this topic.

3.4 Microstructural characterisation of PBF stainless steels

3.4.1 Sample preparation and experimental characterisation techniques

After the destructive tensile coupon tests, small metallurgical samples were sectioned from the gripped sections of the coupons. To investigate the potential anisotropic mechanical properties resulting from the laser scan paths, three faces of the PBF samples, parallel to three orthogonal planes TD2-BD, TD1-TD2 and TD1-BD, were examined. All samples were prepared for microstructural characterisation in accordance with ASTM E3-11 (ASTM, 2012); the procedure is shown in Figure 3.8. The samples were mounted in bakelite, ground with silicon carbide paper (progressing from 500, 800, 1200 to 2000 grit size) and polished to a mirror finish, using 3 μm and 1 μm diamond suspensions and finally a mixture of OPS colloidal silica solution (H_2O_2:OPS:H_2O = 3:7:10). To reveal the solidification microstructure, the polished samples were then electrolytically etched using a 10%wt oxalic acid solution at 6 volts for 60 seconds as recommended by ASTM E407-07 (ASTM, 2015), and then ultrasonically cleaned in acetone to remove any residual reagents. Kalling's 2 reagent (5 g $CuCl_2$, 100 mL HCl and 100 mL ethanol) for 30 seconds was also found to be effective as an etchant for the CX stainless steel.

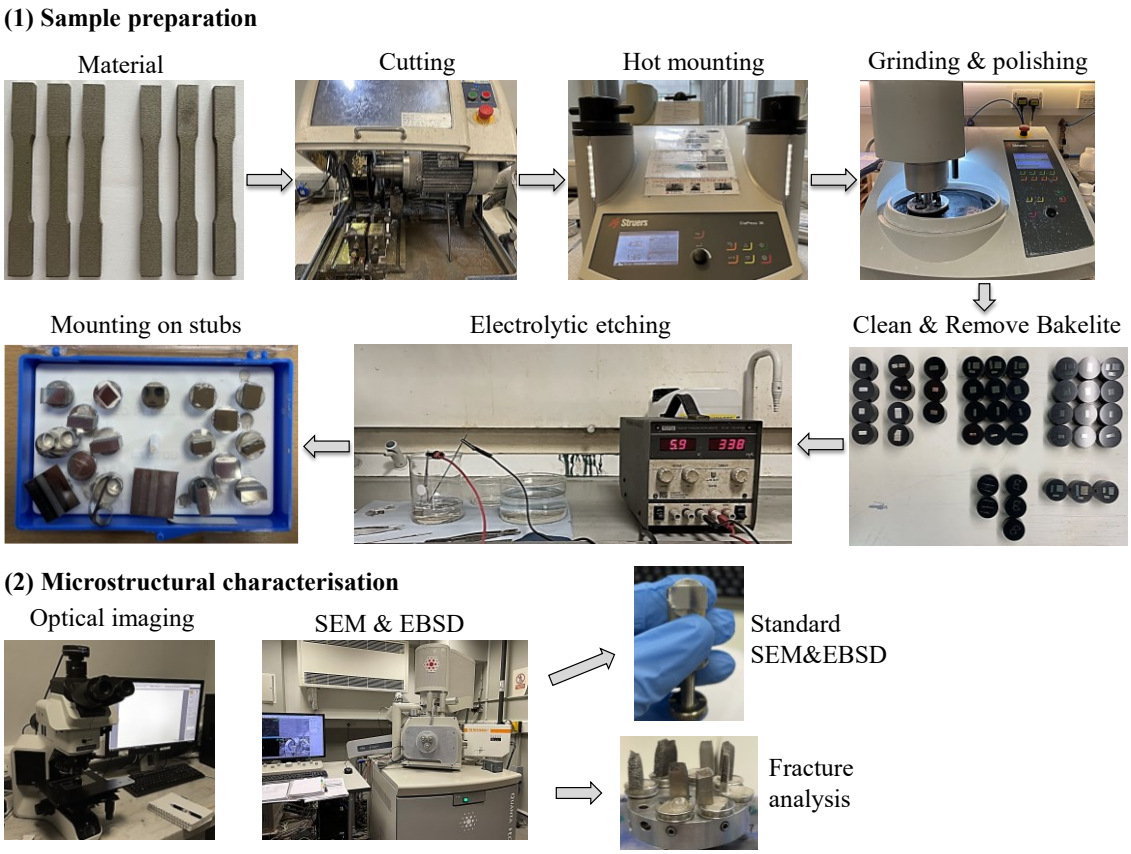

Figure 3.8: Procedure for sample preparation and microstructural examinations

The as-etched surfaces were first examined using an Olympus BX51 optical microscope. EBSD characterisation was then performed to analyse the grain orientation, morphology, size distribution and texture. The EBSD test setup and schematic of the detection geometry are shown in Figure 3.9. For consistency, all inverse pole figure (IPF) maps were constructed with respect to the build direction (IPF-BD) for all samples. The crystal reference frame, X-Y-Z, user-defined global reference frame, *x*-*y*-*z*, and scanning reference frame X_s-Y_s-Z_s, are shown along with the EBSD pattern that would appear on the data collection software Bruker. The samples were tilted to 70° relative to the horizontal, positioned at a working distance of 15 mm and scanned at a beam acceleration voltage of 20 kV using an FEI Quanta 650 SEM equipped with a Bruker eFlash^{HD} EBSD detector and Argus forescatter diodes (FSD) imaging. EBSD patterns were acquired using the Esprit 2.2 software (Bruker, 2018) and reconstructed using the Matlab toolbox MTEX 5.6.0 (Bachmann, Hielscher & Schaeben, 2010). The PBF 316L and CX samples were scanned at magnifications of ×300 and ×4000 over an area of 1427×936 μm^2 and 104×70 μm^2, with a scan step size of 1.43 μm and 0.13 μm, respectively, while the 316L cross-section sample was scanned at ×500 magnification over an 856.2×561.7 μm^2 area with a

step size of 2.14 µm. The settings employed for the EBSD analysis ensured a sufficiently large scan area to increase the reliability of information acquisition without losing substructure details. The grain segmentation and dilution for cleaning non-indexed data points, and smoothing with a spline filter were conducted through MTEX scripts, in which a grain tolerance angle of 5° and a minimum grain size of 5 pixels were adopted. The particle size distribution of the PBF CX stainless steel was examined using a laser diffraction particle machine (Mastersizer 2000, Malvern Instruments Ltd., UK).

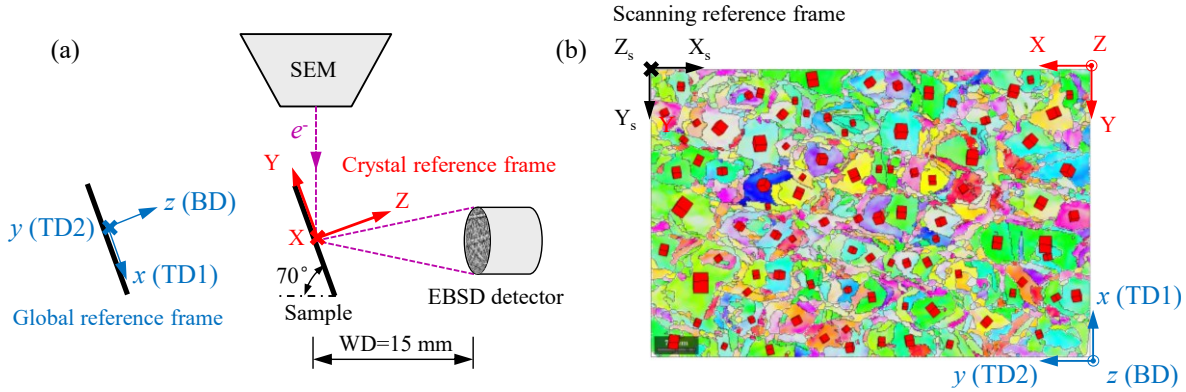

Figure 3.9: (a) Schematic of typical EBSD detection showing the orientation of the crystal reference frame, X-Y-Z, as well as a user-defined global reference frame *x*-*y*-*z* and (b) IPF-BD map (i.e. coloured with respect to the build direction) with red cubes showed the crystal orientations of the grains in the data collection software with relevant coordinate frames, including the scanning reference frame, X_s-Y_s-Z_s

3.4.2 Microstructural characterisation of PBF 316L stainless steel

The front, cross-section and side samples (see Figure 3.10) extracted from the 316L-3 and 316L-4 coupons were examined under an optical microscope and scanning electron microscope; the microstructure and texture of samples extracted from the 316L-4 coupon were also characterised through EBSD. Figure 3.10 shows 3D-view optical micrographs of PBF 316L stainless steel. The samples exhibited a typical layered microstructure, characterised by melt pool boundaries generated along the laser scanning paths and a chequerboard macrostructure in the scan layers. Inspection of the SEM images reveals the formation of cellular solidification microstructure inside the melt pools, as shown in Figure 3.11. Periodic melt pools were revealed at high magnification, showing a half ellipse morphology and a depth and width of about 70 µm and 130 µm, respectively. Note that the differently oriented melt

pools are the result of the bidirectional scanning strategy, i.e. 45° rotation after each layer, and partial remelting occurred in the overlapping melt pools. A continuous epitaxial growth roughly along the build direction, which follows the direction of the maximum temperature gradient, results in the occurrence of slender columnar grains near the centreline of the melt pools. Figure 3.11(e) shows both the longitudinal (left region) and cross-section views (right region) of cells, with a rod-like structure and an average cell spacing of 0.90 µm.

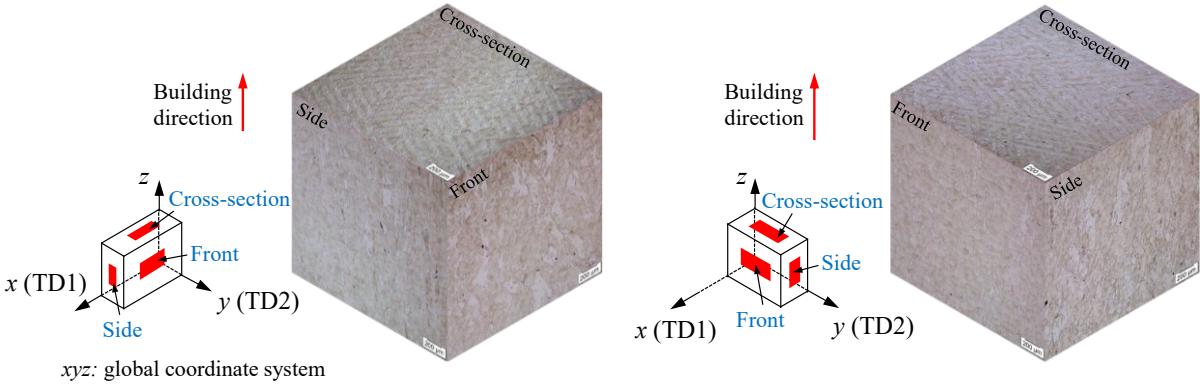

(a) (b)

Figure 3.10: 3D OM microstructure reconstruction of samples extracted from PBF (a) 316L-3 and (b) 316L-4 coupons, both showing the laser tracks along the build direction and the scanning pattern

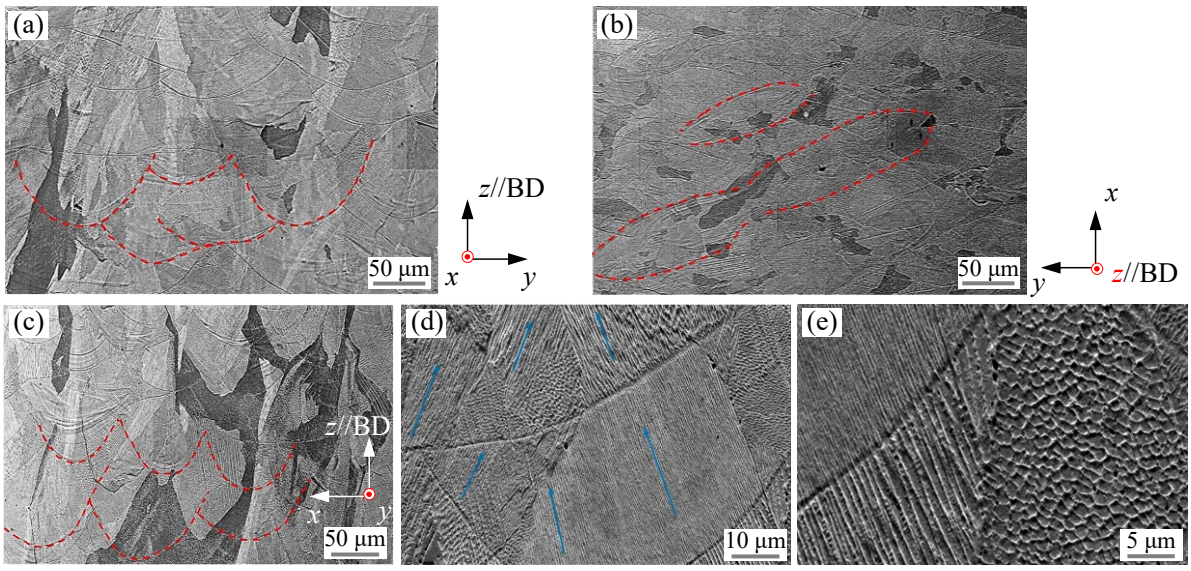

Figure 3.11: SEM micrographs of the (a) front views, (b) cross-section views and (c, d, e) side views of the samples. The red dash lines outline the melt pool boundaries, and the blue arrows denote the grain orientations

The examined PBF 316L stainless steel was found to comprise a single-phase austenitic face-centred cubic (FCC) crystal structure through EBSD analysis. Inverse pole figures are 2D representations of sample directions in the crystallographic coordinate system, whereas crystallographic directions in the sample coordinate system are plotted in pole figures. Figure 3.12 presents the EBSD orientation maps with respect to the build direction (IPF-BD) of the front, cross-section and side samples extracted from the 316L-4 coupon, coupled with the (100), (110) and (111) pole figures. The contour levels of orientations in the pole figures show the strength of the texture as a multiple of random occurrence. Wide/long columnar grains grew mainly along the <001> and <011> directions, which are the preferred growth directions for FCC crystals (Pham et al., 2020; Bahshwan et al., 2020). The epitaxial growth without changing cell direction along the centreline of melt pools promotes a set of slender columnar grains (coloured in red in Figure 3.12) with all the <001> being aligned with BD, TD1 and TD2, although the rotated scanning directions and the remelted layers can partially interrupt the formation of columnar grains across layers and weaken the texture intensity along the build direction, to a possible extent leading to finer microstructural features. Grains along the side of the melt pool boundaries (coloured in green in Figure 3.12) with <011> direction parallel with the BD, i.e. having two <001> directions aligned about 45° to the BD, which is due to the occurrence of side-branching. Side-branching of crystals between adjacent deposition tracks is prevalent due to the frequent changes in heat flux across the melt pool boundaries, which leads to the strongest texture with the maximum intensity of 8.4 times the random intensity, as shown in the (111) pole figure in Figure 3.12(f). The grain size is known to strongly affect the proof strength of the material according to the Hall-Petch relationship (Hall, 1951; Petch, 1953). Grain sizes were determined as equivalent circular diameter values; average grain sizes in the scanned areas of the front, cross-section and side samples were 36.7 μm, 28.2 μm and 41.7 μm, respectively.

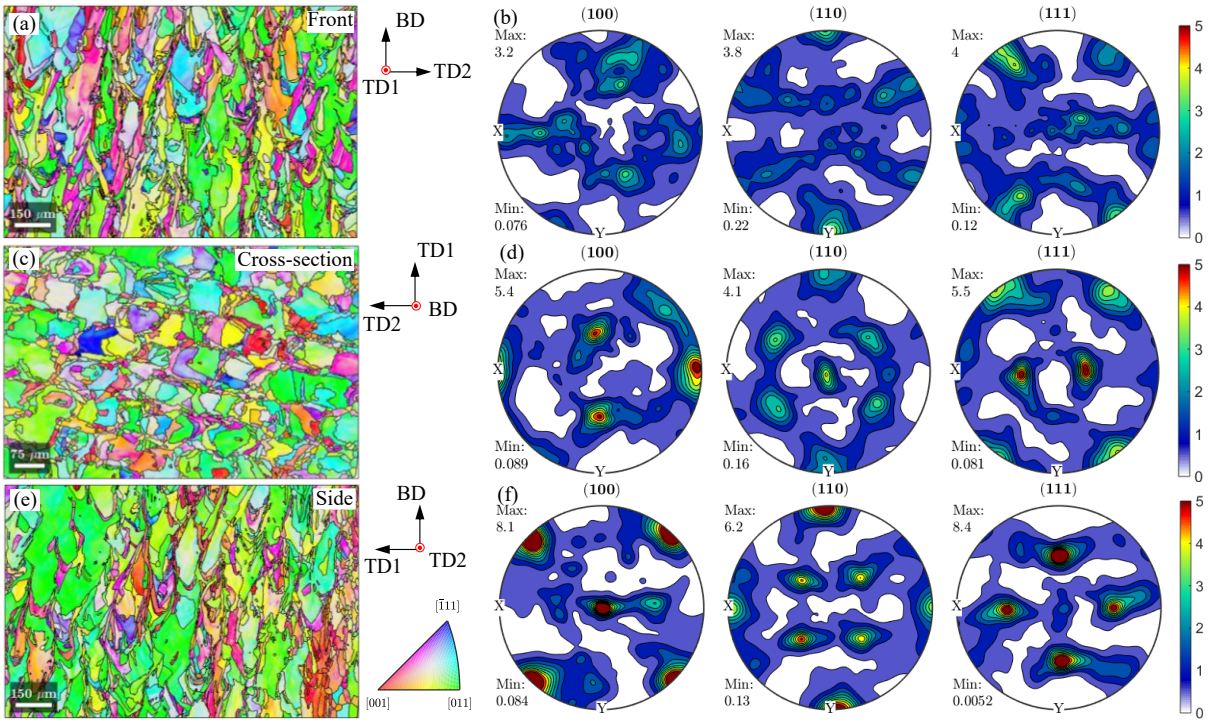

Figure 3.12: EBSD IPF-BD orientation maps with respect to the build direction (a, c, e) and pole figures (b, d, f) of (a, b) front, (c, d) cross-section and (e, f) side samples extracted from the 316L-4 coupon

3.4.3 Microstructural characterisation of PBF CX stainless steel

The cross-sectional microstructure and particle size distribution of the employed CX stainless steel powder are shown in Figure 3.13. The powder particles were mainly spherical with smooth surfaces, and only a small portion of satellite particles were adhered. A hybrid cellular and dendritic microstructure without secondary dendrites was observed. The average particle size was measured to be approximately equal to 37.4 μm, within the range of 20~65 μm as provided by the EOS manufacturer (EOS, 2019).

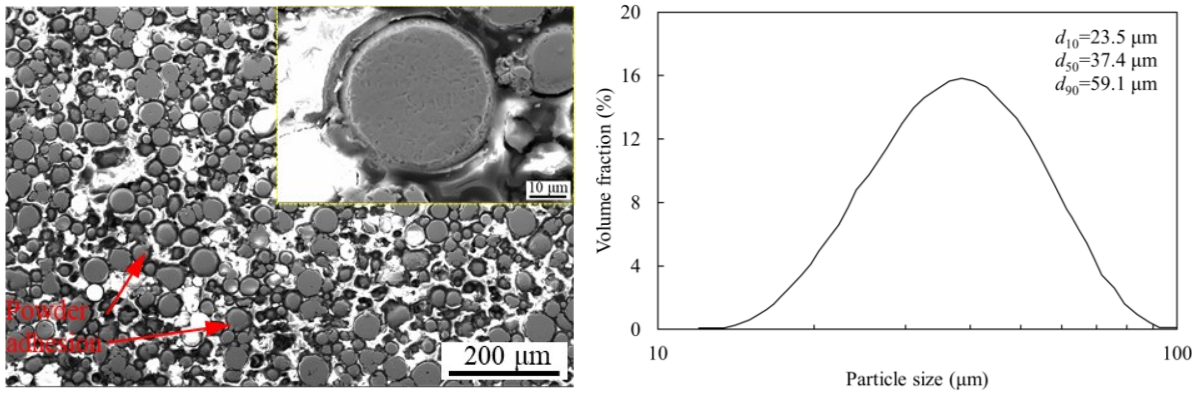

(a) (b)

Figure 3.13: (a) SEM image of the cross-sections and (b) particle size distribution of CX powder

Figure 3.14 shows the SEM images of the front (*yz* plane), cross-section (*xz* plane) and side (*xy* plane) samples at different magnifications, where some of the melt pool boundaries are marked by red dashed lines. The melt pools were half-elliptical in shape and overlapped with adjacent layers and scan tracks, which is typical of AM rapid solidification. At high magnification, fine epitaxial growth of the prior austenite grains from the melt pool boundaries (see Figure 3.14 (c) and (d)) and blocks of parallel martensite lathes with a random distribution inside the prior austenitic grains can be seen. The martensite laths have a length of a few microns and a width of a few nano metres, thus individual laths are too small to be clearly observed in the SEM images. When the material undergoes a non-equilibrium cooling condition during solidification, undercooled austenite may partially transform into fine lath martensite, and a very small amount of austenite may be retained after solidification, resulting in a fine microstructure.

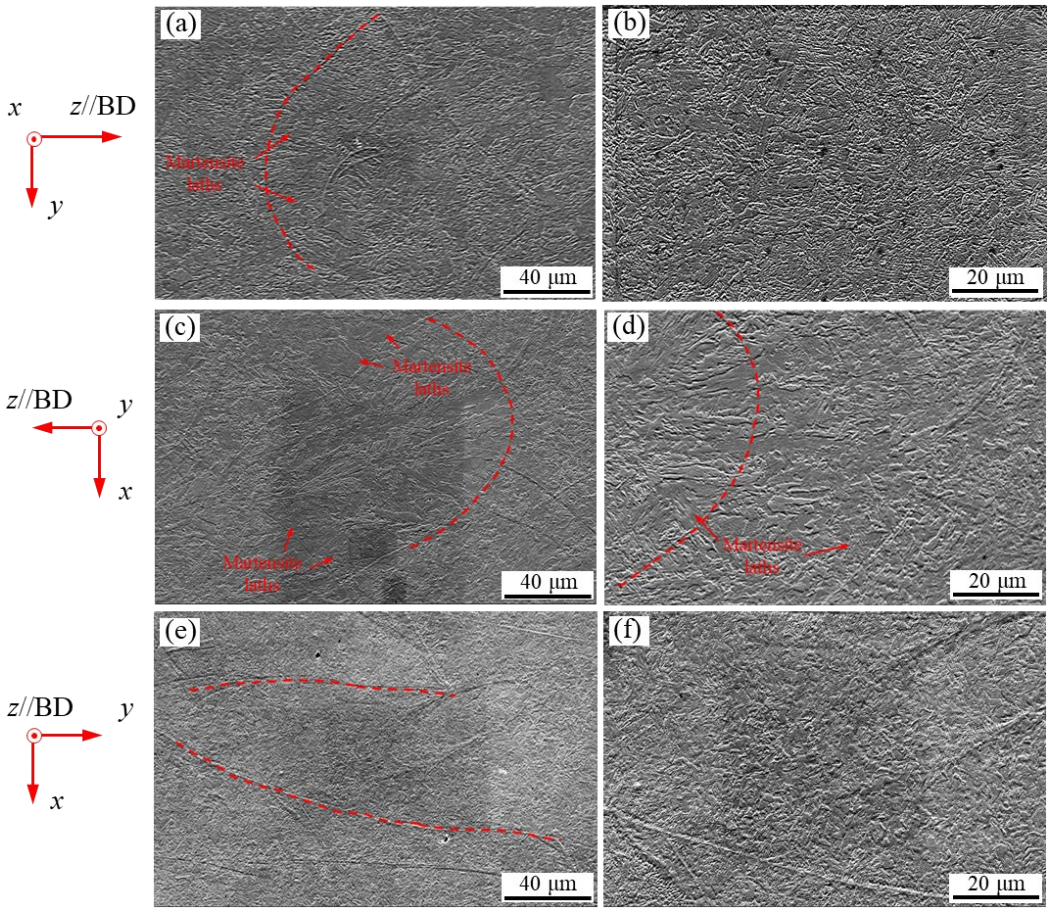

Figure 3.14: Microstructure of the (a, b) front faces, (c, d) cross-sections and (e, f) side faces of the PBF CX stainless steel samples extracted from the test CX-3 coupon. Left column: SEM images at ×2000 magnification. Right column: Enlarged SEM images at ×4000 magnification

EBSD analysis was employed to determine the proportion of body- and face-centred cubic (BCC-FCC) phases representing the martensite-austenite fraction. The phase map and grain size distribution from the PBF CX stainless steel side sample are shown in Figure 3.15. The CX stainless steel was found to be comprised dominantly of martensite BCC phase (coloured in red) and small fractions of austenite FCC phase (coloured in light green). The front, cross-section and side samples exhibited the presence of 1.1%, 3.2% and 1.9% FCC phase; this can be explained by different thermal histories that these three faces experienced during the PBF process. The average grain sizes for the front, cross-section and side samples were 2.1 μm, 2.5 μm and 2.1 μm, respectively, and 95% of grains observed were smaller than 8 μm. The formation of such fine grains can be attributed to the rapid solidification of the PBF CX parts, and also explains the high strength of PBF CX stainless steel.

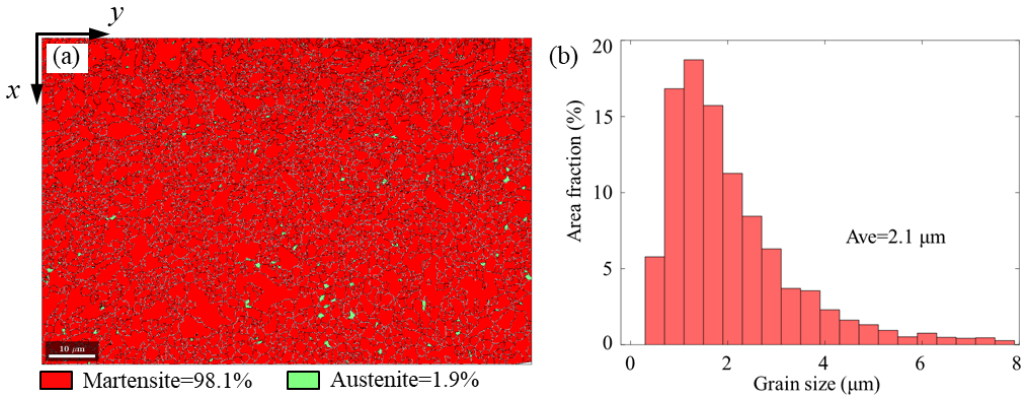

Figure 3.15: (a) Typical phase map and (b) grain size distribution of the PBF CX stainless steel side sample (in TD1-TD2 plane)

The EBSD orientation maps constructed using the IPF-BD colouring and grain boundary maps of the front, cross-section and side samples and their corresponding (100), (110) and (111) pole figures are depicted in Figure 3.16. It can be seen from the IPF maps that the side sample exhibited a slightly stronger texture (coloured in blue), and the corresponding pole figure showed a preferred orientation in the <111> direction (i.e. near the BD direction); this is in agreement with the (111) poles of the cross-section sample that showed a stronger texture in the BD direction. Nevertheless, the pole figures have a maximum texture intensity of 3.2 times the random intensity (parallel to BD), thus overall grains have no clearly specific crystallographic orientation or strongly preferred growth directions, and the CX stainless steel showed a weak cube texture.

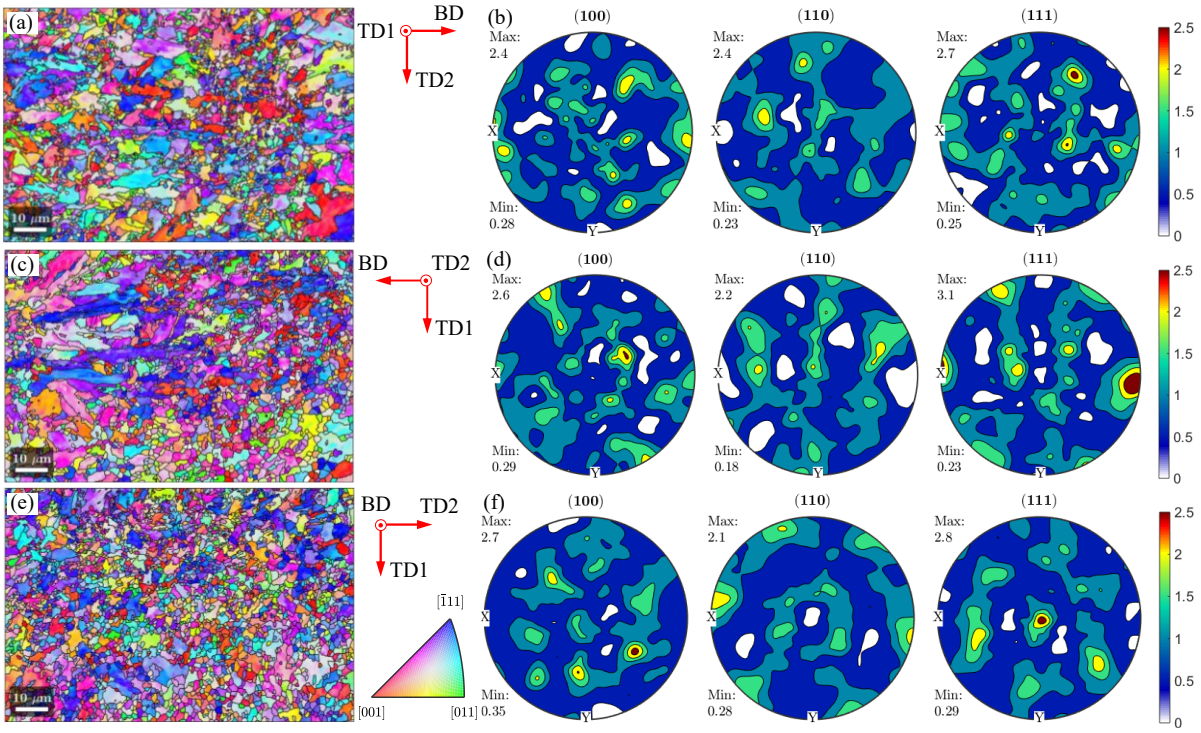

Figure 3.16: EBSD orientation maps (a, c, e) and pole figures (b, d, f) of (a, b) front, (c, d) cross-section and (e, f) side samples extracted from the CX-3 coupon, with IPF maps coloured with respect to the build direction (IPF-BD)

3.5 Tensile coupon tests on PBF stainless steel

3.5.1 Setup and data acquisition

Six vertical 316L and six horizontal CX tensile coupons (leading to twelve in total), with dog-bone shapes, were tested using a 250 kN Instron 8802 testing machine, as shown in Figure 3.17. Prior to tensile testing, a series of standard gauge lengths ($5.65\sqrt{S_0}$, where S_0 is the original cross-sectional area of the parallel length) were marked onto the front and back faces for the post-test measurement of the fracture strains. A four-camera LaVision DIC system (LaVision, 2017) was employed to measure strains over the parallel length on both coupon surfaces, with two cameras observing each side. The front and back faces of the coupons were painted white and sprayed with a random black speckle pattern to create trackable features along the parallel length. The testing machine was operated under displacement control, with two strain rates of 0.007% s^{-1} and 0.025% s^{-1} before and after yielding and a gradual transition between the two rates to avoid any abrupt change in rate, as recommended in EN ISO 6892-1 (CEN, 2016). The

applied load was measured using a load cell within the testing machine and recorded via an analogue to digital converter within the DIC system. The frequency for capturing the loading data and DIC images, was set to 1 Hz. The longitudinal strain was obtained by averaging the strains over the parallel length on both coupon faces, and the stress was derived using the measured applied load and cross-sectional area.

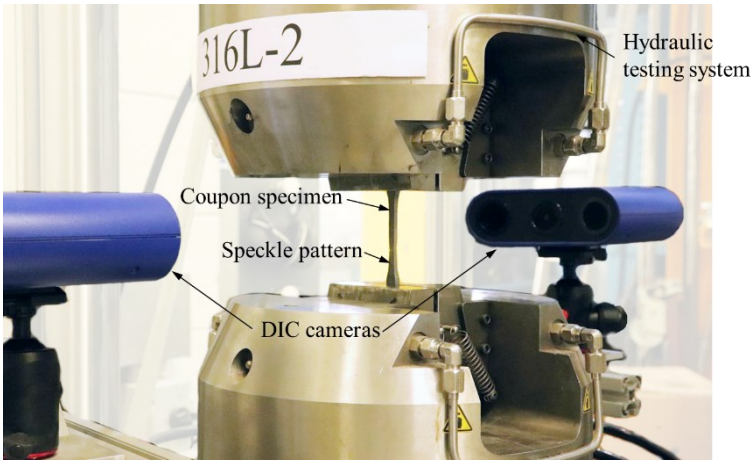

Figure 3.17: Tensile coupon test setup with 4-camera stereo-DIC system

3.5.2 Tensile properties

The measured engineering tensile stress-strain curves obtained from the coupon tests on the 316L and CX stainless steels are plotted in Figures 3.18 and 3.19, respectively, and the key material properties – the Young's modulus E, 0.2% proof strength $\sigma_{0.2}$, 1.0% proof strength $\sigma_{1.0}$, ultimate tensile strength σ_u, strain at the ultimate tensile strength ε_u, fracture strain over the marked gauge length ε_f, are reported in Tables 3.5 and 3.6. Also presented are the Ramberg-Osgood parameter n (Ramberg & Osgood, 1943) and the extended strain hardening parameters $m_{1.0}$ and m_u (Rasmussen, 2003; Gardner & Ashraf, 2006; Mirambell & Real, 2000), which were fitted to the measured stress-strain curves using the method described in Arrayago, Real and Gardner (2015) and Gardner and Yun (2018).

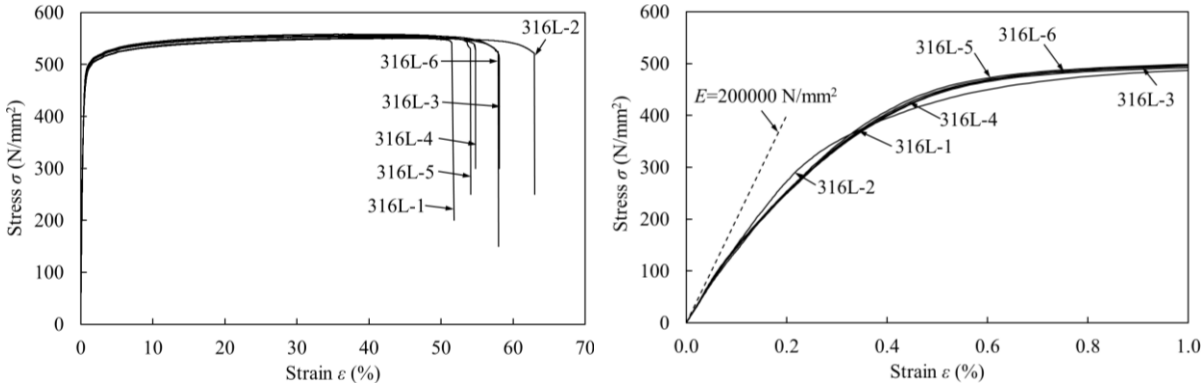

(a) (b)

Figure 3.18: Stress-strain curves of PBF 316L stainless steel tensile coupons in the (a) full range and (b) initial range

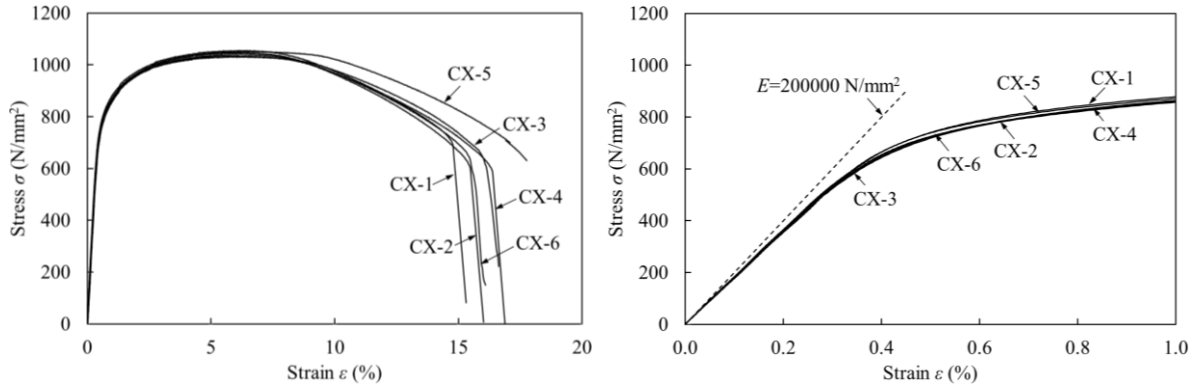

(a) (b)

Figure 3.19: Stress-strain curves of PBF CX stainless steel tensile coupons in the (a) full range and (b) initial range

The measured 0.2% proof stress, ultimate stress and fracture strain of PBF 316L and CX stainless steels were comparable to those reported in the EOS material datasheet (Table 3.2) (EOS, 2017, 2019). Generally, the PBF 316L base metal had higher proof and ultimate strengths ($\sigma_{0.2}$, $\sigma_{1.0}$ and σ_u) than 316L stainless steel formed by other means (Mower & Long, 2016; Yadollahi et al., 2015; ASTM, 2019), as indicated in Table 3.7. The increase in ultimate strength σ_u is smaller than that of the 0.2% proof stress $\sigma_{0.2}$, and the fracture strain ε_f of the PBF base metal and the conventionally formed material is similar. As previously discussed in Subsection 3.4.2, PBF 316L stainless steel has a finer microstructure compared with its conventionally produced counterparts, leading to a higher measured strength, following the Hall-Petch relationship (Hall, 1951; Petch, 1953). It should be noted that there is some scatter in the measured tensile properties of PBF 316L stainless steel among previous studies, in terms of

material strengths (Casati, Lemke & Vedani, 2016; Wang et al., 2016) and elongations at fracture (Casati, Lemke & Vedani, 2016). The PBF CX stainless steel exhibited higher proof and ultimate strengths but lower fracture strains than those of the as-built PBF 316L stainless steel. The superior mechanical strength of the PBF CX stainless steel is due to the fine grains caused by extremely rapid cooling, as described in Subsection 3.4.3. The Young's moduli E of PBF 316L and CX stainless steels were slightly lower than the typically assumed value of E=200000 N/mm^2 for conventional stainless steels (Arrayago, Real & Gardner, 2015).

Table 3.5: Measured material properties from vertical tensile coupon tests

Coupon	E (N/mm^2)	$\sigma_{0.2}$ (N/mm^2)	$\sigma_{1.0}$ (N/mm^2)	σ_u (N/mm^2)	ε_u (%)	ε_f (%)	n	$m_{1.0}$	m_u
316L-1	174100	439	499	551	39.6	60.7	3.4	6.0	7.4
316L-2	162100	420	496	550	45.7	62.0	5.1	7.6	9.4
316L-3	170900	433	502	556	39.7	59.3	3.0	6.6	8.1
316L-4	164400	437	503	555	36.7	59.0	3.0	6.4	7.9
316L-5	172500	443	505	558	35.6	58.5	3.0	5.9	7.2
316L-6	160000	439	502	553	37.4	60.5	3.3	6.2	7.8
Average	167300	435	501	554	39.1	60.0	3.5	6.5	8.0

Table 3.6: Measured material properties from horizontal tensile coupon tests

Coupon	E (N/mm^2)	$\sigma_{0.2}$ (N/mm^2)	$\sigma_{1.0}$ (N/mm^2)	σ_u (N/mm^2)	ε_u (%)	ε_f (%)	n	$m_{1.0}$	m_u
CX-1	177200	804	940	1054	6.3	15.9	10.8	4.6	3.6
CX-2	180000	777	924	1046	6.6	20.2	8.2	4.7	3.5
CX-3	180400	779	928	1033	5.9	20.8	8.5	4.7	3.8
CX-4	181300	779	926	1030	6.1	21.2	8.9	4.9	3.9
CX-5	183000	792	934	1052	6.5	21.7	9.8	4.7	3.6
CX-6	183800	775	921	1038	6.2	21.1	8.7	4.5	3.6
Average	181000	784	929	1042	6.3	20.1	9.2	4.7	3.7

Table 3.7: Comparison of mechanical properties of conventionally manufactured and PBF 316L stainless steel from this study

Reference	Type of 316L stainless steel	E (N/mm^2)	$\sigma_{0.2}$ (N/mm^2)	σ_u (N/mm^2)	ε_f (%)	n
This study (Section 3.5)	PBF vertical base metal	167300	435	554	60.0	3.5
This study (Section 3.8)	PBF horizontal base metal	179200-206300	501-567	-	-	8.3
	PBF vertical base metal	168700-191700	452-471	553-563	42.0-46.8	5.7
Mower & Long (2016)	Wrought	187000	345	563	30.0	-
Yadollahi et al. (2015)	Cast	-	262	552	55.0	-
ASTM (2019)	Forged	-	170	450	40.0	-
CEN (2014)	Hot-rolled	193000	220	530-680	40.0	-
	Cold-rolled	193000	240	530-680	40.0	-

3.6 Microstructural characterisation on PBF stainless steel with laser welded joints

3.6.1 Sample preparation and experimental characterisation techniques

Prior to the destructive tensile tests on laser-welded coupons, a total of nine samples, listed in Table 3.8, with varying build orientations, laser power and scanning speeds, were selected from the specimen pool. One face of each selected sample was prepared for microstructural observations in accordance with ASTM E3-11 (ASTM, 2012). The as-polished surfaces were observed using an Olympus BX51 optical microscope and analysed using the image processing software ImageJ (Rasband, 1997) to calculate the porosity of the examined surface. In order to reveal the material microstructure, aqua regia and Kalling's No. 2 solutions, which were previously used by others for PBF 316L microsamples (Wang et al., 2016; Yusuf et al., 2017), were first employed as the chemical etchants, but were found to be not effective for the large dimension samples. The sample surfaces were instead successfully electrolytically etched using a 10%wt oxalic acid solution, at 6 volts for 60 seconds as recommended by ASTM E407-07 (ASTM, 2015), and then ultrasonically cleaned in an acetone bath to remove any residues.

Table 3.8: Tensile coupons selected for microstructural observations and microhardness tests

Coupon type	Optical microscopy and microhardness tests			SEM and EBSD
Horizonal	H1/3	H2/3	H3/1	H1/1 & H1/3
Vertical	V1/2	V2/2	V3/1	V1/3
Combined	X1/3	X3/3	X4/1	-

3.6.2 Porosity of the PBF base metal

Representative optical micrographs of as-polished horizontal and vertical base metal samples are presented in Figure 3.20, where the process-induced and gas-induced pores are clearly visible. The gas-induced pores, highlighted in Figure 3.20(a), had a spherical morphology that is consistent with the use of powder feedstock and were found to be nonuniformly distributed. A small fraction of processed-induced pores with irregular shapes, formed due to lack of fusion, as shown in Figure 3.20(b). The area fraction of pores was calculated using ImageJ (Rasband, 1997) and the results showed that the porosity was less than 0.5% in the PBF base metal. Additionally, there was no significant difference in porosity between the examined surfaces of

the horizontal and vertical samples, which is consistent with previous research (Tomus et al., 2016). Previous studies have reported that the porosity decreases with an increase in laser power and a reduction in scanning speed (Meier & Haberland, 2008; Choo et al., 2019; Gu & Shen, 2008). Although it was challenging to observe the weld boundaries prior to etching, the weld regions were seen to be almost pore-free, which was expected since the weld was formed with both a higher laser power and slower welding speed than those used in the PBF manufacturing process.

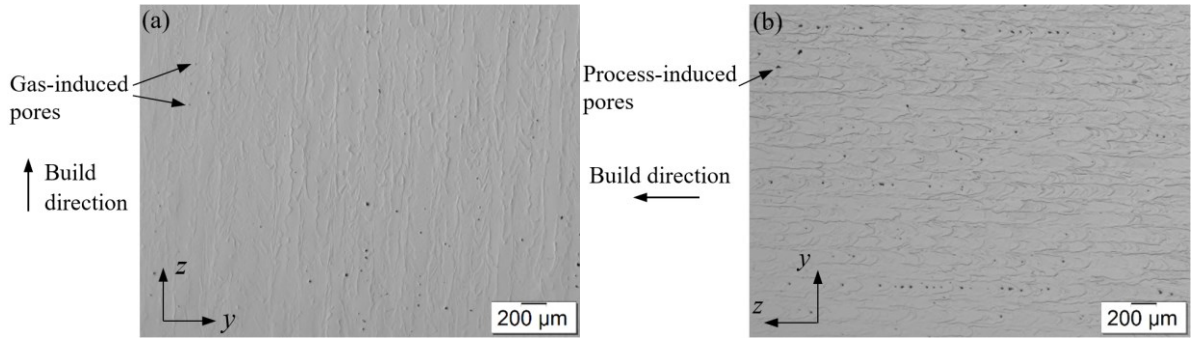

Figure 3.20: Typical micrographs of an as-polished (a) horizontal coupon (H1/1) and (b) vertical coupon (V3/1)

3.6.3 Microstructural characterisation of the PBF base metal

The microstructural features of the base metal were examined using OM and SEM analysis. The examined surface was parallel to the build direction, covering multiple print layers, and is shown as the *yz* plane in Figure 3.4.

Figures 3.21 and 3.22 depict typical optical micrographs of the PBF base metal for as-etched horizontal and vertical specimens, respectively, where the build direction is labelled, the red dashed lines denote the melt pool boundaries, the blue arrows indicate the grain orientations and the blue dashed lines show the grain boundaries. Periodic melt pools were revealed after electrolytic etching. At high magnification (Figure 3.21(b) and Figure 3.22(b)), the melt pools were observed to have half-ellipse shapes, with a depth and width of approximately 60 µm and 120 µm respectively, and their size correlated with the heat input and laser spot diameter (Campanelli et al., 2014). Overlapping scan areas of melt pools were observed between the adjacent PBF laser scan tracks and layers, indicating that partial remelting occurred (see Figures 3.21 to 3.23). Smaller hatch distance and layer thickness employed for the printing, when

compared with the measured width and depth of melt pools, led to larger overlapping degrees of laser-remelted traces, as illustrated in Figure 3.23.

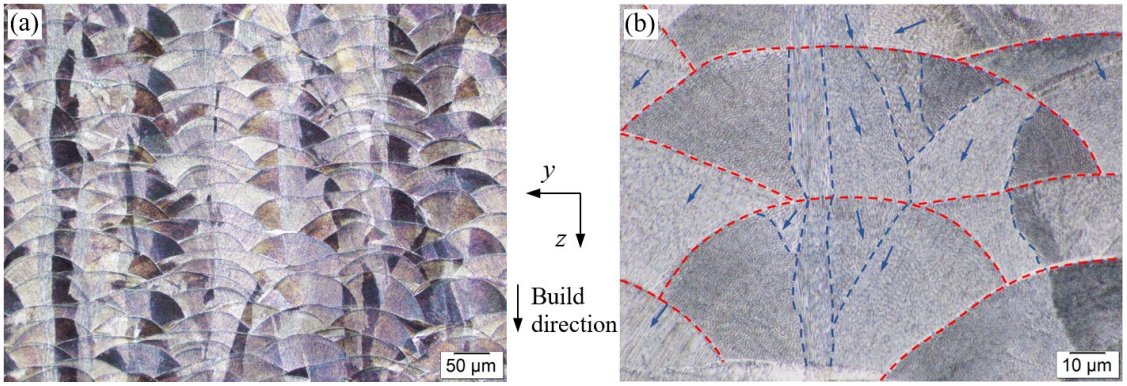

Figure 3.21: Typical optical micrographs in front view for an as-etched horizontal specimen (H1/3) for the (a) base metal and (b) melt pools

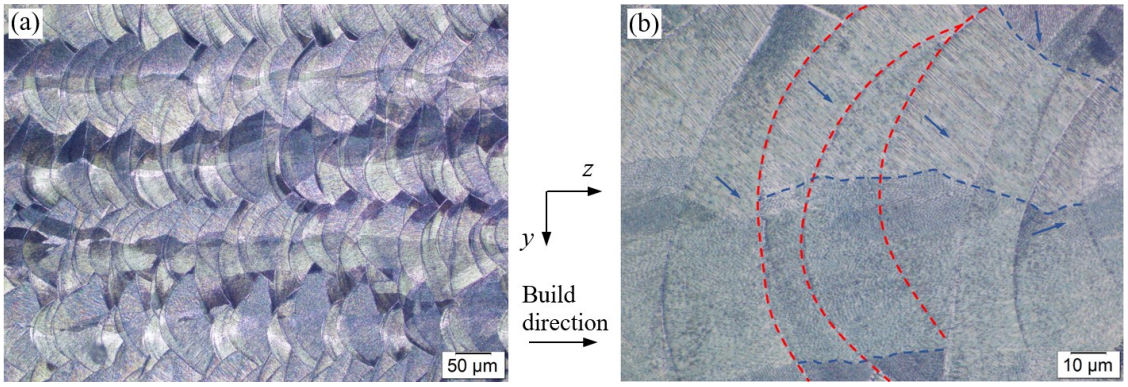

Figure 3.22: Typical optical micrographs in front view for an as-etched vertical specimen (V1/2) for the (a) base metal and (b) melt pools

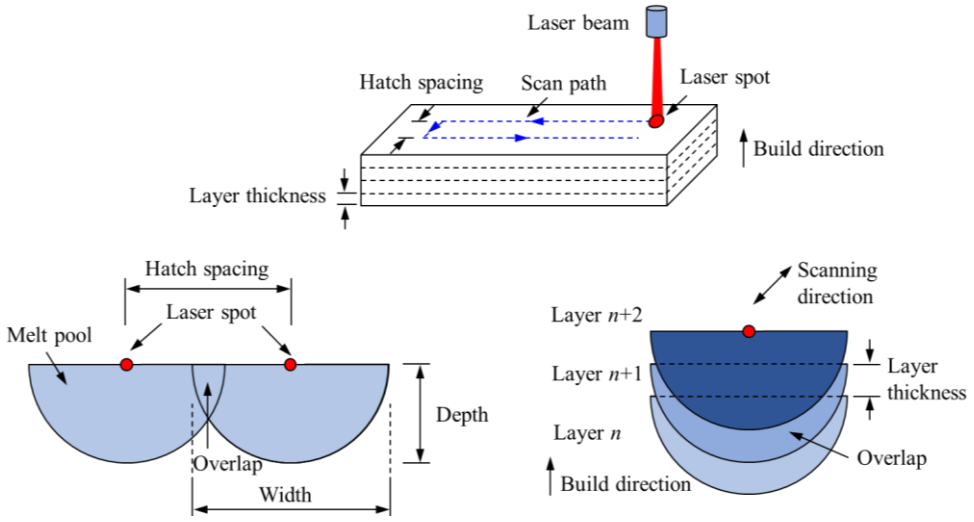

Figure 3.23: Formation of scan tracks and partial remelting

SEM and EBSD characterisations were performed after the conclusion of the tensile tests to examine the underlying grain structure of the horizontal and vertical base metal further. Small metallographic pieces were extracted from the gripped regions of the H1/3 and V1/3 coupons. These were ground, polished, etched using a 10%wt oxalic acid solution and then examined using an FEI Quanta 650 scanning electron microscope equipped with a Bruker *e*-Flash HD and Esprit 2.2 (Bruker, 2018). The samples were scanned covering an area of 834.3×555.5 μm^2 (microscope magnification of ×500), with a scan step size of 1.67 µm. Aqua regia was found to be effective to reveal microstructural features of small PBF 316L stainless steel samples; the EBSD characterisation of horizontal samples etched by aqua regia was described in Zhang et al. (2021a).

The SEM images of front, cross-section and side samples extracted from horizontal and vertical coupons are shown in Figure 3.24. The microstructure in the scan layers (normal to the build direction) showed a chequerboard pattern in line with the adopted scanning strategy. The PBF 316L base metal exhibited a typical cellular microstructure, which is consistent with previous observations on PBF 316L stainless steel (Trelewicz et al., 2016; Mertens et al., 2014; Ghasri-Khouzani et al., 2018; Liverani et al., 2017; Suryawanshi, Prashanth & Ramamurty, 2017; Casati, Lemke & Vedani, 2016), and was formed due to the very high cooling rates, of the order of 10^3-10^8 K/s (Casati, Lemke & Vedani, 2016), encountered in the manufacturing process. Epitaxial grain growth occurred during remelting, spanning over the melt pools within a layer and across multiple layers. Elongated grains formed with a preferential orientation aligned with the build direction, close to the direction of the maximum thermal gradient.

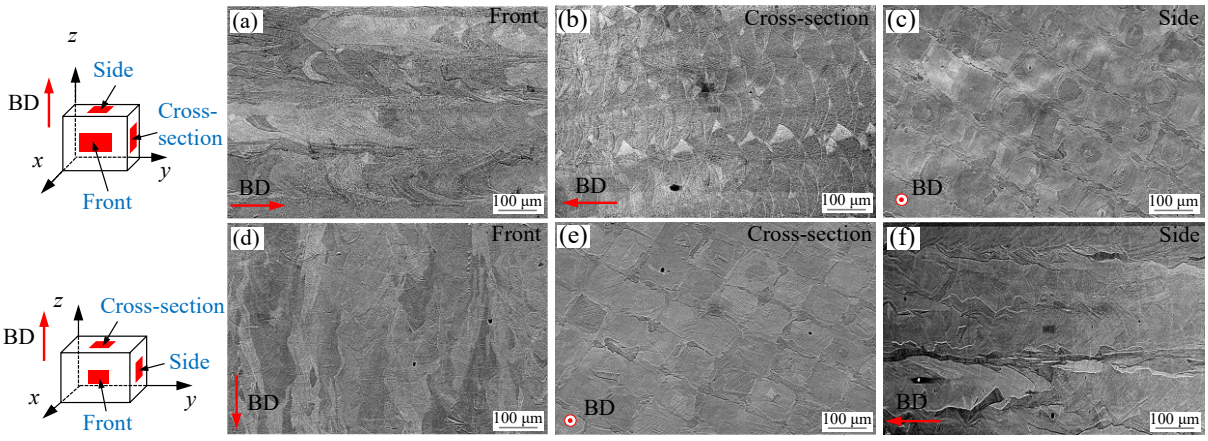

Figure 3.24: SEM images of horizontal (a, b, c) and vertical (d, e, f) of samples in (a, d) front, (b, e) cross-section and (c, f) side views

Figure 3.25 shows a typical FSD image taken from an as-etched vertical subsample (extracted from V1/3), along with the corresponding inverse pole figure (IPF) map with respect to the build direction. A typical grain size distribution and (100), (101) and (111) pole figures of the examined surface are shown in Figure 3.25 (c) and (d), where the high localised intensities on the pole figures represent the preferred orientations of the grain's pole. The microstructure of the scan layers (i.e. normal to the build direction) exhibited a chequerboard pattern (i.e. nearly square-like), which is in line with the adopted scanning strategy (i.e. Bidirectional stripe hatching), and a slightly preferred grain texture in the <011> direction with a maximum intensity of 5.3 times random. The grains had an average size of about 21.2 µm, and the maximum size was 189.2 µm.

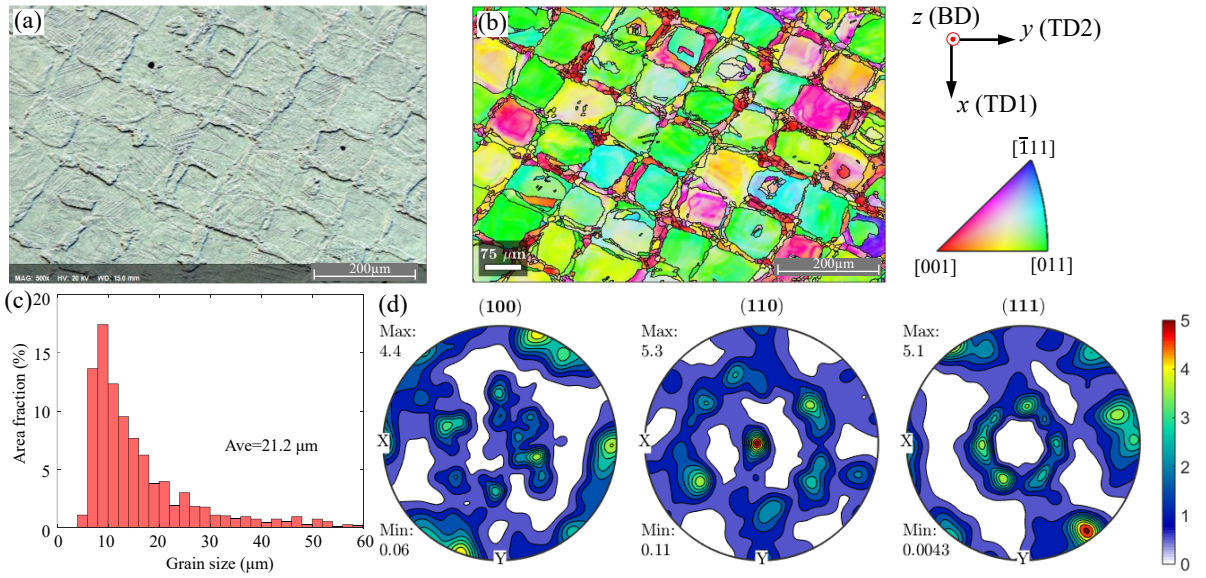

Figure 3.25: Typical (a) FSD image, (b) EBSD inverse pole figure maps, with colours presented with respect to the build direction and (c) grain size distribution and (d) pole figures of the base metal subsample for the vertical coupon V1/3

Figure 3.26 presents EBSD inverse pole figure maps and pole figures of the front, cross-section and side samples extracted from the horizontal (H1/3) coupon. The solidification characteristics of the PBF 316L base metal can be seen, with a typical cellular microstructure, which is consistent with that observed from the earlier OM and SEM analysis in Subsection 3.6.3. The columnar grains exhibited epitaxial growth, roughly parallel to the build direction, leading to a slightly stronger preference for grains oriented in the <001> direction; another preferred crystal orientation was the <011> direction, which is due to the occurrence of side-branching of crystals

in the side of melt pools. But overall, the material exhibited a weak crystallographic texture, which is in line with other studies employing a similar bidirectional scanning strategy with rotation between adjacent layers (Choo et al., 2019; Niendorf et al., 2013). The grains in the front, cross-section and side samples had average sizes of about 40.2 µm, 34.9 µm and 19.3 µm, respectively. The texture and potential phase transformation in laser welds produced with different welding parameters requires further exploration.

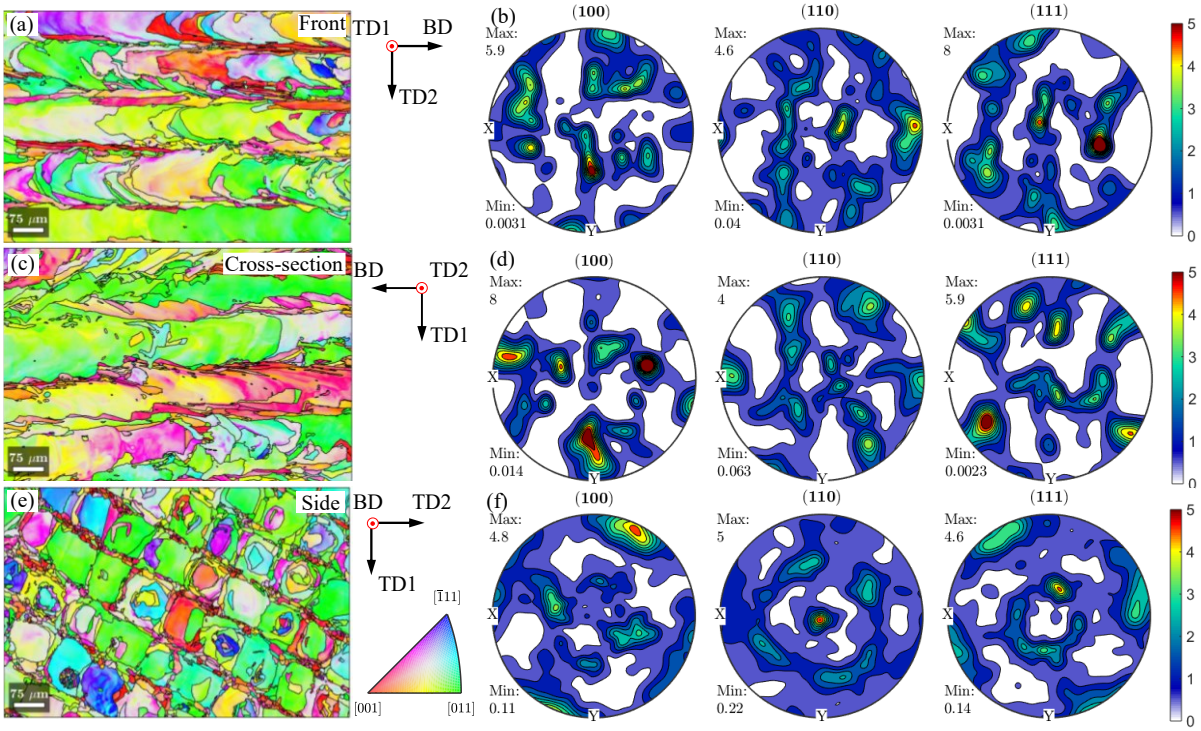

Figure 3.26: EBSD inverse pole figure (IPF) maps (a, c, e) along the build direction and pole figures (b, d, f) of (a, b) front, (c, d) cross-section and (e, f) side samples extracted from the horizontal coupon H1/3

3.6.4 Microstructural characterisation of laser welded joints

Figure 3.27 shows the morphology of the laser weld regions, where the fusion lines and weld centrelines can be clearly observed. The welds are straight and nearly symmetric in shape about the welding path axes, unlike the bead weld profiles in conventional material that has been laser welded (Matilainen, Pekkarinen & Salminen, 2016). The observed difference in weld shapes is due to the different absorption properties of these two base materials (Matilainen, Pekkarinen & Salminen, 2016); the higher roughness of the PBF base material results in a higher absorption rate, and therefore a straight and full penetration weld is more likely to form, compared with

cold-rolled metallic material.

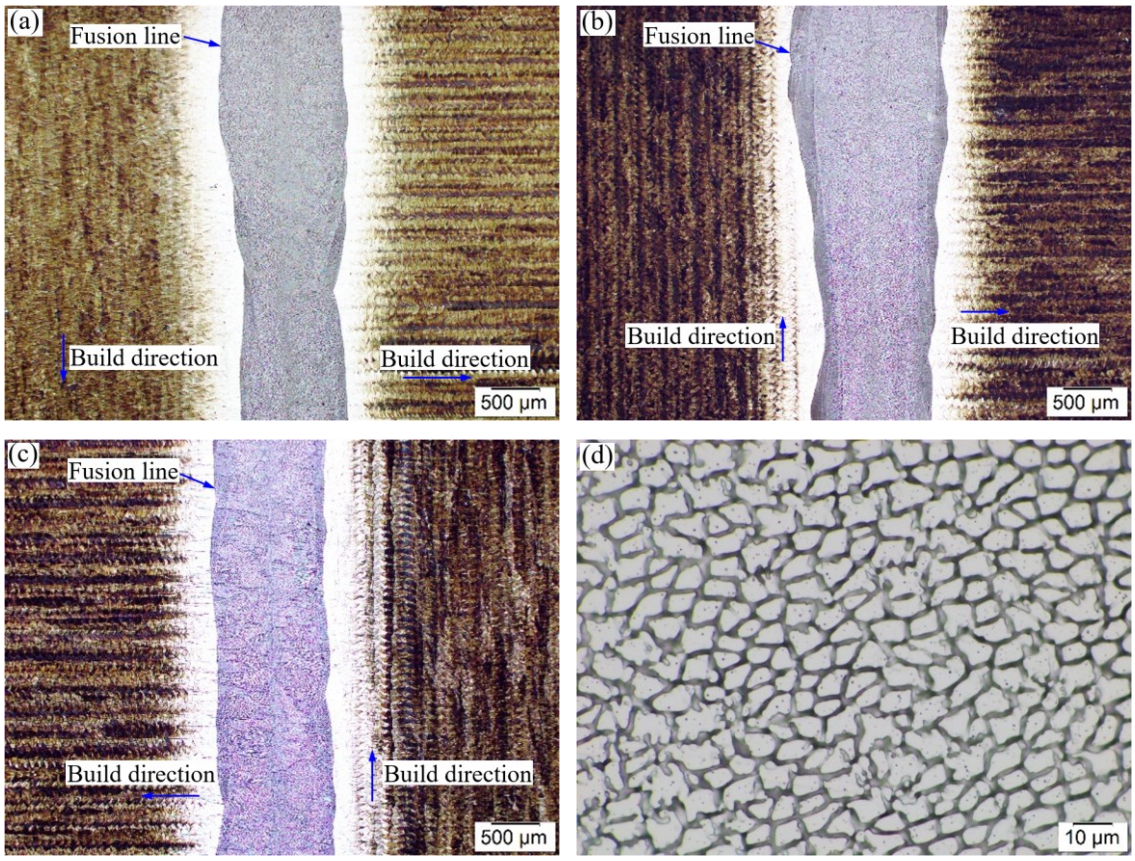

Figure 3.27: Typical weld micrographs for the coupon (a) X1/3 (P=3.5 kW, S=1750 mm/min), (b) X3/3 (P=4 kW, S=1750 mm/min), (c) X4/1 (P=4 kW, S=2000 mm/min) and (d) X4/1 (centre of the weld)

Under a high-magnification optical microscope, the weld centre was observed to be dominated by equiaxed dendrites (Figure 3.27(d)); this morphology results from the low G/R ratio at the weld centre, where G is the temperature gradient and R is the solidification growth rate. Figure 3.28 shows typical optical micrographs for the fusion line and weld centre, with the observed microstructure consisting of cellular dendrites, columnar dendrites and equiaxed dendrites. The grain size in the weld was generally larger than that in the PBF base metal. The extremely high energy input of laser welding leads to a relatively slow cooling rate, which allows more time for grain coarsening and for the dendrites to propagate further during solidification.

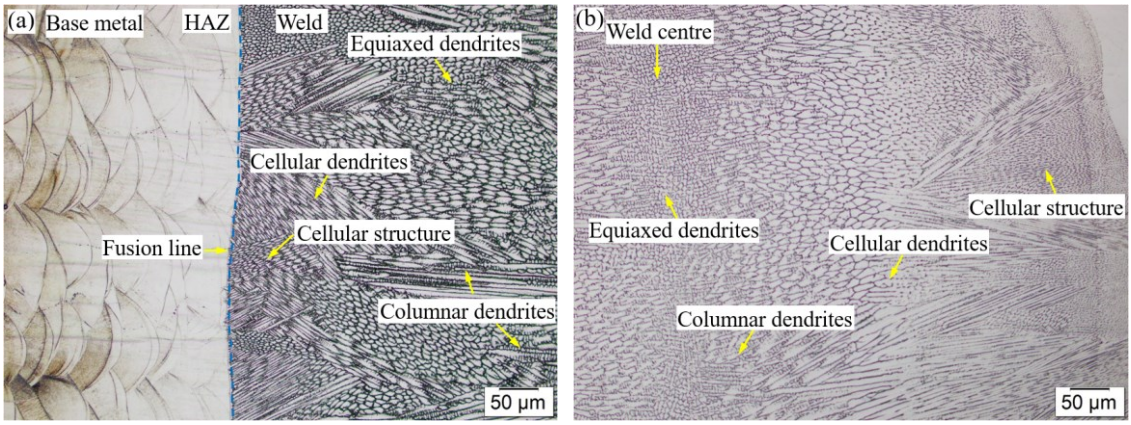

Figure 3.28: Typical micrographs at the fusion line, showing (a) the transition zone from base metal to weld and (b) the grain structure of the weld

The HAZ exhibited a similar microstructure to the PBF base metal. Although the boundaries between the HAZ and the base metal are obscure under an optical microscope, they can be distinguished by the colour change. The average widths of the weld region and HAZ were determined from individual measurements taken at ten uniformly distributed locations across the specimen width. The average measured weld and HAZ widths for all specimens were around 1000 µm and 500 µm respectively. The measured widths of the weld and HAZ are plotted against the energy input of the laser welding in Figure 3.29. The weld width increases from 900 µm to 1200 µm and the HAZ width varies from 450 µm to 600 µm, as the energy input increases from 105 J/mm to 137 J/mm. It can therefore be concluded that upon the suitable selection of welding parameters, the PBF 316L base material can be laser welded with full penetration and narrow weld and HAZ widths, enabling small PBF elements to be mechanically joined to form larger parts; special attention needs to be paid to the potentially reduced strength and ductility of the weld compared to the printed base metal, and in the case of thicker metal pieces.

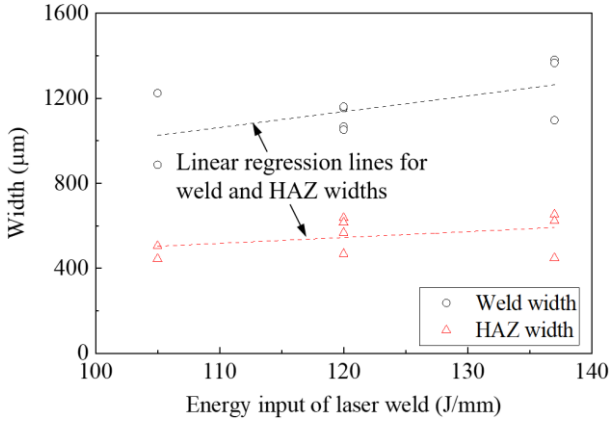

Figure 3.29: Variation of the weld and HAZ width with the laser welding energy input

3.7 Microhardness tests on PBF stainless steel with laser welded joints

Microhardness measurements were carried out on the as-etched specimens, in compliance with ISO 6507-1 (CEN, 2018), using a Zwick/Roell ZHV Vickers hardness tester equipped with an optical microscope. An applied load of 0.98 N, with a dwell time of 10 s, was used for all indentations. To evaluate the variation of the microhardness in the weld, HAZ and base metal, indentations were made along the parallel length of the tensile coupons, at the locations shown in Figure 3.30(a). Working along the longitudinal coupon axis, indentations were made at 0.5 mm intervals for the base metal and 0.1 mm intervals for the weld and expected HAZs, to measure the microhardness profile along the coupon. Average values of the microhardness for these three regions were calculated by taking measurements in the transverse direction, at 0.5 mm intervals, along the weld centre, within the HAZ and for the base metal away from the HAZ (Figure 3.30(b)).

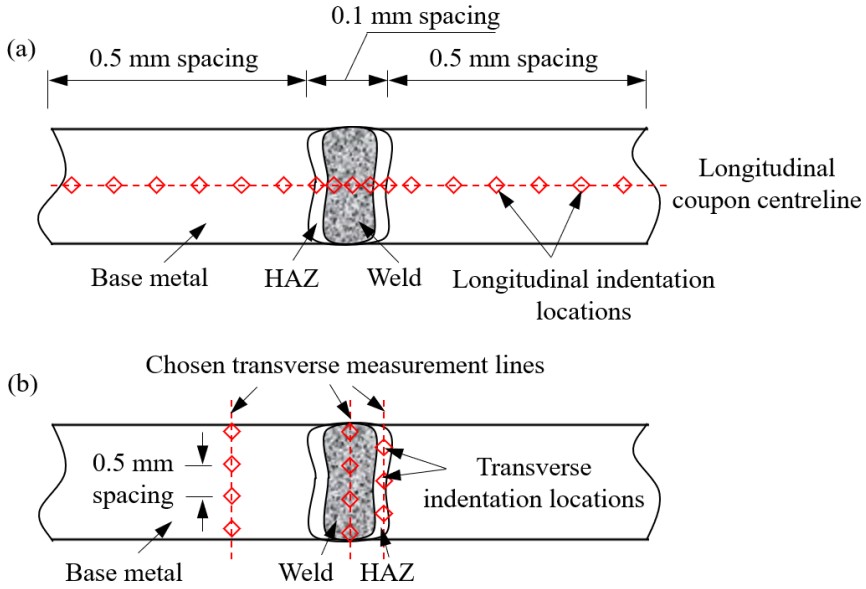

Figure 3.30: Microhardness measurement locations for the weld, HAZ and base metal, showing indentation positions and intervals in the (a) longitudinal and (b) transverse directions (not to scale)

Figure 3.31 shows typical microhardness profiles across the laser welded joints in the horizontal, vertical and combined coupons, showing a relatively uniform microhardness profile that reduces at the laser weld. The average microhardness (HV) values for the measurements made in the transverse direction across the coupon width for the weld, HAZ and base metal, are reported in Table 3.9. The PBF base material had microhardness values between 214 HV and 234 HV, higher than those of conventionally produced counterparts (150~160 HV) (Sun et al., 2016). The adopted build direction was observed to have no significant effect on the microhardness of the PBF 316L base metal, in line with previous studies (Tolosa et al., 2010). The weld was found to have a slightly lower average microhardness (197 HV) than the HAZ (207 HV) and base metal (222 HV), which was also observed in other studies (Casalino, Campanelli & Ludovico, 2013; Rossini et al., 2015), and is attributed to the coarser weld microstructure that was described in Subsection 3.6.5 (Sun et al., 2016; Ventrella, Berretta & Rossi, 2010).

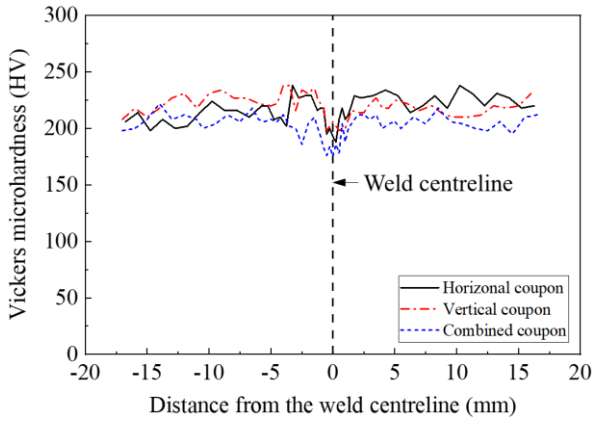

Figure 3.31: Variation of microhardness along the longitudinal coupon axis

Table 3.9: Summary of the weld, HAZ and base metal microhardness (HV)

Location	H1	H2	H3	V1	V2	V3	X1(H)	X1(V)	X3(H)	X3(V)	X4(H)	X4(V)
Weld	213	243	198	189	178	181	204	204	198	198	181	181
HAZ	196	242	200	203	198	198	220	207	204	212	208	201
Base metal	217	227	227	225	219	214	234	226	218	218	227	216

3.8 Tensile coupon tests on PBF stainless steel with laser welded joints

3.8.1 Setup and data acquisition

Tensile coupon tests were undertaken to evaluate the strength of the laser welded joints in line with EN ISO 6892-1 (CEN, 2016) using an Instron 8802 testing machine; The same test setup was adopted with tensile tests on nonwelded coupons, as shown in Figure 3.17. In order to calculate the global strain from DIC measurements which is consistent with the tensile strain defined in EN ISO 6892-1 (CEN, 2016) using an extensometer, the global longitudinal strain was derived by averaging the strains over the full area of the parallel length on both faces for each coupon. The local longitudinal strains were also extracted from 1 mm long rectangular boxes, each covering the full width of the coupons, in order to show the strain variation along the parallel length of the welded coupon.

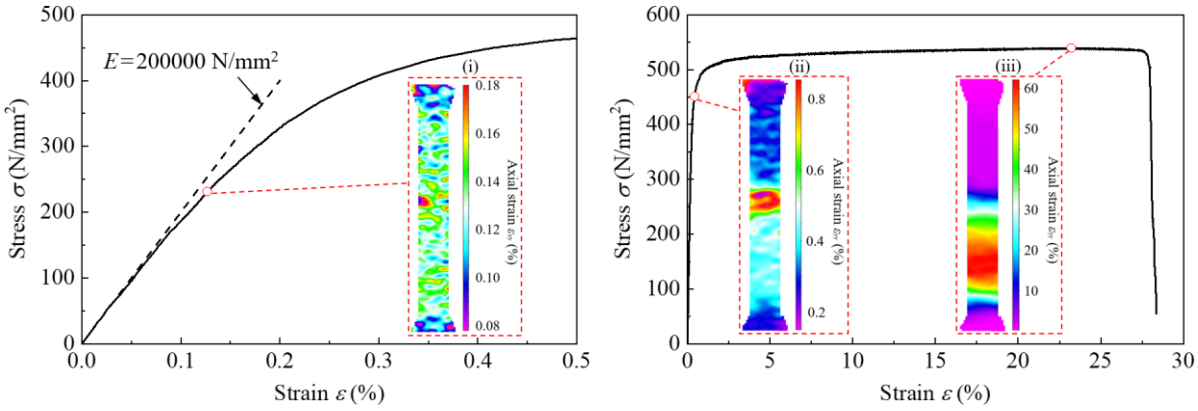

Figure 3.32: Measured global stress-strain relationship for the X1/1 tensile coupon showing (a) the initial response and (b) the full response, with DIC axial strain plots at (i) $0.5\sigma_{0.2}$, (ii) $\sigma_{0.2}$ and (iii) σ_u

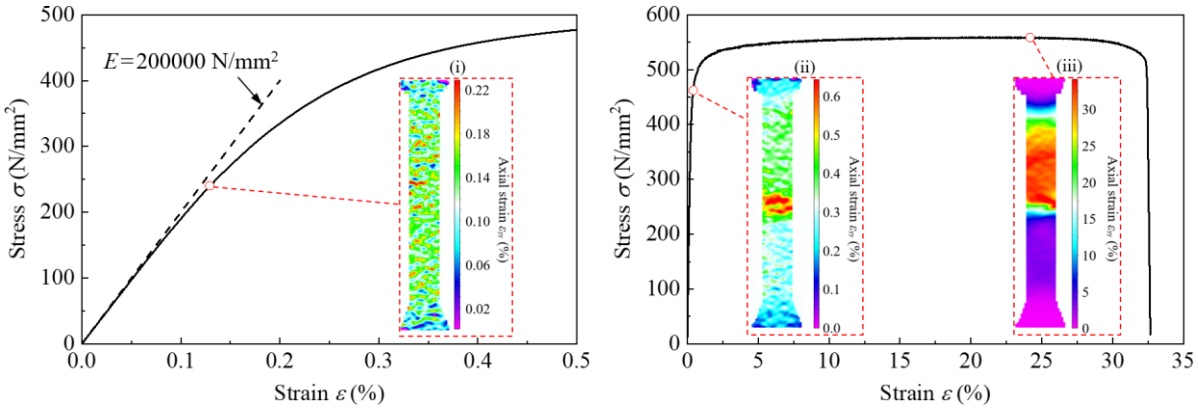

Figure 3.33: Measured global stress-strain relationship for the X3/2 tensile coupon showing (a) the initial response and (b) the full response, with DIC axial strain plots at (i) $0.5\sigma_{0.2}$, (ii) $\sigma_{0.2}$ and (iii) σ_u

3.8.2 Tensile properties and their correlation with microstructure

The stress-strain responses were determined (i) globally (across the weld, HAZ and base metal), calculated over the parallel length and (ii) locally, within 1 mm long boxes, along the parallel length, capturing separately the properties of the base metal, HAZ and weld regions. Typical global stress-strain curves and single side DIC strain fields at key points during the tensile testing are shown in Figures 3.32 and 3.33 for coupons X1/1 and X3/2 respectively. It can be seen that the X1/1 coupon fractured in the base metal (in the vertical half part), whereas the X3/2 coupon failed in the laser weld. The weld zone is not visible from the DIC strain field until the macroscopic stress level reaches approximately half the 0.2% proof stress (i.e. $0.5\sigma_{0.2}$);

beyond this value, the fusion zone exhibits higher local strains than the base metal (under the same load level). The global stress-strain curves are shown in Figure 3.34, while the global tensile properties, averaged per welding parameter and build direction combination, are reported in

Table 3.10; the reported properties are the Young's modulus E, the 0.2% proof strength $\sigma_{0.2}$, the 1.0% proof strength $\sigma_{1.0}$, the ultimate tensile stress σ_u, the average global strain at the ultimate stress over the parallel length $\varepsilon_{u,gl}$, the fracture strain over the marked gauge length ε_f, the Ramberg-Osgood parameter n (Ramberg & Osgood, 1943) and the extended parameters $m_{1.0}$ and m_u (Mirambell & Real, 2000; Rasmussen, 2003; Gardner & Ashraf, 2006). In general, the vertical coupons loaded parallel to the building direction exhibited a slightly lower Young's modulus, which can be attributed to the typical <001> texture and the columnar grain morphology of AM stainless steel (Hosseini & Popovich, 2019).

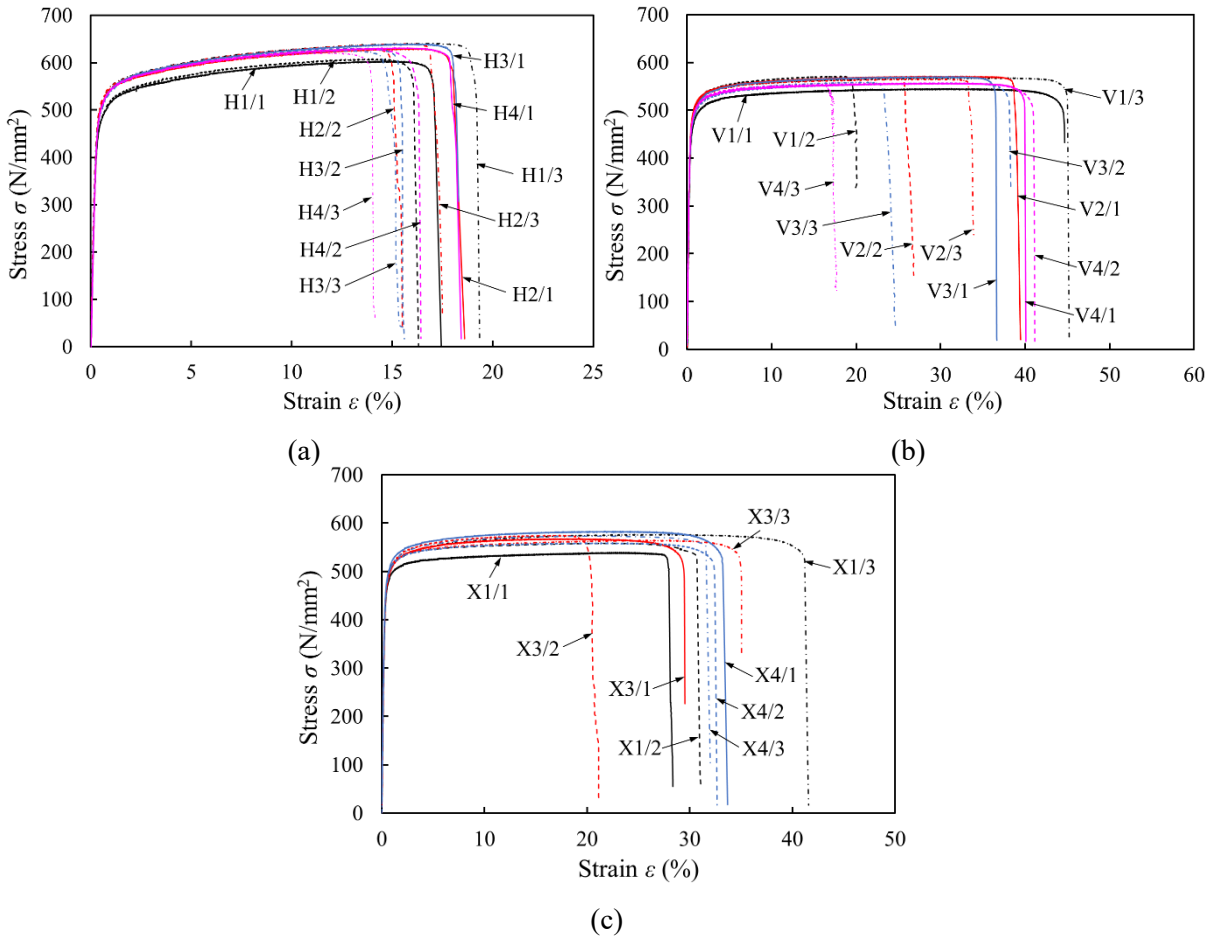

Figure 3.34: Global stress-strain curves for the (a) horizontal, (b) vertical and (c) combined tensile coupons

Table 3.10: Summary of average global tensile properties from PBF 316L stainless steel coupons with laser welded joints

Welding parameter family	Coupon type	E (N/mm^2)	$\sigma_{0.2}$ (N/mm^2)	$\sigma_{1.0}$ (N/mm^2)	σ_u (N/mm^2)	$\varepsilon_{u,gl}$ (%)	ε_f (%)	n	$m_{1.0}$	m_u
1	H	194500	480	539	617	15.2	20.3	7.2	3.6	4.0
	V	179400	450	512	561	27.0	39.6	6.1	5.8	7.0
	X	188500	463	515	558	24.6	43.5	6.4	5.8	6.7
2	H	192500	503	555	632	15.3	20.0	7.1	3.3	3.7
	V	184700	459	519	567	27.9	38.7	5.8	5.9	7.2
3	H	193200	490	554	631	14.0	19.3	8.2	3.7	4.1
	V	181800	446	508	561	27.4	38.7	6.2	5.5	6.8
	X	183100	462	521	568	20.5	39.3	7.0	5.4	6.3
4	H	191400	495	553	627	13.6	20.0	7.9	3.5	3.9
	V	177600	451	511	555	24.8	37.3	6.2	6.0	7.1
	X	186000	469	526	571	20.5	42.0	6.5	5.4	6.3

Figures 35 to 37 show the horizontal, vertical and combined coupons after fracture, respectively. The horizontal specimens fractured in the weld, the vertical specimens fractured either in the base metal (V1/1, V4/1 and V4/2) or in the weld, while the combined specimens all fractured in the base metal of the vertical half parts, except X3/2 which fractured in the weld. The specimens which fractured in the weld generally had a lower fracture strain ($\varepsilon_f \approx 20\%$) compared with the specimens that fractured in the vertical base metal ($\varepsilon_f \approx 40\%$). There is a transition from a cellular microstructure near the PBF base metal to an equiaxed microstructure in the weld centre, where the long cellular or dendrite boundaries and grain boundaries allow cracks to develop more easily with less deformation (Tjong et al., 1995), which leads to a lower fracture strain in the weld than in the vertical base metal. The coupons fractured either at weak points where defects were located or at regions that exhibited a lower ultimate strength. For the vertical and combined coupons, fracture occurred at random positions (in the vertical base metal or weld) along the parallel length due to the fact that the weld has a similar ultimate strength to that of the vertical base metal.

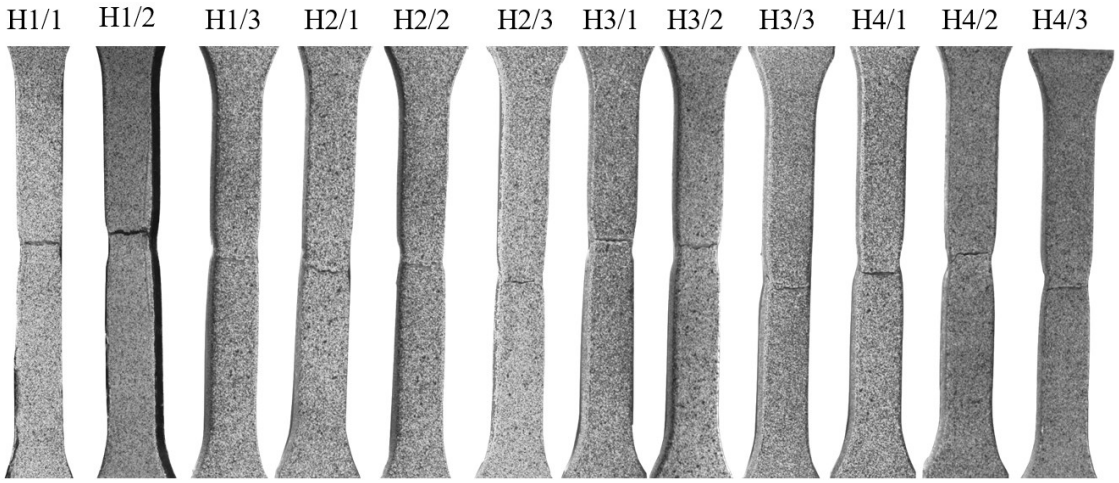

Figure 3.35: Horizontal coupons after fracture

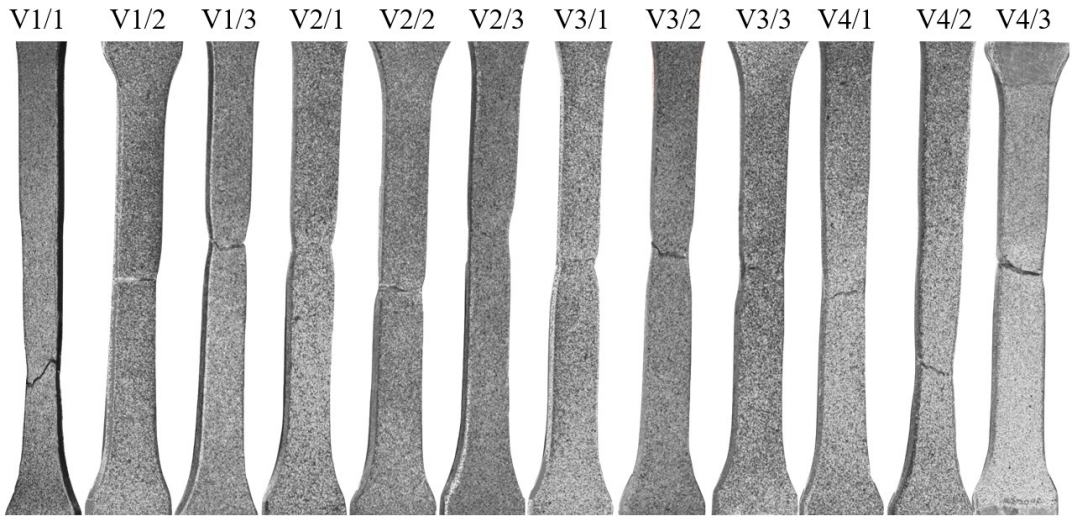

Figure 3.36: Vertical coupons after fracture

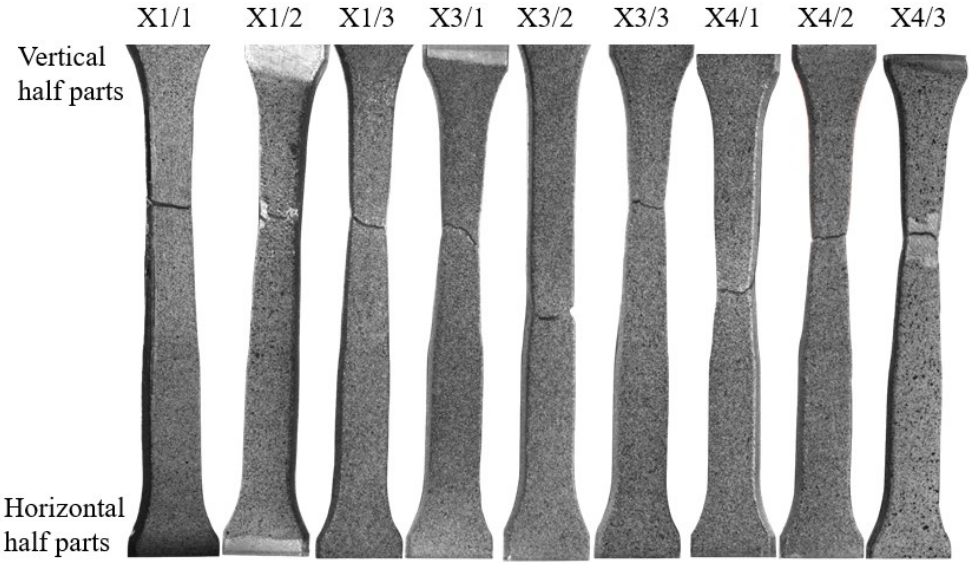

Figure 3.37: Combined coupons after fracture

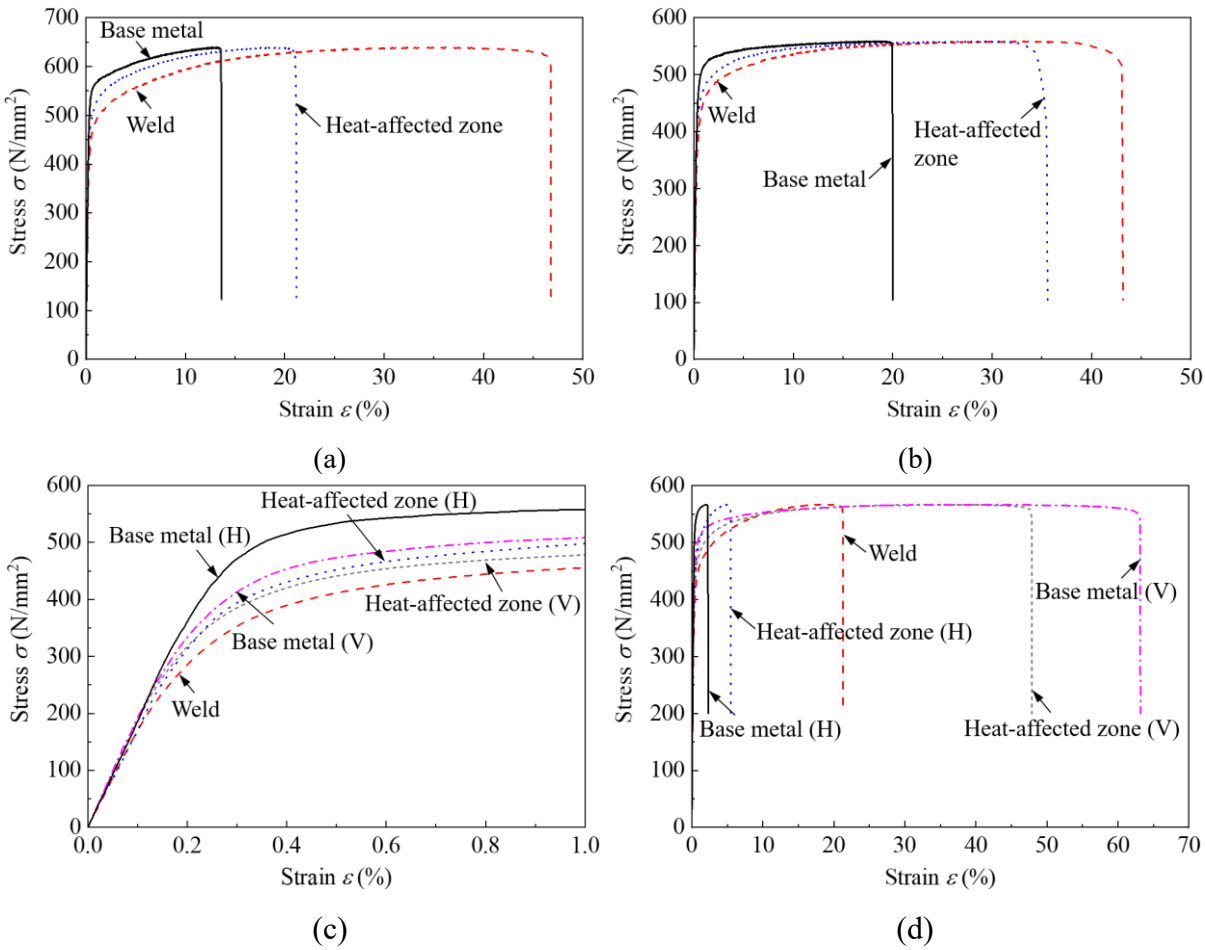

Figure 3.38: Typical measured engineering tensile stress-strain curves for a (a) horizontal coupon (H3/1), (b) vertical coupon (V3/3), (c) combined coupon (X3/1, initial response) and (d) combined coupon (X3/1, full response)

Typical engineering stress-strain curves for the horizontal, vertical and combined specimens are shown in Figure 3.38, where the local stress-strain responses of the weld, HAZ and base metal are shown. The local stress-strain response is presented in Figures. 3.39 to 3.41 for three regions: (i) the centre of the weld, (ii) the centre of the HAZ and (iii) the base metal, away from the fusion line of the weld. Three specimens were tested for each coupon family; the key mechanical properties, averaged per coupon family, as well as the fracture location, are provided in Tables 3.11 to 3.13, where $\varepsilon_{u,gl}$ is the global strain at the ultimate tensile stress. The H and V in the brackets in Table 3.13 indicate the horizontally and vertically built half parts of the combined specimens. The ultimate tensile stress σ_u and corresponding local strain ε_u are only applicable in the regions where fracture occurred, and are considered as lower bounds for the other two regions.

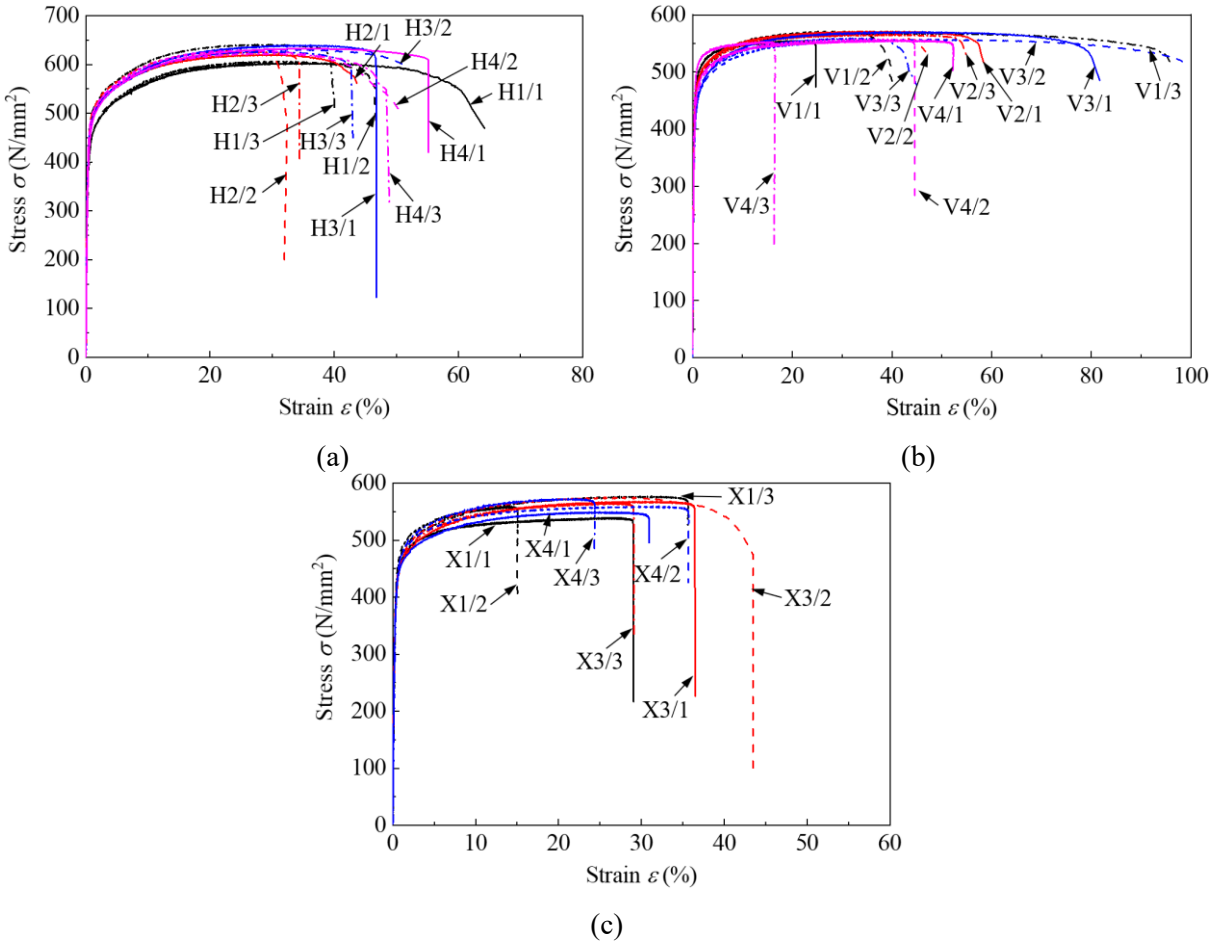

Figure 3.39: Measured engineering stress-strain curves for the weld region of the (a) horizontal, (b) vertical and (c) combined tensile coupons

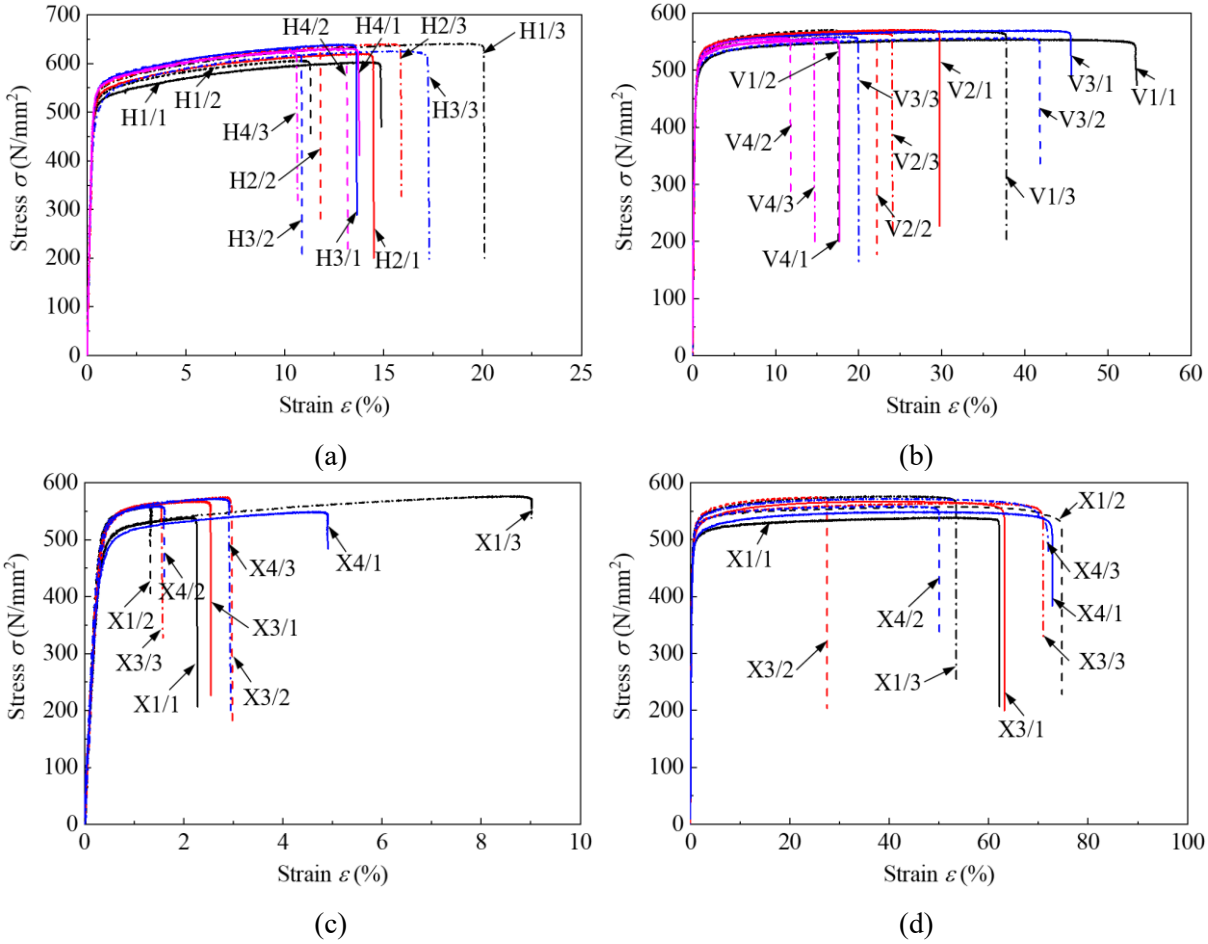

Figure 3.40: Measured engineering stress-strain curves for the base metal of the (a) horizontal coupons, (b) vertical coupons, (c) combined coupons (horizontal half parts) and (d) combined coupons (vertical half parts)

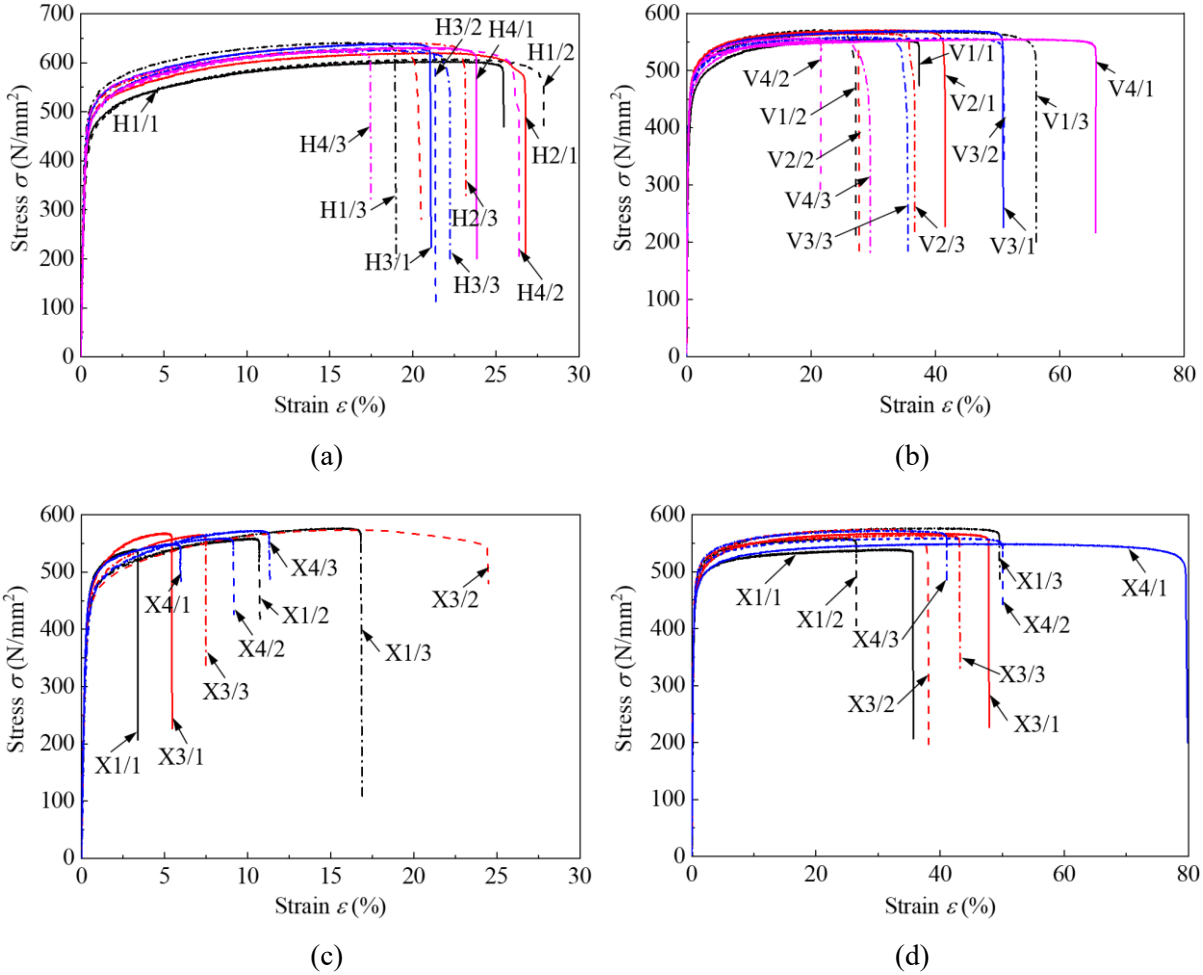

Figure 3.41: Measured engineering stress-strain curves for the heat-affected zone (HAZ) of the (a) horizontal coupons, (b) vertical coupons, (c) combined coupons (horizontal half parts) and (d) combined coupons (vertical half parts)

Table 3.11: Summary of average local tensile properties from the horizontal coupons

Coupon family name	Fracture location	$\varepsilon_{u,gl}$ (%)	ε_f (%)	Location	E (N/mm^2)	$\sigma_{0.2}$ (N/mm^2)	$\sigma_{1.0}$ (N/mm^2)	σ_u (N/mm^2)	ε_u (%)	n	$m_{1.0}$	m_u
H1	Weld	15.2	20.3	Weld	187900	391	473	608	31.7	5.1	3.8	4.9
				HAZ	201900	429	499	-	-	5.8	3.5	-
				Base metal	206300	502	541	-	-	6.4	2.9	-
H2	Weld	15.3	20.0	Weld	184300	424	505	627	28.1	5.9	4.0	4.9
				HAZ	183200	467	528	-	-	6.6	3.3	-
				Base metal	196900	526	560	-	-	8.7	2.7	-
H3	Weld	14.0	19.3	Weld	174000	426	489	623	32.8	9.0	3.3	4.4
				HAZ	195700	452	514	-	-	6.6	3.1	-
				Base metal	193500	510	556	-	-	8.4	3.1	-
H4	Weld	13.6	20.0	Weld	164600	431	499	627	29.9	8.0	3.5	4.5
				HAZ	180400	459	523	-	-	6.9	3.3	-
				Base metal	192900	537	567	-	-	10.2	2.5	-
Family average	-	14.5	19.9	Weld	177700	418	492	621	30.6	7.0	3.7	4.7
				HAZ	190300	452	516	-	-	6.5	3.3	-
				Base metal	197400	519	556	-	-	8.4	2.8	-

Table 3.12: Summary of average local tensile properties from the vertical coupons

Coupon family name	Fracture location	Averaged coupons	$\varepsilon_{u,gl}$ (%)	ε_f (%)	Location	E (N/mm^2)	$\sigma_{0.2}$ (N/mm^2)	$\sigma_{1.0}$ (N/mm^2)	σ_u (N/mm^2)	ε_u (%)	n	$m_{1.0}$	m_u
V1	Base metal	V1/1	31.9	46.8	Weld	164300	397	462	-	-	5.3	4.4	-
					HAZ	169800	399	468	-	-	5.2	4.6	-
					Base metal	173300	453	514	555	50.4	5.1	7.0	7.2
	Weld	V1/2 and V1/3	24.6	36.0	Weld	155800	416	479	562	34.4	6.3	4.5	6.0
					HAZ	159200	420	484	-	-	6.9	4.4	-
					Base metal	171000	467	523	-	-	6.7	6.3	-
V2	Weld	All	27.9	38.7	Weld	173900	404	480	559	37.5	5.0	5.3	7.2
					HAZ	175900	425	490	-	-	5.6	4.9	-
					Base metal	168700	469	521	-	-	7.6	6.3	-
V3	Weld	All	27.4	38.7	Weld	163100	377	448	544	42.1	6.7	4.6	6.4
					HAZ	180000	412	470	-	-	6.8	4.5	-
					Base metal	177500	452	505	-	-	6.8	6.8	-
V4	Base metal	V4/1 and V4/2	29.5	45.0	Weld	163500	400	476	-	-	4.9	5.4	-
					HAZ	172200	432	495	-	-	6.3	5.2	-
					Base metal	175100	471	520	556	65.8	5.5	6.2	6.7
	Weld	V4/3	15.3	22.0	Weld	156500	405	471	552	29.4	5.6	4.5	5.9
					HAZ	196900	401	473	-	-	5.1	4.6	-
					Base metal	177500	462	523	-	-	6.4	7.2	-
Family average	-	-	26.8	38.6	Weld	165700	398	469	554	37.4	5.7	4.9	6.5
					HAZ	174800	418	482	-	-	6.2	4.7	-
					Base metal	177800	462	517	556	60.7	5.4	6.5	6.9

Table 3.13: Summary of average local tensile properties from the combined coupons

Coupon family name	Fracture location	Averaged coupons	$\varepsilon_{u,gl}$ (%)	ε_f (%)	Location	E (N/mm^2)	$\sigma_{0.2}$ (N/mm^2)	$\sigma_{1.0}$ (N/mm^2)	σ_u (N/mm^2)	ε_u (%)	n	$m_{1.0}$	m_u
X1	Base metal (V)	All	24.6	43.5	Weld	181300	409	478	-	-	5.4	4.5	-
					HAZ (V)	188000	432	490	-	-	5.8	5.1	-
					HAZ (H)	192400	424	492	-	-	4.8	3.7	-
					Base metal (V)	181200	461	512	553	50.1	6.7	7.2	8.3
					Base metal (H)	202100	501	535	-	-	7.1	2.9	-
X3	Base metal (V)	X3/1 and X3/3	22.0	46.0	Weld	169500	386	459	-	-	5.7	4.1	-
					HAZ (V)	187600	430	488	-	-	6.0	5.0	-
					HAZ (H)	175800	426	493	-	-	6.6	3.0	-
					Base metal (V)	191600	452	509	555	47.3	5.7	6.9	8.1
					Base metal (H)	189700	518	552	-	-	8.5	3.0	-
	Weld	X3/2	17.4	26.0	Weld	183800	416	477	573	27.0	6.3	3.6	4.8
					HAZ (V)	158800	435	494	-	-	8.5	4.3	-
					HAZ (H)	176400	416	479	-	-	7.5	3.4	-
					Base metal (V)	180600	470	530	-	-	6.0	6.3	-
					Base metal (H)	180600	523	560	-	-	7.9	3.4	-
X4	Base metal (V)	All	20.5	42.0	Weld	175800	403	477	-	-	5.1	4.6	-
					HAZ (V)	166900	446	500	-	-	7.2	4.9	-
					HAZ (H)	177100	428	499	-	-	6.0	3.6	-
					Base metal (V)	184700	460	520	563	41.3	5.9	7.2	8.4
					Base metal (H)	179200	516	551	-	-	9.1	3.2	-
Family average	-	-	21.9	41.6	Weld	177100	403	473	573	27.0	5.5	4.4	4.8
					HAZ (V)	177600	437	493	-	-	6.6	4.9	-
					HAZ (H)	181800	425	493	-	-	5.9	3.5	-
					Base metal (V)	184600	460	516	557	46.1	6.1	7.0	8.3
					Base metal (H)	189300	512	547	-	-	8.2	3.1	-

The mechanical properties of the base material within the welded tensile coupons were comparable to the properties reported in the EOS material datasheet (Table 3.2) and exhibited clear anisotropy. The 0.2% proof stress $\sigma_{0.2}$ and ultimate stress σ_u are plotted against the build direction angle θ in Figure 3.42, together with existing data from the literature (Mower & Long, 2016; Buchanan et al., 2017; Alsalla, Smith & Hao, 2018; Mertens et al., 2014; Liverani et al., 2017; Casati, Lemke & Vedani, 2016; Shifeng et al., 2014; Meier & Haberland, 2008; Tolosa et al., 2010; Spierings, Herres & Levy, 2011b). The 0.2% proof stress $\sigma_{0.2}$ and ultimate stress σ_u are observed to decrease with increasing angle θ to the build direction, as shown by the plotted linear regression lines, which matches prior observations (Mower & Long, 2016; Buchanan et al., 2017; Alsalla, Smith & Hao, 2018; Mertens et al., 2014; Liverani et al., 2017; Casati, Lemke & Vedani, 2016; Shifeng et al., 2014; Meier & Haberland, 2008; Tolosa et al., 2010; Spierings, Herres & Levy, 2011b). Note that a regression line cannot be produced for the ultimate stress as none of the horizontal and combined coupons fractured in the horizontal base metal in this study.

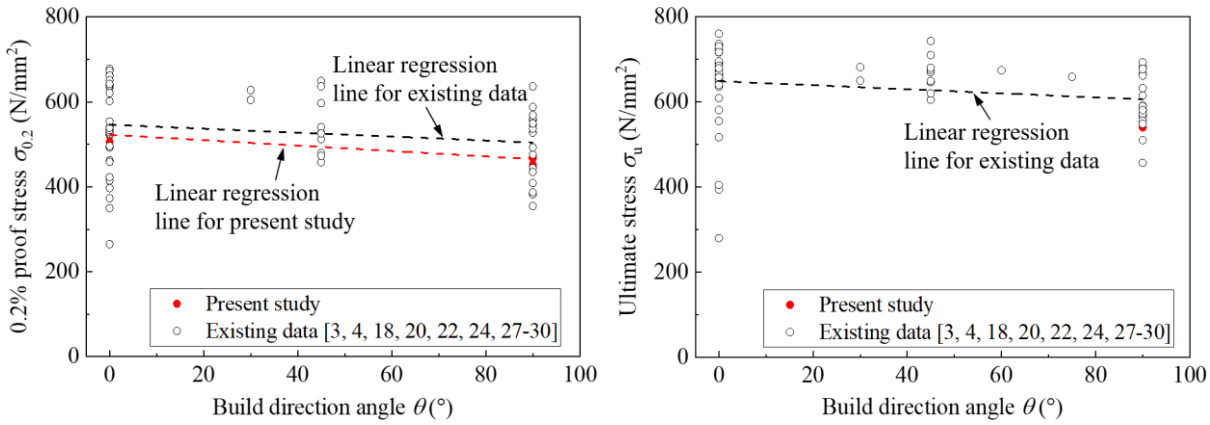

(a) (b)

Figure 3.42: Variation of the (a) 0.2% proof stress $\sigma_{0.2}$ and (b) ultimate stress σ_u with the build direction angle for the PBF base metal

Previous studies have indicated that epitaxial grain growth due to remelting of the previous layers by the subsequent layers (Sistiaga et al., 2016; Mertens et al., 2014; Leicht, Klement & Hryha, 2018), strong crystallographic texture (Kyvelou et al., 2020; Niendorf et al., 2013) and lack-of-fusion defects (Mower & Long, 2016; Mertens et al., 2014; Casati, Lemke & Vedani, 2016; Zhang et al., 2017) may contribute to the observed anisotropy in the mechanical properties. The EBSD map and pole figures in Figures 3.25 and 3.26 indicate a weak

crystallographic texture in the PBF 316L stainless steel, so the texture is not expected to be the primary cause of the observed strength anisotropy. The relative density is deemed to be approaching 100% with very few lack-of-fusion pores observed; hence, the observed material anisotropy is unlikely to stem from lack-of-fusion defects. As reported in Subsections 3.6.3 and 3.6.4, the presence of elongated grains with epitaxial growth following the maximum temperature gradient, parallel to the build direction, indicates the potential correlation between the grain morphology and the exhibited strength anisotropy. The presence of substructures (such as columnar and equiaxed grains) with acute-angle grain boundaries and finer grain size are two possible causes for the greater measured proof and ultimate strengths of the horizontal specimens when compared to the vertical specimens and vertically built half parts of the combined welded coupons. Previous studies have also reported that fracture strains in horizontal specimens were lower than those in vertical specimens (Buchanan et al., 2017); this may be due to the different mean free paths of dislocations induced by the difference in grain aspect ratio and the orientation of the grain long axes with respect to the loading direction. The vertical specimens exhibited columnar grains parallel to the build direction, as well as the loading direction. The tensile stress was applied perpendicular to the longer axis of the columnar grains for the horizontal specimens. The vertical specimens therefore have more slipping surfaces per unit length than the horizontal specimens. The directional variation of the Young's modulus of steel is related to the crystallographic texture (Ledbetter, 1984; Ledbetter, Frederick & Austin, 2008), associated with the local interatomic potential. For the examined non-textured PBF 316L stainless steel, the anisotropy of the Young's modulus was found to be quite small, which accords with previous studies on austenitic stainless steel (Ledbetter, 1984; Ledbetter, Frederick & Austin, 2008).

The laser welds were observed to have lower 0.2% and 1.0% proof strengths and fracture strains for all the test coupons, compared with the PBF base material. To understand the variation in the 0.2% and 1.0% proof stresses away from the weld centre, typical proof stress distributions along the parallel length of the coupons are presented in Figure 3.43. The longitudinal strain fields from one coupon side, prior to fracture, are also provided in Figure 3.43, with the largest strain values denoting the fracture locations. For all specimens, the 0.2% and 1.0% proof stresses increase gradually from minimum values in the weld region to steady values in the base metal. For the combined specimens, the lower proof strengths of the vertically built half parts relative to the horizontally built parts, away from the weld region, are clearly visible in Figure

3.43(c). To evaluate the dependency of the energy input on the weld strength, the 0.2% and 1.0% proof stresses of the weld are plotted against the energy input in Figure 3.44. The 0.2% and 1.0% proof stresses decrease as the energy input of the laser welding increases; this is due to the grains in the weld and HAZ becoming coarser (as seen in Subsection 3.6.4). The results presented in Tables 3.12 and 3.13 indicate that the welds had similar ultimate strengths to that of the vertical base metal. Overall, it can be concluded that PBF manufactured parts can be effectively laser welded using suitable welding parameters, but there is a need to consider the potentially lower strength and ductility of the weld compared to the printed base material.

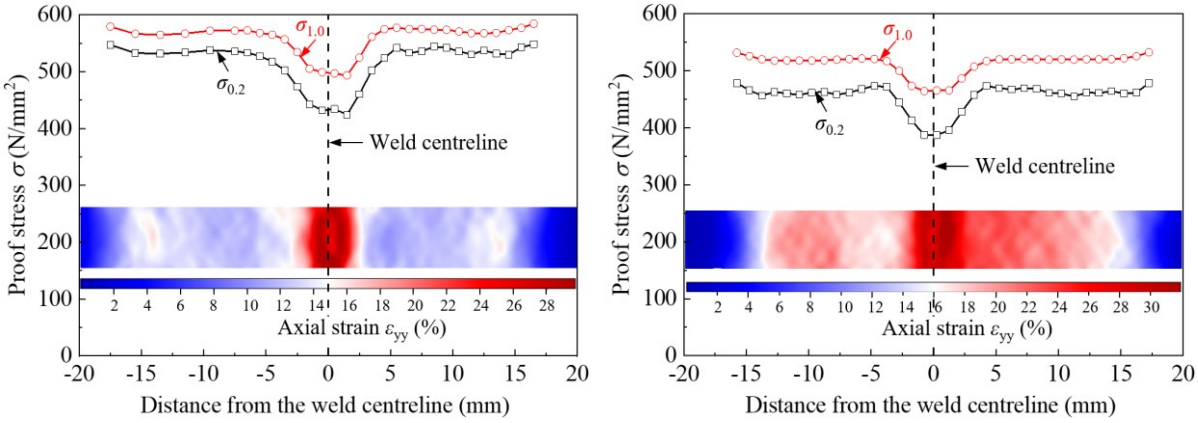

(a) (b)

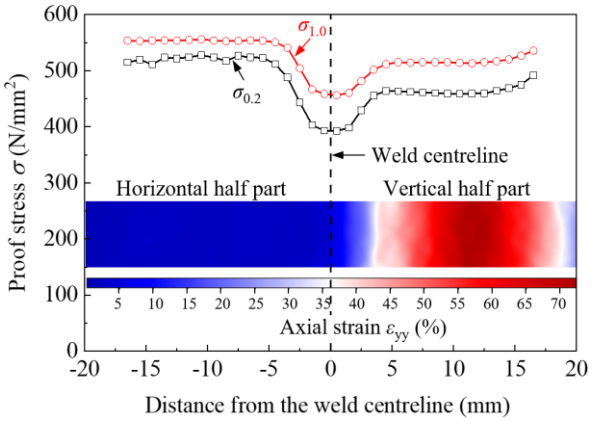

(c)

Figure 3.43: Variation in the 0.2% and 1.0% proof stress moving away from the weld centre for typical (a) horizontal (H3/1), (b) vertical (V3/3) and (c) combined (X3/1) tensile coupons

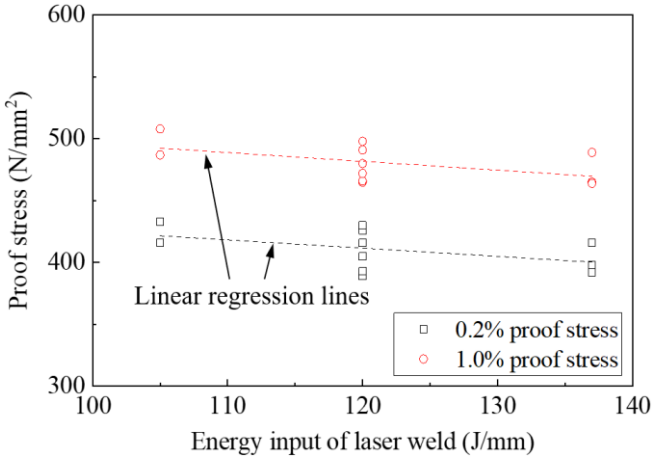

Figure 3.44: Variation of the weld strength with the laser welding energy input

3.9 Concluding remarks

An experimental study into the microstructure, mechanical properties and weldability of additively manufactured metallic materials is presented in this chapter. Grade 316L and CX stainless steel tensile coupons were manufactured using powder bed fusion (PBF) and tested; tensile coupon tests were also undertaken on the laser-welded coupons, which were mechanically joined from Grade 316L stainless steel coupon half parts produced by PBF. In total, six 316L tensile coupons, six CX tensile coupons and 33 316L tensile coupons with laser welded joints were tested, and a series of microstructural tests were carried out. The experiments represent a significant expansion to the very limited existing dataset on PBF base metal and consider different combinations of build directions for laser-welded coupons.

The underlying microstructure and crystallographic texture of austenitic 316L and martensitic CX stainless steels were characterised through optical microscopy, scanning electron microscopy and electron backscattered diffraction. The examined PBF 316L stainless steel exhibited a microstructure typical of additively manufactured material, a chequerboard macrostructure in the scan layers and a columnar grain structure roughly along the build direction, which was attributed to the rapid solidification during AM process. A combination of equiaxed, columnar and cellular dendritic structures was observed in the laser weld region of laser-welded coupons. The PBF CX stainless steel exhibited a fine martensite microstructure with overlapping melt pools containing a large amount of lath martensite and a small fraction of retained austenite.

The stress-strain response (including global and local behaviour for laser-welded coupons) of all coupons was measured using digital image correlation (DIC). The PBF 316L base material typically had higher proof and ultimate strengths as a result of the finer microstructure, without reduced ductility, but with a lower Young's modulus, when compared with conventionally produced stainless steel. The PBF CX stainless steel exhibited a comparable strength and ductility with its conventional counterparts. The PBF horizontal base material showed a higher proof stress than the vertical base material; this is attributed to the epitaxial grain growth orientation with respect to the loading direction. The laser weld regions exhibited a lower hardness, proof strength and fracture strain when compared with the PBF base metal, due to the coarser and inhomogeneous microstructure in the weld generated from the high energy laser welding. The widths of the weld and HAZ were observed to be generally narrow and to increase as the energy input of laser welding increased, while the weld strength was observed to decrease. Overall, it has been shown that PBF stainless steels had at least comparable mechanical properties with their conventional counterparts, and laser welding could be employed to allow additive manufacturing techniques, such as PBF, to be used to produce large-scale components, such as those used in the construction sector, but, the potentially lower mechanical properties of the welds compared to those of the base metal must be considered in the design process.

Chapter 4

Testing and analysis of AM stainless steel CHS in compression

4.1 Introduction

An important challenge to overcome before additively manufactured structural elements can gain wider use in the construction industry is the provision of structural design guidance, underpinned by a suitable pool of experimental and numerical data. As a high value material, stainless steel particularly lends itself to the emerging opportunities, highlighted previously, offered by additive manufacturing (Gardner, 2019). This chapter describes a comprehensive experimental and finite element (FE) investigation into the structural performance of 316L stainless steel circular hollow sections additively manufactured by power bed fusion (PBF) under axial compression. Tubular compression members are widely used in the construction industry, for example as columns, in trusses and as bracing elements. The experimental programme included material coupon tests, initial local geometric imperfection measurements and stub column tests. The parallel numerical study involved, first, validation of the FE models against the test results and, then, parametric studies to generate further structural performance data. The generated experimental and numerical results are used to assess the applicability of the current cross-section design provisions specified in EN 1993-1-4 (CEN, 2015) to 316L stainless steel CHS produced by PBF. Comparisons are also made against the performance of conventional and DED formed stainless steel CHS and the resistance predictions of the continuous strength method (CSM) (Gardner, 2008; Buchanan, Gardner & Liew, 2016). The work in this chapter has been reported by Zhang et al. (2021).

4.2 Overview of experimental programme

An experimental programme was undertaken to investigate the cross-sectional behaviour of circular hollow sections (CHS), produced by PBF from Grade 316L stainless steel powder, and included material coupon tests, initial imperfection measurements and stub column tests. Five CHS stub columns, with nominal cross-section sizes (outer diameter D × thickness t) of CHS 75×1, 75×2, 75×3, 75×4 and 75×5 were tested. The test specimens covered the cross-section classes from Class 1 to Class 4 according to the local slenderness limits given in EN 1993-1-4 (CEN, 2015). Regular (i.e. circular) cross-sections were examined to enable the influence of the manufacturing process to be isolated by allowing direct comparisons to be made with the performance and design of conventionally produced sections.

The nominal chemical composition and material properties of parts built using the employed EOS 316L stainless steel powder are provided in Tables 3.1 and 3.2 respectively. The tensile coupons were manufactured at the Fraunhofer Institute for Laser Technology, while the stub columns were manufactured at EOS Finland; the tests were conducted in the Structures Laboratory of the Department of Civil and Environmental Engineering at Imperial College London.

4.3 PBF manufacturing of test specimens

The coupons were manufactured using an EOS M270 PBF machine while the stub columns were built using a modified research EOS M280 PBF machine. A detailed description of PBF process is provided in Section 3.3. The stub column specimens were printed vertically, with their longitudinal axis perpendicular to the layers, as shown schematically in Figure 4.1, where the scanning strategy is also depicted – the laser scanning direction rotates 45° between each layer. A photograph of the stub columns during printing is shown in Figure 4.2.

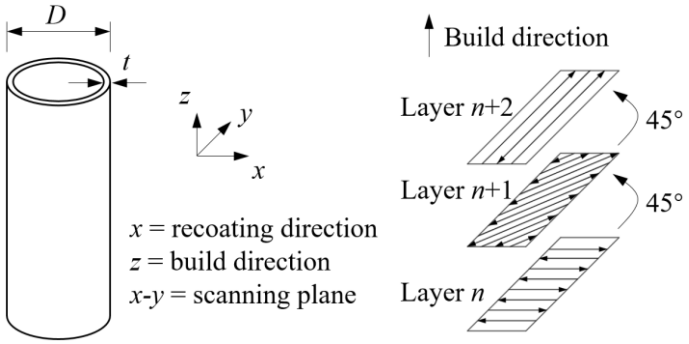

Figure 4.1: Axis convention and laser scanning strategy used for PBF manufacture of CHS test specimens

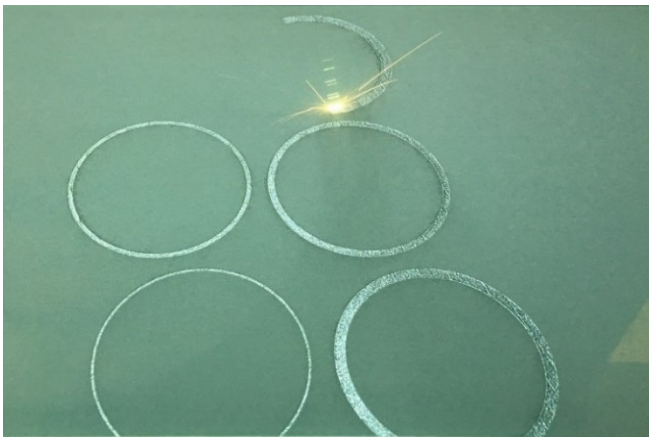

Figure 4.2: CHS stub columns during printing

4.4 Material coupon tests

The tensile and compressive properties of the powder bed fusion 316L stainless steel with direction were investigated in Buchanan et al. (2017). Apart from the anisotropy arising from different build directions, this PBF material exhibited non-symmetric stress-strain responses – the Young's modulus and 0.2% proof stress were observed to be higher in compression than tension. The material coupon tests have been reported previously (Buchanan et al., 2017), but since the analysis of the stub column test data and development of the numerical models utilises their results, the tensile results of the two vertical coupons (i.e. θ = 90° is a coupon normal to the build plate) built in the same manner with the stub columns, is briefly summarised herein.

The tensile coupon tests were undertaken using a 250 kN Instron 8802 testing machine, as shown in Figure 4.3. Standard gauge lengths of $5.65\sqrt{S_0}$, where S_0 is the original cross-sectional

area within the parallel length, were marked onto both faces of the coupons for the future measurement of fracture strain. Electrical resistance strain gauges were attached to the midpoints of the sides of the tensile coupons to measure axial strains before material yielding, and a video extensometer was used to monitor the relative movements of two dots painted on the front face of the coupon to measure the average axial strain post material yielding. The tensile testing was conducted under displacement control in accordance with EN ISO 6892-1 (CEN, 2016). The load, strain gauge and video extensometer readings were recorded at a frequency of 2 Hz.

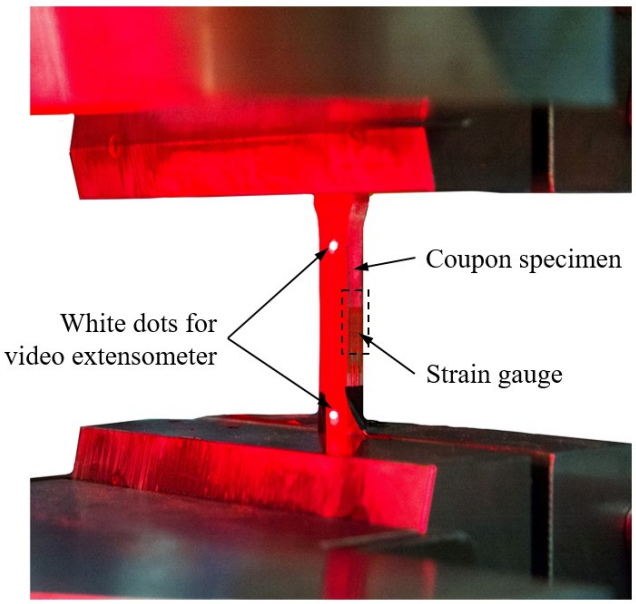

Figure 4.3: Tensile coupon test setup

The measured engineering tensile stress-strain curves of the two vertical coupons ($\theta = 90°$) are plotted in Figure 4.4, while the key material properties – the Young's modulus E, 0.2% proof strength $\sigma_{0.2}$, 1.0% proof strength $\sigma_{1.0}$, ultimate tensile strength σ_u, strain at the ultimate tensile strength ε_u and fracture strain over the marked gauge length ε_f – are reported in Table 4.1. Also presented are the Ramberg-Osgood parameter n (Ramberg & Osgood, 1943) and the extended strain hardening parameters $m_{1.0}$ and m_u (Rasmussen, 2003; Gardner & Ashraf, 2006; Mirambell & Real, 2000), which were fitted to the measured stress-strain curves using the method described in Arrayago, Real & Gardner (2015) and Gardner & Yun (2018).

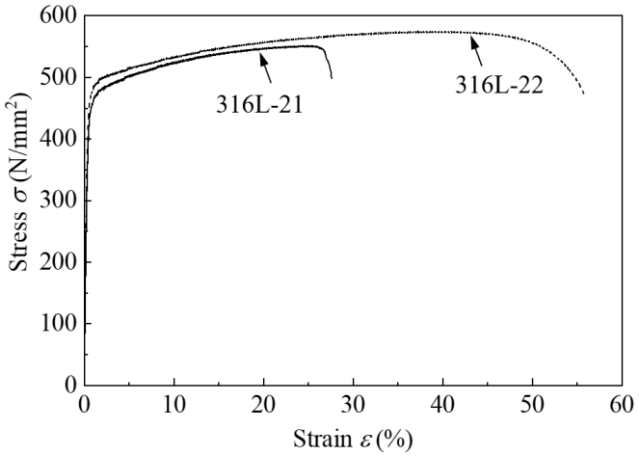

Figure 4.4: Measured engineering stress-strain curves from tensile coupon tests (Buchanan et al., 2017)

Table 4.1: Measured material properties from vertical ($\theta = 90°$) tensile coupon tests (Buchanan et al., 2017)

Coupon	θ (°)	ϕ (°)	E (N/mm^2)	$\sigma_{0.2}$ (N/mm^2)	$\sigma_{1.0}$ (N/mm^2)	σ_u (N/mm^2)	ε_u (%)	ε_f (%)	n	$m_{1.0}$	m_u
316L-21	90	0	183700	407	471	551	24.8	28.0	3.2	4.2	4.3
316L-22	90	90	180300	435	489	574	38.3	50.3	3.5	4.1	4.1
Average	90	-	182000	422	480	562	31.6	39.2	3.4	4.2	4.2

4.5 Geometric properties

4.5.1 3D laser-scanning and data processing

All stub column test specimens had a nominal outer diameter of 75 mm, while the nominal wall thickness was varied from 1 mm to 5 mm to provide a range of cross-section slenderness values. The geometric properties of the CHS specimens were measured prior to stub column testing. The average outer diameter D and wall thickness t were measured at eight locations around the circumference at both ends of the specimens using callipers. The average stub column length L was similarly measured at 45° intervals around the circumference of the specimens. The setup for the measurement of local geometric imperfections is shown in Figure 4.5. The outer surface of the specimens was scanned using a Faro ScanARM, which is a three-dimensional non-contact laser scanner, and recorded using the 3D scanning software Geomagic Wrap (3D Systems, 2017). The scan data were initially processed in Geomagic Wrap, with operations including noise reduction, removal of unwanted data and model alignment; a processed 3D

polygon model was then formed for each test specimen, a typical example of which is shown in Figure 4.5(b).

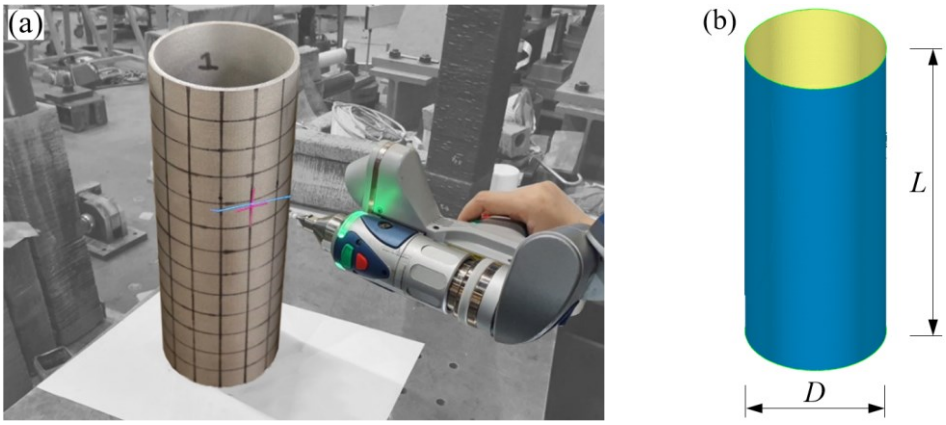

Figure 4.5: Arrangement for geometric imperfection measurement: (a) 3D laser-scanning; (b) Polygon model from Geomagic Wrap

4.5.2 Imperfection analysis and results

The polygon models were each saved as an STL file, imported into Rhino 3D (Robert McNeel & Associates, 2012), contoured and sectioned along 12 equally spaced longitudinal lines. A best fit line to each of the resulting 12 sets of data points for each specimen was determined using least squares regression and used as a reference datum from which deviations, representing local geometric imperfections, were measured. This definition of local geometric imperfection amplitude was chosen since it is the deviations from flatness along the longitudinal axis of structural elements that trigger local buckling and hence have the most influence on the structural response; this imperfection amplitude can also be readily used to scale eigenmodes in subsequent numerical analyses. Similar approaches to the measurement of local geometric imperfections were adopted in Buchanan et al. (2017), Meng and Gardner (2020a, 2020c) and Afshan and Gardner (2013a). The measured local longitudinal geometric imperfections along the length of specimen CHS 75×1 are plotted in Figure 4.6, where the deviations from four fitted lines (*A*, *B*, *C*, *D*) are displayed. The measured initial local imperfections were generally very small; the largest imperfections were generally towards the ends of the specimens sawn off from the build plate. To provide a representative imperfection for the specimens without end effects, only the data in the central 80% of the length were used for the local imperfection analysis. For each stub column, the maximum deviation along all 12 measurement lines was

taken as the local imperfection amplitude ω_0, as reported in Table 4.2. The measured geometric properties of the stub columns, including the member length L, outer diameter D, wall thickness t, cross-sectional area A and local imperfection amplitude ω_0 are reported in Table 4.2.

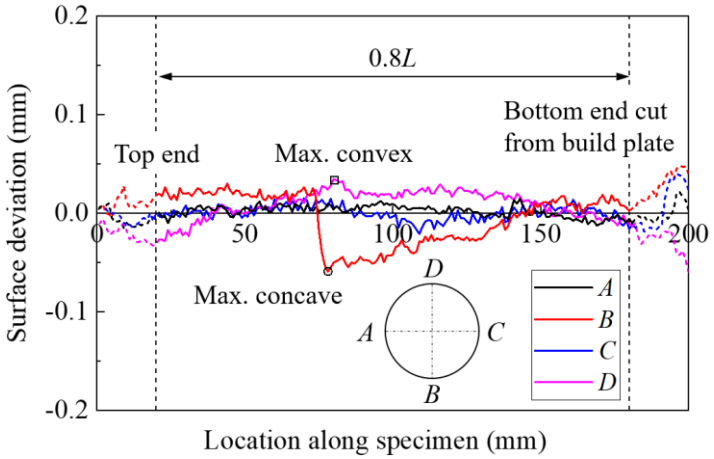

Figure 4.6: Measured local geometric imperfections along the length of specimen CHS 75×1

Table 4.2: Measured geometric properties of PBF CHS stub column specimens

Specimen	D (mm)	t (mm)	L (mm)	A (mm^2)	ω_0 (mm)
CHS 75×5	75.01	5.10	207.62	1120.1	0.087
CHS 75×4	75.01	4.06	207.42	905.0	0.078
CHS 75×3	74.97	3.10	207.65	699.9	0.048
CHS 75×2	74.97	2.09	207.65	478.5	0.076
CHS 75×1	74.97	1.07	207.74	248.4	0.060

4.6 Stub column tests

4.6.1 Preparation of stub column specimens

The stub column tests were conducted to investigate the compressive response and load-bearing capacity of stainless steel CHS manufactured by PBF. The nominal lengths of the stub columns were approximately equal to three times the outer diameter, which was deemed to be short enough to prevent global buckling but still sufficiently long to contain a representative pattern of local imperfections (Ziemian, 2010). The specimen printing and removal from the build plate was carried out to a high degree of manufacturing accuracy, achieving flat and parallel end

sections in all cases, except specimen CHS 75×4 where the variation in length measured at different points around the circumference exceeded 0.2 mm. This specimen was machined prior to testing to ensure the ends of the stub column were in full contact with the end platens, thereby ensuring uniform load introduction.

4.6.2 Setup and data acquisition

The stub column tests were carried out using an Instron 3500 kN-SPL testing machine, together with a datalogger and data acquisition software. A photograph and schematic diagram of the test setup are shown in Figure 4.7; this setup has been successfully adopted for previous CHS stub column tests (Buchanan, Wan & Gardner, 2020; Buchanan, Real & Gardner, 2018). Square grids with a grid size of approximately 16 mm were marked onto one half of each of the CHS specimens for the direct visualisation of deformations. The other half of each of the specimens was painted white and then sprayed with a random black speckle pattern to create contrasting features to be tracked during testing by a digital image correlation (DIC) system. A two-camera LaVision DIC system (LaVision, 2017) was used to monitor the development of deformations and strains. The axial deformation was also recorded by three strain gauges equally spaced around the circumference at the mid-height of the specimens and three LVDTs positioned at 120° intervals, as shown in Figure 4.7. Both ends of the specimens were constrained by 10 mm thick metallic ring stiffeners to prevent premature end failure (Ma, Chan & Young, 2016). The compressive load was recorded using a load cell within the actuator. The specimens were axially compressed under displacement control at a constant displacement rate of 0.2 mm/min, with testing continued until the axial load had decreased to about 80% of the peak load. The test outputs, including the compressive load, top platen movement, strain gauge readings and LVDT readings were recorded at a frequency of 2 Hz, while the DIC images were captured at a frequency of 1 Hz.

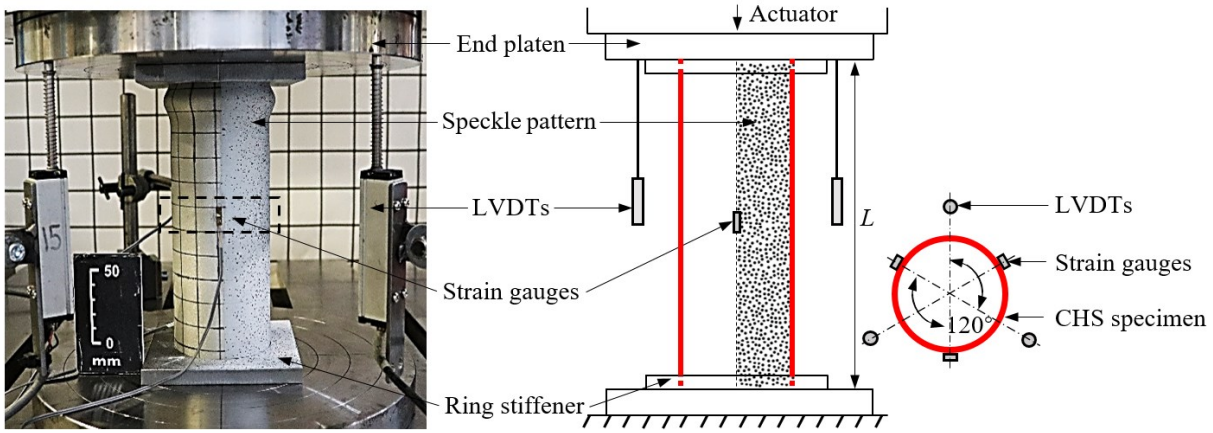

(a) Test setup (b) Schematic diagram of test setup

Figure 4.7: Stub column test configuration

4.6.3 Results

The deformed specimens are shown in Figure 4.8. All stub columns failed by the formation of a ring-like bulge, known as elephant foot buckling, near one or both ends of the specimens. This is a common local failure mode in compressed tubular cross-sections (Buchanan et al., 2017; Buchanan, Real & Gardner, 2018; Zhao, Gardner & Young, 2016a), and is particularly prevalent in specimens with very low imperfections (Insausti & Gardner, 2011). Typical DIC results for specimen CHS 75×4 are displayed in Figure 4.9, where the strain field evolution before and after local buckling can be clearly seen. All load-end shortening curves are plotted in Figure 4.10. Note that the true end shortenings of the stub columns using the LVDT and strain gauge readings were determined by eliminating the elastic deformations of the end platens, as recommended in Rasmussen (1990) and Gardner (2002); the DIC end shortening values were derived by exporting and subtracting vertical displacements at the two ends of the stub columns. The DIC derived curves can be seen in Figure 4.10 to be essentially identical to those obtained from the LVDT and strain gauge readings.

Figure 4.8: Deformed CHS stub column test specimens, with increasing wall thickness from left to right

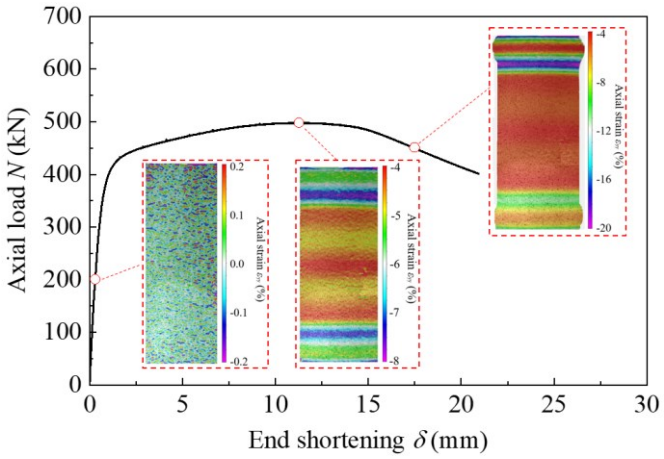

Figure 4.9: Typical DIC results from stub column tests (CHS 75×4)

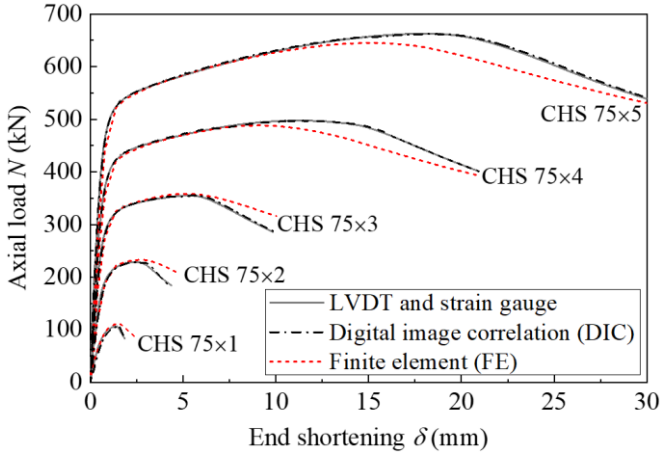

Figure 4.10: Experimental and numerical load end-shortening curves of stub columns

The key test results, including the ultimate load N_u, the end shortening at the ultimate load δ_u and the ultimate load N_u normalised by the yield load N_y (equal to $A\sigma_{0.2}$, with $\sigma_{0.2}$ taken as the

average measured 0.2% proof stress in the $\theta = 90°$ direction, equal to 422 N/mm^2), are reported in Table 4.3. Also presented are the local slenderness values $D/t\varepsilon^2$, where

$$\varepsilon^2 = \frac{235}{\sigma_{0.2}} \frac{E}{210000}, \tag{4.1}$$

the cross-section class determined on the basis of the EN 1993-1-4 slenderness limits and the local cross-section slenderness $\bar{\lambda}_c$, calculated as

$$\bar{\lambda}_c = \sqrt{\sigma_{0.2} / \sigma_{cr}}, \tag{4.2}$$

where σ_{cr} is the elastic local buckling stress. The elastic local buckling stress σ_{cr} of a compressed CHS is given by Equation 4.3, in which ν is Poisson's ratio, taken as 0.3. The 0.2% proof stress was taken as the average measured value from the $\theta = 90°$ tensile coupon tests (i.e. $\sigma_{0.2} = 422$ N/mm^2).

$$\sigma_{cr} = \frac{E}{\sqrt{3(1-\nu^2)}} \frac{2t}{D} \tag{4.3}$$

It can be seen from Table 4.3 that the tested stub columns show the anticipated trend of reducing normalised capacity (i.e. reducing N_u/N_y values) with increasing local slenderness, reflecting the greater susceptibility to local buckling; this is explored further in Section 4.8.

Table 4.3: Geometric properties and key test results of stub columns

Specimen	$D/t\varepsilon^2$	EC3 class	$\bar{\lambda}_c$	N_u (kN)	δ_u (mm)	N_u/N_y
CHS 75×5	29.5	1	0.17	663.4	18.26	1.45
CHS 75×4	37.1	1	0.19	498.0	11.27	1.35
CHS 75×3	48.6	1	0.21	356.3	5.54	1.24
CHS 75×2	72.0	3	0.26	229.0	2.38	1.17
CHS 75×1	140.7	4	0.36	106.4	1.38	1.05

4.7 Numerical modelling

A finite element study of the compressive cross-sectional behaviour of CHS produced by PBF was undertaken in conjunction with the experimental programme. The FE models were first

validated against the experimental results and subsequently employed for parametric studies to generate further cross-sectional resistance data for additively manufactured CHS.

4.7.1 Description of FE models

The FE models were developed using the software package Abaqus (Dassault Systèmes, 2017). The four-noded shell element with reduced integration, S4R, was chosen as the element type owing to its suitability for predicting the response of both thin and thick-walled structural cross-sections; this element type has been successfully utilised in previous numerical studies on metallic tubular cross-sections (Buchanan, Real & Gardner, 2018; Zhao, Gardner & Young, 2016a; Meng & Gardner, 2020b; Wang & Gardner, 2017; Meng et al., 2020). The adopted mesh size was set equal to $0.1(Dt)^{1/2}$, which is equal to approximately 8% of the theoretical axisymmetric elastic local buckling half-wavelength of a CHS, as recommended by Meng and Gardner (2020b); this mesh size was found to be sufficiently refined to capture the local buckling pattern and to predict the cross-sectional resistance accurately, while remaining computationally efficient. Computational efficiency was further ensured by modelling only half of the cross-section and half of the member length of the CHS specimens (i.e. creating quarter-models), and applying suitable symmetry boundary conditions along the planes of symmetry (see Figure 4.11); this method has been successfully adopted in previous numerical simulations (Wang & Gardner, 2017; Meng et al., 2020). The end sections were coupled to reference points, where only longitudinal translation was allowed, to simulate the fixed-ended boundary conditions employed in the tests. The influence of the ring stiffeners, at the ends of the stub columns, was reflected in the FE models by coupling the horizontal translational degrees of freedom over the depth of the stiffeners to the reference points. This approach has also been adopted in previous studies (Meng & Gardner, 2020a; Ma, Chan & Young, 2016; Meng & Gardner, 2020b). Note that the symmetric boundary conditions and imperfections in the FE models result in symmetric failure modes (i.e. elephant foot bulges at both ends of the models), while in the tests, depending primarily on the pattern of imperfections, both symmetric (bulges at both ends) and non-symmetric (bulges at one end only) were observed.

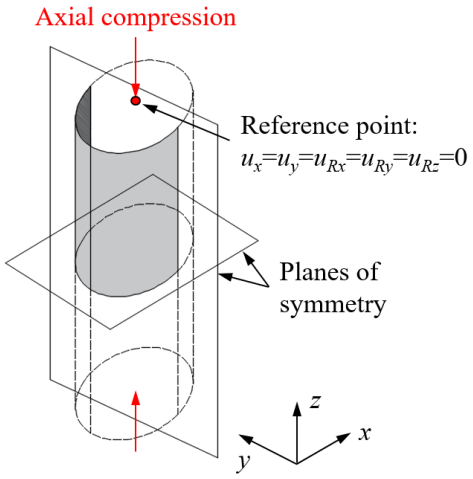

Figure 4.11: Geometry, loading and boundary conditions of FE models for CHS

For both the FE model validation and the parametric studies, the adopted material stress-strain curve was derived from the two-stage Ramberg-Osgood relationship (Rasmussen, 2003; Gardner & Ashraf, 2006), incorporating the average measured material properties in the vertical (θ = 90°) direction, as reported in Table 4.1. The resulting stress-strain relationship was converted into true stress and plastic strain and then inputted into Abaqus. Local geometric imperfections were incorporated into the FE models in the form of the lowest eigenmode pattern obtained from a prior linear bifurcation analysis (LBA), as described in Subsections 4.7.2 and 4.7.3.

4.7.2 Validation

The developed FE models were first validated against the key results from the stub column tests, considering the ultimate loads, deformations at ultimate loads, full load-deformation histories and failure modes. The numerical results were obtained through geometrically and materially nonlinear analyses with imperfections (GMNIA); models without imperfections (GMNA) were also run. The initial imperfection pattern was taken as the lowest elastic buckling mode shape obtained from an LBA of the modelled geometry, as shown in Figure 4.12 for the CHS 75×5 specimen, but with a modified thickness equal to $D/5$ (referred to as the LBA-t_{mod} mode), as recommended in Meng and Gardner (2020b). This method was established in preference to using an LBA with the real thickness to achieve more realistic imperfection patterns in comparison to physical measurements, and to avoid, in particular, the very short wavelengths obtained from an LBA in the case of thin-walled CHS columns (Meng & Gardner,

2020b). Three imperfection amplitudes – the measured value ω_0 (Table 4.2), $0.1t$ and $0.01(Dt)^{1/2}$ (Meng & Gardner, 2020b), were used to factor the imperfection patterns to assess imperfection sensitivity and to determine a suitable imperfection amplitude for the subsequent parametric investigations.

Table 4.4: Comparisons of test results with FE results for varying local imperfection amplitudes

Specimen	$N_{u,FE}/N_{u,test}$				$\delta_{u,FE}/\delta_{u,test}$			
	GMNA	GMNIA			GMNA	GMNIA		
		ω_0	$0.1t$	$0.01(Dt)^{1/2}$		ω_0	$0.1t$	$0.01(Dt)^{1/2}$
CHS 75×5	0.95	0.95	0.91	0.95	0.85	0.85	0.58	0.85
CHS 75×4	0.96	0.96	0.95	0.96	0.85	0.84	0.79	0.85
CHS 75×3	0.98	0.98	0.98	0.98	0.96	0.95	0.90	0.96
CHS 75×2	1.00	1.00	1.00	1.00	1.06	1.05	1.18	1.06
CHS 75×1	1.05	1.05	1.05	1.05	1.10	1.10	1.10	1.10
Mean	0.99	0.99	0.98	0.99	0.96	0.96	0.91	0.96
COV	0.04	0.04	0.05	0.04	0.11	0.11	0.24	0.11

The ratios of the numerical to experimental ultimate loads $N_{u,FE}/N_{u,test}$ and corresponding deformations $\delta_{u,FE}/\delta_{u,test}$ for the three local imperfection amplitudes, are presented in Table 4.4, where COV is the coefficient of variation. The results show that the test ultimate loads are generally well predicted for all three local imperfection amplitudes, which indicates the relative insensitivity of the modelled CHS geometries to local imperfections. The deformations at the ultimate loads are more sensitive to the imperfection amplitudes. Use of the measured imperfection amplitudes ω_0 and the values of $0.01(Dt)^{1/2}$ yields the most accurate on average and least scattered predictions of the deformations at the ultimate loads. The full load-deformation curves obtained from the FE models with the imperfection amplitudes equal to $0.01(Dt)^{1/2}$ in the LBA-t_{mod} shape and the experiments for all CHS stub columns are shown in Figure 4.10; the developed FE models are shown to accurately replicate the initial stiffness, general equilibrium path and ultimate response from the tests. The small deviations between the experimental and numerical load-deformation curves may be due to some variation in material properties with thickness, the chosen imperfection shape (i.e. eigenmode-affine) or the influence of residual stresses. Good agreement between the numerical and experimental failure modes can also be observed for the typical case of the CHS 75×5 specimen, as shown in Figure 4.12. Overall, it can be concluded that the developed FE models with the imperfection amplitude of $0.01(Dt)^{1/2}$ and the LBA-t_{mod} pattern are able to accurately replicate the cross-

sectional behaviour of CHS stub columns manufactured by PBF observed in the physical experiments and are hence suitable for use in parametric studies.

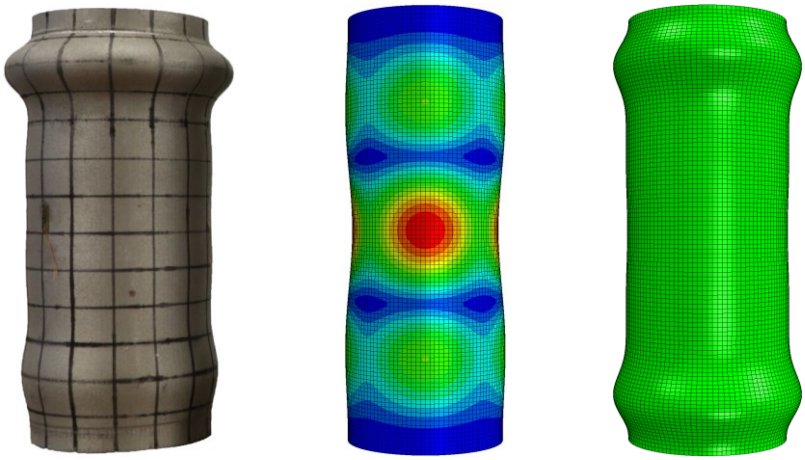

(a) Test failure mode (b) FE eigenmode (c) FE failure mode

Figure 4.12: Typical (a) experimental failure mode, (b) numerical eigenmode and (c) numerical failure mode of stub columns (CHS 75×5 specimen shown)

4.7.3 Parametric studies

Upon validation of the developed FE models, parametric studies were carried out to generate further resistance data to cover a wider range of cross-section slenderness values. The modelled CHS had outer diameters ranging from 50 mm to 200 mm and the thicknesses varying between 0.5 mm and 20 mm, which led to values of local slenderness $D/t\varepsilon^2$ ranging from 10 to 404, covering all four cross-section classes according to the slenderness limits of EN 1993-1-4 (CEN, 2015). The length of the modelled stub columns was set to three times the outer diameter. In total, 130 cross-sectional resistance results on CHS under axial compression were generated.

4.8 Comparisons with existing design provisions

In this section, the applicability of two existing sets of design rules for stainless steel structures, namely EN 1993-1-4 (CEN, 2015) and the continuous strength method (Gardner, 2008; Gardner, Wang & Liew, 2011; Buchanan, Gardner & Liew, 2016), to CHS manufactured by PBF, is evaluated. The accuracy of each method is assessed by comparing the experimental and numerical ultimate loads with the predicted ultimate loads. In the comparisons, the measured

(or modelled) material properties and geometries are employed in the resistance calculations and all partial safety factors are set to unity. In total, 5 experimental and 130 numerical results on stainless steel CHS manufactured by PBF are considered. In addition, a further 97 experimental results on stainless steel CHS are examined, 84 of which were produced by conventional cold-forming (Zhao, Gardner & Young, 2016a; Burgan, Baddoo & Gilsenan, 2000; Gardner & Nethercot, 2004; Kuwamura, 2003; Lam & Gardner, 2008; Rasmussen, 2000; Talja, 1997; Gardner & Theofanous, 2008; Uy, Tao & Han, 2011; Young & Hartono, 2002) and 13 of which were manufactured by DED (WAAM) (Buchanan, Wan & Gardner, 2020; Laghi et al., 2020a).

4.8.1 Assessment of yield slenderness limit

The test and numerical results are first used to assess the yield slenderness limit. The yield slenderness limit is an important threshold slenderness that is used to distinguish between slender and non-slender cross-sections. The limit can be assessed by plotting the normalised cross-sectional capacity data N_u/N_y against the local slenderness $\bar{\lambda}_c$, as shown in Figure 4.13, for the test and numerical data generated herein. The collected test data on conventionally formed (Zhao, Gardner & Young, 2016a; Burgan, Baddoo & Gilsenan, 2000; Gardner & Nethercot, 2004; Kuwamura, 2003; Lam & Gardner, 2008; Rasmussen, 2000; Talja, 1997; Gardner & Theofanous, 2008; Uy, Tao & Han, 2011; Young & Hartono, 2002) and DED (Buchanan, Wan & Gardner, 2020; Laghi et al., 2020a) CHS and the yield (Class 3) slenderness limits of EN 1993-1-4 (CEN, 2015; Gardner & Theofanous, 2008) and the CSM (Gardner, 2008; Gardner, Wang & Liew, 2011; Buchanan, Gardner & Liew, 2016) are also shown. Note that the EN 1993-1-4 yield slenderness limit of $D/t\varepsilon^2 = 90$ corresponds to a value of local slenderness $\bar{\lambda}_c$ equal to 0.288 for the measured value of $E = 182000$ N/mm^2 and $\nu = 0.3$; the CSM yield slenderness limit is similar, at $\bar{\lambda}_c = 0.3$. The capacities of all five tested PBF CHS stub columns, even the Class 4 specimen, exceeded the cross-section yield load, reducing previous concerns over the performance of PBF cross-sections of slender proportions (Buchanan et al., 2017). The trend of the PBF CHS data generally follows that of the conventionally produced stainless steel CHS and indicates the applicability of both the EN 1993-1-4 and CSM yield slenderness limits to PBF CHS.

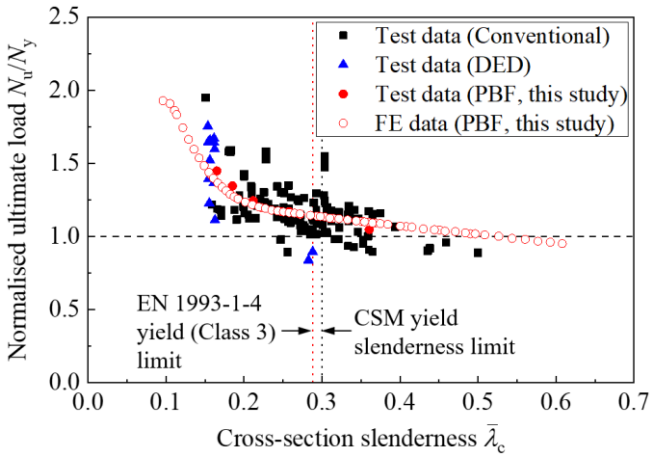

Figure 4.13: Normalised ultimate axial resistance N_u/N_y versus local slenderness $\bar{\lambda}_c$, showing EN 1993-1-4 and CSM yield slenderness limits

4.8.2 Assessment of resistance predictions

Comparisons of the experimental and numerical results with the EN 1993-1-4 and CSM resistance predictions are made in this subsection. The ratios of the experimental and numerical ultimate loads N_u to the predicted ultimate resistances $N_{u,pred}$ are reported in Figure 4.14 and Table 4.5, where $N_{u,EC3}$ and $N_{u,csm}$ are the resistance predictions calculated according to EN 1993-1-4 and the CSM, respectively. The EN 1993-1-4 resistance predictions for Class 4 cross-sections utilised the effective area formulation (Buchanan, Real & Gardner, 2018; Chan, Gardner & Law, 2010) given in the latest draft of the revised code. Note that the EN 1993-1-4 upper local slenderness limit of $D/t\varepsilon^2 = 250$ corresponds to a value of local slenderness $\bar{\lambda}_c$ equal to 0.48 for E = 182000 N/mm^2 and ν = 0.3, while the CSM can be applied up to a local slenderness limit of $\bar{\lambda}_c$ = 0.6. A value of $N_u/N_{u,pred}$ greater than unity indicates that a given resistance prediction lies on the safe side. Both EN 1993-1-4 and CSM were found to provide consistently safe-sided predictions for the cross-sectional resistances of the PBF CHS, indicating their applicability to structural cross-sections produced using this method of manufacture. The EN 1993-1-4 and CSM compressive resistance predictions for the PBF CHS stub columns tests, and previous DED and conventional CHS stub columns tests (Zhao, Gardner & Young, 2016a; Burgan, Baddoo & Gilsenan, 2000; Gardner & Nethercot, 2004; Kuwamura, 2003; Lam & Gardner, 2008; Rasmussen, 2000; Talja, 1997; Gardner & Theofanous, 2008; Uy, Tao & Han, 2011; Young & Hartono, 2002; Buchanan, Wan & Gardner, 2020; Laghi et al., 2020a) are compared in Table 4.6. The DED CHS data are clearly more scattered (see Table

4.6) than the PBF CHS data owing to their greater geometric variability; as-built DED elements have surface profiles that are inherently undulating, which results in more variable measured geometric properties and ultimate capacities (Kyvelou et al., 2020; Buchanan, Wan & Gardner, 2020). As observed in previous studies (Buchanan et al., 2017; Gardner, 2019; Wang & Gardner, 2017; Bock, Gardner & Real, 2015; Zhao, Gardner & Young, 2016a), the resistance predictions obtained using the CSM are more accurate and less scattered than the EN 1993-1-4 predictions for all three manufacturing techniques, which is attributed to the rational exploitation of strain hardening in non-slender cross-sections and a base curve relating cross-section deformation capacity to local slenderness, which considers the element interaction.

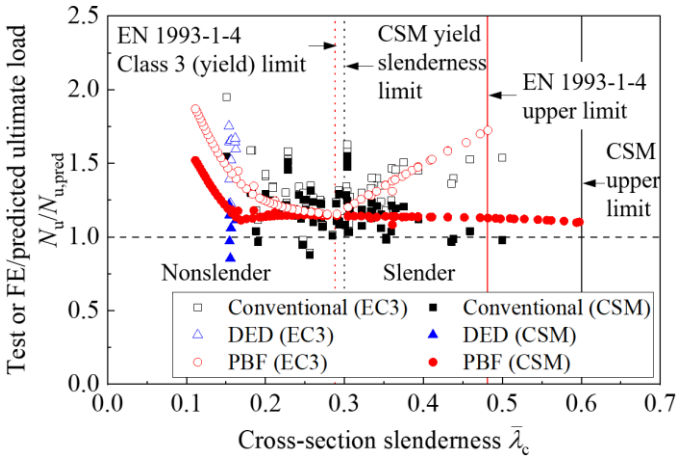

Figure 4.14: Comparisons of experimental and numerical axial resistances with EN 1993-1-4 and CSM resistance predictions for CHS in compression

Table 4.5: Comparisons of experimental and numerical results with predicted compression resistances for stainless steel CHS manufactured by PBF

Evaluation parameter	Test data			FE data		
	No. of data	$N_u/N_{u,EC3}$	$N_u/N_{u,csm}$	No. of data	$N_u/N_{u,EC3}$	$N_u/N_{u,csm}$
Mean	5	1.28	1.14	130	1.50	1.23
COV		0.11	0.07		0.23	0.10

Table 4.6: Comparisons of experimental results with EN 1993-1-4 and CSM compressive resistance predictions for PBF, and for previous DED and conventional CHS tests

Manufacturing method	Mean		COV	
	$N_{u,test}/N_{u,EC3}$	$N_{u,test}/N_{u,csm}$	$N_{u,test}/N_{u,EC3}$	$N_{u,test}/N_{u,csm}$
PBF stainless steel	1.28	1.14	0.11	0.07
DED stainless steel	1.41	1.02	0.31	0.15
Conventional stainless steel	1.28	1.17	0.18	0.14
All test data	1.30	1.15	0.20	0.15

4.9 Concluding remarks

An experimental and numerical study into the cross-sectional behaviour of additively manufactured stainless steel circular hollow sections (CHS) under axial compression has been presented. Five stainless steel CHS stub columns, with a range of local slendernesses, were manufactured by powder bed fusion (PBF) and tested under axial compression. The stub column test setup, experimental procedure, full load end-shortening curves, failure modes and key test results (i.e. ultimate loads and corresponding deformations) have been fully reported. Geometric imperfections were measured using 3D laser-scanning and material properties were obtained from previously reported tests (Buchanan et al., 2017). During testing, digital image correlation was used to record the development of deformations and strains in the stub column specimens. The specimens revealed the anticipated trend of reducing capacity relative to the yield load with increasing local slenderness, reflecting the increasing vulnerability to local buckling.

In parallel with the experimental programme, shell FE models were developed, validated against the test results and then employed for parametric studies, generating 130 additional structural performance data over a wide range of cross-section slenderness values. This study has provided new underpinning experimental and numerical data for PBF additively manufactured stainless steel CHS. The experimental and numerical results were compared with existing test data on stainless steel CHS stub columns produced by conventional cold-forming and directed energy deposition additive manufacturing, where, on a normalised basis, similar performance was observed. The experimental and numerical results were also used to assess the applicability of the design provisions of EN 1993-1-4 and the continuous strength method (CSM) to stainless steel circular hollow sections manufactured by PBF. The comparisons revealed safe-sided resistance predictions in both cases, with the CSM providing more accurate and consistent results.

Chapter 5

Shape optimisation of corrugated cylindrical shells for additive manufacturing

5.1 Introduction

Axially compressed circular cylindrical shells with large diameter-to-thickness ratios are highly susceptible to local buckling, and their load-carrying capacities are known to be very sensitive to initial geometric imperfections. This issue can be addressed by optimising the cross-section profile of the shell, and the fabrication of such free-form wavy shells now becomes practical with the innovative metal additive manufacturing technique. The focus of the present study is on the shape optimisation of compressed free-form wavy shells, considering both geometric and material nonlinearities. The adopted framework based on particle swarm optimisation (PSO), is firstly described. A selection of free-form wavy profiles has been obtained from the optimisation study, and the improvement in buckling resistance and sensitivity to initial geometric imperfections over their reference circular shells are analysed. The effects of other geometric parameters on the optimisation results, including the length and diameter-to-thickness ratio, have also been examined. Comparisons of the optimised free-form wavy shells with circular shells and other forms of non-circular shells, in terms of imperfection sensitivity, local buckling resistance and mass efficiency, are then made. The structural performance of the proposed optimised shells will be further verified through physical experiments described in Chapter 6. The work in this chapter has been reported by Zhang et al. (2021d, Submitted).

5.2 Optimisation framework

The framework developed for the optimisation of the free-form wavy shells is presented in this section. The parametrisation method to describe the free-form corrugated cross-section profile is firstly introduced. The formulation of the optimisation problem, and the description of the adopted algorithm – particle swarm optimisation (PSO), are then presented. Finally, implementation of the optimisation approach, incorporating geometrically and materially nonlinear analyses without and with imperfections (GMNA and GMNIA respectively), is described.

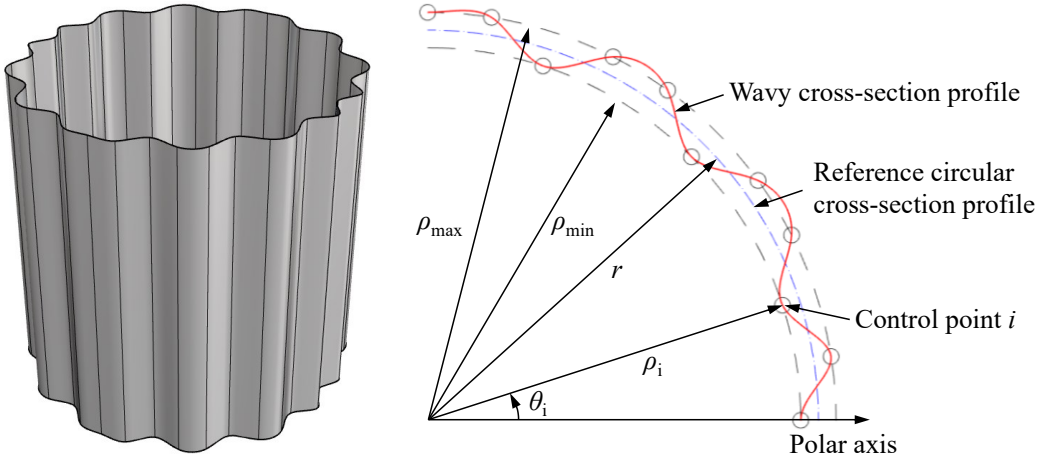

Figure 5.1: Schematic of the (a) overall view and (b) a quarter of a wavy cross-section profile

5.2.1 Parametrisation of cross-sections

The free-form wavy cross-section profiles were represented by closed non-uniform rational basis spline (NURBS) curves passing through a series of control points. The curves were set to be smooth with uniform knot spacing, of order 3 (i.e. cubic) and have a minimum of 16 control points, allowing a sufficient degree of geometric freedom in the free-form profile (Robert McNeel & Associates, 2012). A typical wavy cross-section profile is shown in Figure 5.1, where r is the radius of the reference circular cross-section profile, and ρ_{max} and ρ_{min} are the upper and lower radius limits for the control points respectively to avoid excessive curvature in the wavy profile. The following geometric constraints were imposed to enable rapid space exploration: (i) the cross-sections were assumed to be either mirror-symmetric about the x and y axes or rotationally symmetric (see Figure 5.2), leading to only a quarter of the cross-section

profile needing to be considered in the optimisation, as highlighted in Figure 5.2, and (ii) the control points lying on the curves were equally spaced circumferentially and were only allowed to move in the radial direction.

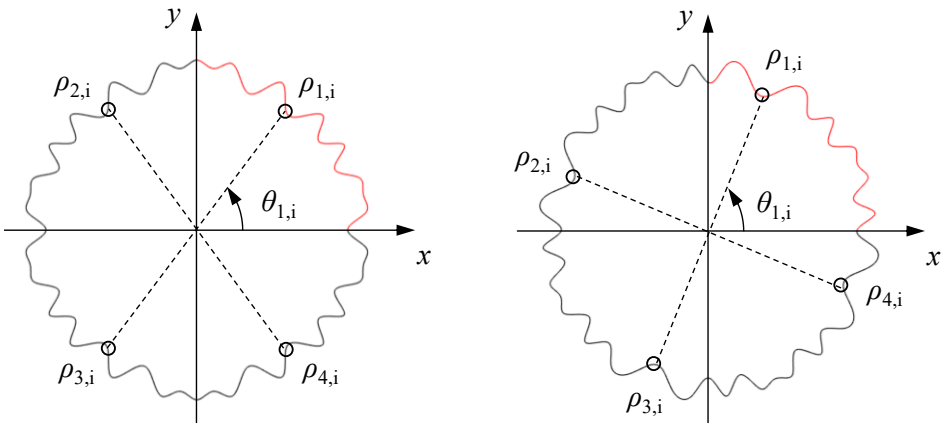

Figure 5.2: Definition of cross-section profiles with (a) mirror-symmetry and (b) 4-fold rotational symmetry

The radial positions of the control points in the first quadrant, as highlighted in Figure 5.2, were employed as the design variables. A total of N control points, with two lying on the x and y axes, were considered. For the cross-sections that were mirror-symmetric with respect to the x and y axes, all control points in the first quadrant were independent from each other, while for the rotationally symmetric cross-sections, only N-1 out of the N control points were independent since the two control points lying on the x and y axes must have the same radial position. Each control point i in the first quadrant can be described by the radial position ρ_i and circumferential position θ_i, as given by Equations 5.1 and 5.2.

$$\rho_{min} \leq \rho_i \leq \rho_{max} \tag{5.1}$$

$$\theta_i = \frac{\pi(i-1)}{2(N-1)} \tag{5.2}$$

5.2.2 Formulation of optimisation problem

The objectives of the optimisation procedure were to maximise the resistance of the free-form shells to local buckling and to minimise the sensitivity to local geometric imperfections. The

buckling loads of both perfect and imperfect shells were considered in the optimisation process, as recommended by Reitinger and Ramm (1995).

The objective function was taken as the average compressive stress at the ultimate load of the shell f_{ult} in order to achieve the maximum load-carrying capacity for a given quantity of material, as given by Equation 5.3, where P_0, P_+ and P_- are the buckling loads of the perfect shell, imperfect shells with positive imperfection amplitudes and imperfect shells with negative imperfection amplitudes (i.e. with the inversed imperfection pattern) respectively, and A is the cross-sectional area (equal to $l_p t$, where l_p is the perimeter of the cross-section centreline and t is the shell thickness). The free-form wavy shells can potentially exhibit different types of bifurcation instabilities, including asymmetric, unstable and stable symmetric responses, as illustrated by the Case I, II and III respectively in Figure 5.3, where P is the axial load, P_{cl} is the elastic buckling load, δ is the lateral deflection, and ω is the imperfection amplitude. The inversed imperfection patterns were therefore considered to account for the different levels of imperfection sensitivity associated with the sign of imperfection amplitudes in the case of asymmetric bifurcations (Brush & Almroth, 1975).

$$f_{ult} = \frac{\min(P_0, P_+, P_-)}{A} \tag{5.3}$$

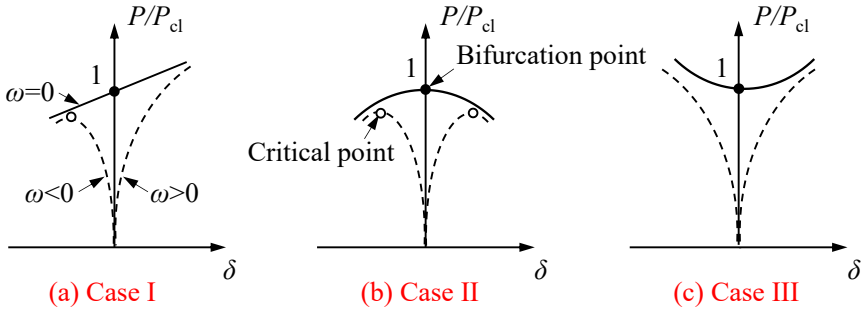

Figure 5.3: Effect of geometric imperfections for (a) asymmetric, (b) unstable symmetric and (c) stable symmetric bifurcation instabilities in perfect structures (Brush & Almroth, 1975)

The nonlinear optimisation problem can be formulated as follows:

Objective: to maximise ultimate stress f_{ult}

Optimisation variables: radial position vector of control points $\boldsymbol{\rho}=[\rho_1, \rho_2, \ldots, \rho_N]$

Geometric constraints: the cross-sections were assumed to be 4-fold mirror-symmetric or

rotationally symmetric

Bounds: $\left|\rho_i - r\right| \leq \Delta r$, where r is the radius of the shell middle surface, and Δr is the maximum allowable radial deviation of the control points and is equal to $(\rho_{max}\text{-}\rho_{min})/2$

The dimensions and parameters assumed in the optimisation of the wavy shells are presented in Table 5.1. The optimisation was performed based on a reference circular cross-section with an outer diameter D equal to 200 mm and a maximum allowable radial deviation Δr equal to 4.5 mm, as discussed below. The wall thickness t was set equal to 0.7 mm, and the nominal length L was set equal to the outer diameter of the reference circular cross-section, which was greater than twice the axisymmetric meridional elastic buckling half-wavelength and has been adopted in several previous studies on shell buckling (Weingarten, Seide & Peterson, J, 1968; Arbocz & Babcock, 1968). The shell was assumed to be fixed-ended under axial compression. The adopted stress-strain curve was described using the two-stage Ramberg-Osgood expression (Ramberg & Osgood, 1943; Arrayago, Real & Gardner, 2015; Gardner & Yun, 2018) based on the average measured material properties in the longitudinal direction for stainless steel CHS produced by powder bed fusion, as reported in Zhang et al. (2021c) and Buchanan et al. (2017). The measured engineering stress-strain curves from the tensile coupon tests and key mechanical parameters are presented in Figure 5.4 and Table 5.2, respectively.

Table 5.1: Dimensions and parameters of wavy shell designs

D (mm)	t (mm)	L (mm)	Δr (mm)	ω (mm)	Candidate design ID	Symmetry	N
200	0.7	200	4.5	$\frac{1}{25}\sqrt{rt}$	1	Mirror	16
					2	Mirror	21
					3	Rotational	16
					4	Rotational	21

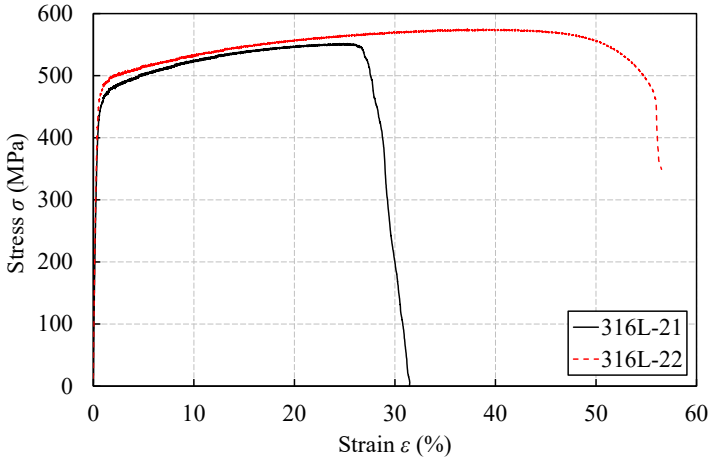

Figure 5.4: Measured engineering stress-strain curves from tensile coupon tests

Table 5.2: Measured material properties from vertical ($\theta = 90°$) tensile coupon tests (Buchanan et al., 2017)

Coupon	θ (°)	ϕ (°)	E (MPa)	$\sigma_{0.2}$ (MPa)	$\sigma_{1.0}$ (MPa)	σ_u (MPa)	ε_u (%)	ε_f (%)	n	$m_{1.0}$	m_u
316L-21	90	0	183700	407	471	551	24.8	28.0	3.2	4.2	4.3
316L-22	90	90	180300	435	489	574	38.3	50.3	3.5	4.1	4.1
Average	90	-	182000	422	480	562	31.6	39.2	3.4	4.2	4.2

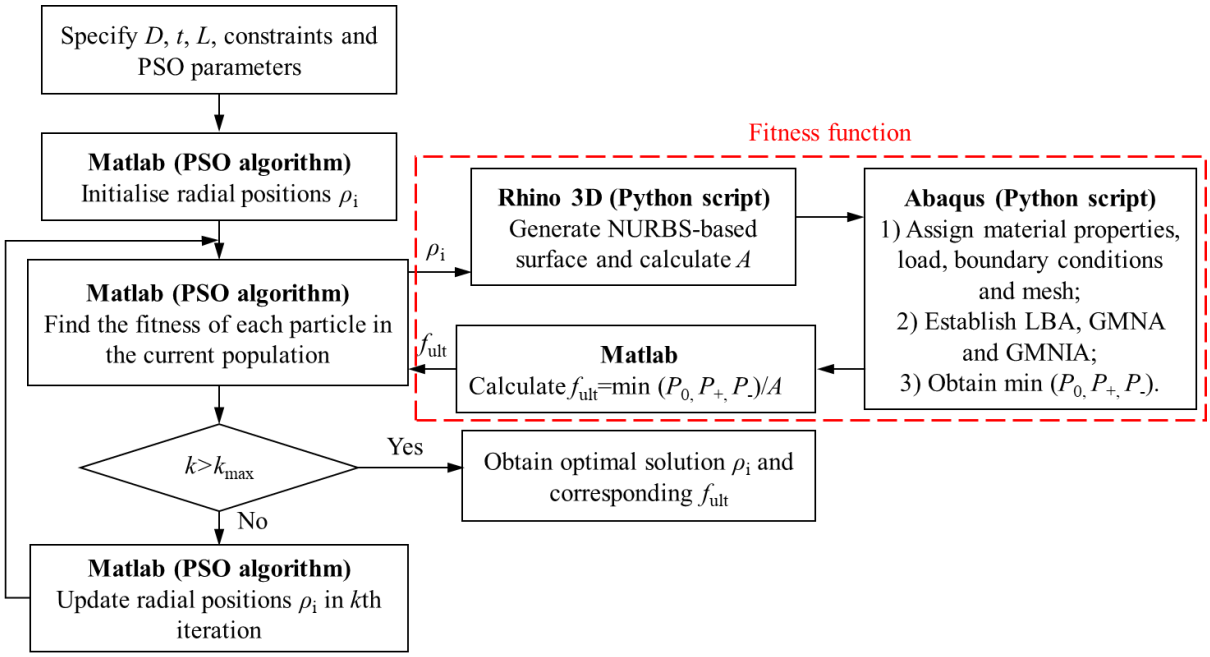

Figure 5.5: Flowchart of the optimisation process

5.2.3 Optimisation technique and selection of parameters

Particle Swarm Optimisation (PSO), inspired by the social behaviour observed in bird flocking, fish schooling and animal herding and first proposed by Kennedy and Eberhart (1995), Eberhart and Kennedy (1995) and Shi and Eberhart (1998, 1999, 2000) is a swarm intelligence method for nonlinear optimisation problems. It has a range of benefits, including memory (i.e. the best solution for each particle is saved and considered in the subsequent iteration), no genetic operators (such as crossover and mutation) required, constructive cooperation between particles and reasonable computation time to achieve optimal solutions (Ye et al., 2016, 2018), and was therefore adopted in this study. A swarm consists of N_p individuals (or particles) that fly through an N-dimensional search space of design variables. Each particle in the swarm represents a potential solution, and a fitness function (see Figure 5.5) is used to guide the particles in search of the global optimal solution in the swarm. A basic PSO algorithm starts with swarm initialisation, followed by iterative updates of velocities and positions until the stopping criteria are met, as described in Figure 5.5.

The PSO swarm size N_p and the maximum number of iterations k_{max}, along with the key design parameters, including the maximum allowable deviation from the reference circle Δr and the number of control points N, were tuned through a prior parametric sensitivity analysis. A swarm size of 50, a maximum number of iterations of 100, a deviation from the reference circle of 4.5 mm and the numbers of control points of 16 and 21, were found to yield converging solutions, while remaining computationally efficient, and were therefore adopted in the optimisation. Three key parameters – the inertia weight factor w, cognitive acceleration factor c_1 and and social acceleration factor c_2, affect the search performance of the PSO algorithm. A large inertia weight w facilitates global exploration and mitigates premature convergence, which is often applied in the early stages of the optimisation, while a small inertia weight w corresponds to an intensified search in local regions, which can accelerate the convergence in the later stages. The balance between the global and local searches can be dynamically adjusted by linearly decreasing w with successive iterations according to Shi and Eberhart (1998, 1999, 2000), as given by Equation 5.4, where k and k_{max} are the current iteration number and the maximum number of iterations respectively, and w_{max} and w_{min} are the maximum and minimum inertia weights respectively. A linearly decreasing inertia weight w from 0.95 to 0.4, coupled with a maximum velocity V_{max} in the range of the maximum radial distance ρ_{max}, as recommended by

Shi and Eberhart (1998, 1999, 2000), was used in this study. The acceleration coefficients c_1 and c_2, which reflect the confidence levels of the solutions from each particle and the whole swarm, respectively, were both taken equal to 2, following the recommendations of Shi and Eberhart (1998, 1999, 2000). A summary of the adopted PSO parameters is shown in Table 5.3.

$$w_{k+1} = w_{\max} - k\frac{w_{\max} - w_{\min}}{k_{\max}} \tag{5.4}$$

Table 5.3: Adopted parameters for PSO algorithm

c_1	c_2	w	r_1, r_2	$V_{\max}$	N_p	$k_{\max}$
2.0	2.0	0.95~0.4	[0, 1]	[$-\rho_{\max}$, $\rho_{\max}$]	50	100

Upon selection of the PSO and design parameters, the initial velocity and position vectors of each particle within the swarm were randomly generated. In the kth iteration, the velocity and position vectors of the jth particle, as denoted by $\boldsymbol{V}_j^k = [v_{j1}^k, v_{j2}^k, ..., v_{jN}^k]$ and $\boldsymbol{\rho}_j^k = [\rho_{j1}^k, \rho_{j2}^k, ..., \rho_{jN}^k]$ respectively, with j=(1, 2, …, N_p), were updated based on their individual best ever positions and the global best position of all particles in the swarm in the previous iteration, as expressed by Equations 5.5 and 5.6 (Shi & Eberhart, 1998), where j and k represent the IDs of the particle and the iteration respectively, Δt is the pseudo time increment, $\boldsymbol{P}_{best,j}^k = [p_{j1}^k, p_{j2}^k, ..., p_{jN}^k]$ denotes the best position that gives the best fitness value of particle j over its history up to the kth iteration, $\boldsymbol{G}_{best}^k = [g_1^k, g_2^k, ..., g_N^k]$ represents the global best position of all particles in the swarm up to the kth iteration, and r_1 and r_2 are two random values within the range [0, 1]. Figure 5.6 shows the dynamic movement with the velocity and position updates of a particle j in a two-dimensional search space. The search was terminated once the maximum number of iterations of 100 was reached. Note that the employed PSO algorithm does not guarantee that the global best solutions are found due to the non-convex nature of the problem with multiple local minima, but usually converges to near-global best solutions. In total, four combinations of symmetry types (mirror or rotational) and numbers of control points (N = 16 or 21) were considered in the present study.

$$\boldsymbol{V}_j^{k+1} = w\boldsymbol{V}_j^k + c_1 r_1(\boldsymbol{P}_{best,j}^k - \boldsymbol{\rho}_j^k)/\Delta t + c_2 r_2(\boldsymbol{G}_{best}^k - \boldsymbol{\rho}_j^k)/\Delta t \tag{5.5}$$

$$\boldsymbol{\rho}_{\mathrm{j}}^{\mathrm{k+1}} = \boldsymbol{\rho}_{\mathrm{j}}^{\mathrm{k}} + \boldsymbol{V}_{\mathrm{j}}^{\mathrm{k+1}} \Delta t \tag{5.6}$$

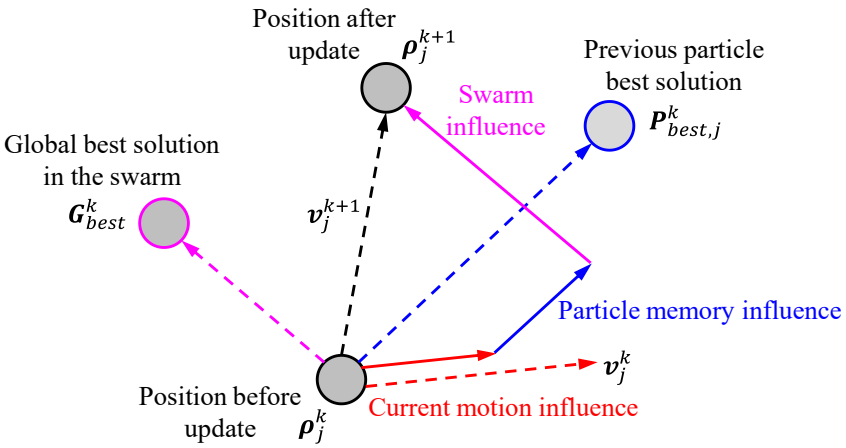

Figure 5.6: Description of velocity and position updates for a particle *j* in a two-dimensional search space

5.2.4 Numerical implementation

The PSO algorithm was implemented using Matlab scripts (Mathworks, 2018), where the positions of control points were dynamically adjusted. NURBS curves through control points and surfaces (i.e. wavy shell geometries) were generated using Rhino 3D (Robert McNeel & Associates, 2012) and exported as an Initial Graphics Exchange Specification (.IGES) file; this procedure was automated using a Python script. The IGES file was then imported into Abaqus (Dassault Systèmes, 2017) for the establishment of finite element models, and finally the GMNA and GMNIA were conducted to assess the structural performance of the generated wavy shells.

The four-noded shell element with reduced integration (S4R) from the Abaqus element library (Dassault Systèmes, 2017) was chosen, which has been successfully used for the simulation of structural hollow sections (Meng et al., 2020; Meng & Gardner, 2020b; Yun & Gardner, 2018). A mesh size of $0.2(Dt)^{1/2}$ were adopted for modelling the wavy shells, to enable the developed models to capture the local buckling pattern and to accurately predict the buckling loads at a reasonable computational cost. A typical established FE model is shown in Figure 5.7, where u_x, u_y and u_z are the displacements in the x, y and z direction respectively, and u_{Rx}, u_{Ry} and u_{Rz} are the rotations about the x, y and z axis respectively; fixed-ended boundary conditions were

simulated by means of coupling the end sections to a pair of reference points, where only the longitudinal translation of the top reference point was allowed (i.e. u_x=u_y=u_{Rx}=u_{Ry}=u_{Rz}=0).

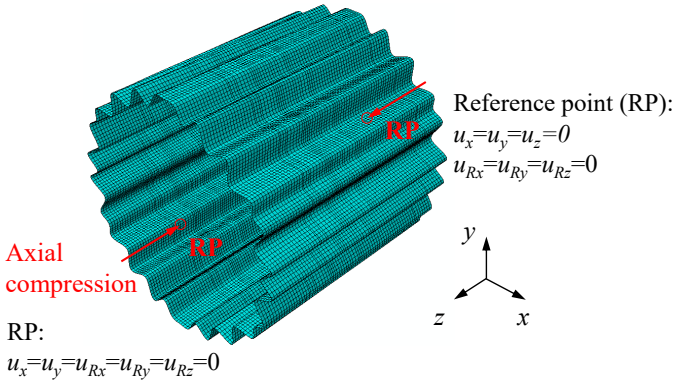

Figure 5.7: Geometry, loading and boundary conditions of FE models for wavy shells

The lowest elastic buckling mode shape obtained from a linear bifurcation analysis (LBA) was chosen to represent the initial geometric imperfection pattern, and an imperfection amplitude ω equal to $\frac{1}{Q}\sqrt{rt}$ was employed to factor the imperfection pattern, where Q is the fabrication quality parameter, r is the radius of the circular shell (or the radius of the reference circular shell for the corrugated shells) and t is the wall thickness; the value of Q was taken equal to 25 for fabrication quality Class B in EN 1993-1-6 (CEN, 2017) based on previous experimental results on additively manufactured stainless steel shells (Zhang et al., 2021d).

5.3 Optimisation results and analysis

The optimised mirror-symmetric and rotationally symmetric wavy cross-sections with the different numbers of control points (N=16 and 21) are shown in Figures 5.8 and 5.9 respectively, while the radial deviations of the control points from the reference circle in the first quadrant are provided in Table 5.4. The convergence histories of the ultimate stress f_{ult} for the four candidate shells are plotted in Figures 5.10 and 5.11, where the particle function value and global best value in each iteration are displayed, along with the ultimate stress of the reference circular cylindrical shell $f_{ult,cyl}$ obtained from GMNIA. It can be seen that the optimisation runs converged after about 40 iterations, though new PSO particles (i.e. new cross-section profiles) in the search space continued to be explored before the final iteration, but all new particle function values were found to fall below the converged global best values. In order to save

computation time, the ultimate stress was automatically called from the previous iterations if the percentage change between the new and previous radial positions was within 0.01%. The scattered data with the ultimate stresses f_{ult} approximately equal to 200 MPa correspond to the considered cylindrical shells (circular or near-circular) constrained by the maximum allowable radial deviation. The key results for the four optimised candidate shell designs and their reference circular shell are summarised in Table 5.5, where A is the cross-sectional area of the shell, σ_{cr} is the elastic local buckling stress, γ is the imperfection sensitivity factor that describes the sensitivity of the buckling load to the imperfection amplitude, as given by Equation 5.7, and $f_{ult,cyl}$ is the ultimate stress of the reference circular shell.

$$\gamma = \frac{\min(P_+, P_-)}{P_0} \tag{5.7}$$

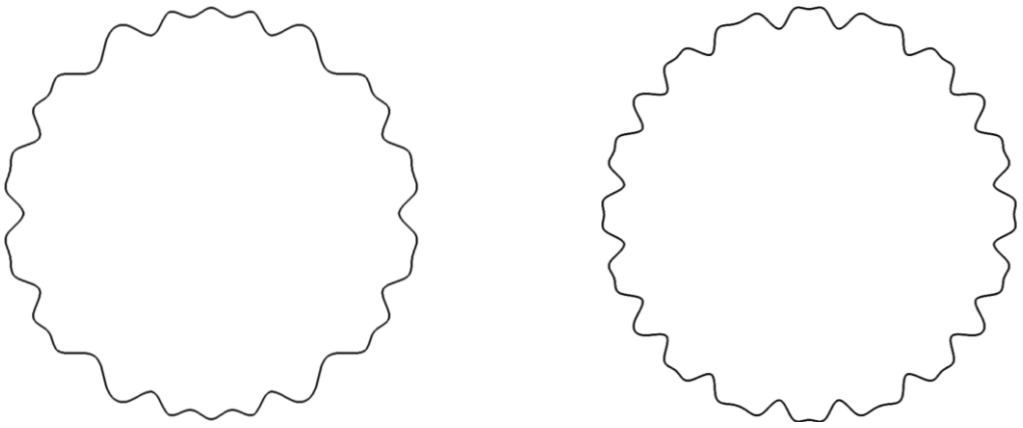

(a) (b)

Figure 5.8: Cross-section profiles of mirror-symmetric wavy shells with (a) N=16 and (b) N=21

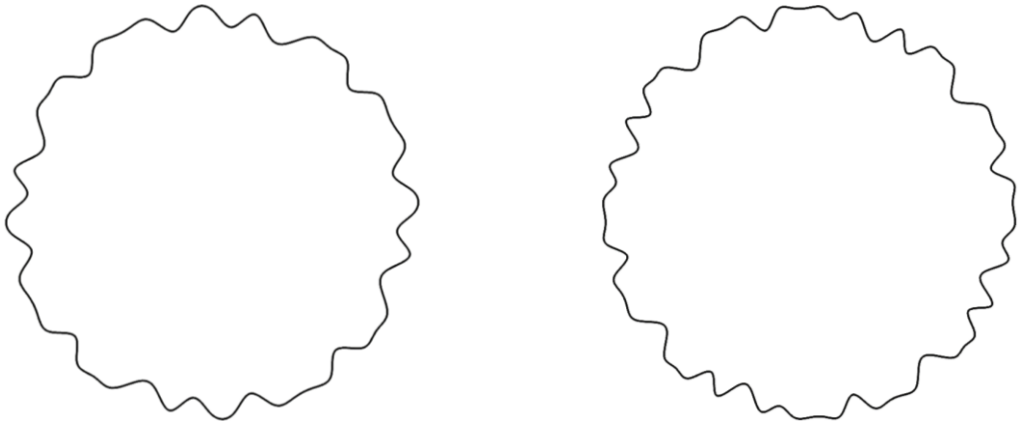

(a) (b)

Figure 5.9: Cross-section profiles of rotationally symmetric wavy shells with (a) N=16 and (b) N=21

Table 5.4: Radial deviations of control points of wavy shell designs, ρ_i-r (mm)

Symmetry	N	1	2	3	4	5	6	7	8	9	10	11	12	13	14	15	16	17	18	19	20	21
Mirror	16	-4.50	4.50	4.50	4.50	-4.50	4.50	4.50	4.50	-4.50	-4.50	4.50	4.50	-4.50	4.50	1.23	4.50					
Mirror	21	4.50	4.50	-4.50	4.50	4.50	4.50	-4.50	4.50	4.50	-4.50	4.50	4.50	4.50	-4.50	4.50	4.50	4.50	4.50	-4.33	4.50	4.50
Rotational	16	4.50	4.50	-4.50	4.50	4.50	4.50	4.50	-4.50	4.50	4.50	4.50	-4.50	-4.50	4.50	-3.85	4.50					
Rotational	21	4.50	4.50	4.50	-4.50	4.50	4.50	4.50	4.50	-4.50	-4.50	4.50	4.50	4.50	-4.50	4.50	-4.50	-4.50	4.50	-0.17	4.50	4.50

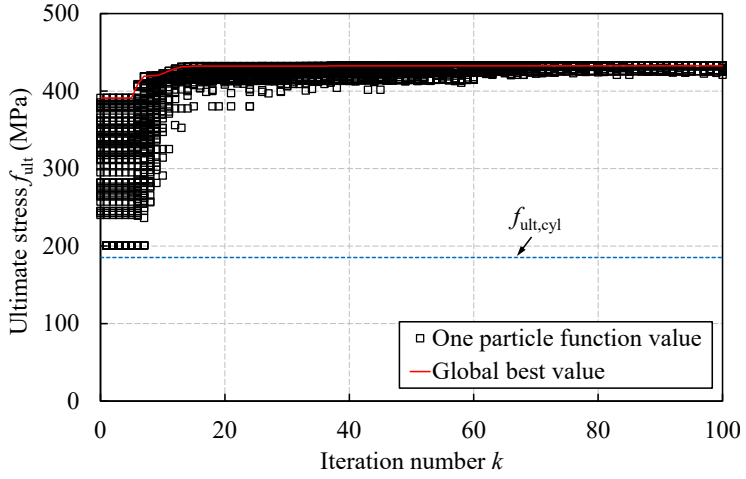

(a)

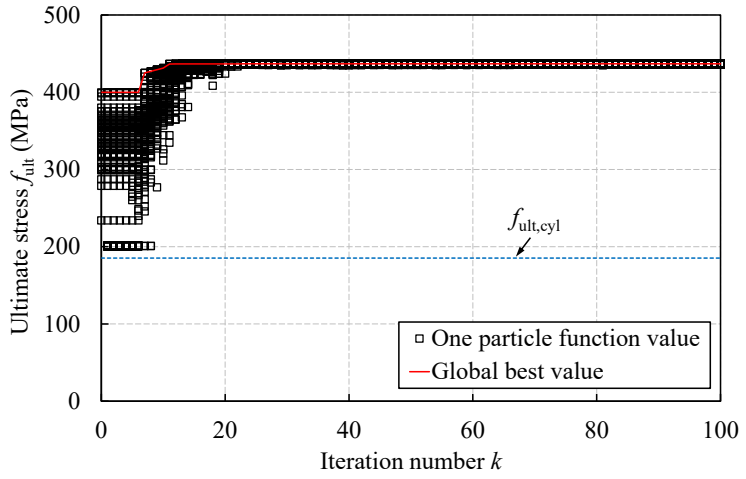

(b)

Figure 5.10: Convergence histories of ultimate stresses for mirror-symmetric wavy shells with (a) N=16 and (b) N=21 and with L/D=1

Table 5.5: Optimisation results for wavy shells with L/D=1 and their reference circular cylindrical shell

Symmetry	N	A (mm^2)	σ_{cr} (MPa)	P_0 (kN)	P_+ (kN)	P_- (kN)	min(P_+, P_-) (kN)	f_{ult} (MPa)	γ	$\frac{f_{ult}}{\sigma_{0.2}}$	$\frac{f_{ult}}{f_{ult,cyl}}$
Circular	-	438.3	672.2	158.3	81.3	83.0	81.3	185.2	0.513	0.440	-
Mirror	16	528.4	1152.3	231.4	228.6	228.6	228.6	432.6	0.988	1.027	2.335
Mirror	21	583.6	1596.5	256.2	254.9	254.8	254.8	436.8	0.994	1.037	2.358
Rotational	16	533.5	849.7	235.4	232.1	231.5	231.5	435.0	0.983	1.033	2.349
Rotational	21	563.9	1263.9	248.0	246.5	246.5	246.5	437.2	0.994	1.038	2.360

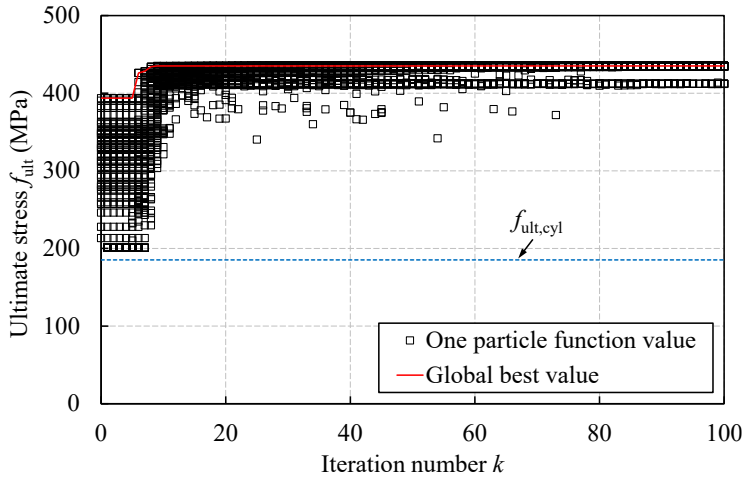

(a)

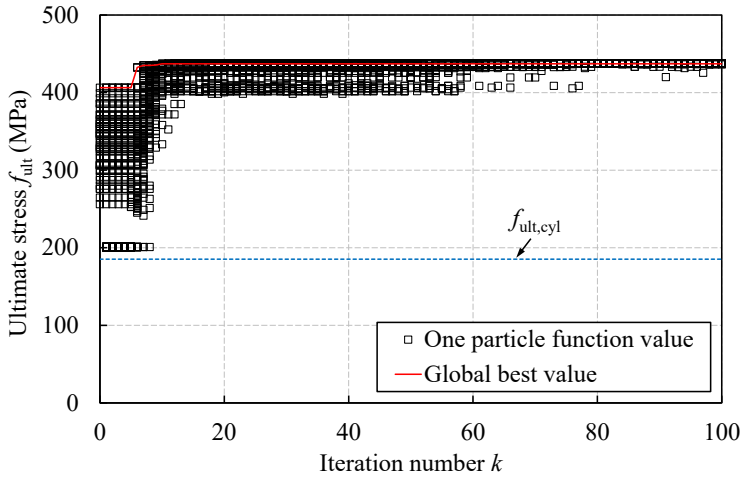

(b)

Figure 5.11: Convergence histories of ultimate stresses for rotationally symmetric wavy shells with (a) N=16 and (b) N=21 and with L/D=1

A lower value of the imperfection sensitivity factor γ corresponds to a higher level of sensitivity to geometric imperfections, while an imperfection sensitivity factor γ close to unity indicates that the considered shell is imperfection-insensitive. The reference circular cylindrical shell was shown to be highly sensitive to imperfections with γ=0.513; the four optimised wavy shells, on the other hand, were found to be imperfection-insensitive with γ ranging between 0.983 and 0.994. In terms of the compressive load-carrying capacity, the four optimised shells were shown to be capable of reaching their respective plastic resistances with the corresponding ultimate stresses being approximately 135% higher than that of their reference circular cylindrical shell, reflecting their significantly reduced susceptibility to local buckling. Overall, the rotationally symmetric wavy shell with 21 control points performed best, with the highest ultimate stress

and the lowest imperfection sensitivity among the four candidate designs, although the differences are marginal. The evolution of the cross-section profiles for the rotationally symmetric shell with N=21 control points is presented in Figure 5.12, where a quarter of the cross-section profile (i.e. the control curve) is highlighted. The failure modes of the reference circular cylindrical shell and the optimised wavy shell with rotationally symmetry and N=21 are compared in Figure 5.13. The optimised wavy shell showed an axisymmetric deformation mode and failed by local buckling in the troughs of corrugations, while the circular cylindrical shell exhibited a chequerboard failure mode.

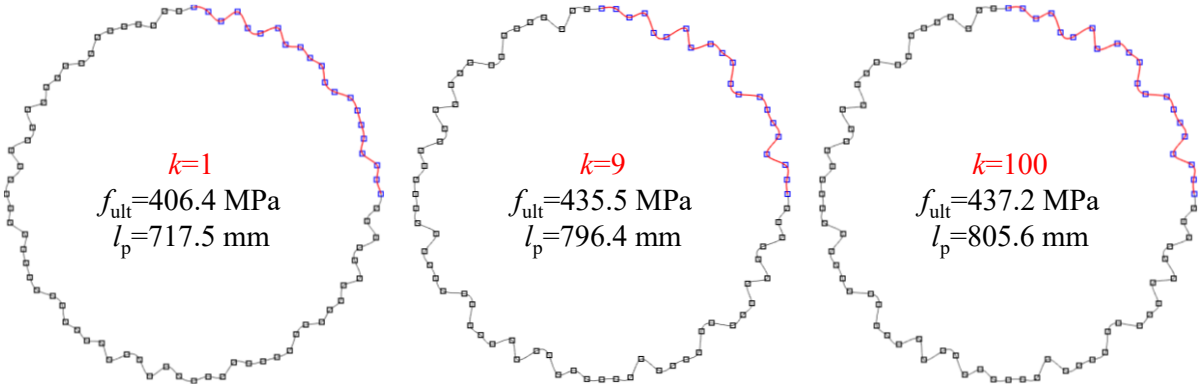

(a) (b) (c)

Figure 5.12: Evolution of cross-section profiles for optimised wavy shell at Iteration (a) 1, (b) 9 and (c) 100

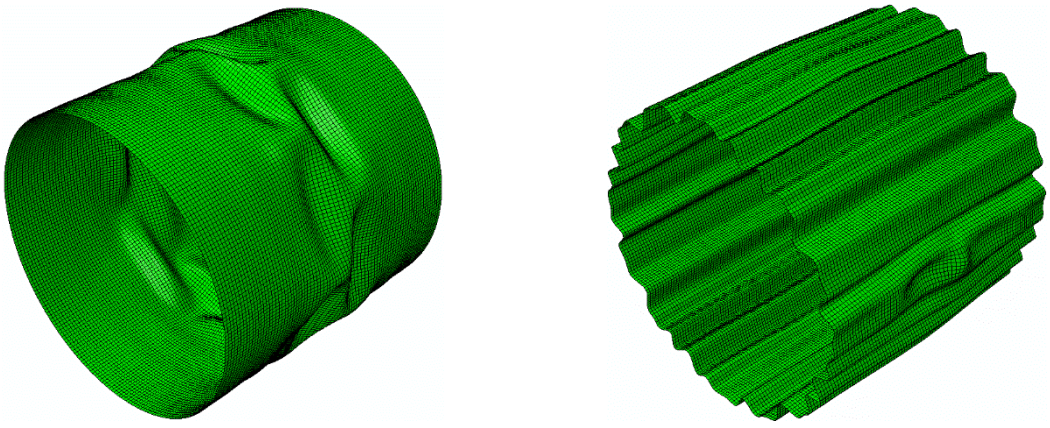

(a) (b)

Figure 5.13: Failure modes for (a) reference circular cylindrical shell and (b) optimised wavy shell

5.4 Influence of other geometric parameters

5.4.1 Length-to-diameter ratio

To investigate the effect of length on the performance of wavy shells under axial compression, an optimisation study was carried out on wavy shells with different lengths using the same method outlined in Section 5.2. The design parameters were taken as the same as those listed in Table 5.1, except for the length L, which was set equal to twice the outer diameter (i.e. L=2D) in this optimisation. The key results for the four candidate wavy shells and their reference circular cylindrical shell, also with L=2D, are presented in Table 5.6. The rotationally symmetric wavy shell with 16 control points was found to perform best, with a load-carrying capacity 116% higher than that of the reference cylindrical shell and significantly reduced sensitivity to imperfections (γ≈0.964). The evolution of ultimate stress and cross-section profile for the aforementioned optimised wavy shell are plotted in Figure 5.14, while the failure mode is presented in Figure 5.15, alongside that of the reference circular cylindrical shell with L/D=2. The optimised wavy shell exhibited a non-axisymmetric deformation pattern and buckled locally in the region of minimum curvature, while its reference circular cylindrical shell showed a typical chequerboard failure mode. The ultimate stress of the optimised wavy shell with L/D=2 was shown to be approximately 7% lower than that of its counterpart with L/D=1; this is because compared with the case of L/D=1, a different failure mode with a longer half-wavelength was allowed to develop for the case of L/D=2, thus resulting in a slightly reduction in the ultimate stress.

Table 5.6: Optimisation results for wavy shells with L/D=2 and their reference circular cylindrical shell

Symmetry	N	A (mm^2)	σ_{cr} (MPa)	P_0 (kN)	P_+ (kN)	P_- (kN)	min(P_+,P_-) (kN)	f_{ult} (MPa)	γ	$\frac{f_{ult}}{\sigma_{0.2}}$	$\frac{f_{ult}}{f_{ult,cyl}}$
Circular	-	438.3	666.7	156.5	82.1	82.1	82.1	187.3	0.525	0.446	-
Mirror	16	527.9	314.1	205.3	209.8	209.2	209.2	397.4	1.019	0.944	2.116
Mirror	21	561.1	586.4	229.2	225.4	225.4	225.4	401.7	0.983	0.954	2.139
Rotational	16	532.6	619.9	219.3	216.1	215.4	215.4	405.8	0.982	0.964	2.161
Rotational	21	554.8	895.3	228.6	219.0	218.3	218.3	394.8	0.955	0.938	2.103

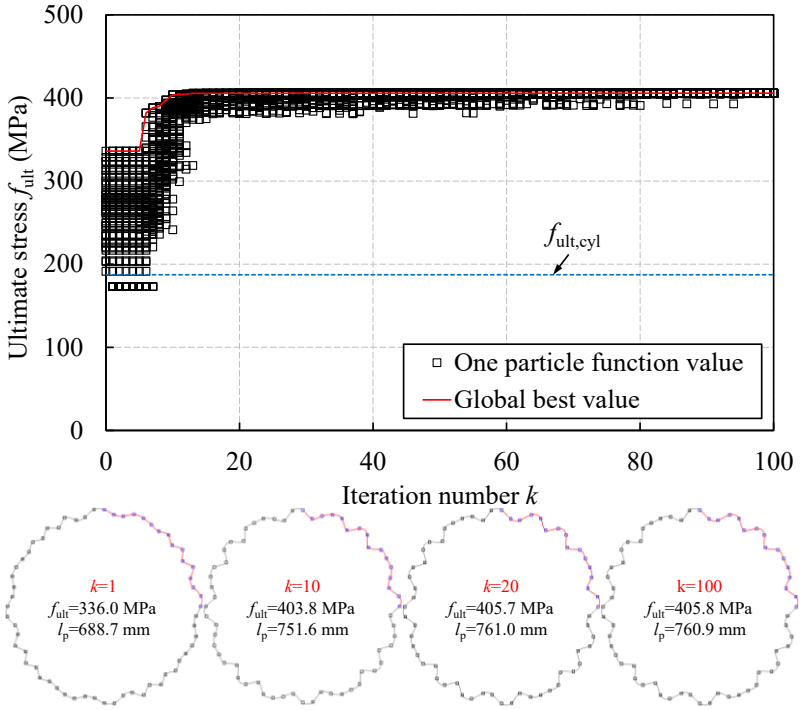

Figure 5.14: Evolution of ultimate stresses and cross-section profiles for wavy shell with L/D=2

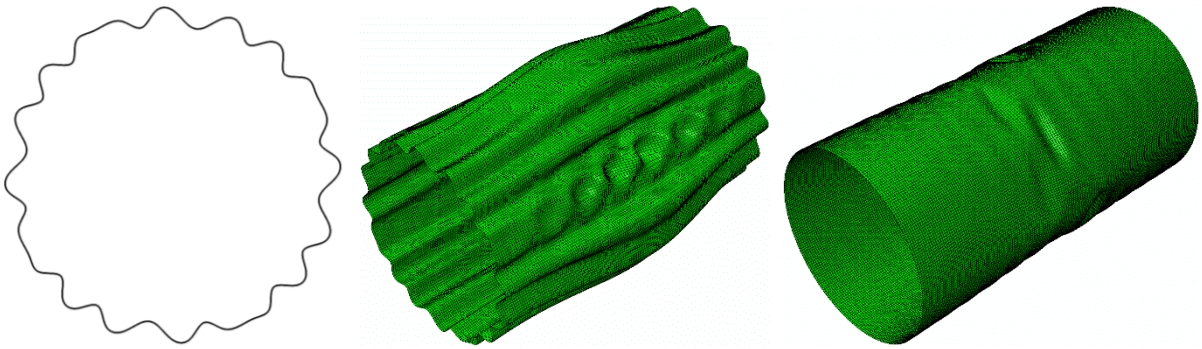

(a) (b) (c)

Figure 5.15: (a) Cross-section profile and (b) failure modes of optimised wavy shell and (c) reference circular cylindrical shell with L/D=2

Table 5.7: Optimisation results for wavy shells with various diameter-to-thickness ratios and their reference circular cylindrical shells

Cross-section	L	Δr	Symmetry	N	A (mm^2)	σ_{cr} (MPa)	P_0 (kN)	min(P_+, P_-) (kN)	f_{ult} (MPa)	γ	$\frac{f_{ult}}{\sigma_{0.2}}$	$\frac{f_{ult}}{f_{ult,cyl}}$
C150×1.0	150	-	-	-	468.1	1279.8	198.6	152.4	325.5	0.767	0.770	-
C180×1.0	180	-	-	-	562.3	1067.9	232.0	162.5	289.0	0.700	0.690	-
C200×1.0	200	-	-	-	625.2	958.4	252.2	164.9	263.8	0.654	0.630	-
C150×0.7	150	-	-	-	328.3	895.0	129.9	81.7	248.8	0.629	0.590	-
C180×0.7	180	-	-	-	394.3	746.0	148.2	85.2	216.2	0.575	0.510	-
C200×0.7	200	-	-	-	438.3	672.2	158.3	81.3	185.2	0.513	0.440	-
W150×1.0	150	4.5	Rotational	21	654.7	2102.8	299.1	298.3	455.7	0.997	1.083	1.406
W180×1.0	180	5.0	Rotational	21	815.6	1967.2	368.1	367.1	450.2	0.997	1.069	1.549
W200×1.0	200	5.5	Rotational	21	837.6	1726.6	379.6	377.1	450.2	0.993	1.069	1.700
W150×0.7	150	4.0	Rotational	21	440.0	1792.2	197.2	197.0	447.7	0.998	1.063	1.802
W180×0.7	180	4.5	Rotational	21	544.3	1099.2	242.5	240.5	442.1	0.992	1.050	2.045
W200×0.7	200	4.5	Rotational	21	563.9	1263.9	248.0	246.5	437.2	0.994	1.038	2.360

5.4.2 Diameter-to-thickness ratio

In addition to the optimised wavy shell designs presented in Section 5.3, further optimisation, using a similar approach to that described in Section 5.2, but for a wider range of diameter-to-thickness ratios, was conducted. Reference circular cylindrical shells – C150×1.0, C180×1.0, C200×1.0, C150×0.7, C180×0.7 and C200×0.7 (outer diameter × thickness, in mm), covering a range of local slenderness values $\bar{\lambda}_c$, defined in Equation 4.2, from 0.58 to 0.80, were selected, and the corresponding optimised wavy shells were denoted W150×1.0, W180×1.0, W200×1.0, W150×0.7, W180×0.7 and W200×0.7, respectively. The deviations from the reference circles Δr, which were determined based on a prior parametric sensitivity analysis, are presented in Table 5.7.

The optimisation results of the considered wavy shells, along with the key results for their reference circular cylindrical shells, are summarised in Table 5.8. The imperfection sensitivity factors of all the optimised shells were shown to be close to unity, indicating very low sensitivity to geometric imperfections. The ratio of the ultimate stress of the optimised wavy shells to that of the corresponding circular cylindrical shells, were found to increase from 1.41 to 2.36 as the diameter-to-radius ratio increased from 150 to 286, showing the increased benefits from the optimisation for more slender shell structures.

Table 5.8: Comparisons of results for circular cylindrical shell, optimised free-form wavy shell and alternative optimised shell designs

Shell type	M or N_s	A (mm^2)	σ_{cr} (MPa)	P_0 (kN)	min (P_+, P_-) (kN)	f_{ult} (MPa)	γ	$\frac{f_{ult}}{\sigma_{0.2}}$	$\frac{f_{ult}}{f_{ult,cyl}}$
Circular	-	438.3	672.2	158.3	81.3	185.2	0.513	0.440	-
Sinusoidally corrugated	42	524.5	1376.2	224.1	203.5	387.9	0.908	0.921	2.093
Aster	20	459.8	883.7	192.8	180.6	392.7	0.937	0.937	2.120
Externally stringer-stiffened	38	548.7	1205.1	246.7	235.1	428.4	0.953	1.018	2.314
Internally stringer-stiffened	46	571.9	815.2	255.0	202.4	354.0	0.794	0.841	1.911
Free-form wavy	-	563.9	1263.9	248.0	246.5	437.2	0.994	1.038	2.360

5.5 Alternative designs and comparisons

In addition to the free-form wavy shells, a selection of alternative non-circular cross-section profiles, including sinusoidally corrugated shells (Yadav & Gerasimidis, 2019, 2020), Aster shells (Jullien & Araar, 1991; Araar, Derbali & Jullien, 1998; Combescure & Jullien, 2015) and stringer-stiffened shells (Singer, Arbocz & Babcock, 1971; Hutchinson & Frauenthal, 1969), was considered in the present study for comparison purposes. The cross-section profile of each considered alternative, based on a typical reference cylinder with t=0.7 mm and L=D=200 mm, was optimised by means of numerical parametric studies following the same modelling assumptions detailed in Section 5.2. GMNIA of the alternative designs were performed, and the responses under axial compression were compared with that of the optimised free-form wavy shells.

5.5.1 Sinusoidally corrugated shells

A simpler approach to creating an efficient corrugated cross-section profile, rather than performing computationally demanding iterations, as required for the free-form wavy shells, is to superpose a series of predefined waves onto a reference circular cross-section profile. A sinusoidally corrugated cross-section profile, obtained by superposing sinusoidal waves with a specific wavelength and amplitude on the reference circular cross-section profile, is shown in Figure 5.16 and can be expressed by Equation 5.8, where ρ_i is the radial position of the trace point i, r is the radius of the reference circle, θ_i is the angular position of the trace point i, and Δr and M denote the amplitude and the number of half-sine waves, respectively.

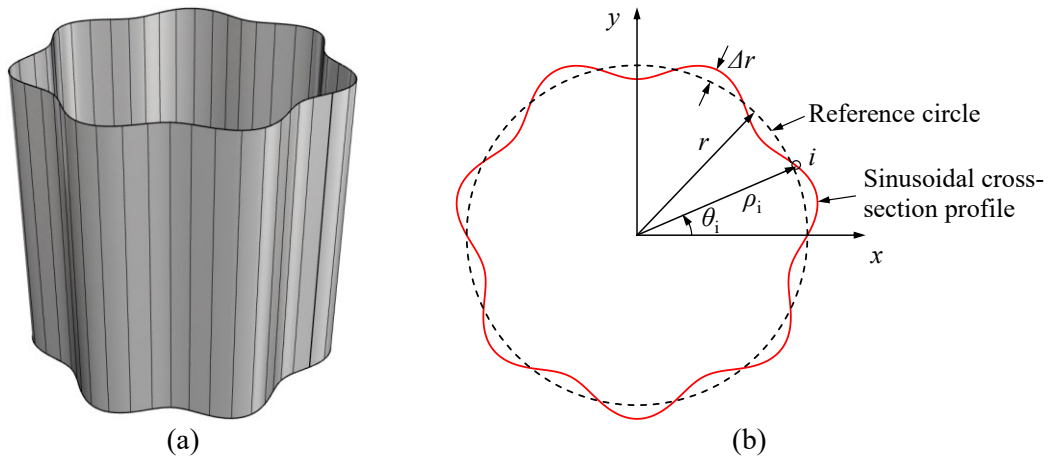

Figure 5.16: Schematic (a) overall view and (b) cross-section profile of sinusoidally corrugated shells

$$\rho_i = r + \Delta r \cdot \sin(\theta_i \cdot M/2) \tag{5.8}$$

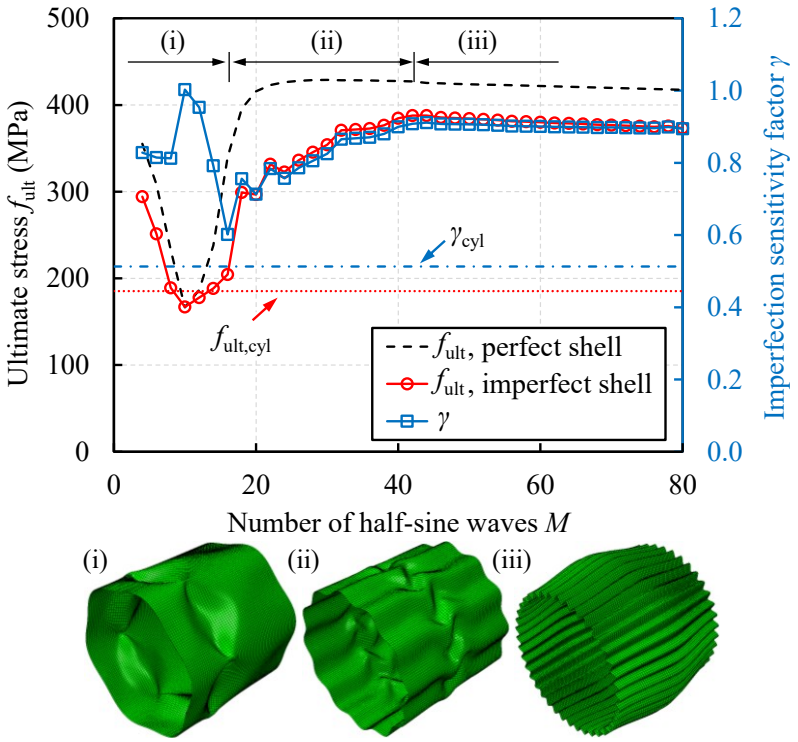

Figure 5.17: Ultimate stresses, imperfection sensitivity factors and typical failure modes of sinusoidally corrugated shells

The amplitude of the half-sine waves Δr was set equal to 4.5 mm for consistency with the assumption adopted for the free-form wavy shells, and a range of the number of half-sine waves M between 4 and 80 was considered in the optimisation. The normalised ultimate stress $f_{ult}/\sigma_{0.2}$ and the imperfection sensitivity factor γ are plotted against the number of half-sine waves M, along with typical failure modes, in Figure 5.17, where f_{ult} for the imperfect shells was determined using Equation 5.3. It can be seen that, as the number of half-sine waves M increased, different responses in terms of the ultimate stress and imperfection sensitivity, linked to changes in failure mode, occurred. Also presented in Figure 5.17 are the normalised ultimate stress and the imperfection sensitivity factor of the corresponding circular cylindrical shell, revealing that, in general, significantly improved buckling resistance and reduced imperfection sensitivity were achieved by the sinusoidally corrugated shells. Overall, the sinusoidally corrugated shell with 42 half-sine waves was found to achieve the greatest enhancement in buckling resistance relative to the reference circular cylindrical shell, with significantly reduced sensitivity to imperfections.

5.5.2 Aster shells

Aster shells have been shown to have significantly higher load-carrying capacities than their reference circular cylindrical shells in Jullien & Araar (1991), Araar, Derbali & Jullien (1998) and Combescure & Jullien (2015). A typical Aster cross-section profile, as shown in Figure 5.18, can be achieved by superposing a series of outward half-sine waves with an amplitude Δr and a wave number M onto its reference circular cross-section profile and can be parametrised using Equation 5.9.

$$\rho_i = r + \left|\Delta r \cdot \sin(\theta_i \cdot M/2)\right| \tag{5.9}$$

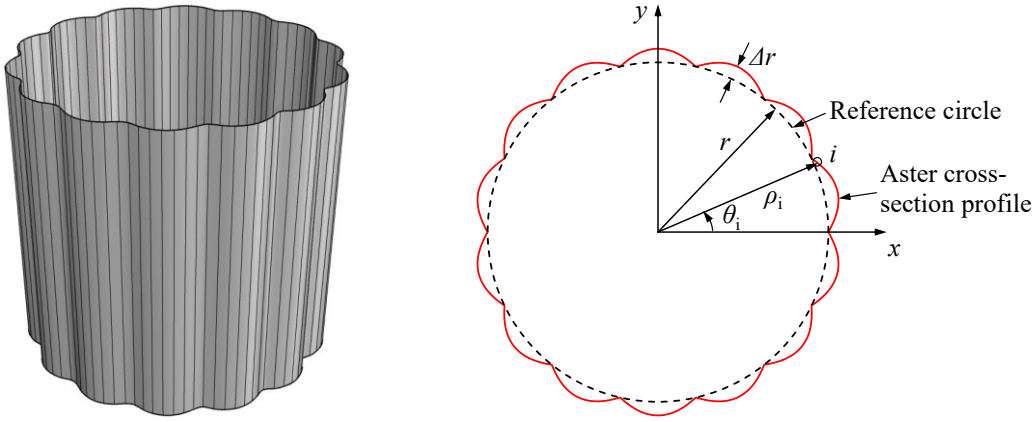

(a) (b)

Figure 5.18: Schematic (a) overall view and (b) cross-section profile of Aster shells

Parametric studies were conducted on the Aster shells with the number of half-sine circumferential waves M ranging from 4 to 80 and a wave amplitude Δr equal to that adopted for the wavy shells (i.e. 4.5 mm). Similar to Figure 5.17, the normalised ultimate stresses are plotted against the number of half-sine waves M in Figure 5.19, along with the imperfection sensitivity factors and failure modes of the imperfect Aster shells, where different trends of ultimate stresses and imperfection sensitivity factors are again associated with the change of failure modes. Overall, the number of half-sine waves of 20 was found to be optimal with the highest ultimate stress and an imperfection sensitivity factor close to unity, which indicated a much less sensitivity to geometric imperfections.

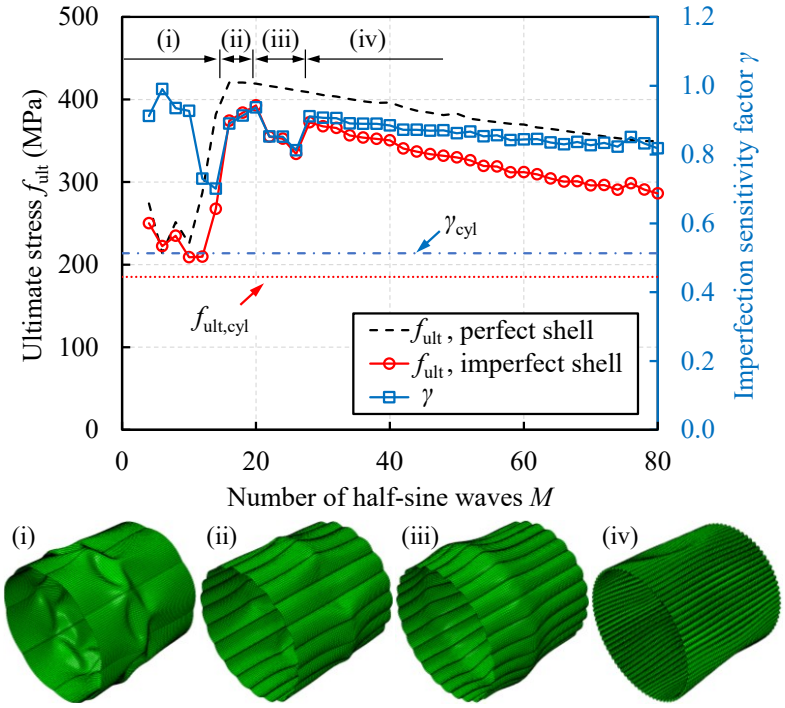

Figure 5.19: Ultimate stresses, imperfection sensitivity factors and typical failure modes of Aster shells

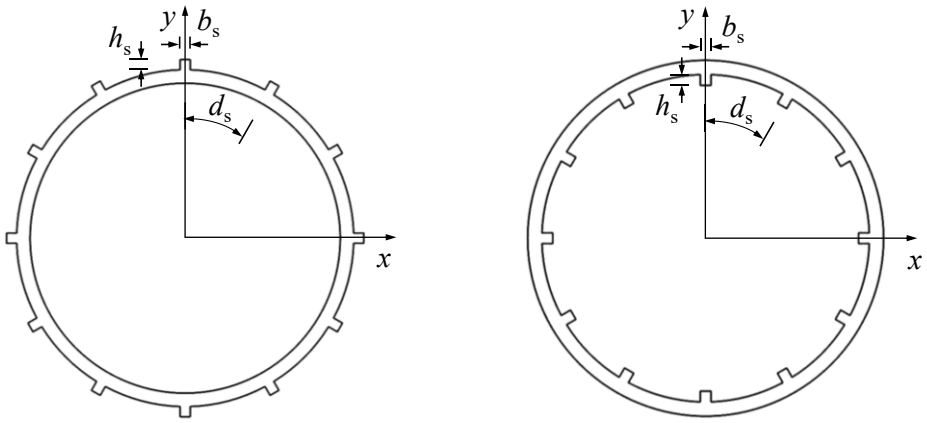

Figure 5.20: Cross-section profiles of (a) externally and (b) internally stringer-stiffened shells

5.5.3 Stringer-stiffened cylindrical shells

There are various means of stiffening circular cylindrical shells used today in the aerospace, marine, mechanical and construction industries, including stringers and rings, sandwich construction, corrugated reinforcement, material stiffening, 45°-waffle stiffeners and integrally machined stringers and rings (Teng & Rotter, 2004). Stringer-stiffened cylindrical shells have

been extensively tested in previous studies e.g. Singer, Arbocz & Babcock (1971) and Kenny (1992), showing high efficiency in increasing axial compressive resistance and reducing imperfection sensitivity. Stringer-stiffened cylindrical shells (externally or internally), as illustrated in Figure 5.20, were considered in this study for comparison purposes.

The examined externally or internally stringer-stiffened shells had stiffener numbers N_s ranging from 4 to 200 (i.e. the stiffener spacing $d_s=\pi D/N_s$), while the stiffener height h_s and width b_s were set equal to the maximum allowable deviation from the reference circle for the free-form wavy shells Δr (i.e. 4.5 mm) and the shell thickness t, respectively. All stringers were distributed uniformly around the circumference of the cylinders. In the FE models, the shell and stringers were modelled using the shell element S4R, and a tie constraint was adopted to connect the shell and stringers rigidly to each other. The normalised ultimate stresses $f_{ult}/\sigma_{0.2}$ and imperfection sensitivity factors γ of the externally and internally stringer-stiffened shells are plotted in Figures 5.21 and 5.22, where the values ($f_{ult,cyl}/\sigma_{0.2}$ and γ_{cyl}) of the reference circular cylindrical shell are also shown. Also presented are the change of failure mode and behaviour with increasing stiffener numbers.

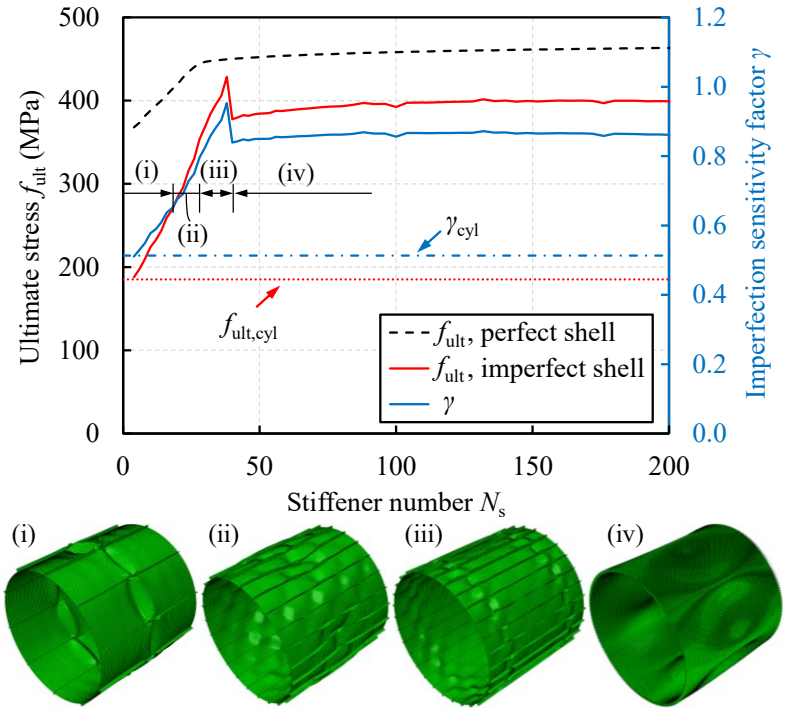

Figure 5.21: Ultimate stresses and imperfection sensitivity factors and typical failure modes of externally stringer-stiffened shells

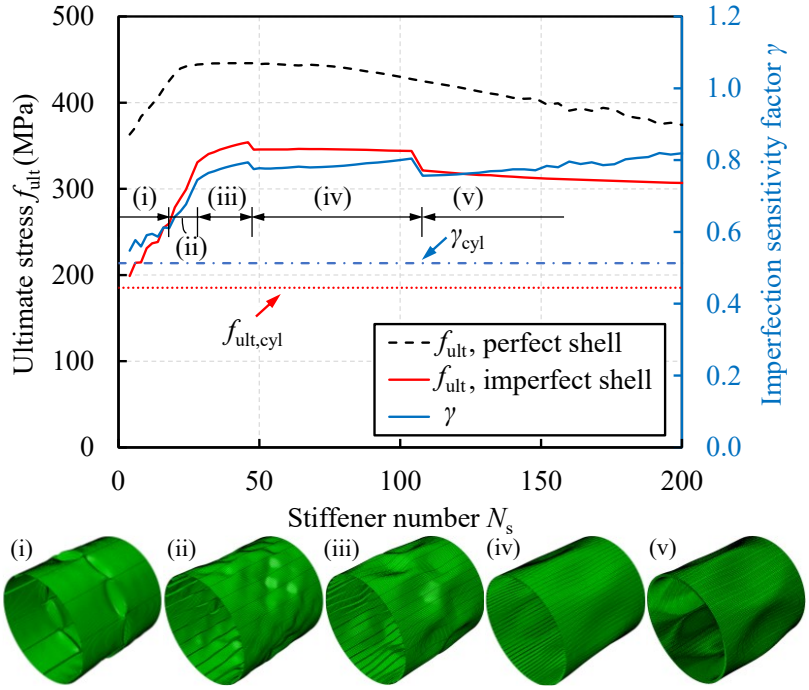

Figure 5.22: Normalised ultimate stresses, imperfection sensitivity factors and typical failure modes of internally stringer-stiffened shells

The externally stiffened shell with 38 circumferentially spaced stringers was shown to lead to the greatest increase in axial compressive resistance, and a reduced sensitivity to imperfections (γ=0.953). The internally stiffened shell with 46 stringers was found to be optimal with the greatest increase in buckling resistance relative to that of its reference circular cylindrical shell, but was more imperfection sensitive than the optimised externally stiffened shell. For lightly stiffened cylinders (N_s<30), the buckling behaviour was found to be similar for external and internal stiffening. Larger differences were observed for the more heavily stiffened cylinders, with external stringers leading to higher elastic critical stresses and higher buckling resistances; this behaviour has also been observed in some previous experimental studies (Houghton & Chan, 1960; Block, Card & Mikulas, 1965; Baruch & Singer, 1963). A brief explanation of this phenomenon is given as follows. Longitudinal and circumferential membrane forces are generated in the shell after buckling due to the stretching of mid-plane surface, and additional bending moments are created by this longitudinal membrane force about the local geometric centroid of the shell-stringer combination, which has a favourable effect on the buckling resistance of shells when the stringers are placed externally. Interested readers are referred to Singer, Baruch and Harari (1967) for further details on the influence of stringer positions on shell buckling.

5.5.4 Comparisons and discussion

The key results of the optimised wavy shell, the optimised alternative shells and their reference circular cylindrical shell with a diameter of 200 mm, a thickness of 0.7 mm, a length of 200 mm and an imperfection amplitude of $\frac{1}{25}\sqrt{rt}$, are summarised in Table 5.8. All the considered optimised shell designs were shown to lead to significantly increased ultimate stresses and reduced imperfection sensitivities relative to the reference circular cylindrical shell, as reflected by the $f_{ult}/f_{ult,cyl}$ and γ values in Table 5.8 respectively, but the optimised free-form wavy shell exhibited the best performance overall.

A direct assessment of the mass efficiency of the different shell designs under axial compression was conducted following the recommendations of Rahimi, Zandi and Rasouli (2013) and Malek, Ochsendorf and Wierzbicki (2011). The ultimate loads P_u normalised by the ultimate load of the optimised wavy shell $P_{u,wavy}$ are plotted against the weight W normalised by that of the optimised wavy shell $W_{u,wavy}$ with rotational symmetry and N=21, which exhibited the highest ultimate stress and the lowest imperfection sensitivity, as shown in Figure 5.23, where the points appearing on the top left indicate those shells with higher load-carrying capacities at a lower material use. The selected benchmark, i.e. the optimised wavy shell with rotational symmetry and 21 control points, was also shown to yield the highest mass efficiency, illustrated by all other data points falling below the dashed line in Figure 5.23. Future work could be dedicated to the optimisation of material use at a given cross-sectional resistance or the increase in the cross-sectional resistance of free-form wavy shells relative to the circular cylindrical shells with the same amount of material.

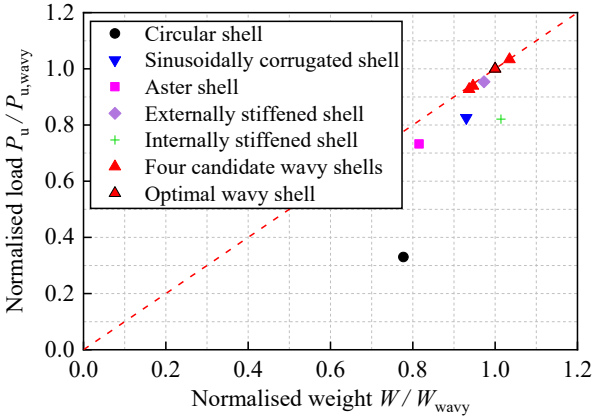

Figure 5.23: Comparisons of structural efficiency of all examined cylindrical shells under axial compression

5.6 Concluding remarks

An optimisation study into free-form wavy shells subjected to axial compression for additive manufacturing has been conducted. The employed optimisation method, combining Particle Swarm Optimisation (PSO) with cross-section profile generation and geometrically and materially nonlinear finite element analyses, aimed at maximising the ultimate stress of the shells, is described.

The optimised wavy shells were shown to have significantly improved load-carrying capacities and reduced imperfection sensitivities compared with their reference circular cylindrical shells. The increase in the ultimate stress was due mainly to the reduced local radius of curvature and the stiffening effect from the waviness. The influence of other geometric parameters, including the length and diameter-to-thickness ratio, was also investigated. The ultimate stress of the optimised wavy shell with L/D=2 was shown to be lower than that of its counterpart with L/D=1, which can be due primarily to a different failure mode associated with a longer axial half-wavelength allowed to develop in longer cylinders. The wavy shells with larger reference diameter-to-thickness ratios were shown to benefit to the greatest extent from the optimisation in terms of both the ultimate stress and the imperfection insensitivity.

Alternative designs, including sinusoidally corrugated shells, Aster shells and stringer-stiffened cylindrical shells, were also considered and compared with the optimised free-form wavy shells. The optimised wavy shell exhibited the highest load-carrying capacity, the lowest imperfection sensitivity and the highest mass efficiency, revealing great potential for structural applications. The optimised profiles of the free-form wavy shells and Aster shells obtained from the present study had been manufactured by powder bed fusion to enable the findings described herein and verified experimentally in Chapter 6.

Chapter 6

Testing and analysis of AM corrugated cylindrical shells in compression

6.1 Introduction

Optimised corrugated cylindrical shells are largely insensitive to imperfections and hence exhibit excellent load-bearing capacities, but their complex geometries make their construction difficult and costly using conventional manufacturing techniques; this can be overcome through additive manufacturing (AM). In this chapter, the structural performance, load-bearing resistance and imperfection sensitivity of nine optimised, additively manufactured corrugated cylindrical shells with different diameter-to-thickness ratios, along with one reference circular cylindrical shell, are examined experimentally. The test specimens were produced from stainless steel by powder bed fusion (PBF). Material coupon tests presented in Chapter 3, initial geometric measurements and compression tests are described; the results are used to verify the benefits derived from the optimised corrugated geometries. A parallel numerical study involved the validation of finite element models and the subsequent generation of additional resistance data through parametric studies. Finally, the applicability of existing design methods to the studied corrugated cross-sections produced by PBF, is evaluated. The work in this chapter has been reported by Zhang et al. (Submitted).

6.2 Overview of experimental programme

An experimental programme to investigate the cross-sectional behaviour of optimised corrugated cylindrical shells produced by PBF, comprised tensile coupon tests which are

described in Section 3.5, initial geometric measurements and compression tests. Two Aster shells and five free-form wavy shells with various diameter-to-thickness ratios, were manufactured by PBF using the 316L stainless steel powder. One Aster shell and one wavy shell, along with a reference circular cylindrical shell with a nominal outer diameter D of 200 mm and thickness of 1.0 mm, were produced by PBF using the CX stainless steel powder. The measured stress-strain curves are presented in Figures 3.18 and 3.19, and key material properties are reported in Tables 3.5 and 3.6. The shell specimens were manufactured in the Laboratory of Laser Processing of the School of Energy Systems at LUT University, while the compression tests were performed in the Structures Laboratory of the Department of Civil and Environmental Engineering at Imperial College London.

The corrugated cross-section profiles were established following the approach developed by Reitinger et al. (1994, 1995), with the mathematical programming techniques, sensitivity analysis and computer aided geometric design method integrated into the optimisation process. Typical examples of Aster and wavy cross-section profiles are shown in Figure 5.1 and Figure 5.18. Details of the employed optimisation method for Aster and wavy shells have been reported in Subsection 5.5.2 and Section 5.2; the cross-section profiles and optimisation results for the print shells are presented herein.

The nominal cross-section sizes (outer diameter D × thickness t) of the circular (C200×1.0), Aster (A200×1.0, A180×0.7 and A200×0.7) and wavy (W150×1.0, W180×1.0, W200×1.0, W150×0.7, W180×0.7 and W200×0.7) cylindrical shells, together with the involved optimisation parameters, are listed in Table 6.1, where D is the nominal outer diameter of the reference circular cylindrical shell, t is the nominal thickness, L is the nominal length, ω_a is the assumed imperfection amplitude, corresponding to Class B fabrication quality in EN 1993-1-6 (CEN, 2017) for the 316L stainless steel shells and to the thickness t for the CX stainless steel shells, Δr is the maximum allowable radial deviation from the reference circle, M is the number of half waves of the Aster cross-section and N is the number of control points lying on one quarter of the wavy cross-section profile, which is 4-fold rotationally or mirror symmetric to the profiles in other quadrants. The cross-section profiles of the final printed Aster and wavy shells are shown in Figures 6.2 and 6.3, where the control points lying on the wavy cross-section profile are highlighted, and the radial positions of the control points are provided in Table 6.2. The optimisation results of the examined Aster and wavy shells, coupled with the results of

their reference circular cylindrical shells, are summarised in Table 6.3, where l_p is centreline perimeter, σ_{cr} is the elastic local buckling stress, P_0, P_+ and P_- are the buckling loads of the perfect shells and imperfect shells with positive and negative imperfections, respectively, f_{ult} is the ultimate stress of the corrugated cylindrical shells (given by Equation 5.3), γ is the imperfection sensitivity factor that describes the sensitivity of the buckling load to the imperfection amplitude, given by Equation 5.7, and $f_{ult,cyl}$ is the ultimate stress of the reference circular cylindrical shell.

Table 6.1: Overview of the examined circular, Aster and wavy cylindrical shells, with nominal dimensions and parameters

Cross-section	Material	D (mm)	t (mm)	L (mm)	ω_a (mm)	Δr (mm)	M	Symmetry	N
C200×1.0	CX stainless steel	200	1.0	200	1.00	-	-	-	-
A200×1.0	CX stainless steel	200	1.0	200	1.00	11	18	-	-
A180×0.7	316L stainless steel	180	0.7	180	0.32	4.5	20	-	-
A200×0.7	316L stainless steel	200	0.7	200	0.33	4.5	20	-	-
W150×1.0	316L stainless steel	150	1.0	150	0.35	4.5	-	Rotational	21
W180×1.0	316L stainless steel	180	1.0	180	0.38	5.0	-	Rotational	21
W200×1.0	CX stainless steel	200	1.0	200	1.00	4.5	-	Mirror	16
W150×0.7	316L stainless steel	150	0.7	150	0.29	4.0	-	Rotational	21
W180×0.7	316L stainless steel	180	0.7	180	0.32	4.5	-	Rotational	21
W200×0.7	316L stainless steel	200	0.7	200	0.33	4.5	-	Rotational	16

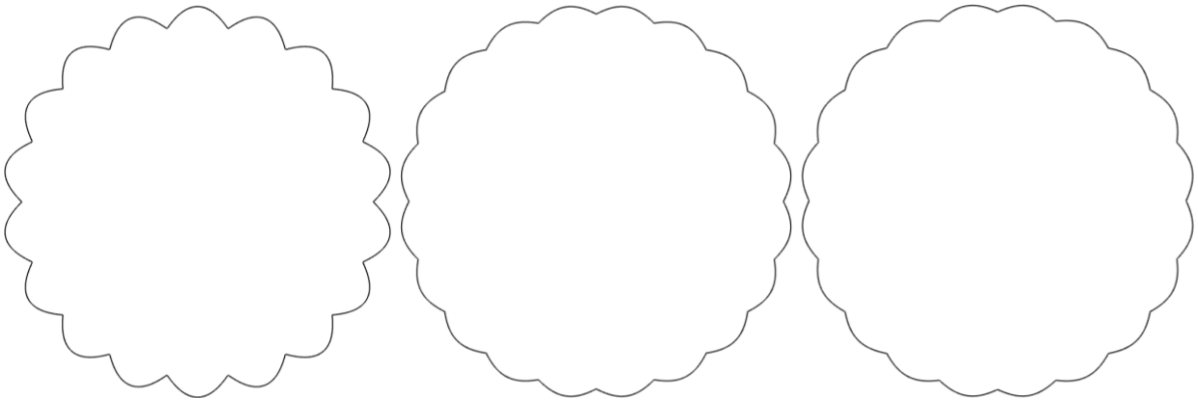

(a) (b) (c)

Figure 6.1: Cross-section profiles of printed Aster shells: (a) A200×1.0, (b) A180×0.7 and (c) A200×0.7

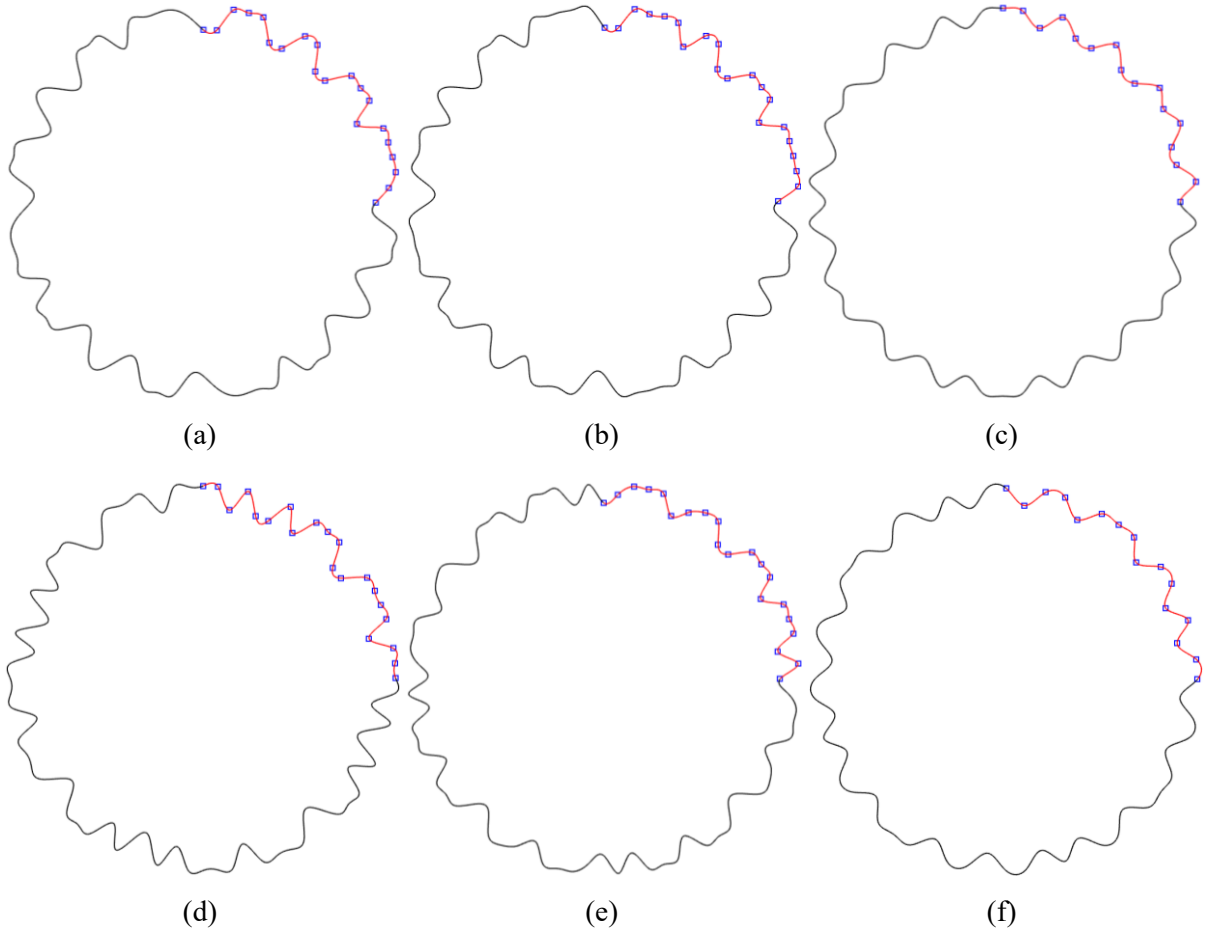

Figure 6.2: Cross-section profiles of printed wavy shells: (a) W150×1.0, (b) W180×1.0, (c) W200×1.0, (d) W150×0.7, (e) W180×0.7 and (f) W200×0.7

6.3 PBF manufacturing of test specimens

All shell specimens were built using a modified EOSINT M-series PBF research machine that can print components with a maximum size of approximately 400 mm×400 mm×400 mm. The PBF manufacturing process involves the layering of metallic powder that is fused by a high-energy laser beam to build the final components; a more detailed description of this process is provided in Chapter 3.3.1. The processing parameters set by the machine manufacturers are presented in Table 3.3. The shells were printed vertically, with their longitudinal axis perpendicular to the print layers (i.e. θ=90°, where θ is the angle between the longitudinal axis of the coupon and the build plate). Photographs of typical circular, Aster and wavy cylindrical shell specimens are shown in Figures 6.3 and 6.4. Figure 6.5 shows photographs of three shell specimens within the same batch during and after printing.

Table 6.2: Radial deviations of control points of wavy shell designs, ρ_i-r (mm)

Cross-section	1	2	3	4	5	6	7	8	9	10	11	12	13	14	15	16	17	18	19	20	21
W150×1.0	-4.50	1.02	4.50	4.50	4.50	4.50	-4.50	4.50	4.50	4.50	-4.50	-4.50	4.50	4.50	-4.50	-4.50	4.50	4.50	4.50	-4.50	4.50
W180×1.0	-5.00	5.00	5.00	5.00	5.00	5.00	-5.00	5.00	5.00	5.00	-5.00	-5.00	5.00	5.00	-5.00	4.50	5.00	4.06	5.00	-5.00	5.00
W200×1.0	-4.50	4.50	-4.50	-4.50	4.50	0.00	4.50	-4.50	-4.50	4.20	-4.50	-3.60	4.50	-4.50	3.30	4.20					
W150×0.7	4.35	4.35	4.35	-4.65	4.35	4.35	4.35	4.35	-4.65	-4.65	4.35	4.35	4.35	-4.65	4.35	-4.65	-4.65	4.35	-4.65	4.35	4.35
W180×0.7	-4.50	4.50	-4.50	4.50	4.50	4.50	-4.50	4.50	4.50	4.50	-4.50	-4.50	4.50	4.50	0.63	-4.50	4.50	4.47	4.50	-0.33	4.50
W200×0.7	4.50	4.50	-4.50	4.50	-4.50	4.50	4.50	-4.50	4.50	4.50	4.50	-4.50	4.50	4.50	-4.50	4.50					

Table 6.3: Optimisation results for wavy shells with various diameter-to-thickness ratios and their reference circular cylindrical shells

Cross-section	l_p (mm)	σ_{cr} (N/mm^2)	P_0 (kN)	min(P_+, P_-) (kN)	f_{ult} (N/mm^2)	γ	$\frac{f_{ult}}{\sigma_{0.2}}$	$\frac{f_{ult}}{f_{ult,cyl}}$
C150×1.0	468.1	1279.8	199.0	152.5	325.8	0.766	0.774	-
C180×1.0	562.3	1067.9	231.8	162.6	289.2	0.701	0.687	-
C200×1.0	625.2	1106.3	427.1	260.3	416.3	0.609	0.531	-
C150×0.7	469.0	895.0	130.1	81.7	248.8	0.628	0.591	-
C180×0.7	563.3	746.0	148.3	85.3	216.2	0.575	0.514	-
C200×0.7	626.1	672.2	158.8	80.5	183.7	0.507	0.436	-
A200×1.0	796.0	2283.4	613.5	606.5	761.9	0.989	0.972	1.831
A180×0.7	615.0	970.0	179.9	171.0	397.3	0.951	0.944	1.837
A200×0.7	674.7	861.6	192.9	180.7	382.5	0.937	0.909	2.085
W150×1.0	653.1	2247.4	298.2	296.9	454.7	0.996	1.080	1.395
W180×1.0	773.3	1048.1	350.2	346.3	447.9	0.989	1.064	1.549
W200×1.0	770.8	2220.8	596.0	575.0	746.0	0.965	0.952	1.793
W150×0.7	709.2	1520.4	224.0	217.9	438.9	0.973	1.042	1.763
W180×0.7	760.2	1531.9	236.3	235.2	442.0	0.995	1.050	2.043
W200×0.7	799.3	1182.2	246.5	244.3	436.7	0.991	1.037	2.378

Figure 6.3: Photograph of three types of PBF shell specimens (from left to right: circular, Aster and wavy)

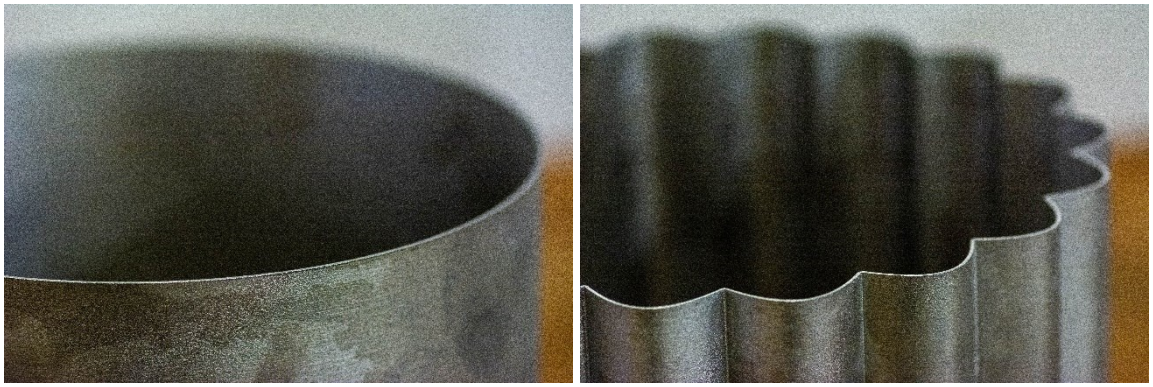

(a) (b)

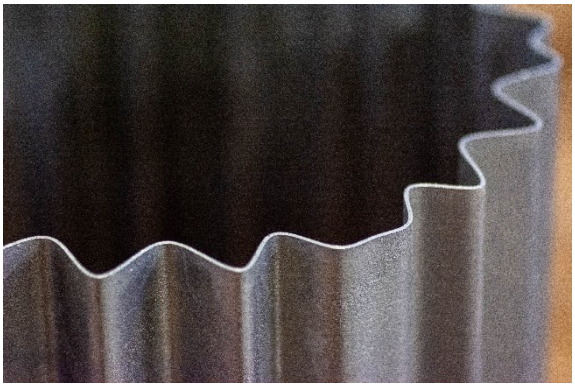

(c)

Figure 6.4: Close-up view of typical PBF (a) circular, (b) Aster and (c) wavy cylindrical shells

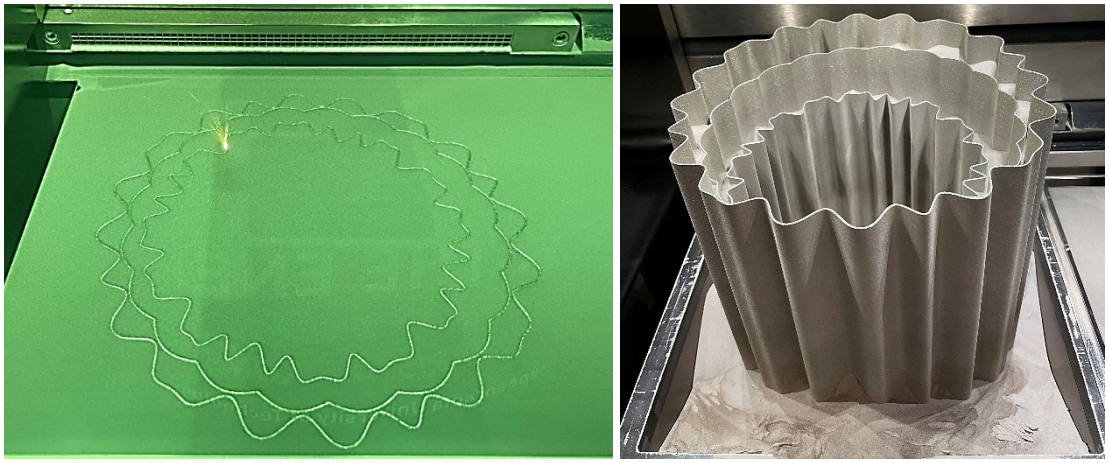

(a) (b)

Figure 6.5: Shell specimens (a) during and (b) after printing

6.4 Geometric properties

6.4.1 Geometric measurements

The geometric properties of the shell test specimens were determined before end potting through (i) hand measurements using digital callipers, (ii) Archimedes' method, which is useful for determining the volume of irregular objects, and (iii) laser scanning – an advanced 3D full-field measurement technique. The setups for the latter two measuring techniques are shown in Figure 6.6. The length L and wall thicknesses t (at both ends) at the peak, trough and middle points of each corrugation of the specimens were measured using callipers. The weights of each specimen in air W_{air} and in water W_{water} were measured using a high-precision balance, and the volume V_{Arch} and the density ρ were calculated based on Archimedes' method (see Equations 6.1 and 6.2, where ρ_{w} is the density of water, and g is the gravitational acceleration). An average density of 7.55×10^3 kg/m^3 and 7.54×10^3 kg/m^3 was obtained for the 316L and CX stainless steels based on the weight and volume measurement data, respectively.

$$V = \frac{W_{\text{air}} - W_{\text{water}}}{\rho_{\text{w}} g} \tag{6.1}$$

$$\rho = \frac{W_{\text{air}}}{gV} \tag{6.2}$$

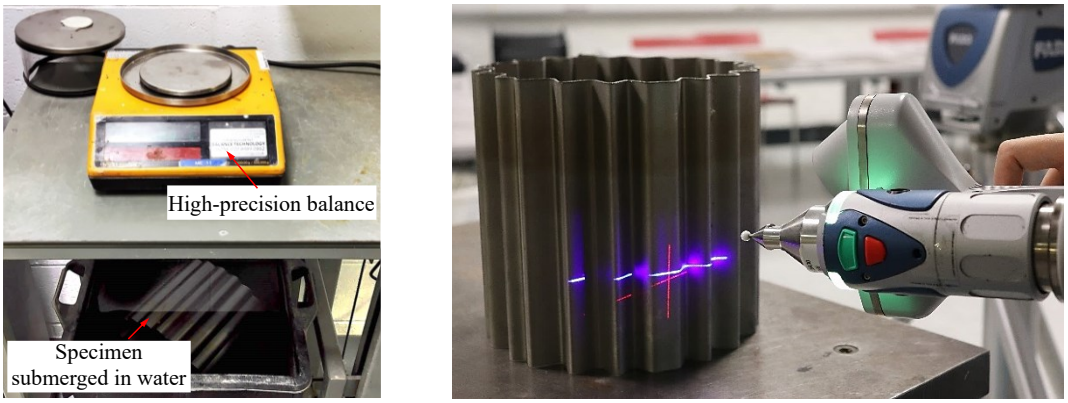

(a) (b)

Figure 6.6: Setup for geometric measurements: (a) Archimedes' method and (b) laser scanning

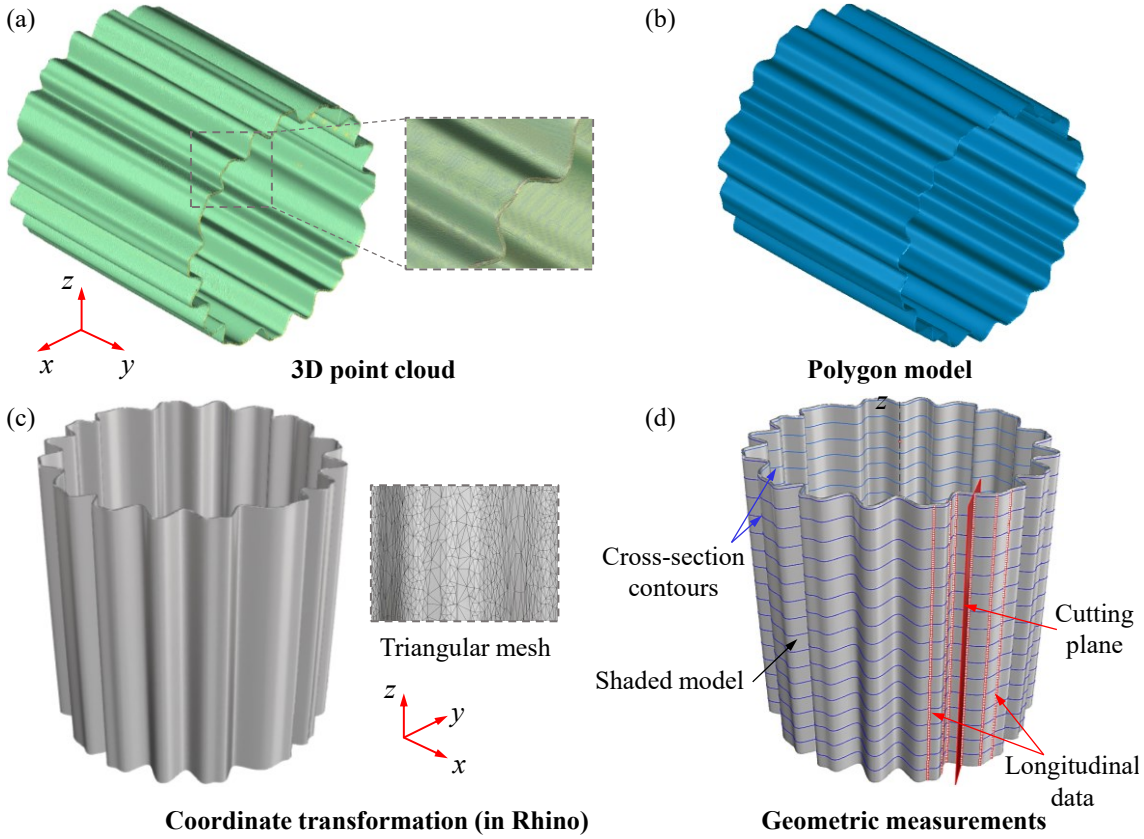

Figure 6.7: Schematic diagram of geometric measurements based on 3D laser-scanning: (a) 3D point cloud, (b) polygon model, (c) coordinate transformation and (d) extraction of cross-section profiles and longitudinal points

The volume V_{Laser}, cross-sectional area A_{Laser} and geometric imperfection distribution can also be determined through laser scanning. The outer and inner surfaces of the shell specimens were scanned using a Faro ScanARM laser scanner and pre-processed in Geomagic Wrap (3D

Systems, 2017); the workflow for processing the raw scanned geometric data from laser scanning is shown in Figure 6.7. The pre-processed 3D point data were saved as a polygon model and imported in Rhino 3D (Robert McNeel & Associates, 2012); the model was then aligned with the global coordinate system and contoured into cross-section slices along the specimen length. The average cross-sectional area A_{Laser} for each specimen was then determined, and compared with that obtained through Archimedes' method (i.e. the volume V_{Arch} divided by the specimen length L_{cal}), as shown in Table 6.4. Note that the accuracy of the cross-sectional areas obtained from laser scanning could not be guaranteed due to its difficulty in detecting the corner and edge features, i.e. the peaks and troughs of the shell corrugations (Zhang et al., 2021e); thus the measured cross-sectional areas obtained from Archimedes' method A_{Arch} are utilised for the following experimental and numerical analyses.

6.4.2 Imperfection analysis and results

Local imperfection measurements were made based on the geometry captured using 3D laser-scanning. First, a series of vertical planes were defined through the cross-section slices to provide sets of longitudinal points along the lengths of the shells. A straight line was fitted to each set of longitudinal points using linear regression, which served as a reference datum from which the deviations were determined, representing the local imperfections (Zhang et al., 2021c; Meng & Gardner, 2020c); a schematic for the determination of the longitudinal imperfections using laser scan data is shown in Figure 6.8. Typical measured imperfection distributions for the circular, Aster and wavy cylindrical shells (specimen C200×1.0, A200×1.0 and W200×0.7) are shown in Figures 6.9 to 6.11, where outward deviations are recorded as positive, and inward deviations are recorded as negative. The maximum deviation over the entire specimen was taken as the local imperfection amplitude ω_{max}, which lay between 0.14 mm and 0.73 mm (corresponding to $0.2t$~t), as reported in Table 6.4. An analysis of imperfection amplitude data associated with the slenderness or thickness of the shell specimens revealed no clear trend.

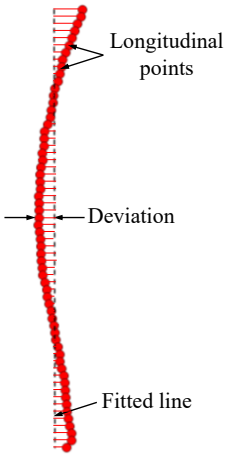

Figure 6.8: Schematic showing determination of longitudinal imperfection values

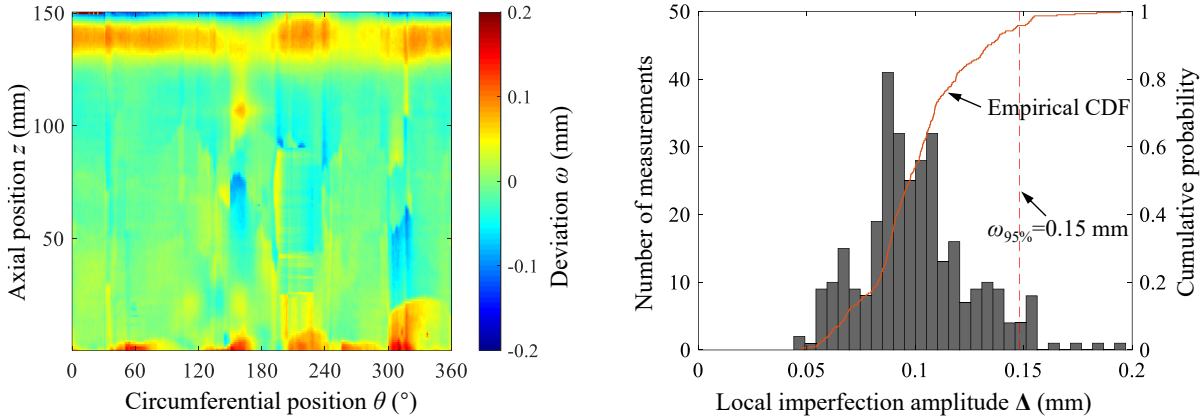

(a) (b)

Figure 6.9: (a) Measured imperfection distribution and (b) histogram and CDFs of longitudinal imperfections in the C200×1.0 circular cylindrical shell specimen

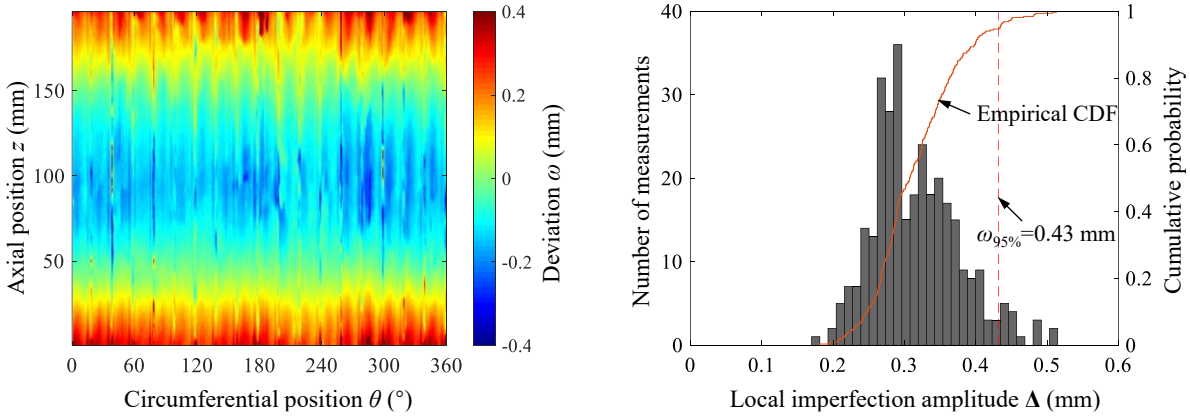

(a) (b)

Figure 6.10: (a) Measured imperfection distribution and (b) histogram and CDFs of longitudinal imperfections in the A200×1.0 Aster shell specimen

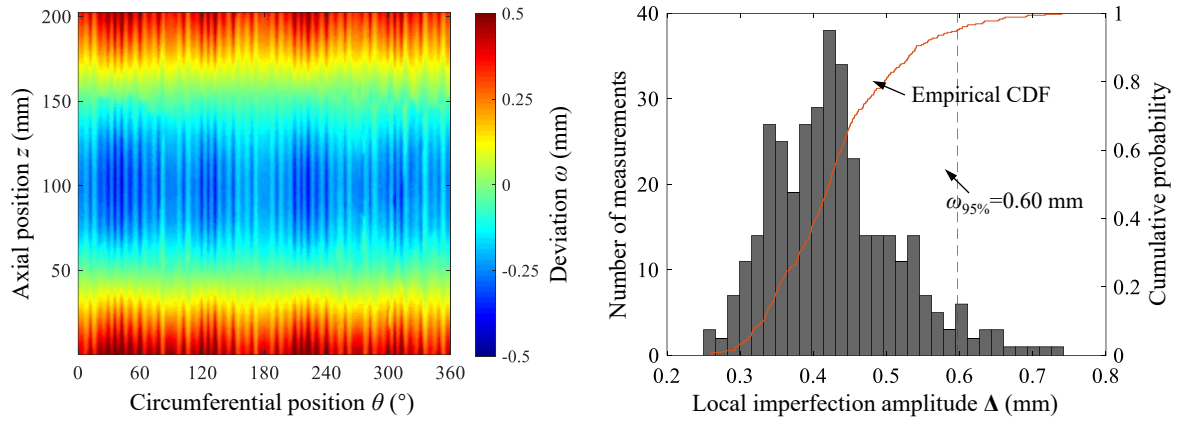

Figure 6.11: (a) Measured imperfection distribution and (b) histogram and CDFs of longitudinal imperfections in the W200×0.7 wavy shell specimen

Table 6.4: Measured geometric properties of the test shells and key test results

Specimen	V_{Arch} (mm^3)	V_{laser} (mm^3)	L_{cal} (mm)	A_{Arch} (mm^2)	A_{laser} (mm^2)	t_{cal} (mm)	ω_{max} (mm)	$\omega_{95\%}$ (mm)	N_u (kN)	δ_u (mm)	$N_u/\sigma_{0.2}A$	$\frac{f_{ult}}{f_{ult,cyl}}$
C200×1.0	93761	95542	152.7	614.0	625.7	1.02	0.19	0.15	366.4	0.57	0.76	-
A200×1.0	152227	154643	199.9	761.5	773.6	1.08	0.51	0.43	601.8	1.31	1.01	1.33
A180×0.7	83380	84782	189.6	439.8	447.2	0.72	0.20	0.13	164.5	0.68	0.86	-
A200×0.7	101073	102993	208.9	483.8	493.0	0.74	0.14	0.08	176.3	0.75	0.84	-
W150×1.0	107071	108452	159.9	669.6	678.2	1.03	0.52	0.37	298.8	1.04	1.03	-
W180×1.0	151174	151425	188.2	803.3	804.6	1.07	0.38	0.29	344.2	1.14	0.99	-
W200×1.0	167332	170572	199.8	837.5	853.7	1.06	0.53	0.30	726.8	1.62	1.11	1.46
W150×0.7	80792	82128	159.7	505.9	514.3	0.76	0.32	0.27	221.0	0.97	1.00	-
W180×0.7	99870	101310	189.5	527.0	534.6	0.75	0.41	0.27	220.5	0.98	0.96	-
W200×0.7	122267	124074	209.7	583.1	591.7	0.73	0.74	0.60	215.3	0.87	0.85	-

A probabilistic study was also carried out to examine the variation in longitudinal imperfection amplitudes around the circumference of the shell specimens. Histograms of local imperfection amplitudes from 360 measurements (at intervals of 1°) were constructed, and are shown for a typical circular, Aster and wavy cylindrical shell in Figures 6.9 to 6.11, respectively, along with the empirical cumulative distribution function (CDF) curves for the 360 measurements. A CDF value represents the probability that a set of randomly selected imperfection amplitude $\mathbf{\Delta}$ will be less than a given imperfection amplitude value ω_p, i.e. $P(\mathbf{\Delta} < \omega_p)$ (Schafer & Peköz, 1998; Schafer et al, 1996). Imperfection values for various probabilities along with the mean and standard deviation (std.) for each specimen are summarised in Table 6.5. Suitable imperfection amplitudes based on the CDF values can be utilised in finite element (FE) modelling, as recommended by Yu and Schafer (2004). The $P(\mathbf{\Delta}<\omega_p)$=95% imperfection value $\omega_{95\%}$ represents an imperfection amplitude that would not be expected to be exceeded in 95% of PBF

shell specimens; use of this imperfection amplitude is assessed in the FE model validation presented in Subsection 6.6.2. All dimensions and CDF values with corresponding imperfection amplitudes for the shell test specimens are summarised in Table 6.4.

Table 6.5: CDF values and corresponding characteristic imperfection amplitudes measured from shell specimens

$P(\Delta < \omega_p)$	ω_p (mm)									
	C200×1.0	A200×1.0	A180×0.7	A200×0.7	W150×1.0	W180×1.0	W200×1.0	W150×0.7	W180×0.7	W200×0.7
25%	0.09	0.27	0.04	0.04	0.15	0.15	0.14	0.16	0.16	0.37
50%	0.10	0.31	0.05	0.05	0.19	0.20	0.18	0.19	0.19	0.42
75%	0.11	0.35	0.07	0.06	0.23	0.23	0.23	0.22	0.22	0.47
95%	0.15	0.43	0.13	0.08	0.37	0.29	0.30	0.27	0.27	0.60
99%	0.17	0.48	0.18	0.11	0.45	0.33	0.33	0.30	0.30	0.66
Mean	0.10	0.32	0.06	0.05	0.21	0.19	0.19	0.19	0.19	0.43
Std.	0.02	0.06	0.03	0.02	0.08	0.06	0.07	0.04	0.05	0.09

6.5 Compression tests

6.5.1 Preparation of shell specimens

A total of ten axial compression tests were carried out to investigate the compressive response and load-bearing capacity of the circular, Aster and free-form wavy cylindrical shells manufactured by PBF. For each shell specimen, the printed (top) end had a high degree of manufacturing precision, while the lower end that was cut from the build plate had to be machined flat and square, removing any residual support structures, to facilitate uniform introduction of load during testing. Wooden blocks were precisely machined and inserted into the specimens to strengthen the clamped regions during end machining, as shown in Figure 6.12(a). An unexpected crack was observed near the end of the circular cylindrical shell C200×1.0; the end segment containing the crack was cut off and discarded, resulting in a final length of 152.7 mm, shorter than the original intended length of 200.0 mm. Prior to testing, the top and bottom ends of each specimen were confined using Araldite 2011 epoxy adhesive potting, supported by outer and inner metallic ring stiffeners with a thickness of 10 mm, in order to avoid premature end failure, as shown in Figure 6.12(b).

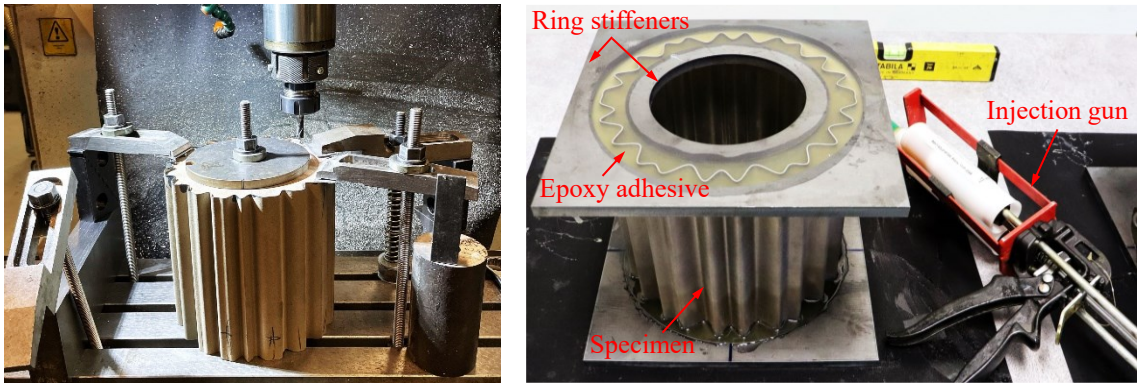

(a) (b)

Figure 6.12: Shell specimen preparation for testing: (a) end machining and (b) potting

6.5.2 Setup and data acquisition

All the tests were conducted using an Instron 3500 kN-SPL testing machine; the test setup is presented in Figure 6.13. A ball seating was placed between the crosshead of the testing machine and the top end platen to accommodate any potential gaps and to ensure that the axial loads were uniformly applied to the cylinder edges. Hardened end platens were placed at both ends of the specimens to prevent damage to the testing machine from the high localised stresses. Prior to testing, the surface of each specimen was painted white and sprayed with a random black speckle pattern with a minimum size of 3 to 5 pixels to create trackable features. A four-camera LaVision DIC system was adopted to track the relative movement of the speckles from two sides at 90° to each other, with two cameras monitoring each side; the DIC system layout is schematically shown in Figure 6.14. The axial deformations were measured using three potentiometers and three strain gauges affixed to the mid-height of each specimen at 120° intervals, as shown in Figure 6.13. The compressive load was applied under displacement control such that a compressive strain rate of 0.1% min^{-1} was achieved, and recorded using a load cell within the testing machine. The test outputs, including the axial load, top platen movement, potentiometer and strain gauge readings and DIC images were recorded at a frequency of 1 Hz. Post-test correlation and analysis were conducted on the captured DIC images using Davis 8 (LaVision, 2017) with a subset size of 19×19 pixels (to contain 4 to 10 speckles in each subset), a 5-pixel step size and a strain smoothing filter to obtain the surface deformation and strain fields of the specimens.

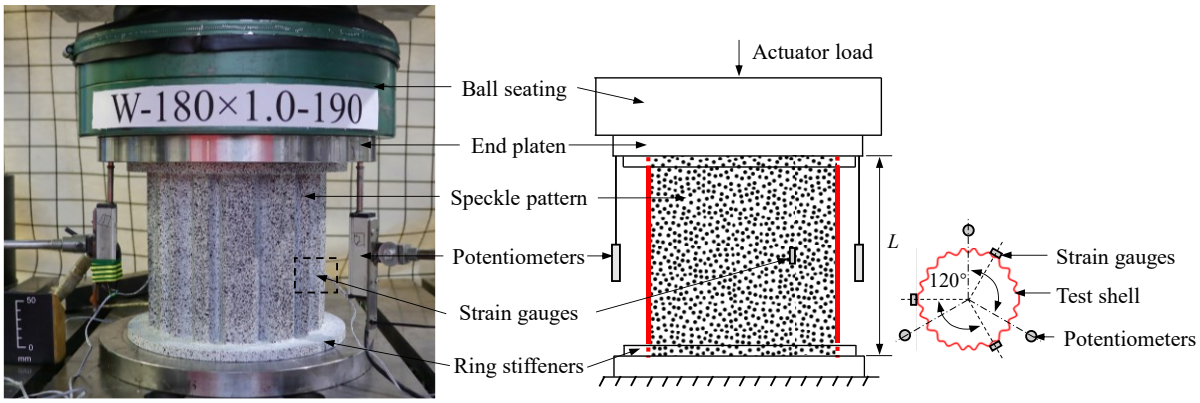

Figure 6.13: Experimental configuration for shell compression tests

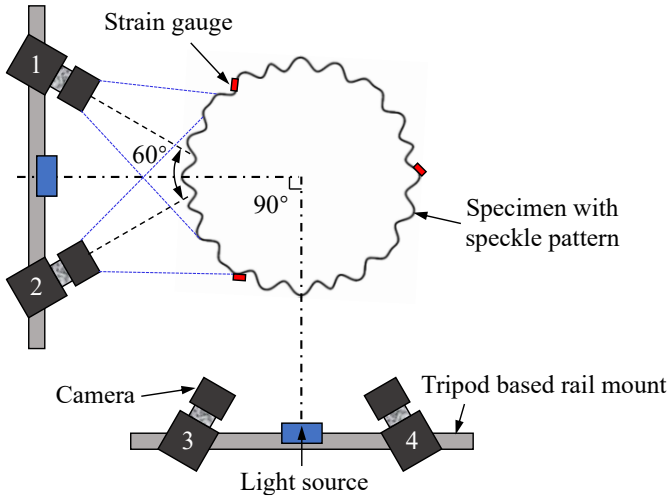

Figure 6.14: Plan view of DIC system layout

6.5.3 Results

The post-ultimate distributions of out-of-plane deformations of all test specimens are presented in Figures 6.15 to 6.17 for better visualisation of the failure modes, where positive deformations (coloured in red) are outward, while the negative deformations (coloured in purple) are inward. Note that the speckle images and processed displacements could have relatively large rotations or distortions in the non-overlapping regions, especially in the troughs and the two sides of the measured lateral surfaces, while the axial displacements derived from the central lateral face were found to have small stereo reconstruction errors and were thus adopted for the experimental data analysis, including the construction of the load-end shortening curves. The circular cylindrical shell (C200×1.0) failed by 'chequerboard' local buckling with one half longitudinal wave and 7 circumferential waves. The Aster shells deformed in an axisymmetric

mode with outward bulging; there were no visible local buckles observed near the peak load, but after testing, localised buckles were seen in the troughs of the corrugations, as shown in Figure 6.16. The free-form wavy shells also exhibited an axisymmetric deformation mode and failed by local buckling in the troughs of the corrugations and in the regions of minimum curvature (see Figure 6.17).

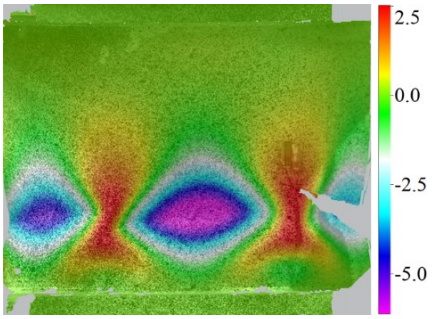

Figure 6.15: Post-ultimate out-of-plane deformations (unit: mm) of circular cylindrical shell C200×1.0

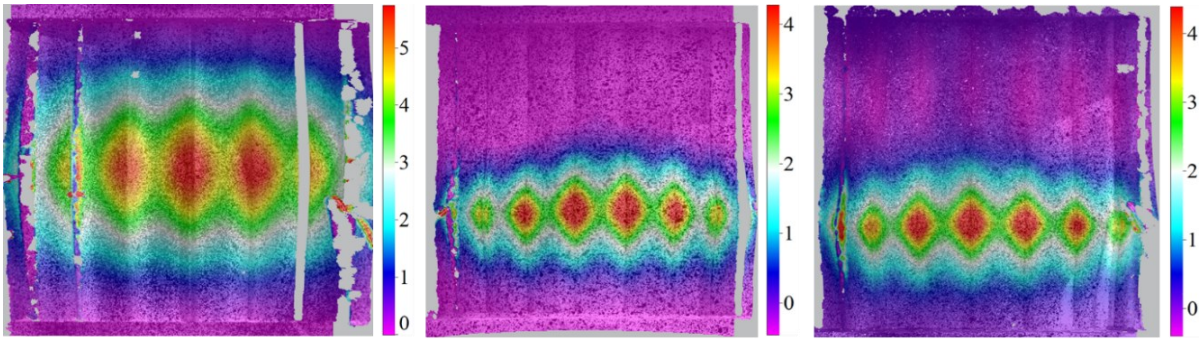

(a) A200×1.0 (b) A180×0.7 (c) A200×0.7

Figure 6.16: Post-ultimate out-of-plane deformations (unit: mm) of Aster shells (a) A200×1.0, (b) A180×0.7 and (c) A200×0.7

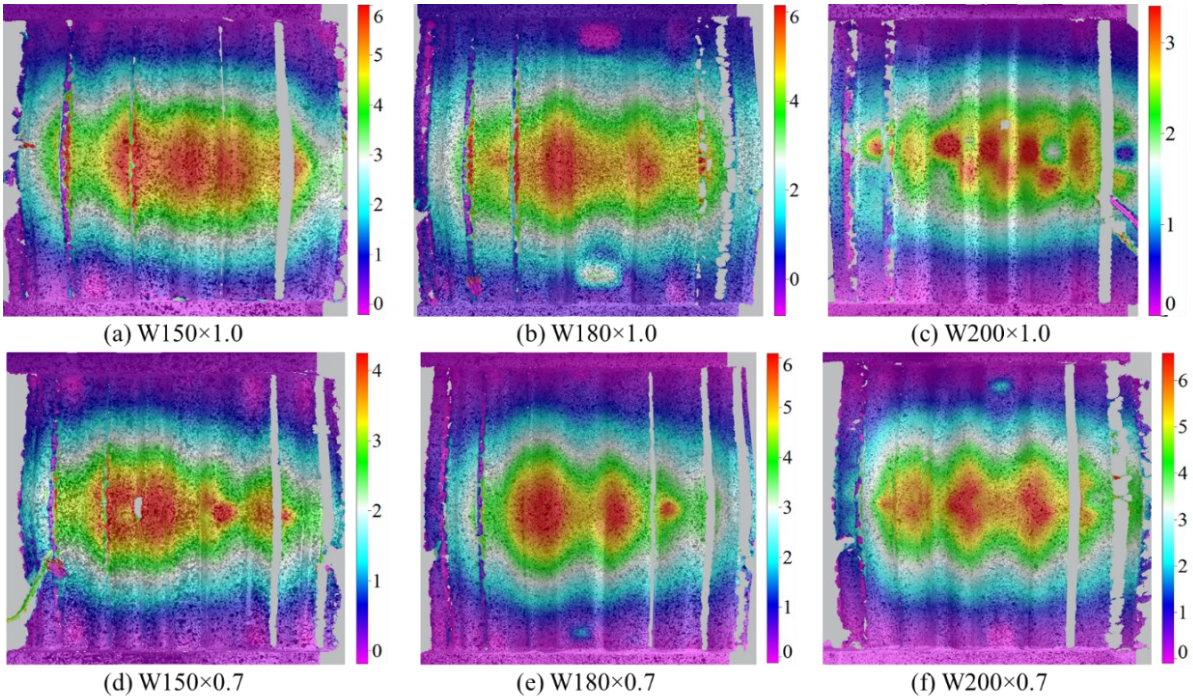

Figure 6.17: Post-ultimate out-of-plane deformations (unit: mm) of wavy shells (a) W150×1.0, (b) W180×1.0, (c) W200×1.0, (d) W150×0.7, (e) W180×0.7 and (f) W200×0.7

Typical axial load-end shortening curves and DIC results from the compression tests on the circular (C200×1.0), Aster (A200×1.0) and wavy (W200×1.0) cylindrical shells, are presented in Figures 6.18 to 6.20, where the evolution of the axial strain fields can be clearly seen. All axial load-end shortening curves obtained from (i) the potentiometer and strain gauge readings (LVDT+SG in Figure 6.21), with the elastic deformations of the end platens eliminated (Rasmussen, 1990), and (ii) the DIC data, are plotted in Figure 6.21. The two approaches to the calculation of end shortenings were shown to produce essentially identical results. The buckling of the circular cylindrical shell occurred abruptly, with an audible 'snap' and a sudden drop in the applied load; the shell stablished again at about half of the peak load. The Aster and free-form wavy shells, on the other hand, exhibited a more gentle failure. The key test outputs, including the peak load N_u, the end shortening at the peak load δ_u, the ratio between the peak load N_u and the plastic load $\sigma_{0.2}A$ (i.e. equivalent, in terms of stresses, to $f_{ult}/\sigma_{0.2}$), and the ratio of the normalised ultimate load of the Aster or wavy shells to that of the reference circular cylindrical shells expressed, in terms of stresses, as $f_{ult}/f_{ult,cyl}$, are reported in Table 6.4. All wavy shells, except the specimen W200×0.7, and the Aster shell with the largest wave amplitude failed at a load level around or beyond the plastic load $\sigma_{0.2}A$, while failure of the other Aster shells and all circular shells occurred below this load level. Regarding the shell specimens built

from CX stainless steel, the Aster and wavy shells had a 33% and 46% increase respectively in their failure stress over that of the circular cylindrical shell. This increase in failure stress is lower than the expected 180% value; this is attributed to the better-than-expected performance of the circular shell due to the measured imperfection amplitude being lower than the assumed value in the prediction (Zhang et al., 2021d).

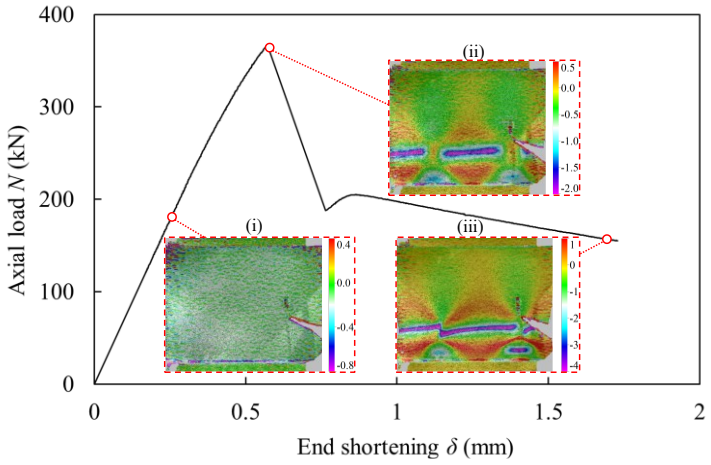

Figure 6.18: Typical axial load end-shortening curve and DIC results from compression tests (C200×1.0), showing axial strain distributions (unit: %) (i) at 0.5N_u, (ii) just after N_u and (iii) when unloading

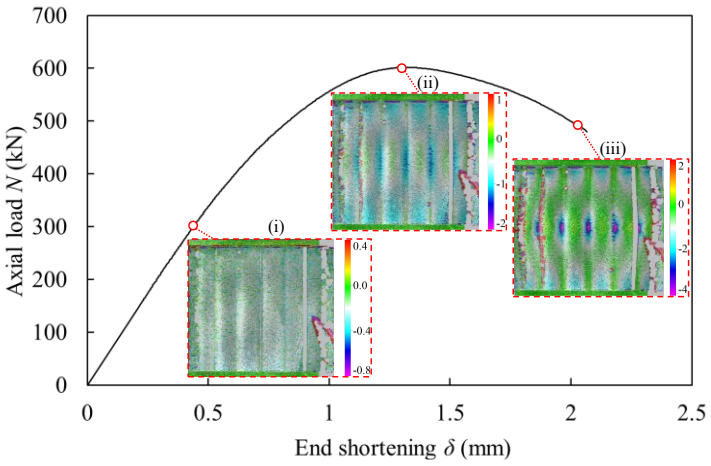

Figure 6.19: Typical axial load end-shortening curve and DIC results from compression tests (A200 ×1.0), showing axial strain distributions (unit: %) at (i) 0.5N_u, (ii) N_u and (iii) when unloading

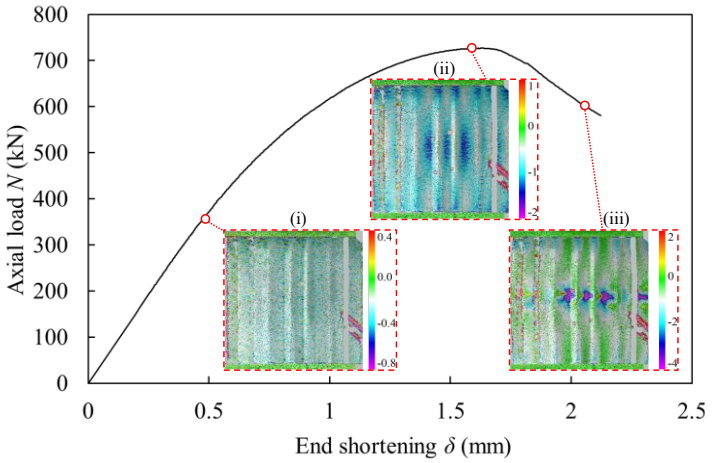

Figure 6.20: Typical axial load end-shortening curve and DIC results from compression tests (W200×1.0), showing axial strain distributions (unit: %) at (i) 0.5N_u, (ii) N_u and (iii) when unloading

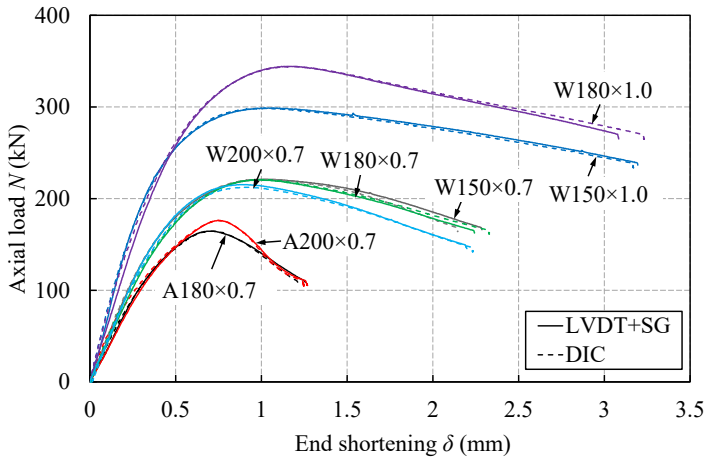

(a)

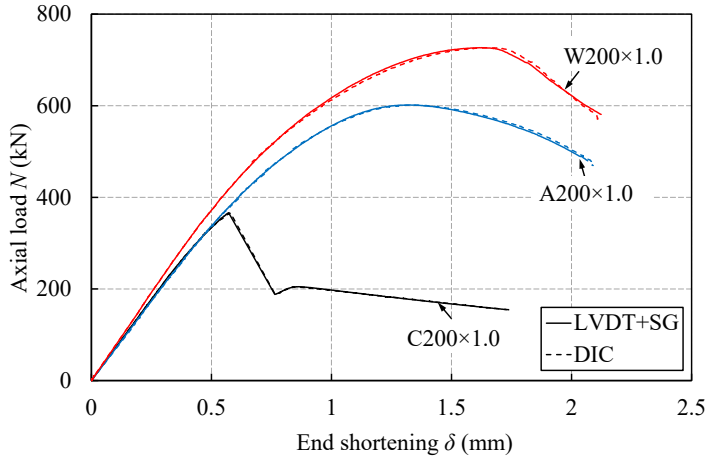

(b)

Figure 6.21: Measured axial load end-shortening curves of the tested (a) 316L and (b) CX stainless steel shells

6.6 Numerical modelling

In parallel with the experimental programme, a numerical simulation study of the compressive cross-sectional behaviour of corrugated cylindrical shells produced by PBF was undertaken. FE models based on the measured geometries and material properties were first developed and validated against the experimental results. Parametric studies were then conducted using the validated models to generate additional buckling reduction factors for corrugated cylindrical shells.

6.6.1 Description of FE models

Geometrically and materially nonlinear analyses without and with imperfections (GMNA, GMNIA) were carried out using the software package Abaqus (Dassault Systèmes, 2017) to simulate the cross-sectional behaviour of corrugated cylindrical shells under axial compression. The four-noded shell element with reduced integration, S4R, was adopted as the element type. A mesh size of $0.2(Dt)^{1/2}$, which was found to be sufficiently fine for capturing the local buckling behaviour of circular hollow sections with good computational efficiency (Zhang et al., 2021c; Meng & Gardner, 2020a; Meng et al., 2020), was utilised. The fixed-ended boundary conditions employed in the tests were simulated by coupling the end sections of the shells to reference points, where only longitudinal displacement of the top reference point was allowed, as shown in Figure 5.7. The adopted material stress-strain curves for the 316L and CX stainless steels were constructed from the two-stage Ramberg-Osgood parameters (E, $\sigma_{0.2}$, n, σ_u, ε_u, and m_u) averaged from the measured properties, as reported in Tables 3.5 and 3.6. The resulting stress-strain relationships were converted into true stress and plastic strain and inputted into the FE analyses.

Initial geometric imperfections were considered in two ways. In Method 1, imperfect shell models were reconstructed directly from the scan data points, while in Method 2, eigenmode-affine imperfection patterns, scaled by a measured imperfection value, were employed. For Method 1, the scan data were pre-processed in Geomagic Wrap (3D Systems, 2017) and imported in Rhino (Robert McNeel & Associates, 2012) in the form of a polygon model, which was contoured into transverse slices at a spacing of 1 mm and then radially sectioned into points at intervals of 1°. The data points were regenerated into an interpolated curve and then a smooth

surface was fitted; the generated Initial Graphics Exchange Specification (IGES) files were imported into Abaqus (Dassault Systèmes, 2017) as shell models and used in the GMNIA. For Method 2, the lowest eigenmode from a prior linear bifurcation analysis (LBA) was used to represent the local geometric imperfection pattern and was factored by measured imperfection amplitudes in the GMNIA.

6.6.2 Validation

The accuracy of the established FE shell models was evaluated by comparing the FE results with the key test outputs in terms of the ultimate loads, load-deformation histories and failure modes. Comparative studies were undertaken considering both measured and eigenmode-affine geometric imperfection shapes with different amplitudes. Four groups of FE analyses were carried out: (i) GMNA on the perfect shells, (ii) GMNIA on the scanned shell geometries, (iii) GMNIA on the shells with the LBA mode shape scaled by the measured $\omega_{95\%}$ and (iv) GMNIA on the shells with the LBA mode shape scaled by ω_{max}.

Table 6.6: Comparisons of test results with FE results for varying imperfections patterns and amplitudes

Specimen	$N_{u,FE}/N_{u,test}$				$\delta_{u,FE}/\delta_{u,test}$			
	GMNA	GMNIA			GMNA	GMNIA		
		Scanned geometries	LBA+$\omega_{95\%}$	LBA+ω_{max}		Scanned geometries	LBA+$\omega_{95\%}$	LBA+ω_{max}
C200×1.0	1.19	1.00	0.98	0.93	1.23	0.90	0.89	0.84
A200×1.0	1.09	0.98	1.08	1.08	0.99	0.89	1.13	1.13
A180×0.7	1.03	1.02	1.02	1.00	1.19	1.12	1.20	1.17
A200×0.7	1.05	1.01	1.03	1.00	1.21	1.00	1.10	1.07
W150×1.0	1.04	0.99	1.03	1.03	1.09	0.98	1.09	1.09
W180×1.0	1.02	0.99	1.01	1.01	1.12	1.06	1.13	1.13
W200×1.0	0.95	0.98	0.93	0.92	0.90	0.99	0.91	0.91
W150×0.7	1.00	0.99	1.00	1.00	1.06	1.03	1.05	1.05
W180×0.7	1.04	1.00	1.04	1.04	1.03	1.00	1.04	1.04
W200×0.7	1.07	1.00	1.06	1.06	1.18	1.05	1.19	1.19
Mean	1.05	1.00	1.02	1.01	1.10	1.00	1.07	1.06
COV	0.06	0.01	0.04	0.05	0.10	0.07	0.10	0.10

The ratios of the numerical to experimental ultimate loads $N_{u,FE}/N_{u,test}$ and corresponding deformations $\delta_{u,FE}/\delta_{u,test}$ for the four different local imperfection patterns and amplitudes, are reported in Table 6.6, where COV is the coefficient of variation. It can be seen from the comparisons that the use of the scanned geometries yields the most accurate on average and least scattered predictions of the ultimate loads and corresponding deformations. The numerical

load-deformation curves from the FE models with the scanned geometries are plotted in Figure 6.22; the developed FE models were found to accurately replicate the observed test responses. Note that the shell specimens made from the CX stainless steel were printed vertically (i.e. θ=90°), while the available material data were derived from the tensile tests on horizontally printed coupons (i.e. θ=0°); this can account for the slight deviations between the experimental and numerical load-deformation curves of the CX stainless steel shells. The local imperfection modelling technique that employed the lowest eigenmode pattern and the measured amplitude ω_{max} was also found to accurately predict the buckling response of the examined shells, as shown in the comparisons of typical failure modes (see Figure 6.23) and the load-deformation histories (see Figure 6.24) obtained using the lowest eigenmode pattern and the measured amplitude ω_{max}. The failure mode and buckling load of the specimen C200×1.0 were found to be not affected by the shortened length through numerical simulations.

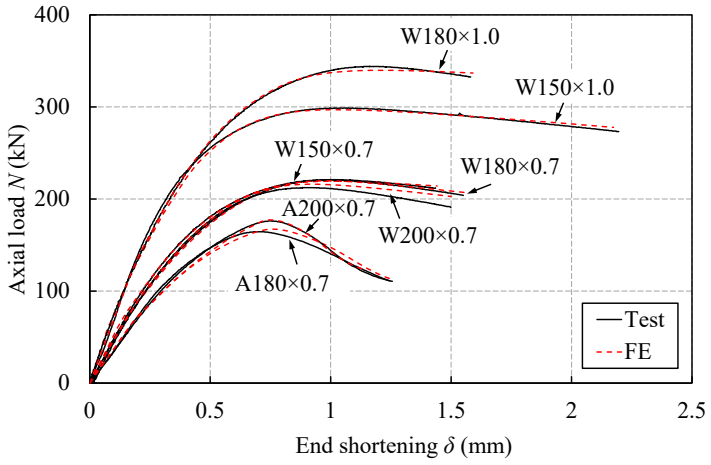

(a)

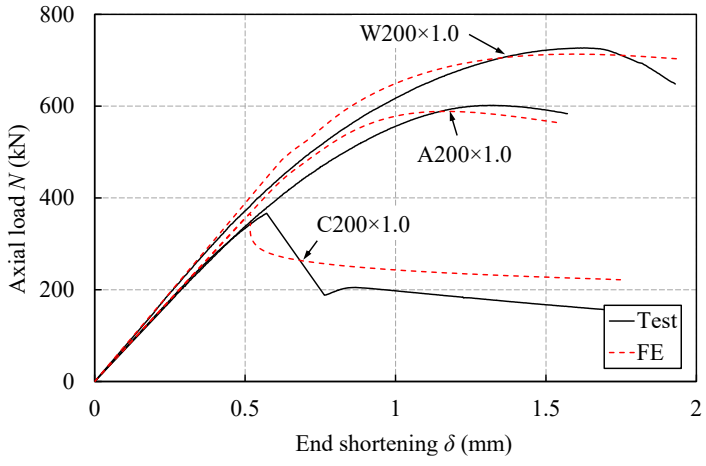

(b)

Figure 6.22: Experimental and numerical load-deformation curves of axially compressed shells made from (a) 316L and (b) CX stainless steels, with numerical data derived based on scanned geometries

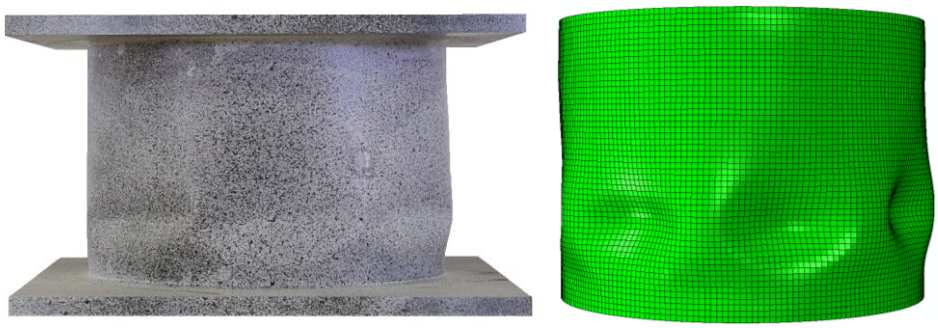

(a)

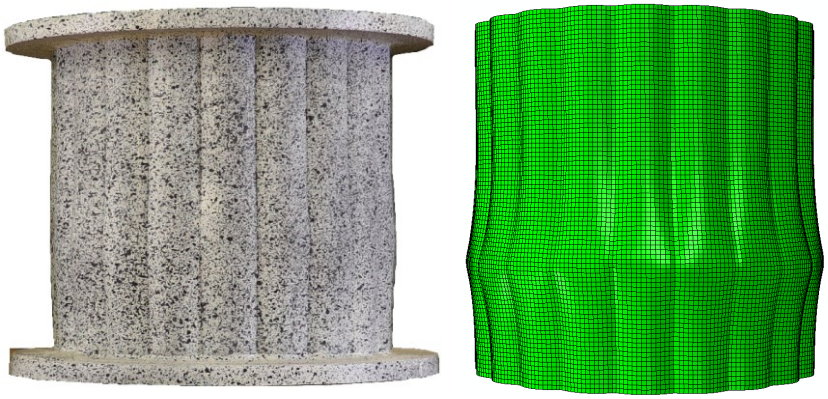

(b)

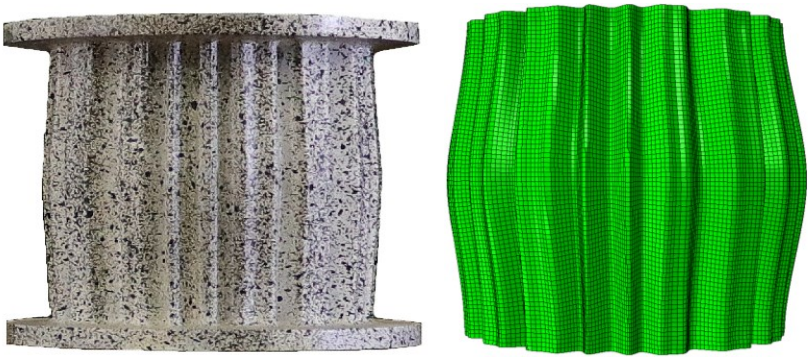

(c)

Figure 6.23: Typical experimental and numerical failure modes of (a) circular, (b) Aster and (c) free-form wavy cylindrical shells, with numerical results derived based on eigenmode-affine imperfections

As can be seen from Table 6.6, the load-carrying capacities of the Aster and wavy shell specimens were almost insensitive to imperfections, while the circular cylindrical shell C200×1.0 with the measured imperfection amplitude ω_{max} of only 0.19 mm exhibited an approximately 20% reduction in load-bearing capacity relative to the perfect shell. This dramatic difference in imperfection sensitivity can also explain the numerical ultimate loads and corresponding deformations obtained using ω_{max} and $\omega_{95\%}$ being quite close for all

corrugated shells, but not for the reference circular shell. Overall, it can be concluded that FE simulations featuring either direct modelling of imperfections (i.e. through the use of scan data) or using eigenmode shapes with measured imperfection amplitudes can accurately replicate the buckling behaviour of thin circular and corrugated cylindrical shells manufactured by PBF; the developed models are therefore considered to be suitable for use in parametric studies.

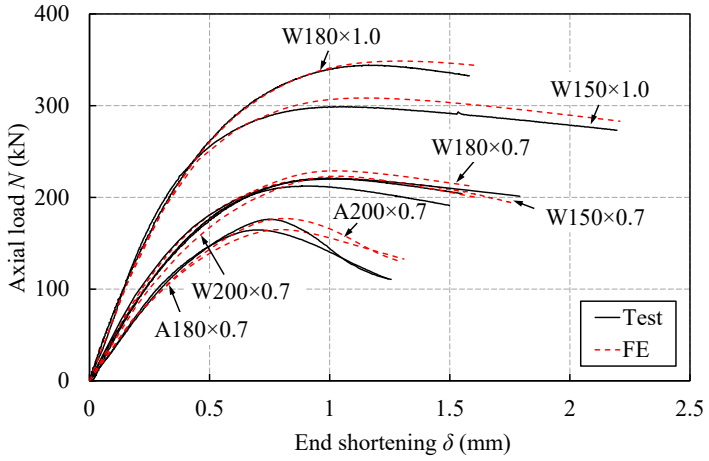

Figure 6.24: Comparisons of experimental load-deformation curves with the results from FE simulations using eigenmode-affine imperfections for 316L stainless steel shells

6.6.3 Parametric studies

Upon validation of the developed FE models, parametric studies were conducted to generate numerical data to cover a wider range of cross-sectional slendernesses, numbers of waves and amplitudes of corrugations, with a focus on the Aster shells. Class B imperfection amplitudes, determined according to EN 1993-1-6 (CEN, 2017) were assumed. Four shell slendernesses were considered, with diameter D × thickness t of A150×1.0, A180×1.0, A180×0.7 and A200×0.7. The number of half waves was varied between 4 and 30, while the wave amplitude was varied from 1 mm to 25 mm. The length of the modelled shells was set equal to the outer diameter of the reference circular cross-sections. In total, 2764 cross-sectional axial compression resistance results were generated in the numerical simulations. The numerical results are presented, and used together with the experimental data for the assessment of existing design methods in the following section.

6.7 Comparisons with existing design provisions

The applicability of existing structural design rules to the studied additively manufactured corrugated profiles, is appraised in this section. Emphasis is placed on the European design code for steel shell structures, EN 1993-1-6 (CEN, 2017), but comparisons are also made with the provisions of EN 1993-1-4 (CEN, 2015) and EN 1993-1-5 (CEN, 2014) for stainless steel and plated structures, respectively. The accuracy of the design rules is assessed through comparisons of the experimental and numerical ultimate loads with the predicted ultimate loads. In the comparisons, the measured (or modelled) material properties and geometries are used in the resistance calculations, and all partial factors for resistance are set to unity. A total of 10 experimental and 2764 numerical data points pertaining to axially compressed stainless steel corrugated cylindrical shells manufactured by PBF are considered.

6.7.1 Design provisions

For the design of stainless steel CHS with local slenderness values $D/t\varepsilon^2$ up to 250, EN 1993-1-4 (CEN, 2015) employs the concept of effective area A_{eff}, which can be expressed in terms of the buckling reduction factor χ through Equation 6.3.

$$\chi = \frac{A_{\text{eff}}}{A} \tag{6.3}$$

For more slender shells, reference is made to EN 1993-1-6 (CEN, 2017), which employs a generic three-stage capacity curve (see Figure 6.25) that relates the dimensionless buckling resistance χ (equal to R_k/R_{pl}) of a shell to its relative slenderness $\bar{\lambda}_c$ defined by Equation 6.4, where R_k is the characteristic buckling load factor, and R_{pl} and R_{cr} are the load factors at the plastic limit and the elastic critical buckling condition.

$$\bar{\lambda}_c = \sqrt{R_{pl} / R_{cr}} \tag{6.4}$$

The relative buckling strength χ, involving the hardening limit χ_h, the squash limit slenderness $\bar{\lambda}_0$, the elastic buckling reduction factor α, the plastic range factor β, the interaction exponent factor η and the plastic limit relative slenderness $\bar{\lambda}_p$, can be calculated from Equation 6.5.

$$\chi = \begin{cases} \chi_h - \bar{\lambda}_c / \bar{\lambda}_0 \left(\chi_h - 1\right) & \text{when } \bar{\lambda}_c \le \bar{\lambda}_0 \\ 1 - \beta \left(\dfrac{\bar{\lambda}_c - \bar{\lambda}_0}{\bar{\lambda}_p - \bar{\lambda}_0} \right)^{\eta} & \text{when } \bar{\lambda}_0 < \bar{\lambda}_c < \bar{\lambda}_p \\ \dfrac{\alpha}{\bar{\lambda}_c^{\,2}} & \text{when } \bar{\lambda}_p \le \bar{\lambda}_c \end{cases} \tag{6.5}$$

The capacity parameters for medium-length cylinders under uniform axial compression, as specified in EN 1993-1-6 (CEN, 2017), are summarised in Table 6.7, where $\Delta\omega_k = \frac{1}{Q}\sqrt{rt}$ is the characteristic imperfection amplitude, and Q is the fabrication quality parameter. The two reference resistances R_{pl} and R_{cr} would typically be determined by numerical analysis, i.e. materially nonlinear and linear bifurcation analyses (MNA and LBA) respectively. GMNIA results coupled with the experimental data were used to evaluate the EN 1993-1-6 design curve defined by the capacity parameters, as listed in Table 6.7.

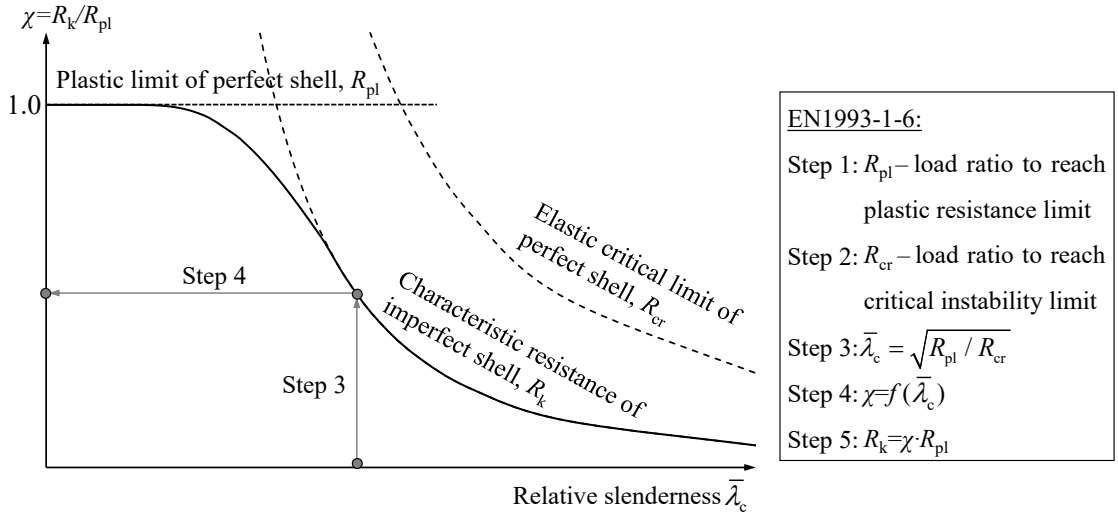

Figure 6.25: Basic concept and procedure for buckling design specified in EN 1993-1-6 (2017)

Table 6.7: Meridional buckling parameters for medium-length cylinders from EN 1993-1-6 (2017)

α	β	η	χ_h	$\bar{\lambda}_0$	$\bar{\lambda}_p$
$\dfrac{0.83}{1+2.2(\Delta\omega_k / t)^{0.88}}$	$1-\dfrac{0.95}{1+1.2(\Delta\omega_k / t)}$	$\dfrac{5.4}{1+4.6(\Delta\omega_k / t)}$	1.0	0.2	$\sqrt{\dfrac{\alpha}{1-\beta}}$

For steels with nonlinear stress-strain behaviour, an elastic-plastic representation that employs

a reduced value of the elastic modulus E_{red}, which can be conservatively taken as the secant modulus at the 0.2% proof stress E_{sec}, and the 0.2% proof stress $\sigma_{0.2}$ (see Figure 6.26), is recommended in EN 1993-1-6 (CEN, 2017). Direct comparisons are made between the strength reduction factors obtained from GMNIA (i.e. R_{GMNIA}/R_{pl}) for axially compressed circular cylindrical shells made from 316L stainless steel with various D/t ratios from 20 to 2726 and the design curves using the initial tangent modulus E_0 and the secant modulus at the 0.2% proof stress E_{sec} in Figure 6.27, where Class B levels of imperfection amplitudes have been applied. It can be seen that use of E_{sec} leads to over-conservative buckling resistance predictions for stainless steel circular cylindrical shells, while the straightforward use of the E_0 is unsafe for stainless steel circular cylindrical shells of medium slenderness. Comparisons are also made in the following subsection against the elastic buckling curve, given by Equation 6.6, and the strength curve for stainless steel internal plate elements provided in EN 1993-1-4 and given by Equation 6.7.

$$\chi = \frac{1}{\bar{\lambda}_c^{\,2}} \leq 1 \tag{6.6}$$

$$\rho = \frac{0.772}{\bar{\lambda}_c} - \frac{0.079}{\bar{\lambda}_c^{\,2}} \leq 1 \tag{6.7}$$

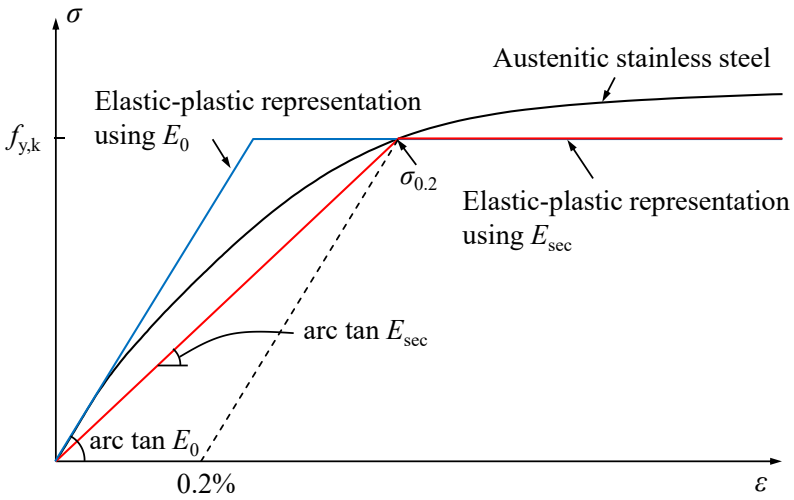

Figure 6.26: Schematic stress-strain relationship for austenitic stainless steel and elastic-plastic models, with the characteristic yield strength $f_{y,k}$ taken equal to the 0.2% proof strength

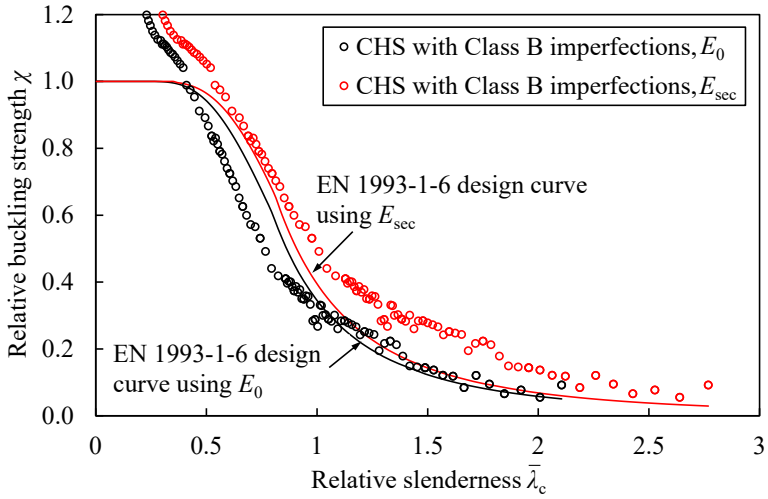

Figure 6.27: Strength reduction factors for circular hollow sections using initial tangent modulus E_0 and secant modulus at 0.2% proof stress E_{sec}

6.7.2 Assessment of resistance predictions

In this subsection, consideration is given to the design of the studied shells. The numerical results generated from the parametric studies on Aster shells, together with the experimental data on circular, Aster and wavy shells produced by PBF, are compared with the resistance predictions obtained from existing design provisions, principally those set out in EN 1993-1-6 (CEN, 2017). The experimental ultimate loads for the circular (shown by solid circles), Aster (shown by solid squares) and wavy cylindrical shells (shown by solid triangles) and numerical ultimate loads for the Aster shells (shown by hollow squares) and their reference circular cylindrical shells (shown by hollow circles), normalised by the corresponding plastic loads, are plotted against their cross-sectional slendernesses in Figure 6.28. In Figure 6.28(a), the initial tangent modulus E_0 is employed, while in Figure 6.28(b), the secant modulus at 0.2% proof stress E_{sec} is used. The plastic loads of the stainless steel shells were taken equal to $\sigma_{0.2}A$, while the elastic critical loads were determined using LBA. The elastic buckling and the EN 1993-1-4 (CEN, 2015) plate buckling curves are also presented in Figure 6.28.

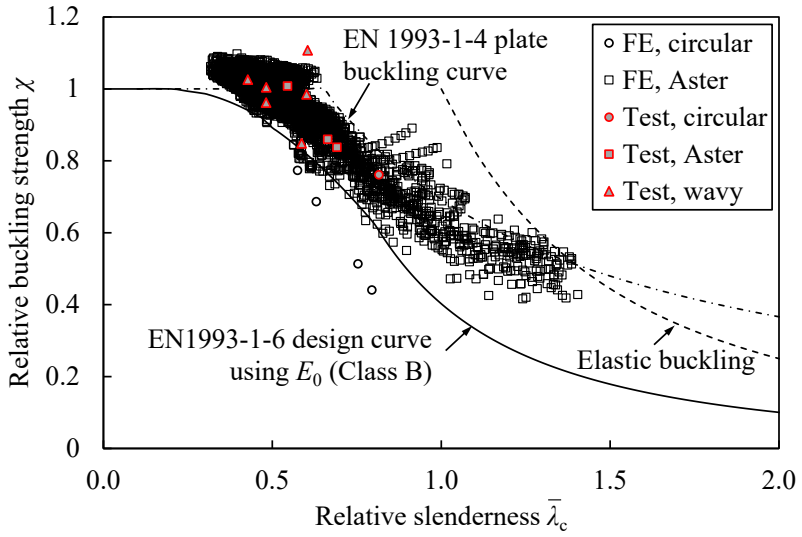

(a)

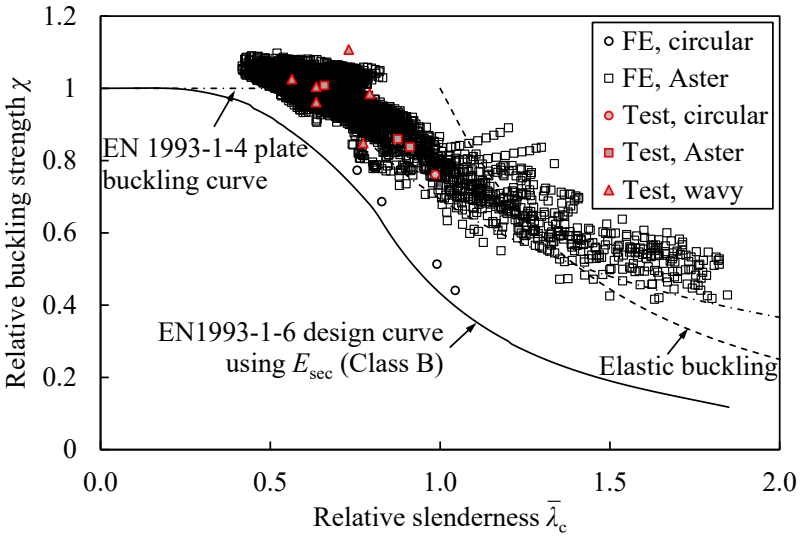

(b)

Figure 6.28: Comparison of experimental and numerical buckling resistance with EN 1993-1-6 resistance predictions using (a) initial tangent modulus and (b) secant modulus at 0.2% proof stress

The relative buckling strength is a function of the relative slenderness associated with the radius-to-thickness ratio of the reference circular cross-section r/t; the EN 1993-1-6 design curve shown in both Figure 6.28 (a) and Figure 6.28 (b), which was averaged from the studied Aster shells with four radius-to-thickness ratios r/t, was employed in the comparisons. It can be confirmed that the compressive resistance predictions using E_0 and E_{sec} generally lie on the safe side for the Aster shells with various amplitudes and numbers of corrugations, with the use of E_0 indicating less conservative predictions even in the medium slenderness range where the EN 1993-1-6 design rules using E_0 yield unsafe resistance predictions for circular cylindrical shells

(see Figure 6.27). The relative local buckling strengths obtained from GMNIA and the physical experiments using E_0 are higher than those of the circular cylindrical shells but still fall short of the EN 1993-1-4 plate buckling strength curve. It is anticipated that more optimised Aster shells tend towards more plate-like buckling behaviour, as represented by the plate buckling strength curve. The improved buckling response of corrugated cylindrical shells may be ascribed to the reduced radius of curvature. Note that the test ultimate load of the circular cylindrical shell is overestimated by the design provisions using E_0 with $N_{u,test}/N_{u,pred}$=0.96 similar to other cylindrical shells of medium slenderness; the overestimation is not presented in Figure 6.28 since this shell test specimen was made from CX stainless steel and did not lie on the Class B level of imperfection amplitudes, both of which will lead to a design curve different from the average design curve for the numerically studied Aster shells.

The ratios of the experimental and numerical ultimate loads N_u to the EN 1993-1-6 (CEN, 2017) resistance predictions (denoted by $N_u/N_{u,EC3}$), which employ both the tangent modulus E_0 and secant modulus E_{sec}, are reported in Table 6.8. A value of $N_u/N_{u,EC3}$ greater than unity indicates a reasonably safe prediction for buckling resistance. It can be seen that EN 1993-1-6 (CEN, 2017) generally provide safe-sided predictions for the buckling resistances of the stainless steel corrugated cylindrical shells produced by PBF, with the use of the initial tangent modulus E_0 revealed less conservative resistance predictions than the secant modulus at the 0.2% proof stress E_{sec}. Overall, it can be concluded that the design provisions of EN 1993-1-6 can be applied to Aster shells produced by PBF in the case of axial compression.

Table 6.8: Comparisons of experimental and numerical buckling resistances with EN 1993-1-6 resistance predictions for corrugated shells in compression

Evaluation parameter	Test data			FE data		
	No. of results	$N_u/N_{u,EC3}$		No. of results	$N_u/N_{u,EC3}$	
		E_0	E_{sec}		E_0	E_{sec}
Mean	10	1.14	1.44	2764	1.20	1.59
COV		0.11	0.15		0.21	0.39

6.8 Concluding remarks

This paper presents an experimental and numerical study into the structural behaviour of stainless steel circular and corrugated cylindrical shells subjected to axial compression. One

circular, three Aster and six wavy cylindrical shells were additively manufactured by powder bed fusion (PBF) using 316L and CX stainless steel powders. 3D laser-scanning and digital image correlation (DIC) techniques were employed to capture the geometries and deformation fields of the test specimens, respectively. The test setup, test procedure and key test results of the compression tests are fully described. The circular cylindrical shell buckled in a chequerboard pattern with a sudden drop in the applied load. The corrugated cylindrical shells exhibited axisymmetric deformation modes and failed by local buckling in the troughs of the corrugations, with substantially higher failure stresses than their reference circular cylindrical shells.

Following the experimental programme, shell FE models were established, validated against the test results and then employed in subsequent parametric studies to expand the current experimental database; a total of 2764 numerical cross-sectional resistance data over a wide range of diameter-to-thickness ratios, amplitudes and numbers of corrugations were generated for Aster shells. Finally, the combined set of experimental and numerical data was utilised to assess the applicability of existing design provisions, particularly those given in EN 1993-1-6 for shell structures, to the design of the examined corrugated cross-sections produced by PBF. Overall, the EN 1993-1-6 design rules are shown to provide safe-sided buckling resistance predictions for stainless steel PBF manufactured corrugated cross-sections.

Chapter 7

Conclusions and suggestions for future work

A comprehensive study into the behaviour and shape optimisation of additively manufactured stainless steel structural hollow sections has been presented in this thesis. This chapter summarises the key output and findings from the current study, with more detailed concluding comments included at the end of each individual chapter, and provides insight into the areas for future research.

7.1 Conclusions

Additive manufacturing (AM) is receiving growing considerable attention in the construction sector due to its ability to produce complex functional parts, but a wider adoption requires greater knowledge of their structural performance. The primary objective of this study has therefore been to investigate the material and cross-sectional behaviour of additively manufactured stainless steel structural hollow sections, as well as joining techniques.

An introduction to the additive manufacturing techniques and the use of stainless steel in construction, with key points including the main manufacturing process, applications and current research associated with metal additive manufacturing, and microstructure, mechanical properties and material models for stainless steels, was first presented. A review of the common mechanical joining methods available to use for small-scale additively manufactured metallic parts and the microstructure and mechanical properties in the joints, was then provided. Following this, previous experimental investigations into the cross-sectional behaviour of thick-walled stainless steel circular hollow sections and thin-walled cylindrical shells were reviewed, and the existing design provisions and innovative shell forms against buckling were described, with the available optimisation methods for cylindrical shells being finally introduced in the

literature review chapter.

Chapter 3 described a series of laboratory experiments conducted on additively manufactured 316L and CX stainless steels to investigate the material stress-strain response and to relate the mechanical characteristics to the underlying microstructure. The mechanical properties of 316L stainless steel with laser welded joints were also determined and analysed at the microstructural level. A series of microstructural tests and a total of 45 tensile coupon tests on 316L and CX stainless steels, of which 33 316L tensile coupons featured laser welds in the middle, were performed. The mechanical properties of additively manufactured stainless steels were compared to those of conventionally manufactured counterparts, and the weldability of the additively manufactured 316L stainless steel was evaluated.

Chapter 4 introduced an experimental and numerical programme, aimed at investigating the cross-sectional behaviour of additively manufactured stainless steel circular hollow sections (CHS) under axial compression. A total of five stainless steel CHS stub columns, spanning from Class 1 to 4 according to the slenderness limits specified in EN 1993-1-4 (CEN, 2015), were tested. Local geometric imperfections were measured using 3D laser-scanning and the evolution of deformations and strains was monitored using digital image correlation that allowed the measurements of strains and displacements over the entire monitored surface rather than only at discrete locations. Numerical models of the test specimens were produced, and parametric studies were undertaken for generating additional cross-sectional resistance data over a wide range of slenderness values. The combined set of experimental and numerical data was utilised for evaluating the applicability of existing design methods to stainless steel circular hollow sections manufactured by powder bed fusion (PBF).

Chapter 5 presented an optimisation study into free-form wavy shells under axial compression for additive manufacturing, with the aim of enhancing load-bearing capacity and reducing sensitivity to geometric imperfections. The employed shape optimisation method combined computer-aided geometric design and geometrically and materially nonlinear numerical simulations with the Particle Swarm Optimisation (PSO) algorithm. The structural performance of the optimised free-form wavy shells was analysed and compared to that of reference circular cylindrical shells, as well as other types of non-circular cylindrical shell profiles, including sinusoidally corrugated shells, Aster shells and stringer-stiffened shells. The optimised free-

form wavy shell profiles were shown to exhibit significantly improved cross-sectional resistance and reduced imperfection sensitivity; the increased load-bearing capacity was due primarily to the stiffening effect from the waviness. Other geometric parameters, including the length and diameter-to-thickness ratio, were also examined; in general, greater benefits can be achieved for more slender cylinders.

Chapter 6 reported an experimental and numerical investigation conducted on the additively manufactured corrugated cylindrical shells with various diameter-to-thickness ratios that had been optimised in Chapter 5, as well as the reference circular cylindrical shells. Initial geometric measurements and compression tests were carried out on the additively manufactured circular and corrugated cylindrical shells to investigate their structural response and to verify the benefits derived from the optimised corrugated geometries. A parallel numerical study involved the validation of finite element models against the observed buckling behaviour of the PBF circular and corrugated cylindrical shells using measured geometric and material properties and a parametric study for generating additional resistance data. The applicability of existing design methods for slender cross-sections to additively manufactured corrugated cross-sections, was evaluated.

Overall, the objectives of this study were to gain insight into the structural performance of additively manufactured stainless steel structural hollow sections at the microstructural, material and cross-section level, to capture the benefits of additive manufacturing for producing structural elements with complex geometries obtained from optimisation and to promote more widespread use of metal additive manufacturing in construction.

7.2 Suggestions for future work

Based on the present study, further work could fall into four main categories: microstructural characterisation and mechanical testing on AM materials, hybrid additive manufacturing, testing and analysis of additively manufactured structural elements and optimisation of novel structures.

7.2.1 Microstructural characterisation and mechanical testing

Most metals that can be cast or welded, in theory, are suitable for PBF processes, and it is expected that the applicability of AM processes will be extended for more metals with improved manufacturability and service properties, particularly for functionally graded metals and hybrid materials. The anisotropy and heterogeneity of the microstructure and mechanical properties induced by complex cyclic thermal histories, may occur in metal AM parts, which necessitate relevant research to be conducted on the microstructure and mechanical properties, including tensile, compressive, impact, fatigue characteristics, etc. of novel AM materials.

7.2.2 Hybrid additive manufacturing

One of the technical challenges that hinders the wider adoption of the PBF technique in industrial applications relates to its limited capacity to produce large parts. Laser welding with a suitable welding power and speed was found to be efficient for joining small PBF parts in the present study; microstructural observations, hardness tests and material coupon tests monitored by digital image correlation were conducted to develop a more in-depth understanding of the laser-welded joints. Future work could be dedicated to the feasibility of the combinations of both additive with other manufacturing processes and dissimilar metals using the same testing approaches employed in this study.

7.2.3 Testing and analysis of AM structural elements

CHS stub columns produced by PBF were tested and analysed in the case of axial compression; for completeness, it is advisable to examine other types of regular sections (such as rectangular hollow sections, elliptical hollow sections, I-sections, angles and channels) produced by PBF or other metal additive manufacturing techniques under pure compression, pure bending and combined compression and bending at both the local and member level.

The buckling response of thin-walled stainless steel cylindrical shells produced by PBF was mainly investigated when loaded in compression because the imperfection sensitivity for axially compressed cylinders is higher than cylinders in other loading cases. The current EN 1993-1-6 buckling design rules employ a reduced value of Young's modulus to cover materials that display plastic strains below the 0.2% proof stress, leading to rather conservative designs,

especially for shells at both low and high slendernesses. Testing and design of stainless steel cylindrical shells under different loading scenarios, such as external pressure, bending or combined loading conditions, could be conducted in the future.

7.2.4 Optimisation of novel structures

The optimisation study and corresponding physical experiments in this thesis have demonstrated the significant benefits of free-form wavy cross-sections obtained from shape optimisation. A further recommendation is to extend this optimisation method to other novel structural elements, such as stiffened plates or shells with stiffeners in different profiles and positions, lattice structures, non-prismatic and streamlined structures and symmetry-breaking material distributions for additive manufacturing. The Particle Swarm Optimisation algorithm employed in this study could be combined with a gradient-based algorithm for future hybrid shape and size optimisation to get robust and globally optimal designs for various objective functions and constraints.

References

3D Systems, Inc. (2017) *Geomagic Wrap 2017* [Computer software].

Abdelwahab, M.M. & Tsavdaridis, K.D. (2019) Optimised 3D-Printed Metallic Node-Connections for Reticulated Structures. In: Lam, D., Dai, X., Yang, T, & Zhou, K. (eds.) *Proceedings of the 9th International Conference on Steel and Aluminium Structures*, *ICSAS19*, 3–5 July 2019, Bradford, United Kingdom.

Abdelwahab, M.M. & Tsavdaridis, K.D. (2020) Application of Topology Optimisation to Steel Node-Connections and Additive Manufacturing. In: Meboldt, M. & Klahn, C. (eds.) *Industrializing Additive Manufacturing*, *AMPA 2020*. Springer, Cham.

Abdulhameed, O., Al-Ahmari, A., Ameen, W. & Mian, S.H. (2019) Additive manufacturing: Challenges, trends, and applications. *Advances in Mechanical Engineering*. 11 (2), 1–27.

Afshan, S. & Gardner, L. (2013a) Experimental study of cold-formed ferritic stainless steel hollow sections. *Journal of Structural Engineering*. 139 (5), 717–728.

Afshan, S. & Gardner, L. (2013b) The continuous strength method for structural stainless steel design. *Thin-Walled Structures*. 68, 42–49.

AISC (2013) *Design guide 27: Structural Stainless Steel*. Chicago, IL, American Institute of Steel Construction (AISC).

Alghamdi, A., Downing, D., Tino, R., Almalki, A., Maconachie, T., Lozanovski, B., Brandt, M., Qian, M. & Leary, M. (2021) Buckling phenomena in AM lattice strut elements: A design tool applied to Ti-6Al-4V LB-PBF. *Materials and Design*. 208, 109892.

Alsalla, H.H., Smith, C. & Hao, L. (2018) Effect of build orientation on the surface quality, microstructure and mechanical properties of selective laser melting 316L stainless steel. *Rapid Prototyping Journal*. 24 (1), 9–17.

Araar, M., Derbali, M. & Jullien, J.F. (1998) Buckling of the multi-vaulted “Aster” shell under axial compression alone or combined with an external pressure. *Structural Engineering and Mechanics*. 6 (7), 827–839.

Arbocz, J. & Babcock, C.D. (1968) *Experimental investigation of the effect of general imperfections on the buckling of cylindrical shells*. National Aeronautics and Space Administration (NASA). Report number: NASA CR–1163.

Arrayago, I., Real, E. & Gardner, L. (2015) Description of stress–strain curves for stainless steel alloys. *Materials and Design*. 87, 540–552.

Asgari, H. & Mohammadi, M. (2018) Microstructure and mechanical properties of stainless steel CX manufactured by Direct Metal Laser Sintering. *Materials Science and Engineering: A*. 709, 82–89.

Askeland, D.R. & Wright, W.J. (2017) *Essentials of Materials Science and Engineering*. 4th edition. Boston, Cengage Learning, Inc.

ASTM (2012) ASTM E3 – 01. *Standard Guide for Preparation of Metallographic Specimens Standard Guide for Preparation of Metallographic Specimens*. West Conshohocken, PA, ASTM International (ASTM).

ASTM (2015) ASTM E407-07:2015. *Standard Practice for Microetching Metals and Alloys*. West Conshohocken, PA, ASTM International (ASTM).

ASTM (2019) ASTM A473-15. *Standard Specification for Stainless Steel Forgings*. West Conshohocken, PA, ASTM International (ASTM).

Bachmann, F., Hielscher, R. & Schaeben, H. (2010) Texture analysis with MTEX–free and open source software toolbox. *Solid State Phenomena*. 160, 63-68.

Bahshwan, M., Myant, C.W., Reddyhoff, T. & Pham, M.S. (2020) The role of microstructure on wear mechanisms and anisotropy of additively manufactured 316L stainless steel in dry sliding. *Materials and Design*. 196, 109076.

Bardi, F.C., Kyriakides, S. & Yun, H.D. (2006) Plastic buckling of circular tubes under axial

compression-part II: Analysis. *International Journal of Mechanical Sciences*. 48 (8), 842–854.

Barnes, E.R. (1977) The shape of the strongest column and some related extremal eigenvalue problems. *Quarterly of Applied Mathematics*. 2, 393–409.

Baruch, M. & Singer, J. (1963) Effect of eccentricity of stiffeners on the general instability of stiffened cylindrical shells under hydrostatic pressure. *Journal of Mechanical Engineering Science*. 5 (1), 23–27.

Bellini, C., Borrelli, R., Di Cocco, V., Franchitti, S., Iacoviello, F. & Sorrentino, L. (2021) Bending properties of titanium lattice structures produced by electron beam melting process. *Fatigue and Fracture of Engineering Materials and Structures*. 44 (7), 1961–1970.

Bhavar, V., Kattire, P., Thakare, S., Patil, S. & Singh, R.K.P. (2017) A Review on Functionally Gradient Materials (FGMs) and Their Applications. In: *2nd International Conference on Advanced Materials Research and Manufacturing Technologies*, *AMRMT 2017*, 2–5 August 2017, Phuket, Thailand.

Block, D.L., Card, M.F. & Mikulas, M.M. (1965) *Buckling of eccentrically stiffened orthotropic cylinders*. National Aeronautics and Space Administration (NASA). Report number: NASA TN D-2960.

Bobbio, L.D., Otis, R.A., Borgonia, J.P., Dillon, R.P., Shapiro, A.A., Liu, Z.K. & Beese, A.M. (2017) Additive manufacturing of a functionally graded material from Ti-6Al-4V to Invar: Experimental characterization and thermodynamic calculations. *Acta Materialia*. 127, 133–142.

Bock, M., Gardner, L. & Real, E. (2015) Material and local buckling response of ferritic stainless steel sections. *Thin-Walled Structures*. 89, 131–141.

Botkin, M.E. (1982) Shape optimization of plate and shell structures. *AIAA Journal*. 20 (2), 268–273.

Botkin, M.E. & Bennett, J.A. (1985) Shape optimization of three-dimensional folded-plate structures. *AIAA Journal*. 23 (11), 1804–1810.

Boyce, B.L., Reu, P.L. & Robino, C. V. (2006) The Constitutive Behavior of Laser Welds in 304L Stainless Steel Determined by Digital Image Correlation. *Metallurgical and Materials Transactions A*. 37, 2481–2492.

Braibant, V. & Fleury, C. (1984) Shape optimal design using B-splines. *Computer Methods in Applied Mechanics and Engineering*. 44 (3), 247–267.

Bruker (2018) *Quantax Esprit 2.2* [Computer software].

Brush, D.O. & Almroth, B.O. (1975) *Buckling of bars, plates, and shells*. McGraw-Hill, Inc., United States.

Bu, Y. & Gardner, L. (2019) Laser-welded stainless steel I-section beam-columns: Testing, simulation and design. *Engineering Structures*. 179, 23–36.

Buchanan, C. & Gardner, L. (2019) Metal 3D printing in construction: A review of methods, research, applications, opportunities and challenges. *Engineering Structures*. 180, 332–348.

Buchanan, C., Gardner, L. & Liew, A. (2016) The continuous strength method for the design of circular hollow sections. *Journal of Constructional Steel Research*. 118, 207–216.

Buchanan, C., Matilainen, V.P., Salminen, A. & Gardner, L. (2017) Structural performance of additive manufactured metallic material and cross-sections. *Journal of Constructional Steel Research*. 136, 35–48.

Buchanan, C., Real, E. & Gardner, L. (2018) Testing, simulation and design of cold-formed stainless steel CHS columns. *Thin-Walled Structures*. 130, 297–312.

Buchanan, C., Wan, W. & Gardner, L. (2018) Testing of wire and arc additively manufactured stainless steel material and cross-sections. In: Chan S.L., Chan, T.K. & Zhu S. (eds.) *Proceedings of the 9th International Conference on Advances in Steel Structures*, *ICASS 2018*, 5–7 December 2018, Hong Kong, China.

Burgan, B.A., Baddoo, N.R. & Gilsenan, K.A. (2000) Structural design of stainless steel members — comparison between Eurocode 3, Part 1.4 and test results. *Journal of Constructional Steel Research*. 54 (1), 51–73.

Calignano, F. (2014) Design optimization of supports for overhanging structures in aluminum and titanium alloys by selective laser melting. *Materials and Design*. 64, 203–213.

Campanelli, S.L., Casalino, G., Contuzzi, N., Angelastro, A. & Ludovico, A.D. (2014) Analysis of the molten/solidified zone in selective laser melted parts. In: *Proceedings of High-Power Laser Materials Processing: Lasers, Beam Delivery, Diagnostics, and Applications III*. 20 February 2014, California, United States.

Casalino, G., Campanelli, S.L. & Ludovico, A.D. (2013) Laser-arc hybrid welding of wrought to selective laser molten stainless steel. *International Journal of Advanced Manufacturing Technology*. 68 (1–4), 209–216.

Casati, R., Lemke, J. & Vedani, M. (2016) Microstructure and Fracture Behavior of 316L Austenitic Stainless Steel Produced by Selective Laser Melting. *Journal of Materials Science & Technology*. 32 (8), 738–744.

CEN (2018) EN ISO 6507-1:2018. *Metallic materials - Vickers hardness test - Part 1: Test method*. Brussels, European Committee for Standardization (CEN).

CEN (2014) EN 1993-1-5:2006. *Eurocode 3 - Design of steel structures - Part 1-5 : Plated structural elements*. Brussels, European Committee for Standardization (CEN).

CEN (2017) EN 1993-1-6: 2007+A1:2017. *Eurocode 3 - Design of steel structures, Part 1-6: Strength and Stability of Shell Structures*. Brussels, European Committee for Standardization (CEN).

CEN (2015) EN 1993-1-4: 2006+A1:2015. *Eurocode 3-Design of steel structures. Part 1-4: General rules-Supplementary rules for stainless steels*. Brussels, European Committee for Standardization (CEN).

CEN (2016) EN ISO 6892-1:2016. *Metallic materials — Tensile testing. Metallic materials — Tensile testing Part 1 : Method of test at room temperature*. Brussels, European Committee for Standardization (CEN).

Rasmussen, K. J. R. (1990) *Compression Tests of Stainless Steel Tubular Columns*. Centre for Advanced Structural Engineering. Report number: S770.

Chan, T. M., Gardner, L. & Law, K.H. (2010) Structural design of elliptical hollow sections: a review. *Proceedings of the Institution of Civil Engineers - Structures and Buildings*. 163 (6), 391–402.

Chen, Q., Liu, J., Liang, X. & To, A.C. (2020) A level-set based continuous scanning path optimization method for reducing residual stress and deformation in metal additive manufacturing. *Computer Methods in Applied Mechanics and Engineering*. 360, 112719.

Chen, S., Zhang, M., Huang, J., Cui, C., Zhang, H. & Zhao, X. (2014) Microstructures and mechanical property of laser butt welding of titanium alloy to stainless steel. *Materials and Design*. 53, 504–511.

Chen, X., Zhang, J., Chen, X., Cheng, X. & Huang, Z. (2018) Electron beam welding of laser additive manufacturing Ti–6.5Al–3.5Mo–1.5Zr–0.3Si titanium alloy thick plate. *Vacuum*. 151, 116–121.

Choi, K.K. & Haug, E.J. (1983) Shape design sensitivity analysis of elastic structures. *Journal of Structural Mechanics*. 11 (2), 231–269.

Choo, H., Sham, K.L., Bohling, J., Ngo, A., Xiao, X., Ren, Y., Depond, P.J., Matthews, M.J. & Garlea, E. (2019) Effect of laser power on defect, texture, and microstructure of a laser powder bed fusion processed 316L stainless steel. *Materials and Design*. 164, 107534.

Combescure, A. & Jullien, J.F. (2015) ASTER Shell: a simple concept to significantly increase the plastic buckling strength of short cylinders subjected to combined external pressure and axial compression. *Advanced Modeling and Simulation in Engineering Sciences*. 2 (1), 1-27.

Crolla, K., Williams, N., Muehlbauer, M. & Burry, J. (2017) Smartnodes pavilion. In: *Proceedings of the 22nd International Conference on Computer-Aided Architectural Design Research in Asia: Protocols, Flows and Glitches*, *CAADRIA*, 5-8 April 2017, Suzhou, China.

Dassault Systèmes (2017) *Abaqus 2017* [Computer software].

Deev, A.A., Kuznetcov, P.A. & Petrov, S.N. (2016) Anisotropy of mechanical properties and its correlation with the structure of the stainless steel 316L produced by the SLM method. *Physics Procedia*. 83, 789–796.

Delgado, J., Ciurana, J. & Rodríguez, C.A. (2012) Influence of process parameters on part quality and mechanical properties for DMLS and SLM with iron-based materials. *The International Journal of Advanced Manufacturing Technology*. 60, 601–610.

Dems, K. & Mroz, Z. (1980) Optimal Shape Design of Multicomposite Structures. *Journal of Structural Mechanics*. 8 (3), 309–329.

Donnell, L.H. & Wan, C.C. (1950) Effect of Imperfections on Buckling of Thin Cylinders and Columns Under Axial Compression. *Journal of Applied Mechanics*. 17, 73–83.

Eberhart, R.C. & Kennedy, J. (1995) A new optimizer using particle swarm theory. In: *MHS'95. Proceedings of the Sixth International Symposium on Micro Machine and Human Science*. 4-6 October 1995, Nagoya, Japan.

Eberhart, R.C. & Shi, Y. (2000) Comparing inertia weights and constriction factors in particle swarm optimization. In: *Proceedings of the 2000 Congress on Evolutionary Computation. CEC00 (Cat. No.00TH8512)*. 16-19 July 2000, La Jolla, CA, United States.

EOS (2019) *EOS Stainless Steel CX Material Data Sheet*.

EOS (2017) *EOS Stainless Steel 316L*.

EOS (2010) *Technical Description EOSINT M 280*.

Farber, B., Small, K.A., Allen, C., Causton, R.J., Nichols, A., Simbolick, J. & Taheri, M.L. (2018) Correlation of mechanical properties to microstructure in Inconel 718 fabricated by Direct Metal Laser Sintering. *Materials Science and Engineering: A*. 712, 539–547.

Farshad, M. & Tadjbakhsh, I. (1973) Optimum shape of columns with general conservative end loading. *Journal of Optimization Theory and Applications*. 11 (4), 413–420.

Feng, Y., Luo, Z., Liu, Z., Li, Y., Luo, Y. & Huang, Y. (2015) Keyhole gas tungsten arc welding of AISI 316L stainless steel. *Materials and Design*. 85, 24–31.

Frazier, W.E. (2014) Metal additive manufacturing: A review. *Journal of Materials Engineering and Performance*. 23 (6), 1917–1928.

Furuya, K., Ida, M., Miyashita, M. & Nakamura, H. (2009) Mechanical properties of F82H/316L and 316L/316L welds upon the target back-plate of IFMIF. *Journal of Nuclear Materials*. 386–388, 963–966.

Galjaard, S., Hofman, S., Ren, S., Perry, N. & Ren, S. (2015) Optimizing Structural Building Elements in Metal by using Additive Manufacturing. In: *Proceedings of the International Association for Shell and Spatial Structures: Future Visions – Emerging Technologies: 3D Printing and Robotics*, *IASS 2015*, 17-20 August 2015, Amsterdam, Netherlands.

Gao, W., Zhang, Y., Ramanujan, D., Ramani, K., Chen, Y., Williams, C.B., Wang, C.C.L., Shin, Y.C., Zhang, S. & Zavattieri, P.D. (2015) The status, challenges, and future of additive manufacturing in engineering. *Computer-Aided Design*. 69, 65–89.

Gardner, L. (2002) *A new approach to structural stainless steel design*. PhD thesis. Imperial College London, London, United Kingdom.

Gardner, L. (2019) Stability and design of stainless steel structures – Review and outlook. *Thin-Walled Structures*. 141, 208–216.

Gardner, L. (2008) The continuous strength method. *Proceedings of the Institution of Civil Engineers: Structures and Buildings*. 161 (3), 127–133.

Gardner, L. & Ashraf, M. (2006) Structural design for non-linear metallic materials. *Engineering Structures*. 28 (6), 926–934.

Gardner, L., Bu, Y. & Theofanous, M. (2016) Laser-welded stainless steel I-sections: Residual stress measurements and column buckling tests. *Engineering Structures*. 127, 536–548.

Gardner, L., Wang, F., & Liew, A. (2011). Influence of strain hardening on the behavior and design of steel structures. *International Journal of Structural Stability and Dynamics*. 11(5), 855-875.

Gardner, L., Kyvelou, P., Herbert, G. & Buchanan, C. (2020) Testing and initial verification of the world's first metal 3D printed bridge. *Journal of Constructional Steel Research*. 172, 106233.

Gardner, L. & Nethercot, D.A. (2004) Experiments on stainless steel hollow sections-Part 1: Material and cross-sectional behaviour. *Journal of Constructional Steel Research*. 60 (9), 1291–1318.

Gardner, L. & Theofanous, M. (2008) Discrete and continuous treatment of local buckling in stainless steel elements. *Journal of Constructional Steel Research*. 64 (11), 1207–1216.

Gardner, L. & Yun, X. (2018) Description of stress-strain curves for cold-formed steels. *Construction and Building Materials*. 189, 527–538.

Ghasri-Khouzani, M., Peng, H., Attardo, R., Ostiguy, P., Neidig, J., Billo, R., Hoelzle, D. & Shankar, M.R. (2018) Direct metal laser-sintered stainless steel: comparison of microstructure and hardness between different planes. *International Journal of Advanced Manufacturing Technology*. 95 (9–12), 4031–4037.

Gouge, M. & Michaleris, P. (2018) An Introduction to Additive Manufacturing Processes and Their Modeling Challenges. In: *Thermo-Mechanical Modeling of Additive Manufacturing*. 3–18. Elsevier Science.

Grekavicius, L., Hughes, J.A., Tsavdaridis, K.D. & Efthymiou, E. (2016) Novel Morphologies of Aluminium Cross-Sections through Structural Topology Optimization Techniques. *Key Engineering Materials*. 710, 321-326.

Gu, D. & Shen, Y. (2008) Processing conditions and microstructural features of porous 316L stainless steel components by DMLS. *Applied Surface Science*. 255 (5), 1880–1887.

Gümrük, R. & Mines, R.A.W. (2013) Compressive behaviour of stainless steel micro-lattice structures. *International Journal of Mechanical Sciences*. 68, 125–139.

Guo, P., Zou, B., Huang, C. & Gao, H. (2017) Study on microstructure, mechanical properties and machinability of efficiently additive manufactured AISI 316L stainless steel by high-power direct laser deposition. *Journal of Materials Processing Technology*. 240, 12–22.

Guo, X., Kyvelou, P., Ye, J., Teh, L.H. & Gardner, L. (Submitted) Testing and analysis of wire arc additively manufactured steel single lap shear bolted connections. *Engineering Structures*.

Hadjipantelis, N., Weber, B., Buchanan, C. & Gardner, L. (2022) Description of anisotropic material response of wire and arc additively manufactured thin-walled stainless steel elements. *Thin-Walled Structures*. 171, 108634.

Hall, E.O. (1951) The deformation and ageing of mild steel: III Discussion of results. *Proceedings of the Physical Society. Section B*. 64 (9), 747–753. IOP Publishing Ltd.

Hao, P., Wang, B., Li, G., Meng, Z. & Wang, L. (2015) Hybrid framework for reliability-based design optimization of imperfect stiffened shells. *AIAA Journal*. 53 (10), 2878–2889.

Hao, P., Wang, B., Li, G., Tian, K., Du, K., Wang, X. & Tang, X. (2013) Surrogate-based optimization of stiffened shells including load-carrying capacity and imperfection sensitivity. *Thin-Walled Structures*. 72, 164–174.

Harraz, M., Elghany, K.A., Schleser, M., Palkowski, H. & Klingner, A. (2017) Characterization of 3D Printed Stainless Steel SS316L Powders Joined by TIG- , Plasma- and Laser Welding. In: *17th International Conference on Aerospace Sciences & Aviation Technology*, *ASAT 2017*. 11-13 April 2017, Cairo, Egypt.

Haug, E.J. & Kwak, B.M. (1978) Contcat stress minimization by contour design. *International Journal for Numerical Methods in Engineering*. 12 (6), 917–930.

He, B., Tian, X.J., Cheng, X., Li, J. & Wang, H.M. (2017) Effect of weld repair on microstructure and mechanical properties of laser additive manufactured Ti-55511 alloy. *Materials and Design*. 119, 437–445.

Heimgartner, J. (2021) *MX3D, Takenaka Use WAAM to Create Steel Connector for Construction*. https://mobile.engineering.com/amp/21300.html [Accessed: 19 January 2022].

Hill, H.N. (1944) *Determination of stress-strain relations from offset yield strength values*. Technical Notes: No. 927. National Advisory Committee for Aeronautics (NACA).

Hossain, U., Ghouse, S., Nai, K. & Jeffers, J.R. (2021) Controlling and testing anisotropy in additively manufactured stochastic structures. *Additive Manufacturing*. 39, 101849.

Hosseini, E. & Popovich, V.A. (2019) A review of mechanical properties of additively

manufactured Inconel 718. *Additive Manufacturing*. 30, 100877.

Houghton, D.S. & Chan, A.S.L. (1960) Design of a Pressurized Missile Body. *Aircraft Engineering and Aerospace Technology*. 32 (11), 320–326.

Hsu, Y. (1994) A review of structural shape optimization. *Computers in Industry*. 26, 3–13.

Huang, X. & Xie, M. (2010) *Evolutionary Topology Optimization of Continuum Structures: Methods and applications*. John Wiley & Sons, Inc.

Hussein, A.Y. (2013) *The Development of Lightweight Cellular Structures for Metal Additive Manufacturing*. 228. PhD thesis. University of Exeter, Devon, United Kingdom.

Hutchinson, J.W. & Amazioo, J.C. (1967) Imperfection-sensitivity of eccentrically stiffened cylindrical shells. *AIAA Journal*. 5 (3), 392–401.

Hutchinson, J.W. & Frauenthal, J.C. (1969) Elastic Postbuckling Behavior of Stiffened an Barreled Cylindrical Shells. *Journal of Applied Mechanics*. 36 (4), 784–790.

Huybrechts, S.M., Hahn, S.E. & Meink, T.E. (1999) Grid Stiffened Structures: a Survey of Fabrication, Analysis and Design Methods. In: *Proceedings of the 12th international conference on composite materials*. 5-9 July 1999, Paris, France.

Ibrahim, Y., Davies, C.M., Maharaj, C., Li, Z., Dear, J.P. & Hooper, P.A. (2020) Post-yield performance of additive manufactured cellular lattice structures. *Progress in Additive Manufacturing*. 5 (2), 211–220.

Imam, M.H. (1982) Three-dimensional shape optimization. *International Journal for Numerical Methods in Engineering*. 18, 661–673.

Insausti, A. & Gardner, L. (2011) Analytical modelling of plastic collapse in compressed elliptical hollow sections. *Journal of Constructional Steel Research*. 67 (4), 678–689.

Islam, M.E., Taimisto, L., Piili, H., Nyrhila, O. & Salminen, A. (2012) Comparison of theoretical and practical studies of heat input in laser assisted additive manufacturing of stainless steel. In: *Proceedings of the 37th International MATADOR Conference*. 9 October 2012, Manchester, United Kingdom.

ISO/ASTM (2017) ISO/ASTM 52900:2017. *Additive manufacturing — General principles — Terminology*. ISO/ASTM International.

Jullien, J.F. & Araar, M. (1991) Towards an optimal shape of cylindrical shell structures under external pressure. In: Jullien J.F. (ed.) *Buckling of Shell Structures, on Land, in the Sea and in the Air*. Elsevier Applied Science.

Kanyilmaz, A., Demir, A.G., Chierici, M., Berto, F., Gardner, L., Kandukuri, S.Y., Kassabian, P., Kinoshita, T., Laurenti, A., Paoletti, I., du Plessis, A. & Razavi, S.M.J. (2022) Role of Metal 3D Printing to Increase Quality and Resource-efficiency in the Construction Sector. *Additive Manufacturing*. 50, 102541.

Kell, J., Tyrer, J.R., Higginson, R.L. & Thomson, R.C. (2005) Microstructural characterization of autogenous laser welds on 316L stainless steel using EBSD and EDS. *Journal of Microscopy*. 217 (2), 167–173.

Kennedy, J. & Eberhart, R.C. (1995) Particle swarm optimization. In: *Proceedings of ICNN'95 - International Conference on Neural Networks*. 27 November-1 December 1995, Perth, WA, Australia.

Kenny, J.P. (1992) *Report of the UK cohesive buckling research programme 1983-1985, Buckling of offshore structural components*. Health and Safety Executive, Report number: OTH 90 329.

Kianersi, D., Mostafaei, A. & Amadeh, A.A. (2014) Resistance spot welding joints of AISI 316L austenitic stainless steel sheets: Phase transformations, mechanical properties and microstructure characterizations. *Materials and Design*. 61, 251–263.

Knapp, R.H. (1976) Pseudo-Cylindrical Shells: a New Concept for Undersea Structures. *Journal of Engineering for Industry*. 99 (2), 485–492.

Kocabekir, B., Kaçar, R., Gündüz, S. & Hayat, F. (2008) An effect of heat input, weld atmosphere and weld cooling conditions on the resistance spot weldability of 316L austenitic stainless steel. *Journal of Materials Processing Technology*. 195 (1–3), 327–335.

Koiter, W.T. (1970) *A Translation of the Stability of Elastic Equilibrium*. Technical Report

AFFDL-TR-70-25.

Kok, Y., Tan, X.P., Wang, P., Nai, M.L.S., Loh, N.H., Liu, E. & Tor, S.B. (2018) Anisotropy and heterogeneity of microstructure and mechanical properties in metal additive manufacturing: A critical review. *Materials and Design*. 139, 565–586.

Koons, G.L., Diba, M. & Mikos, A.G. (2020) Materials design for bone-tissue engineering. *Nature Reviews Materials*. 5 (8), 584–603.

Kreitcberg, A., Brailovski, V. & Turenne, S. (2017) Effect of heat treatment and hot isostatic pressing on the microstructure and mechanical properties of Inconel 625 alloy processed by laser powder bed fusion. *Materials Science and Engineering: A*. 689, 1–10.

Kristensen, E.S. & Madsen, N.F. (1976) On the optimum shape of fillets in plates subjected to multiple in-plane loading cases. *International Journal for Numerical Methods in Engineering.* 10, 1007–1009.

Kuwamura, H. (2003) Local buckling of thin walled stainless steel members. *Steel Structures*. 3, 191–201.

Kyvelou, P., Huang, C., Gardner, L. & Buchanan, C. (2021) Structural Testing and Design of Wire Arc Additively Manufactured Square Hollow Sections. *Journal of Structural Engineering*. 147 (12), 1–19.

Kyvelou, P., Slack, H., Daskalaki Mountanou, D., Wadee, M.A., Britton, T. Ben, Buchanan, C. & Gardner, L. (2020) Mechanical and microstructural testing of wire and arc additively manufactured sheet material. *Materials and Design*. 192, 108675.

Laghi, V., Palermo, M., Gasparini, G., Girelli, V.A. & Trombetti, T. (2020a) Experimental results for structural design of Wire-and-Arc Additive Manufactured stainless steel members. *Journal of Constructional Steel Research*. 167, 105858.

Laghi, V., Palermo, M., Gasparini, G. & Trombetti, T. (2020b) Computational design and manufacturing of a half-scaled 3D-printed stainless steel diagrid column. *Additive Manufacturing*. 36, 101505.

Lam, D. & Gardner, L. (2008) Structural design of stainless steel concrete filled columns. *Journal of Constructional Steel Research*. 64 (11), 1275–1282.

Lange, J., Feucht, T. & Erven, M. (2020) 3D printing with steel: Additive Manufacturing for connections and structures. *Steel Construction*. 13 (3), 144–153.

LaVision (2017) *DaVis 8* [Computer software].

Lebaal, N., Zhang, Y., Demoly, F., Roth, S., Gomes, S. & Bernard, A. (2019) Optimised lattice structure configuration for additive manufacturing. *CIRP Annals*. 68 (1), 117–120.

Ledbetter, H.M. (1984) Monocrystal-Polycrystal Elastic Constants of a Stainless Steel. *Physica Status Solidi (a)*. 85 (1), 89–96.

Ledbetter, H.M., Frederick, N. V. & Austin, M.W. (2008) *Elastic-constant variability in stainless-steel 304*. *Journal of Applied Physics*. 51 (1), 304–309.

Leicht, A., Klement, U. & Hryha, E. (2018) Effect of build geometry on the microstructural development of 316L parts produced by additive manufacturing. *Materials Characterization*. 143, 137–143.

Leitão, C., Galvão, I., Leal, R.M. & Rodrigues, D.M. (2012) Determination of local constitutive properties of aluminium friction stir welds using digital image correlation. *Materials and Design*. 33 (1), 69–74.

Li, H.X., Qi, H.L., Song, C.H., Li, Y.L. & Yan, M. (2018) Selective laser melting of P20 mould steel: investigation on the resultant microstructure, high-temperature hardness and corrosion resistance. *Powder Metallurgy*. 61 (1), 21–27.

Li, R., Liu, J., Shi, Y., Du, M. & Xie, Z. (2010) 316L stainless steel with gradient porosity fabricated by selective laser melting. *Journal of Materials Engineering and Performance*. 19 (5), 666–671.

Li, Y., Hu, S., Shen, J., Hu, B., Li, Y., Hu, S., Shen, J. & Hu, B. (2014) *Dissimilar Welding of H62 Brass-316L Stainless Steel Using Continuous-Wave Nd : YAG Laser*. 29 (8), 916-921.

Liew, A. & Gardner, L. (2015) Ultimate capacity of structural steel cross-sections under

compression, bending and combined loading. *Structures*. 1, 2–11.

Lim, S., Buswell, R.A., Le, T.T., Austin, S.A., Gibb, A.G.F. & Thorpe, T. (2012) Developments in construction-scale additive manufacturing processes. *Automation in Construction*. 21 (1), 262–268.

Liverani, E., Toschi, S., Ceschini, L. & Fortunato, A. (2017) Effect of selective laser melting (SLM) process parameters on microstructure and mechanical properties of 316L austenitic stainless steel. *Journal of Materials Processing Technology*. 249, 255–263.

López Jiménez, F. & Triantafyllidis, N. (2013) Buckling of rectangular and hexagonal honeycomb under combined axial compression and transverse shear. *International Journal of Solids and Structures*. 50 (24), 3934–3946.

Luchi, M.L., Poggialini, A. & Persiani, F. (1980) An interactive optimization procedure applied to the design of gas turbine discs. *Computers & Structures*. 11 (6), 629–637.

Ma, J.L., Chan, T.M. & Young, B. (2016) Experimental Investigation on Stub-Column Behavior of Cold-Formed High-Strength Steel Tubular Sections. *Journal of Structural Engineering*. 142 (5), 04015174.

Malek, S., Ochsendorf, J. & Wierzbicki, T. (2011) Failure limits of shallow grid shells: The physics behind the concept of equivalent thickness and numerical validation. In: *Proceedings of the International Association for Bridge and Structural Engineers and the International Association for Shell and Spatial Structures (IABSE-IASS) Symposium*. London, United Kingdom.

Mathworks (2018) *Matlab R2018b* [Computer software].

Matilainen, V.P., Pekkarinen, J. & Salminen, A. (2016) Weldability of Additive Manufactured Stainless Steel. *Physics Procedia*. 83, 808–817.

Meier, H. & Haberland, C. (2008) Experimental studies on selective laser melting of metallic parts. *Materialwissenschaft und Werkstofftechnik*. 39 (9), 665–670.

Meng, X. & Gardner, L. (2020a) Cross-sectional behaviour of cold-formed high strength steel

circular hollow sections. *Thin-Walled Structures*. 156, 106822.

Meng, X. & Gardner, L. (2020b) Simulation and design of semi-compact elliptical hollow sections. *Engineering Structures*. 202, 109807.

Meng, X. & Gardner, L. (2020c) Testing of hot-finished high strength steel SHS and RHS under combined compression and bending. *Thin-Walled Structures*. 148, 106262.

Meng, X., Gardner, L., Sadowski, A.J. & Rotter, J.M. (2020) Elasto-plastic behaviour and design of semi-compact circular hollow sections. *Thin-Walled Structures*. 148, 106486.

Meng, Z., Hao, P., Li, G., Wang, B. & Zhang, K. (2015) Non-probabilistic reliability-based design optimization of stiffened shells under buckling constraint. *Thin-Walled Structures*. 94, 325–333.

Meps (2020) *Europe stainless steel prices*. https://www.meps.co.uk/gb/en/products/europe-stainless-steel-prices [Accessed: 2 September 2020].

Mertens, A., Reginster, S., Contrepois, Q., Dormal, T., Lemaire, O. & Lecomte-Beckers, J. (2014) Microstructures and Mechanical Properties of Stainless Steel AISI 316L Processed by Selective Laser Melting. *Materials Science Forum*. 783–786, 898–903.

Michell, A.G.M. (1904) The limits of economy of material in frame-structures. *Philosophical Magazine and Journal of Science*. 8 (47), 589–597.

Mirambell, E. & Real, E. (2000) On the calculation of deflections in structural stainless steel beams: An experimental and numerical investigation. *Journal of Constructional Steel Research*. 54 (1), 109–133.

Molak, R.M., Paradowski, K., Brynk, T., Ciupinski, L., Pakiela, Z. & Kurzydlowski, K.J. (2009) Measurement of mechanical properties in a 316L stainless steel welded joint. *International Journal of Pressure Vessels and Piping*. 86 (1), 43–47.

Montero Sistiaga, M., Nardone, S., Hautfenne, C. & Van Humbeeck, J. (2016) Effect of heat treatment of 316L stainless steel produced by selective laser melting (SLM). *Solid Freeform Fabrication 2016: Proceedings of the 27th Annual International Solid Freeform Fabrication*

Symposium - An Additive Manufacturing Conference, *SFF 2016*. 8-10 August 2016. Texas, United States.

Mower, T.M. & Long, M.J. (2016) Mechanical behavior of additive manufactured, powder-bed laser-fused materials. *Materials Science and Engineering A*. 651, 198–213.

Muhammad, F., Ahmad, A., Farooq, A. & Haider, W. (2016) Effect of Post-Weld Heat Treatment on Mechanical and Electrochemical Properties of Gas Metal Arc-Welded 316L (X2CrNiMo 17-13-2) Stainless Steel. *Journal of Materials Engineering and Performance*. 25 (10), 4283–4291.

Munz, O.J. (1956) Photo-Glyph Recording. *United States Patent Office*.

MX3D (2021) *WAAM for architecture and construction*. https://mx3d.com/industries/architecture-construction/ [Accessed: 19 January 2022].

NASA (1968) NASA SP-8007. *Bucking of Thin Walled Circular Cylinders*. National Aeronautics and Space Administration (NASA).

NASA (2020) NASA/SP-8007-2020/REV 2. *Buckling of Thin-Walled Circular Cylinders*. National Aeronautics and Space Administration (NASA).

Ngo, T.D., Kashani, A., Imbalzano, G., Nguyen, K.T.Q. & Hui, D. (2018) Additive manufacturing (3D printing): A review of materials, methods, applications and challenges. *Composites Part B: Engineering*. 143, 172–196.

Niendorf, T., Brenne, F., Krooß, P., Vollmer, M., Günther, J., Schwarze, D. & Biermann, H. (2016) Microstructural Evolution and Functional Properties of Fe-Mn-Al-Ni Shape Memory Alloy Processed by Selective Laser Melting. *Metallurgical and Materials Transactions A: Physical Metallurgy and Materials Science*. 47 (6), 2569–2573.

Niendorf, T., Leuders, S., Riemer, A., Richard, H.A., Tröster, T. & Schwarze, D. (2013) Highly anisotropic steel processed by selective laser melting. *Metallurgical and Materials Transactions B: Process Metallurgy and Materials Processing Science*. 44 (4), 794–796.

Ning, X. & Pellegrino, S. (2017) Experiments on imperfection insensitive axially loaded

cylindrical shells. *International Journal of Solids and Structures*. 115–116, 73–86.

Ning, X. & Pellegrino, S. (2015) Imperfection-insensitive axially loaded thin cylindrical shells. *International Journal of Solids and Structures*. 62, 39–51.

Olakanmi, E.O., Cochrane, R.F. & Dalgarno, K.W. (2015) A review on selective laser sintering/melting (SLS/SLM) of aluminium alloy powders: Processing, microstructure, and properties. *Progress in Materials Science*. 74, 401–477.

Ozdemir, D. (2021) *Germany's First 3D-Printed Residential Building is Near Completion*. https://interestingengineering.com/germanys-first-3d-printed-residential-building-is-near-completion.

Panda, B., Leite, M., Biswal, B.B., Niu, X. & Garg, A. (2018) Experimental and numerical modelling of mechanical properties of 3D printed honeycomb structures. *Measurement*. 116, 495–506.

Panesar, A., Abdi, M., Hickman, D. & Ashcroft, I. (2018) Strategies for functionally graded lattice structures derived using topology optimisation for Additive Manufacturing. *Additive Manufacturing*. 19, 81–94.

Petch, N.J. (1953) The Cleavage Strength of Polycrystals. *Journal of the Iron and Steel Institute*. 174, 25–28.

Pham, M.S., Dovgyy, B., Hooper, P.A., Gourlay, C.M. & Piglione, A. (2020) The role of side-branching in microstructure development in laser powder-bed fusion. *Nature Communications*. 11 (1), 1–12.

Pham, T.Q. (2021) *A Feasibility Study of Non-Homogeneous Soft Magnetic Core for Electrical Machines - an Application of Additive Manufacturing*. PhD thesis, Michigan State University, Michigan, United States.

Popovich, A., Sufiiarov, V., Polozov, I., Borisov, E., Masaylo, D. & Orlov, A. (2016) Microstructure and mechanical properties of additive manufactured copper alloy. *Materials Letters*. 179, 38–41.

Rafi, H.K., Starr, T.L. & Stucker, B.E. (2013) A comparison of the tensile, fatigue, and fracture behavior of Ti-6Al-4V and 15-5 PH stainless steel parts made by selective laser melting. *International Journal of Advanced Manufacturing Technology*. 69 (5–8), 1299–1309.

Rahimi, G.H., Zandi, M. & Rasouli, S.F. (2013) Analysis of the effect of stiffener profile on buckling strength in composite isogrid stiffened shell under axial loading. *Aerospace Science and Technology*. 24 (1), 198–203.

Ramberg, W. & Osgood, W.R. (1943) *Description of stress-strain curves by three parameters*.

Rasband, W.S. (1997) *ImageJ* [Computer software].

Rasmussen, B.K.J.R. & Hancock, G.J. (1993) Design of cold-formed stainless steel tubular members. I: Columns. *Journal of Structural Engineering*. 119 (8), 2349–2367.

Rasmussen, K.J.R. (2003) Full-range stress–strain curves for stainless steel alloys. *Journal of Constructional Steel Research*. 59 (1), 47–61.

Rasmussen, K.J.R. (2000) Recent research on stainless steel tubular structures. *Journal of Constructional Steel Research*. 54 (1), 75–88.

Reitinger, R., Bletzinger, K.U. & Ramm, E. (1994) Shape optimization of buckling sensitive structures. *Computing Systems in Engineering*. 5 (1), 65–75.

Reitinger, R. & Ramm, E. (1995) Buckling and imperfection sensitivity in the optimization of shell structures. *Thin-Walled Structures*. 23, 159–177.

Ren, S. & Galjaard, S. (2015) Topology Optimisation for Steel Structural Design with Additive Manufacturing. In: *Proceedings of Design Modelling Symposium 2015*. 30 September-2 October 2015. Copenhagen, Demark.

Reynolds, A.P. & Duvall, F. (1999) Digital Image Correlation for Determination of Weld and Base Metal Constitutive Behavior. *Welding Research Supplement*. 355–360.

Robert McNeel & Associates (2012) *Rhinoceros 5.0* [Computer software].

Rosenthal, I., Stern, A. & Frage, N. (2014) Microstructure and Mechanical Properties of

AlSi10Mg Parts Produced by the Laser Beam Additive Manufacturing (AM) Technology. *Metallography, Microstructure, and Analysis*. 3 (6), 448–453.

Rossini, M., Spena, P.R., Cortese, L., Matteis, P. & Firrao, D. (2015) Investigation on dissimilar laser welding of advanced high strength steel sheets for the automotive industry. *Materials Science and Engineering A*. 628, 288–296.

Ruffo, M., Tuck, C. & Hague, R. (2006) Cost estimation for rapid manufacturing - Laser sintering production for low to medium volumes. *Proceedings of the Institution of Mechanical Engineers, Part B: Journal of Engineering Manufacture*. 220 (9), 1417–1427.

Sanjari, M., Hadadzadeh, A., Pirgazi, H., Shahriari, A., Amirkhiz, B.S., Kestens, L.A.I. & Mohammadi, M. (2020) Selective laser melted stainless steel CX: Role of built orientation on microstructure and micro-mechanical properties. *Materials Science and Engineering: A*. 786, 139365.

Schafer, B.W. Gigoriu, M. & Pekoz, T. (1996) A Probabilistic Examination of the Ultimate Strength of Cold-formed Steel Elements. In: *13th International Specialty Conference on Cold-Formed Steel Structures*. 17 October 1996, Missouri, United States.

Schafer, B.W. & Peköz, T. (1998) Computational modeling of cold-formed steel: characterizing geometric imperfections and residual stresses. *Journal of Constructional Steel Research*. 47 (3), 193–210.

SCI (2017) *Design Manual for Structural Stainless Steel*. 4th edition. London, The Steel Construction Institute (SCI).

Seifi, H. (2019) *Topology Optimisation and Additive Manufacturing of Structural Nodes of Gridshell Structures*. PhD thesis, RMIT University, Melbourne, Australia.

Seifi, H., Xie, M., O'Donnell, J. & Williams, N. (2016) Design and Fabrication of Structural Connections Using Bi-Directional Evolutionary Structural Optimization and Additive Manufacturing. *Applied Mechanics and Materials*. 846, 571–576.

Shayan, S., Rasmussen, K.J.R. & Zhang, H. (2014) On the modelling of initial geometric imperfections of steel frames in advanced analysis. *Journal of Constructional Steel Research*.

98, 167–177.

Shi, Y. & Eberhart, R.C. (1998) A Modified Particle Swarm Optimizer. In: *Proceedings of IEEE World Congress on Computational Intelligence (Cat. No.98TH8360)*, 4-9 May 1998, Anchorage, AK, United States.

Shi, Y. & Eberhart, R.C. (1999) Empirical Study of Particle Swarm Optimization. In: *Proceedings of the 1999 Congress on Evolutionary Computation-CEC99* (*Cat. No. 99TH8406*), 6-9 July 1999, Washington, DC, United States.

Shu, G., Gu, Y., Zhang, Y., Jin, X., Zheng, B. & Jiang, Q. (2019) Experimental study of cold-drawn duplex stainless steel circular tubes under axial compression. *Thin-Walled Structures*. 138, 95–104.

Simpson, T.W. (2018) *Why does my 3D-printed part cost so much?* https://www.additivemanufacturing.media/blog/post/why-does-my-3d-printed-part-cost-so-much [Accessed: 2 September 2020].

Singer, J., Arbocz, J. & Babcock, C.D. (1971) Buckling of imperfect stiffened cylindrical shells under axial compression. *AIAA Journal*. 9 (1), 68–75.

Singer, J., Baruch, M. & Harari, O. (1967) On the stability of eccentrically stiffened cylindrical shells under axial compression. *International Journal of Solids and Structures*. 3 (4), 445–470.

Smith, C.J., Gilbert, M., Todd, I. & Derguti, F. (2016) Application of layout optimization to the design of additively manufactured metallic components. *Structural and Multidisciplinary Optimization*. 54 (5), 1297–1313.

Song, Y., Li, Y., Song, W., Yee, K., Lee, K.Y. & Tagarielli, V.L. (2017) Measurements of the mechanical response of unidirectional 3D-printed PLA. *Materials and Design*. 123, 154–164.

Spierings, A.B., Herres, N. & Levy, G. (2011a) Influence of the particle size distribution on surface quality and mechanical properties in AM steel parts. *Rapid Prototyping Journal*. 17 (3), 195–202.

Spierings, A.B., Herres, N. & Levy, G. (2011b) Influence of the particle size distribution on

surface quality and mechanical properties in AM steel parts. *Rapid Prototyping Journal*. 17 (3), 195–202.

Stangenberg, H. (2000) *Report to the ECSC-Draft final report ferritic stainless steels*.

Stefanou, G. (2011) Response variability of cylindrical shells with stochastic non-Gaussian material and geometric properties. *Engineering Structures*. 33 (9), 2621–2627.

Storn, R. & Kenneth, P. (1997) Differential Evolution – A Simple and Efficient Heuristic for Global Optimization over Continuous Spaces. *Journal of Global optimization*, 11, 341–359.

Strauß, H. & Knaack, U. (2016) Additive Manufacturing for Future Facades: The potential of 3D printed parts for the building envelope. *Journal of Facade Design and Engineering*. 3 (3–4), 225–235.

Su, M.N., Young, B. & Gardner, L. (2016) The continuous strength method for the design of aluminium alloy structural elements. *Engineering Structures*. 122, 338–348.

Sun, Z., Tan, X., Tor, S.B. & Yeong, W.Y. (2016) Selective laser melting of stainless steel 316L with low porosity and high build rates. *Materials and Design*. 104, 197–204.

Suryawanshi, J., Prashanth, K.G. & Ramamurty, U. (2017) Mechanical behavior of selective laser melted 316L stainless steel. *Materials Science and Engineering: A*. 696, 113–121.

Talja, A. (1997) *Test report on welded I and CHS beams, columns and beam-columns*. Technical Research Centre of Finland (VTT).

Teng, J.G., Lin, X., Rotter, J.M. & Ding, X.L. (2005) Analysis of geometric imperfections in full-scale welded steel silos. *Engineering Structures*. 27 (6), 938–950.

Teng, J.G. & Rotter, J.M. (2004) *Buckling of Imperfect Cylinders*.

Tian, K., Wang, B., Zhang, K., Zhang, J., Hao, P. & Wu, Y. (2018) Tailoring the optimal load-carrying efficiency of hierarchical stiffened shells by competitive sampling. *Thin-Walled Structures*. 133, 216–225.

Tjong, S.C., Zhu, S.M., Ho, N.J. & Ku, J.S. (1995) Microstructural characteristics and creep

rupture behavior of electron beam and laser welded AISI 316L stainless steel. *Journal of Nuclear Materials*. 227 (1–2), 24–31.

Tolosa, I., Garciandía, F., Zubiri, F., Zapirain, F. & Esnaola, A. (2010) Study of mechanical properties of AISI 316 stainless steel processed by "selective laser melting", following different manufacturing strategies. *International Journal of Advanced Manufacturing Technology*. 51 (5–8), 639–647.

Tomashchuk, I., Grevey, D. & Sallamand, P. (2015) Dissimilar laser welding of AISI 316L stainless steel to Ti6–Al4–6V alloy via pure vanadium interlayer. *Materials Science and Engineering: A*. 622, 37–45.

Tomlin, M. & Meyer, J. (2011) Topology Optimization of an Additive Layer Manufactured (ALM) Aerospace Part. In: *The 7th Altair CAE Technology Conference 2011*.

Tomus, D., Tian, Y., Rometsch, P.A., Heilmaier, M. & Wu, X. (2016) Influence of post heat treatments on anisotropy of mechanical behaviour and microstructure of Hastelloy-X parts produced by selective laser melting. *Materials Science and Engineering: A*. 667, 42–53.

Trelewicz, J.R., Halada, G.P., Donaldson, O.K. & Manogharan, G. (2016) Microstructure and Corrosion Resistance of Laser Additively Manufactured 316L Stainless Steel. *Jom*. 68 (3), 850–859.

Tsavdaridis, K.D., Hughes, J.A., Grekavicius, L. & Efthymiou, E. (2017) Novel Optimised Structural Aluminium Cross-Sections Towards 3D Printing. In: *Meboldt, M. & Klahn, C. (eds.) Industrializing Additive Manufacturing – Proceedings of the Conference on Additive Manufacturing in Products and Applications, AMPA 2017*, 13-15 September 2017, Zurich, Switzerland.

TU Darmstadt (2019) *3D-printed bridge on the Lichtwiese*.

Umetani, Y. & Hirai, S. (1978) Shape optimisation for beams subject to displacement restrictions on the basis of the growing-reforming procedure. *Chemical Pharmaceutical Bulletin*. 21 (157), 1113–1119.

Uy, B., Tao, Z. & Han, L.H. (2011) Behaviour of short and slender concrete-filled stainless

steel tubular columns. *Journal of Constructional Steel Research*. 67 (3), 360–378.

Ventrella, V.A., Berretta, J.R. & Rossi, W. (2010) Pulsed Nd:YAG laser seam welding of AISI 316L stainless steel thin foils. *Journal of Materials Processing Technology*. 210 (14), 1838–1843.

Vilaro, T., Colin, C., Bartout, J.D., Nazé, L. & Sennour, M. (2012) Microstructural and mechanical approaches of the selective laser melting process applied to a nickel-base superalloy. *Materials Science and Engineering A*. 534, 446–451.

Von Karman, T. & Tsien, H.S. (1941) The Buckling of Thin Cylindrical Shells Under Axial Compression. *Journal of the Aeronautical Sciences*. 8 (8), 303–312.

Wang, B., Hao, P., Li, G., Zhang, J.X., Du, K.F., Tian, K., Wang, X.J. & Tang, X.H. (2014) Optimum design of hierarchical stiffened shells for low imperfection sensitivity. *Acta Mechanica Sinica/Lixue Xuebao*. 30 (3), 391–402.

Wang, B., Tian, K., Zhou, C., Hao, P., Zheng, Y., Ma, Y. & Wang, J. (2017) Grid-pattern optimization framework of novel hierarchical stiffened shells allowing for imperfection sensitivity. *Aerospace Science and Technology*. 62, 114–121.

Wang, D., Song, C., Yang, Y. & Bai, Y. (2016) Investigation of crystal growth mechanism during selective laser melting and mechanical property characterization of 316L stainless steel parts. *Materials and Design*. 100, 291–299.

Wang, J. & Gardner, L. (2017) Flexural Buckling of Hot-Finished High-Strength Steel SHS and RHS Columns. *Journal of Structural Engineering*. 143 (6), 04017028.

Wardenier, J. (2001) *Hollow Sections in Structural Applications*. Delft University of Technology, Netherlands.

Week, M. & Stelnke, P. (1983) An Efficient Technique in Shape Optimization. *Journal of Structural Mechanics*. 11 (4), 433–449.

Weingarten, V. I., Seide, P. & Peterson, J. P. (1968) Buckling of thin-walled circular cylinders. *NASA SP-8007*. 2019.

Weingarten, V.I., Morgan, E.J. & Seide, P. (1965) Elastic stability of thin-walled cylindrical and conical shells under axial compression. *AIAA Journal*. 3 (3), 500–505.

Wen, S., Li, S., Wei, Q., Yan, C., Zhang, S. & Shi, Y. (2014) Effect of molten pool boundaries on the mechanical properties of selective laser melting parts. *Journal of Materials Processing Technology*. 214 (11), 2660–2667.

Åkerström, T., Jernström, C. & Wierzbicki, T. (1981) Shape Optimisation of Sheet Metal Structures against Crash. *SAE Transactions*. 90, 4091-4101.

Wolfsburg, M. (2018) *World premiere: brake caliper from 3-d printer*. https://www.bugatti.com/media/news/2018/world-premiere-brake-caliper-from-3-d-printer/ [Accessed: 18 January 2022].

Wu, P., Wang, J. & Wang, X. (2016) A critical review of the use of 3-D printing in the construction industry. *Automation in Construction*. 68, 21–31.

Yadav, K.K. & Gerasimidis, S. (2019) Imperfection insensitive thin steel tubular shells under bending. In: *Structural Stability Research Council Annual Stability Conference* 2019, SSRC 2019. 2-5 May 2019, Missouri, United States.

Yadav, K.K. & Gerasimidis, S. (2020) Imperfection insensitive thin cylindrical shells for next generation wind turbine towers. *Journal of Constructional Steel Research*. 172, 106228.

Yadollahi, A., Shamsaei, N., Thompson, S.M. & Seely, D.W. (2015) Effects of process time interval and heat treatment on the mechanical and microstructural properties of direct laser deposited 316L stainless steel. *Materials Science and Engineering: A*. 644, 171–183.

Yan, J.J., Chen, M.T., Quach, W.M., Yan, M. & Young, B. (2019) Mechanical properties and cross-sectional behavior of additively manufactured high strength steel tubular sections. *Thin-Walled Structures*. 144, 106158.

Yang, J., Wang, Y., Li, F., Huang, W., Jing, G., Wang, Z. & Zeng, X. (2019) Weldability, microstructure and mechanical properties of laser-welded selective laser melted 304 stainless steel joints. *Journal of Materials Science & Technology*. 35 (9), 1817–1824.

Yao, Y., Huang, Y., Chen, B., Tan, C., Su, Y. & Feng, J. (2018) Influence of processing parameters and heat treatment on the mechanical properties of 18Ni300 manufactured by laser based directed energy deposition. *Optics & Laser Technology*. 105, 171–179.

Ye, J., Becque, J., Hajirasouliha, I., Mojtabaei, S.M. & Lim, J.B.P. (2018) Development of optimum cold-formed steel sections for maximum energy dissipation in uniaxial bending. *Engineering Structures*. 161, 55-67.

Ye, J., Hajirasouliha, I., Becque, J. & Eslami, A. (2016) Optimum design of cold-formed steel beams using Particle Swarm Optimisation method. *Journal of Constructional Steel Research*. 122, 80–93.

Ye, J., Kyvelou, P., Gilardi, F., Lu, H., Gilbert, M. & Gardner, L. (2021) An End-to-End Framework for the Additive Manufacture of Optimized Tubular Structures. *IEEE Access*. 9, 165476–165489.

Yoshimura Y. (1955) *On the mechanism of buckling of a circular cylindrical shell under axial compression*. National Advisory Committee for Aeronautics (*NACA*).

Young, B. & Hartono, W. (2002) Compression Tests of Stainless Steel Tubular Members. *Journal of Structural Engineering*. 128 (6), 754–761.

Yu, C. & Schafer, B. (2004) *Distortional Buckling of cand Z members in bending*. CFSRC Report, American Iron and Steel Institute, Baltimore, Maryland.

Yu, H., Li, F., Yang, J., Shao, J., Wang, Z. & Zeng, X. (2018) Investigation on laser welding of selective laser melted Ti-6Al-4V parts: Weldability, microstructure and mechanical properties. *Materials Science and Engineering: A*. 712, 20–27.

Yun, X. & Gardner, L. (2018) Numerical modelling and design of hot-rolled and cold-formed steel continuous beams with tubular cross-sections. *Thin-Walled Structures*. 132, 574–584.

Yun, X. & Gardner, L. (2017) Stress-strain curves for hot-rolled steels. *Journal of Constructional Steel Research*. 133, 36–46.

Yusuf, S.M., Chen, Y., Boardman, R., Yang, S. & Gao, N. (2017) Investigation on porosity and

microhardness of 316L stainless steel fabricated by selective laser melting. *Metals*. 7 (2), 1–12.

Zeinoddini, V.M. & Schafer, B.W. (2012) Simulation of geometric imperfections in cold-formed steel members using spectral representation approach. *Thin-Walled Structures*. 60, 105–117.

Zhang, B., Dembinski, L. & Coddet, C. (2013) The study of the laser parameters and environment variables effect on mechanical properties of high compact parts elaborated by selective laser melting 316L powder. *Materials Science and Engineering: A*. 584, 21–31.

Zhang, C., Bao, Y., Zhu, H., Nie, X., Zhang, W., Zhang, S. & Zeng, X. (2019a) A comparison between laser and TIG welding of selective laser melted AlSi10Mg. *Optics & Laser Technology*. 120, 105696.

Zhang, H., Xu, M., Liu, Z., Li, C., Kumar, P., Liu, Z. & Zhang, Y. (2021a) Microstructure, surface quality, residual stress, fatigue behavior and damage mechanisms of selective laser melted 304L stainless steel considering building direction. *Additive Manufacturing*. 46, 102147.

Zhang, L., Song, B., Zhao, A., Liu, R., Yang, L. & Shi, Y. (2019b) Study on mechanical properties of honeycomb pentamode structures fabricated by laser additive manufacturing: Numerical simulation and experimental verification. *Composite Structures*. 226, 111199.

Zhang, M., Sun, C.N., Zhang, X., Goh, P.C., Wei, J., Hardacre, D. & Li, H. (2017) Fatigue and fracture behaviour of laser powder bed fusion stainless steel 316L: Influence of processing parameters. *Materials Science and Engineering: A*. 703, 251–261.

Zhang, R., Buchanan, C., Matilainen, V.P., Daskalaki-Mountanou, D., Britton, T. Ben, Piili, H., Salminen, A. & Gardner, L. (2021b) Mechanical properties and microstructure of additively manufactured stainless steel with laser welded joints. *Materials and Design*. 208, 109921.

Zhang, R., Gardner, L., Amraei, M., Buchanan, C. & Piili, H. (Submitted) Testing and analysis of additively manufactured corrugated cylindrical shells in compression. *Journal of Engineering Mechanics*.

Zhang, R., Gardner, L., Buchanan, C., Matilainen, V.P., Piili, H. & Salminen, A. (2021c)

Testing and analysis of additively manufactured stainless steel CHS in compression. *Thin-Walled Structures*. 159, 107270.

Zhang, R., Gardner, L., Meng, X., Buchanan, C., Matilainen, V.P., Piili, H., & Salminen, A. (2021d). Optimisation and compressive testing of additively manufactured stainless steel corrugated shells. In *Proceedings of Eurosteel 2021 – 9th European Conference on Steel and Composite Structures*, 1–3 September, Sheffield, UK.

Zhang, R., Meng, X. & Gardner, L. (Submitted) Shape optimisation of stainless steel corrugated cylindrical shells for additive manufacturing. *Engineering Structures*.

Zhang, Z., Shi, G., Hou, L. & Zhou, L. (2021e) Geometric dimension and imperfection measurements of box-T section columns using 3D scanning. *Journal of Constructional Steel Research*. 183, 106742.

Zhao, O., Afshan, S. & Gardner, L. (2017) Structural response and continuous strength method design of slender stainless steel cross-sections. *Engineering Structures*. 140, 14–25.

Zhao, O., Gardner, L. & Young, B. (2016a) Structural performance of stainless steel circular hollow sections under combined axial load and bending - Part 1: Experiments and numerical modelling. *Thin-Walled Structures*. 101, 231–239.

Zhao, O., Gardner, L. & Young, B. (2016b) Testing and numerical modelling of austenitic stainless steel CHS beam-columns. *Engineering Structures*. 111, 263–274.

Ziemian, R.D. (2010) *Guide to stability Design Criteria for Metal Structures*. 6th edition. John Wiley & Sons, Inc.